A new approach to model the kinematics of crustal deformation

with applications to the Aegean and Southeast Asia

Proefschrift

ter verkrijging van de graad van doctor
aan de Technische Universiteit Delft,
op gezag van de Rector Magnificus prof.ir. K.F. Wakker,
voorzitter van het College voor Promoties,
in het openbaar te verdedigen op maandag 29 oktober 2001 om 16.00 uur
door Marleen Catharina Johanna NYST
doctorandus in de geofysica,
geboren te Rotterdam.

Dit proefschrift is goedgekeurd door de promotoren:
Prof.ir. B.A.C. Ambrosius
Prof.dr. W. Spakman

Samenstelling promotiecommissie:

Rector Magnificus,	voorzitter
Prof.ir. B.A.C. Ambrosius,	Technische Universiteit Delft, promotor
Prof.dr. W. Spakman,	Universiteit Utrecht, promotor
Prof.dr. R.A.P. Klees,	Technische Universiteit Delft
Prof.dr. H.-G. Kahle,	Eidgenössische Technische Hochschule Zürich
Prof.dr. M.J.R. Wortel,	Universiteit Utrecht
Dr. R. Reilinger,	Massachusetts Institute of Technology
Dr. C. Vigny,	École Normale Supérieure

Published and distributed by: DUP Science

DUP Science is an imprint of
Delft University Press
P. O. Box 98
2600 MG Delft
The Netherlands
Telephone: +31 15 2785678
Telefax: +31 15 2785706
E-mail: DUP@Library.TUDelft.NL

ISBN 90-407-2235-8

Keywords: crustal deformation, Aegean, Southeast Asia

Printed in The Netherlands

‘What, indeed, if you look from a mountain top down the long wastes of the ages? The very stone one kicks with one’s boot will outlast Shakespeare. His own little light would shine, not very brightly, for a year or two, and would then be merged in some bigger light, and that in a bigger still.’

Virginia Woolf, To the lighthouse

Voor mijn ouders

Contents

Summary

An important factor in the study of lithospheric deformation is an accurate representation of the kinematics of the Earth's crust. This thesis presents a new inversion method, introduced in the first part of chapter 2, to model the present-day kinematics of the deformation field of the Earth's surface by the use of (space) geodetic measurements of relative motion. The aim of the method is to represent the kinematics of the crustal deformation field without implicitly relating kinematics to the style of deformation at depth and without restrictions about the spatial scale of the region under consideration.

The method inverts relative motions between all pairs of stations of a particular velocity data set (in this thesis mainly GPS data), in a regularized least-squares approach, for the velocity gradient field in crustal blocks and for fault motion on the active faults or block boundaries. The incorporation of fault motion is motivated by the fact that the velocity field of the Earth's crust on short time scales, as represented by space geodetic data, is not necessarily a continuous function of spatial coordinates. Faults accommodate slip and represent boundaries between moving plates or blocks, whatever the deformation at depth may be.

In the second part of chapter 2 the method is tested on a synthetic velocity field. The synthetic velocities sample a region intersected by two, freely slipping faults and represent a deformation field that results from the application of shear stresses assuming an elastic rheology. Results demonstrate that the method works well in obtaining joint estimates of the velocity gradient field and slip on active faults. The data are fit within their error bounds for solutions that are well resolved and have acceptable covariance. Model misfit patterns can be sufficiently minimized and basically can be understood as a combination of lack of data and absence of a constraint on the coupling between fault position and velocity gradient field, the latter as a direct result of the purely kinematic definition of the method.

To investigate the performance of the method in modeling continental deformation patterns it is applied to a relatively dense data set, which samples the Aegean velocity field, as a first application to the real Earth in chapter 3. Comparison between a solution for the lateral velocity gradient field only (I) and a solution for the lateral velocity gradient field and horizontal fault motion (II), in which the main fault zones and plate-boundaries are incorporated, shows that the main differences are found at the areas, where faults accommodate strong slip rates. Besides decrease of the average magnitude, the spatial distribution of the velocity gradient field is different. Further exploration of the trade-off between fault motion and the velocity gradient field shows that parameterization of large faults only renders a continuous deformation solution that probably represents slip on non-parameterized faults combined with distributed deformation in the crust. If only observation sites are used far away from faults, the estimated fault slip reflects predominantly (long term) crustal block motion, i.e. independent of fault locking. If sites are used close to faults, the actual fault motion prevails in the estimate which includes obtaining zero motion if a fault has been locked during the observation period. Insignificant slip rates in combination with strong variations in the velocity gradient near the fault trace suggest fault locking and/or surface creep processes associated with fault activity at depth. Using observation sites close to faults is the

only possibility to reduce trade-off effects.

In general, the properties of solution I agree with results from earlier geodetic studies solving for the lateral velocity gradient field on regional and local scale. From comparison of solutions I and II with shallow earthquake and stress data both patterns of agreement and disagreement are found. Possible causes for these discrepancies are errors in the model, errors in the moment tensor estimates or differences between the near surface and deeper crustal deformation, the latter suggesting that combining geodetic data with moment tensor solutions is not straightforward. Solution II enables to define the distribution of crustal deformation in terms of concentrated deformation (i.e. fault motion) confined to the main fault zones of the Aegean region and distributed deformation of fault-bounded blocks. The good agreement between orientations of the derived slip solution and geological observations and geodetic derivations and the consistency found between rotation rate results and young paleomagnetic observations suggest that solution II reflects larger-scale crustal block motion. A new, detailed view on the present-day kinematics of the Aegean crustal deformation field is presented.

To investigate the performance of the method in modeling the kinematics of crustal deformation of larger-scale regions where the interaction of tectonic (micro-)plates determines the surface velocity field, the final application of the method, presented in chapter 4, is to a combination of GPS data sets obtained in Southeast Asia. Although the data densely sample some regions within the plate boundary zones of Southeast Asia, the overall density necessitates to apply a relatively sparse parameterization for the whole model region. Comparison of a solution for the lateral velocity gradient field only (I) with a solution for the lateral velocity gradient field and fault motion (II) shows that the velocity gradient field of solution I is relatively strong at the interiors of the plates, whereas the main deformation features of solution II are located in the plate boundary zones. Inversion for the velocity gradient field and fault motion simultaneously enables the accommodation of localized motion on faults or plate boundaries and offers insight in the distribution of relative plate motion in plate boundary zones in terms of slip, (micro-)block rotation and strain rates.

Chapter 1

Background and motivation

1.1 Introduction

During the last 20 years methods and technology to measure active deformation of the Earth's crust have improved impressively. In particular this has resulted in a strongly increased accuracy of space geodetic data derived from the Global Positioning System (GPS), Satellite Laser Ranging (SLR), Synthetic Aperture Radar Interferometry (InSAR) and Very Long Baseline Interferometry (VLBI). Numerous dense data sets have been composed and published and their interpretation has already had strong impact on the development of knowledge of kinematic and dynamic aspects of crustal deformation.

Repeated geodetic observations provide estimates of crustal kinematics in terms of relative motions between point positions at the surface. In dissipative systems, such as associated with crustal deformation, knowledge of kinematics alone is in general insufficient to uniquely determine the dynamics of forcing processes. However, accurate knowledge of surface kinematics poses an indispensable boundary condition for modeling of the dynamics. In this thesis I am primarily concerned with establishing such boundary conditions from an analysis of relative motion measurements. The first part of chapter 2 introduces a new analysis method that inverts relative motions in joint estimates of the strain and rotation rate field and slip rates on active faults. Applications of the method to synthetic data are given in the second part of chapter 2 and to real data in chapters 3 and 4. Our method aims at modeling kinematic features of the deformation field of the brittle upper layer, extensive treatment of the complexity of crustal rheology reaches beyond the scope of this thesis. This introductory chapter primarily provides an overview of main concepts concerning the kinematics of continental deformation that have been developed over the last decades and allows to place our new method in the spectrum of surface deformation analyses. This overview is largely based on Molnar [1988]; England and Jackson [1989]; Gordon and Stein [1992]; King et al. [1994]; Lamb [1994] and Thatcher [1995].

1.2 Aspects of continental deformation

Continental deformation takes place in a complex and distributed manner, often accompanied by intraplate seismicity. For instance, extensively studied regions, as the western United States, the Mediterranean and the Middle East, and central and southern Asia, show patterns of large predominantly aseismic blocks, embedded in seismically active, strongly deforming areas. Discussing the nature of continental deformation requires discrimination between deformation on lithospheric and deformation on crustal time and length scales [e.g., England and Jackson, 1989]. The average thickness of continental crust is 35 km. The brittle upper crust is most seismogenic and encompasses the upper 10 to 20 km. Here, earthquakes occur as a release of built-up interseismic strain. The limiting shear stress, defining the strength of the material, depends on the frictional resistance to fault slip at depth. Except for the deformation directly associated with rupturing, deformation is thought to be predominantly elastic and reversible. Pressure and temperature conditions generally suggest that deformation in the mid- to lower crust takes place as ductile flow, controlled by crystal dislocation and diffusion processes allowing for large strain without rupturing. The duration of the seismic cycle in the shallow crust is indicative for the time scale at which deformation of the ductile crust occurs and can vary between a few tens to hundreds or even thousands of years. Finally, the mechanical strength of the uppermost mantle part of the lithosphere is also of significance. This layer is capable of supporting large deviatoric stresses over millions of years.

Laboratory investigations of deformation mechanisms suggest a relatively strong seismogenic upper layer, a weak lower crust and a strong uppermost mantle to depths between 60 and 100 km. Usually, the latter is assumed to be the strongest. This would imply that on a long time scale the uppermost mantle controls the large-scale deformation pattern and that averaging of surface deformation over time could, in some way, reflect the lithospheric deformation field. However, experiments do not completely exclude the possibility of the upper crust being the strongest layer. This may imply that in some cases the upper crust controls surface deformation and in turn has an important influence on the ductile lower crust [e.g., Lamb, 1994]. Before we further discuss the basic hypotheses regarding crustal deformation, we introduce the main, different observations regarding the kinematics of crustal deformation.

1.3 Main sources of kinematic deformation data

Information on style of continental deformation provided for by observation of crustal kinematics strongly depends on the type of data. Geologic fault slip and paleomagnetic rotation data represent effects of long-term crustal deformation and span time intervals ranging from a few thousands to millions (geology) and from a few millions to hundreds of millions (paleomagnetism) of years.

Another source of information are earthquake moment tensors. Seismic moment tensors are cataloged since 1977 (Harvard centroid moment tensor (CMT) catalogue [Dziewonski et al., 1981]. The seismic observation record may span a time interval of (a few) 100 years [e.g., Ambraseys and Jackson, 1990; Pacheco and Sykes, 1992; Papazachos et al., 1999], but

probably still represents only part of the seismic cycle that may span tens to thousands of years. The mechanisms of small earthquakes within one region are often extremely varied and in some way represent internal crustal deformation. Large intracontinental earthquakes likely nucleate near the seismic-aseismic transition zone. They are associated with faults that break through the entire seismogenic layer and possibly extend into the ductile part of the crust. In general, their mechanisms are consistent with the deformation pattern on lithospheric length and time scales and their summed moment release accounts for almost all of the seismic faulting within active regions: On average the larger events constitute about 10% of all earthquakes, but represent about 95% of the total seismic moment. However, the summed contribution of large earthquakes to crustal deformation is often much smaller than predicted on account of motions derived from rigid plate models and space geodetic data [e.g., McKenzie and Jackson, 1983; Ekström and England, 1989; Ward, 1998a,b; Kreemer et al., 2000]. Probably, a considerable amount of aseismic motion occurs as distributed creep [e.g., Houseman and England, 1986; England and Jackson, 1989] or as creep on faults [Scholz and Cowie, 1990], although effects of a seismicity rate that strongly varies with time or of an incomplete seismic record can not be excluded. Plate motion models like NUVEL-1a [DeMets et al., 1990, 1994] incorporate magnetic anomalies in oceans averaged over the past few million years, earthquake data and directions of transform faults and can be used to predict relative motion for comparison with observations of present-day kinematics.

Nowadays geodetic observation of crustal deformation allows monitoring of nearly instantaneous motion with permanent GPS stations. Campaign type GPS results in time-averages of motion typically on the scale of years. For some regions time-averages on the order of 10 to 100 years are obtained by reoccupation (by GPS) of for instance old triangulation sites. GPS data obtained at relatively stable plate interiors are in good agreement with plate motion vectors. However, strong deviations occur in continental deformation zones with active faults, where crustal motions are often dominated by cyclic build-up and release of elastic strain. Other geodetic sources of observations are, e.g., Synthetic Aperture Radar Interferometry (InSAR), Satellite Laser Ranging (SLR) and Very Long Baseline Interferometry (VLBI). In this thesis we will use mainly GPS observations and therefore be restricted to continental deformation on crustal time and length scales.

1.4 Crustal deformation: models and hypotheses

A basic issue in the discussion about continental deformation is whether the crust deforms as a series of (semi-)rigid blocks or as a continuum [e.g., King and Cisternas, 1991]. Key to a subdivision in these two end-member approaches, the continuum model and the block model, seems whether deformation below the brittle upper crust is narrowly focused on down-dip extensions of seismogenic faults, more associated with block models (figures 1.1A and B), or broadly distributed in bulk flow, more associated with continuum models (figures 1.1C and D). In block models the upper crust is relatively strong with respect to the underlying layers and determines the surface deformation field. In continuum models the upper crust is relatively weak and the ductile lower crust or uppermost mantle part of the lithosphere (depending of the scale of the region under consideration and the time interval represented by the type of the data used) determines the surface deformation field.

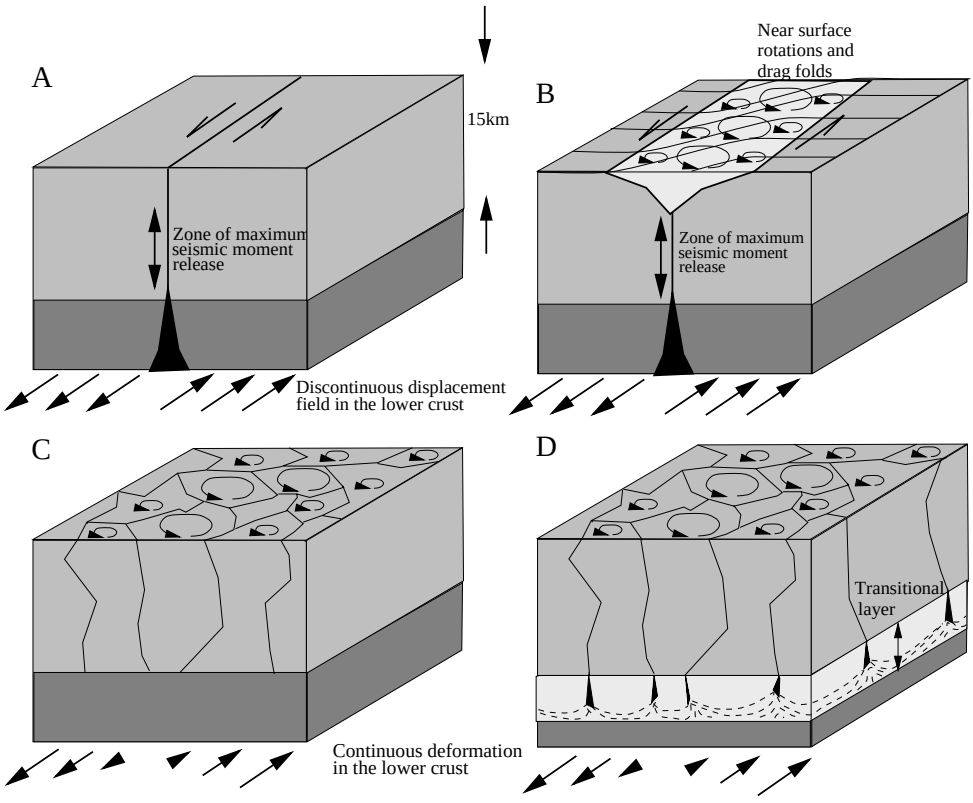

Figure 1.1: Four models for the distribution of deformation as a function of depth: (a) Block deformation with complete localization of slip, (b) Surface drag folding with localized deformation at depth, straight lines indicate elongated, rotating blocks that slide past one another along strike-slip faults within fault zone (see also text), (c) Surface block motion and distributed deformation at depth, (d) Model of (c) with a transitional layer (a, b and c from King et al. [1994], d from Lamb [1994]).

Basically, both models are applied to establish the relation between the observed surface deformation and the deformation mechanism at depth: In the block model observations of crustal deformation are interpreted in terms of the lateral distribution of motion in the ductile regime of the fault zone. In the continuum model these observations are interpreted in terms of the crust responding to tractions applied at its base by flow in the lower crust or uppermost mantle.

1.4.1 Quasi-rigid (or block model) approach

On geological time scales the block model view is motivated by geological and paleomagnetic observations of relatively old and narrow fault zones within continental transform and

compressional settings. These fault zones with widths of 10-20 km have undergone displacements of hundreds of kilometers and usually have persisted for some 10 Ma or more [e.g., Peltzer and Tapponnier, 1988; King et al., 1994; Armijo et al., 1999]. Most (quasi-)rigid block models involve assumptions of a strong crust and the longer-term rigidity of (micro-)plates or crustal/lithospheric blocks of which the motion is coupled through deformation zones or narrow shear zones [e.g., Avouac and Tapponnier, 1993; Peltzer and Saucier, 1996]. Surface deformation is dominated by the relative motion of blocks and results from interactions along block boundaries. Major faults are considered to cut through the seismogenic crust and reach down into the ductile lower crust (figure 1.1a) and maybe into the upper mantle. In the lower crust deformation occurs as localized continuous slip on the extensions of faults into the ductile regime and in the upper crust as accumulation and release of elastic strain.

In its simplest form a crustal scale block model is a half space model with uniform slip on fault extensions in the lower crust and with elastic deformation in the upper crustal layer that result from fault locking before earthquakes occur [e.g., Savage and Burford, 1973; Freund and Barnett, 1976; Matsu'ura et al., 1986]. The depth of this brittle layer is usually indicated as the locking depth. A deficit of seismic moment release on short time scales implies that the fault is locked and that elastic deformation is broadly distributed throughout the block, waiting to be released. Strain rates and the surface velocity field in the vicinity of faults can be predicted assuming elastic dislocation theory and block motion [Okada, 1985]. In general, geodetic measurements across individual faults do not contradict the block model view [Larsen and Reilinger, 1992; Feigl et al., 1993; Larson, 1993; Johnson et al., 1994; Bennett et al., 1996; Walpersdorf et al., 1998, and many others]. In block models of the surface deformation that represents longer time scales, geodetic data can be used to verify the assumption, often made in block models, of minimal elastic strain energy within the blocks, i.e. at large distances from fault zones, where surface deformation is not supposed to be influenced by loading mechanisms imposed by the uninterrupted block motion at depth [e.g., Saucier and Humphreys, 1993; Lundgren et al., 1995].

Several observations obtained within the continental deformation zones have led to adaptations of the simple block model described above. For example, King et al. [1994] find a seismic moment deficit of about 40% in California when deformation rates computed from summed seismic moment tensors are compared to rates estimated from regional plate motion studies. The predominant amount of seismic slip seems to be localized at mid-depths in the seismogenic zone. Assuming that the earthquake catalogue is sufficiently long, they conclude that the slip deficit in the upper and lower parts of the seismogenic zone probably occurs as creep. Accumulation of this deformation causes a superficial brittle-ductile process of drag folding and rotations of small blocks adjacent to the fault (figure 1.1b). Other examples of surface processes within the fault zones that may diffuse a clear view on the block behavior at depth are described for California, eastern Iran and the Aegean area, where crustal deformation has been modeled by rotation of elongated blocks within the deformation zone [e.g., Freund, 1970; McKenzie and Jackson, 1983, 1986].

1.4.2 Continuum approach

On geological time scales the continuum approach is motivated by the spatial scale at which large topographic features, such as mountain belts and basins, occur. These features can only be sustained if the stress is distributed over a depth range much deeper than the crust. In general, continuum models are dynamical models that represent the lower crust and/or uppermost mantle part as a viscous, continuously deforming fluid that dictates crustal deformation by applying shear tractions to the base of the (upper-)crustal layer [e.g., Tapponnier and Molnar, 1976; Bird and Piper, 1980; England and McKenzie, 1982; Houseman and England, 1986]. Faulting is a result of rupturing of the brittle crust as it follows the flow of the lithosphere and faults are restricted to the crust (figure 1.1C and D) [e.g., McKenzie and Jackson, 1983; Houseman and England, 1986; Lamb, 1987]. A more detailed model was proposed by Lamb [1994] and includes a transitional layer that exerts basal tractions on the overlying brittle crust (figure 1.1d).

A simple dislocation model for a weak crust invokes an elastic plate overlying a visco-elastic (Maxwell solid) half space [e.g., Savage, 1990]. During an earthquake the elastic strain, accumulated in the elastic layer, is transferred to the underlying layer. The coseismic rupture cuts through the elastic upper layer whereas the motion in the visco-elastic substrate is continuously distributed [e.g., Pollitz et al., 2000].

Continuum modeling approaches that use space geodetic data attempt to relate the observations to the motions of the ductilely deforming lower crust/lithosphere. For example, Bourne et al. [1998a,b] argue that, in the absence of perturbations due to recent earthquakes, the short-term motion of the surface best reflects the long-term flow of lithosphere. The seismic release of energy, however, makes the blocks move as unstrained bodies over the long term. The time-averaged velocity at a point of the crust will in general differ from that in the ductile layer beneath it, but the time-averaged velocity of the whole crustal block, which may encompass several fault zones, will be equal to the velocity of the deeper lithosphere.

1.4.3 Combined approach

The combination of ideas underlying continuum and block deformation models has also led to other, more hybrid approaches [King and Cisternas, 1991]. The first type invokes strong crustal blocks embedded in weak crust, hence lateral contrast in crustal strength. Examples are, the laboratory model of a rigid block, indenting weak plasticine material [Peltzer and Tapponnier, 1988], and the computerized inclusion of a rigid block into a thin viscous sheet model [e.g., England and Houseman, 1985]. Both simulate the northward moving Indian continent and the deformation of the Himalayas and Southeast Asia. These models nicely mimic the observed continental deformation pattern of blocks embedded in strongly deforming areas, but provide no insight into the style of deformation. The second type originates from fractal theory and is based on the assumption that ductile deformation can be mimicked by self-similar fault motion at any scale of deformation. Consequently, this model should describe the large-scale deformation of the lithosphere as well as localized deformation in the crust. In fact, it means that the only difference between faulting and folding is the scale at which the observer is looking. If this fractal relation is applied to recent seismicity, it only holds for earthquakes with magnitudes smaller than 6.5 [e.g., Ekström and England,

1989; Kreemer et al., 2000]. Larger events in some way behave anomalously. Further, the conclusions from various applications of the fractal relation to geological faults seem to be in contradiction. For example, Scholz and Cowie [1990] find for a variety of tectonic environments that small faults play a minor role in the deformation process, while Walsh et al. [1991] need a continuum approach to explain the extension of the North Sea, because the total amount of faults is not sufficient to accommodate the deformation.

1.5 Discussion

Despite fundamental difference between the two end-member views on lithospheric deformation in terms of coupling between lithosphere and crust, it remains questionable whether it is possible to discriminate between (quasi-)rigid and continuum mechanisms based on observations of surface deformation only. Savage [1990] showed that the two basic classes of crustal rheology that relate surface deformation to the earthquake cycle cannot be distinguished in two-dimensional models by using surface observations. The resemblance between the velocity fields derived for Southeast Asia by the rigid model of Peltzer and Saucier [1996], by the continuum model of England and Molnar [1997] and by the combined approaches of England and Houseman [1985] and Peltzer and Tapponnier [1988] is also indicative for the non-unique relation between surface data and deformation mechanism at depth. This ambiguity can be illustrated by different views of motion partitioning observed in plate-boundary tectonic settings. On the one hand Gilbert et al. [1994b] argue that the strength of the crust can be derived from observed orientations of surface strain: Strain patterns parallel to the regional fault structure are due to a strong crust and vertical loading mechanisms, because the fault controls the stress field. If the crust is weak the strain pattern follows the regional rather than the local stress field. However, another equally acceptable alternative is that fault orientations are dictated by the motion of the underlying velocity field and strongly depend of the shape and orientation of the block in which they are embedded. This view is supported by floating block model studies in which local deformation patterns can be completely different from the regional velocity field [e.g., Freund, 1970; McKenzie and Jackson, 1983, 1986; Taymaz et al., 1991; Lamb, 1994]. A third purely kinematic alternative is proposed by Tikoff and Theyssier [1994], who argue that the degree of partitioning and the orientation of the strain field are not controlled by the deformation mechanism at depth, but by the angle between the relative plate or block motion vector and the plate or block boundary (or the degree of obliquity). For example, pure-shear dominated transpressional settings (such as Sumatra) are inefficient in accommodating strike-slip motions, resulting in a low degree of partitioning, whereas simple-shear dominated settings (such as California) are very efficient, resulting in a high degree of partitioning.

1.6 The subject of this thesis

Although the character of crustal deformation mechanisms at depth may be difficult to obtain from the analysis of surface deformation data only, an important factor in the study of crustal and lithospheric deformation is an accurate representation of the kinematics of the

Earth's crust, both in time and in space. Recently, several purely kinematic methods have been developed that can convert large numbers of deformation measurements (e.g., space geodetic data, seismic moment tensors, geological slip rates) into continuous velocity or velocity gradient fields. These methods can be applied to any arbitrary region, independent of scale or presumed deformation mechanism at depth. The simplest method computes uniform strain and rotation rates in triangles defined by the sites of observation and then performs an integration across the model area to derive the continuous deformation field, for instance from GPS and triangulation data [Davies et al., 1997] or with Quaternary fault slip rates [England and Molnar, 1997]. A continuous velocity field of the upper crust can be obtained from earthquakes by applying the Kostrov [1974] relation to obtain local strain rate from seismic moment tensor summation [e.g., Haines, 1982; Haines and Holt, 1993; Holt and Haines, 1995; Haines et al., 1998]. The central assumption is that the strain rates in the upper crust, when averaged over a suitable length and time scale, represent the vertically averaged strain rates throughout the crust or lithosphere on a longer time scale. The least squares collocation method [Kahle et al., 1995; Straub, 1996; Kato et al., 1998a] and the bicubic spline methods of Bourne [1996] and of Beavan and Haines [2001] differ in design, but share that the continuous velocity field at the Earth's surface is obtained by interpolation of velocity observations. Derivation of the velocity gradient field follows from differentiation of the interpolated velocity field.

The subject of this thesis is the development, testing and application of a new inverse method for the analysis of relative motion data. Like the former methods our new method aims at representing the kinematics of the crustal deformation field without relating it to the style of deformation at depth. However, the velocity field of the Earth's crust on short time scales, as represented by space geodetic data, is not necessarily a continuous function of spatial coordinates. Faults accommodate slip and represent boundaries between moving plates or blocks, whatever the deformation at depth may be. Unlike previous approaches, discontinuous deformation across faults is addressed by our method. The method, presented in the next chapter, incorporates active fault motion and simultaneously solves for a piecewise continuous deformation field in crustal blocks.

Chapter 2

Inversion of relative motion data for estimates of crustal strain rate, rotation rate and fault slip

2.1 Introduction

Relative motions between points at the solid Earth's surface are nowadays mostly derived from repeated observation using space geodetic techniques such as the Global Positioning System (GPS). Surface motions constitute important kinematic boundary conditions in the modeling of processes driving crustal deformation. There are broadly two ways to incorporate relative motion data in the analysis of crustal deformation. One way is dynamic modeling assuming certain general aspects of the dynamics of crustal deformation which are closer specified during computation, by forward or inverse modeling, of a model that can fit the observed relative motions. For instance, elastic-dislocation modeling of fault behavior in an elastic crust is often applied for fitting of observed relative motions near fault zones [e.g., Savage and Burford, 1973; Savage et al., 1979; Matsu'ura et al., 1986; Bennett et al., 1996; Genrich et al., 2000]. In dynamic modeling the kinematic properties such as the strain rate field are implicitly determined by the assumptions underlying the adopted model for crustal dynamics and the rheological relation assumed between stress, material/fault strength, and strain (rate). The other way is kinematic modeling - the subject of this thesis - which avoids using crustal dynamics and rheology. In this case estimates of the strain rate field and other kinematic parameters are derived from the motion data in a purely kinematic way, i.e. independent of crustal dynamics. This does not yield immediate quantitative results about the dynamical behavior of the crust and thus can only be considered an intermediate step towards crustal dynamics. But, a pure kinematic approach does provide quantitative information about for instance the distribution of strain accumulation in the shallow crust and is useful in obtaining qualitative insight into the underlying dynamics. Importantly, the surface fields such as strain rate obtained from a kinematic analysis pro-

vide a spatially continuous and independent boundary condition for subsequent modeling of crustal dynamics. Instead, observations of relative motion constitute a sparse and spatially discrete boundary condition.

A number of kinematic inversion methods exist which focus on determining the velocity gradient field $\boldsymbol{\nabla v}(\boldsymbol{r}, t)$ from observations of relative crustal motion $\Delta \boldsymbol{v}$. The velocity gradient is the spatial derivative of the crustal flow field $\boldsymbol{v}(\boldsymbol{r}, t)$. For incremental deformation strain rate is the symmetric part of $\boldsymbol{\nabla v}(\boldsymbol{r}, t)$. Basically, kinematic inversion methods can be divided into two classes: Methods based on interpolation in data ($\boldsymbol{v}(\boldsymbol{r}, t)$) space and those based on interpolation in model ($\boldsymbol{\nabla v}(\boldsymbol{r}, t)$) space.

Data space methods first perform a spatial interpolation of the observed $\Delta \boldsymbol{v}$ and next obtain $\boldsymbol{\nabla v}$ by spatial differentiation. The interpolation can be based on assuming spatial correlations between velocity observations [e.g., Straub, 1996; Kato et al., 1998a; Ward, 1998a; Kahle et al., 2000] or by parameterizing the unknown velocity field by shape functions leaving coefficients of the shape functions to be determined in an inversion procedure of fitting a smooth velocity field to the velocity data [Beavan and Haines, 2001]. So far, the interpolation methods have not been derived from a particular physical theory relating observations to the velocity gradient field. Also, contributions of fault motion to observed relative motion data are not explicitly incorporated.

Model space methods usually involve a parameterization of the unknown $\boldsymbol{\nabla v}$ field. This is also done by shape functions, defined for instance on triangular domains, for which the coefficients are determined in an inversion of the velocity data. However, now $\boldsymbol{\nabla v}$ is a direct result of data inversion. Importantly, model space methods are based on a physical theory linking observations with model quantities, e.g., in terms of an observation equation. Up to now, theory in applications has been subject to the assumption of constant $\boldsymbol{\nabla v}$ in triangular regions spanned by the observation network [e.g., Frank, 1966; Davies et al., 1997; Bourne et al., 1998a]. This assumption basically allows data inversion for each triangle separately and leads to velocity gradient fields which are discontinuous across the edges of the triangles. Fault motion has not been incorporated in the theory.

In the first part of this chapter we develop a general kinematic formulation which in a natural way leads to working in model space. From basic principles we derive an observation equation which relates observations of relative motions to path integrals over the unknown velocity gradient field. The combination of many of such equations leads to an inverse problem for which there is no theoretical restriction on the complexity of the velocity gradient field. In practice, model complexity is determined by the resolving power of the data. A particular novelty is that we also incorporate terms that exactly account for the effects of fault motion on observed relative motions. In the second part of this chapter we test the performance of the inverse method on synthetic velocity fields. In a first series of tests we consider continuous deformation only and solve for the velocity gradient tensor field $\boldsymbol{\nabla v}$. In a second series the model area comprises two faults and simultaneously with the velocity gradient field we also solve for slip on active faults. We investigate the influence of experiment design (i.e. density of model parameterization, distribution of observation points, data noise) on the quality of the solution and the sensitivity of the solution for regularization.

2.2 Derivation of a general kinematic observation equation

Geodetic observation of crustal deformation yields changes in relative position of points attached to the deforming surface. In a fixed reference frame, adopted at time $t = 0$, the position of a point i is given by $\boldsymbol{r}_i + \boldsymbol{u}(\boldsymbol{r}_i, t)$ where $\boldsymbol{u}$ is the displacement field that evolved since $t = 0$. The relative displacement of a point j with respect to i that developed in the crustal flow during time increment $\Delta t = t_2 - t_1$ is:

$$\Delta \boldsymbol{u}_{ij} = [\boldsymbol{u}(\boldsymbol{r}_j, t_2) - \boldsymbol{u}(\boldsymbol{r}_i, t_2)] - [\boldsymbol{u}(\boldsymbol{r}_j, t_1) - \boldsymbol{u}(\boldsymbol{r}_i, t_1)].$$

If $\Delta \boldsymbol{u}_{ij}$ is caused by pure continuous deformation both terms can be related in a general way to the displacement gradient field $\boldsymbol{\nabla u}(\boldsymbol{r}, t)$ by integration over arbitrary paths $L_{ij}(t_1)$ and $L_{ij}(t_2)$ connecting the two positions at t_1 and t_2, respectively:

$$\Delta \boldsymbol{u}_{ij} = \int_{L_{ij}(t_2)} \boldsymbol{\nabla u}(\boldsymbol{r}, t_2) \cdot \mathrm{d}\boldsymbol{r} - \int_{L_{ij}(t_1)} \boldsymbol{\nabla u}(\boldsymbol{r}, t_1) \cdot \mathrm{d}\boldsymbol{r} \tag{2.1}$$

For the analysis of short term crustal deformation both paths can be taken the same in which case the relative error in $\Delta \boldsymbol{u}_{ij}$ due to the mismatch at the endpoints of integration paths is of the order of $|\boldsymbol{u}(\boldsymbol{r}, t_2) - \boldsymbol{u}(\boldsymbol{r}, t_1)|/l_{ij}$ where l_{ij} is the length of the integration path. This error is negligible in the analysis of crustal deformation based on geodetic data. Taking $L_{ij}(t_1) = L_{ij}(t_2)$, $\Delta \boldsymbol{v}_{ij} = \Delta \boldsymbol{u}_{ij}/\Delta t$, and $\Delta \boldsymbol{u} = \boldsymbol{u}(\boldsymbol{r}, t_2) - \boldsymbol{u}(\boldsymbol{r}, t_1)$ equation 2.1, is rewritten as:

$$\Delta \boldsymbol{v}_{ij} = \int_{L_{ij}} \boldsymbol{\nabla} \left[\frac{\Delta \boldsymbol{u}}{\Delta t} \right] \cdot \mathrm{d}\boldsymbol{r} \tag{2.2}$$

$\Delta \boldsymbol{v}_{ij}$ is the relative motion derived from repeated geodetic observation of sites i and j. Equation 2.2 relates observed relative motion to a linear approximation $\Delta \boldsymbol{u}/\Delta t$ of the crustal flow field $\boldsymbol{v}(\boldsymbol{r}, t) = \mathrm{d}\boldsymbol{u}/\mathrm{d}t$ that developed between t_1 and t_2. If $\boldsymbol{v}$ is time-stationary, hence $\boldsymbol{v} = \Delta \boldsymbol{u}/\Delta t$ for all Δt, or Δt is sufficiently small, as in continuous observation with GPS stations, we find

$$\Delta \boldsymbol{v}_{ij}(t) = \int_{L_{ij}} \boldsymbol{\nabla v}(\boldsymbol{r}, t) \cdot \mathrm{d}\boldsymbol{r}. \tag{2.3}$$

Equation 2.3 is applicable to arbitrary steady or non steady crustal flow in regions without active faults. Effects of fault motion on $\Delta \boldsymbol{v}_{ij}$ are incorporated by considering the relative motion between two points on the integration path at either side of an active fault. An analysis is given in appendix A. If a path L_{ij} crosses K faults the relative motion due to fault slip averaged over a period Δt is:

$$\Delta \boldsymbol{v}_{ij}(t) = \sum_{k=1}^{K} \alpha_k \frac{\Delta \boldsymbol{s}_k}{\Delta t}(\boldsymbol{r}_{ij}^k, t) \tag{2.4}$$

where $\Delta \boldsymbol{s}_k$ is the total slip on fault k at the intersection $\boldsymbol{r}_{ij}^k$ between L_{ij} and the fault. The factor α_k has value +1 or -1 depending on fault orientation with respect to the direction of integration along L_{ij} (see appendix A).

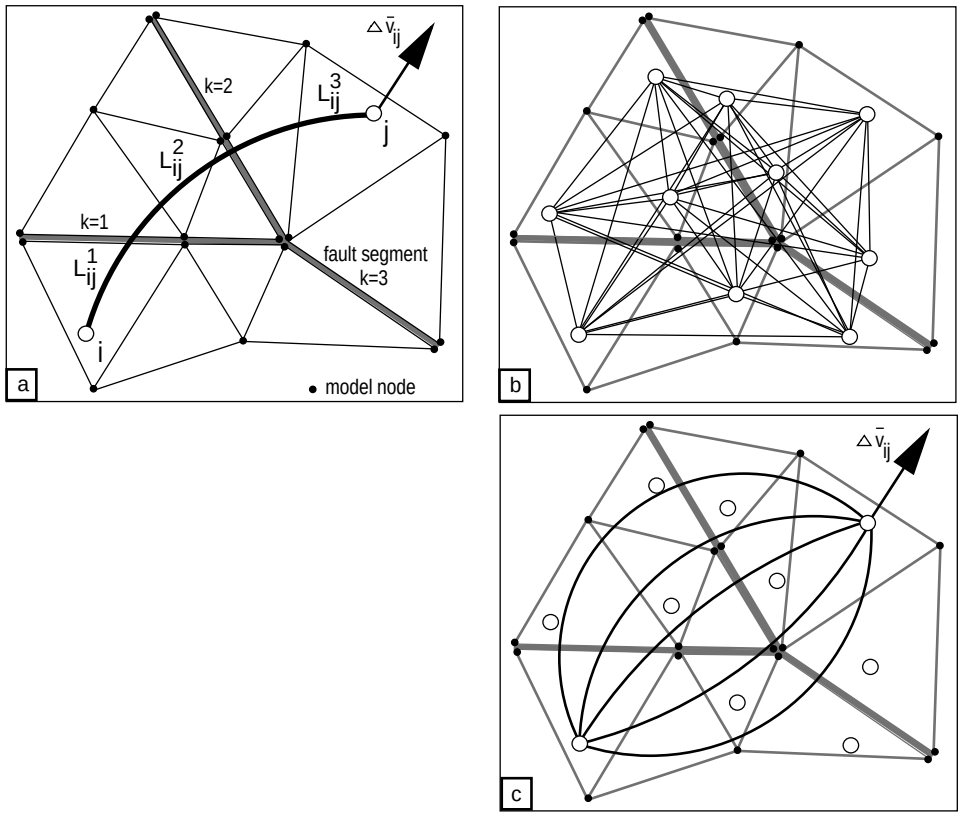

Figure 2.1: Schematic representation of model geometry: a) A study region with a 'Y'-shape fault system is triangulated between model nodes (black dots). Triangles do not intersect faults. Note that nodes at the fault are always doubled to allow the velocity gradient field to be discontinuous across faults. The curved line L_{ij} connects two observation sites i and j with relative motion $\Delta \boldsymbol{v}_{ij}$. Integration along L_{ij} is done in parts along segments L_{ij}^l. b) Ten observation sites (open circles) are connected by 45 geodesics, yielding 90 component equations in the forward problem. c) For observation sites at opposite sides of faults extra path equations (denoted by curved lines) are included to force internal consistency between fault slip and the velocity gradient field in the inversion model.

For general crustal flow the combination of equation 2.3 and 2.4 relates observed relative motion $\Delta \boldsymbol{v}_{ij}$ to the velocity gradient field and fault slip occurring from t_1 to t_2 (figure 2.1a):

$$\Delta \boldsymbol{v}_{ij} = \sum_{l=1}^{K+1} \int_{L_{ij}^l} \boldsymbol{\nabla v}(\boldsymbol{r}, t) \cdot \mathrm{d}\boldsymbol{r} + \sum_{k=1}^{K} \alpha_k \frac{\Delta \boldsymbol{s}_k}{\Delta t}(\boldsymbol{r}_{ij}^k, t) \tag{2.5}$$

The integration over $\boldsymbol{\nabla v}$ is done in parts because $\boldsymbol{\nabla v}$ can be discontinuous at slipping faults. Equation 2.5 needs to be extended in the case that $\Delta \boldsymbol{v}_{ij}$ results from two velocity vectors

that are taken from independent geodetic networks between which an unknown relative rotation between geodetic network solutions may exist. The terms to be added to 2.5 are: $\boldsymbol{\Omega}_j \times \boldsymbol{r}_j - \boldsymbol{\Omega}_i \times \boldsymbol{r}_i$ where $\boldsymbol{\Omega}_m$ denotes the rotation vector for the observation network to which site m belongs. One network rotation vector can be set to zero in which case the remaining $\boldsymbol{\Omega}_m$ describe the relative rotation with respect to this fixed network.

Equation 2.5 is the observation equation which will be used for the inversion of relative motion data and has the nice property that it is purely linear in the unknown quantities $\boldsymbol{\nabla v}$ and $\Delta \boldsymbol{s}_k / \Delta t$. Further, 2.5 provides a purely kinematic description, hence, does not assume anything about crustal dynamics or fault dynamics. Most importantly, equation 2.5 gives a complete description of the relative crustal motion data $\Delta \boldsymbol{v}_{ij}$ resulting from non time-stationary crustal flow. Note that the choice of L_{ij} is completely free. Although this property hints at an inherent complexity in the interpretation of relative motion data we will turn it to our advantage in the inversion stage.

2.3 Setting up an inverse problem

We restrict our analysis to time independent or time averaged problems and leave non steady motion to future developments. Below an inverse problem is set up for all three components of relative velocity vectors.

Assume a set of M point positions of which the motion in some reference frame is obtained from geodetic techniques. These positions yield at least $M(M-1)/2$ vector equations 2.5 along geodesics or other connecting paths L_{ij} for all combinations of sites i and j. These equations are coupled through the velocity gradient field $\boldsymbol{\nabla v}$ and the relative fault slip $\Delta \boldsymbol{s}_k$ on fault (segments) k. In figure 2.1b this coupling is visualized by the sampling of the surface by integration paths L_{ij}. The resulting inverse problem is to solve this coupled set of integral equations.

The study region (which can be the entire Earth's surface) is subdivided into a network of N nodes connected by triangulation (either in cartesian or spherical coordinates). The N nodes at the vertices of the triangles need not coincide with observation sites. Further, triangles do not intersect with faults. We adopt a linear dependence of $\boldsymbol{\nabla v}$ on the spatial coordinates in each triangle. This parameterization allows for quadratic velocity variation within triangles, and continuity of $\boldsymbol{\nabla v}$ across the edges of the triangles. Hence, for each component of the velocity gradient tensor we assume that

$$[\boldsymbol{\nabla v}(\boldsymbol{r})]_{kl} = \sum_{m=1}^{3} [\boldsymbol{\nabla v}]_{kl}(\boldsymbol{r}_m) g_m(\boldsymbol{r}) \tag{2.6}$$

where $\boldsymbol{r}_m$ is a vertex of the triangle and $g_m(\boldsymbol{r})$ are interpolation functions. In appendix B we carry this out in more detail. Faults are divided into fault segments (appendix A) and for each fault segment k the relative fault slip $\Delta \boldsymbol{s}_k$ is parameterized as a simple step function, i.e. we assume that $\Delta \boldsymbol{s}_k$ is constant along segment k.

Substitution of these parameterizations in 2.5 leads, after integration, to an ordinary set of coupled linear equations. These can be put into a matrix-vector form by assembling all velocity gradient parameters into one vector of length $9N$, and by assembling all fault

parameters in a vector of length $3K$. Denote these vectors by $\boldsymbol{p}$ and $\boldsymbol{s}$ respectively, then the matrix-vector equivalent of $M(M-1)/2$ equations 2.5 is:

$$[\boldsymbol{V}|\boldsymbol{F}]\left[\frac{\boldsymbol{p}}{\boldsymbol{s}}\right] = \boldsymbol{d} \tag{2.7}$$

where all data $\Delta\boldsymbol{v}_{ij}$ have been put into one vector $\boldsymbol{d}$. Details of the above steps are presented in appendix B. The submatrix $\boldsymbol{V}$ represents the coefficients linked to continuous deformation, and the non-zero elements of $\boldsymbol{F}$ are +1 or -1 associated with fault segments. It is important to note that going from 2.5 to 2.7 only involves the assumptions of linear velocity gradient in triangles and constant slip on fault segments. Higher order parameterizations are of course possible but that does not affect the principle of the interpretation method we propose.

The matrix system 2.7 can be extended with more data equations using the same observation set $\Delta\boldsymbol{v}_{ij}$. For each observation pair i and j many alternative integration paths L_{ij} can be invented which all lead to the same relative motion $\Delta\boldsymbol{v}_{ij}$ (figure 2.1c). In particular, closed integration paths $L_{ij} - L_{ji}$ between sites i and j will always render zero relative motion. Such equations are welcome because they put implicit constraints on the null space of the inverse problem. Closed paths which sample continuously deforming crust are effectively replaced by the local constraint that $\boldsymbol{\nabla} \times \boldsymbol{\nabla}\boldsymbol{v} = \boldsymbol{0}$ which after substitution of the parameterization (equation B.2) leads for each triangle to 3 additional equations which are added to 2.7. Still, extra paths L_{ij} may be required across faults to ensure internal consistency between fault slip and the velocity gradient field, and to ensure that the solution of the inverse problem is a deformation field. Augmenting 2.7 with these extra equations leads to:

$$\left[\begin{array}{c|c} \boldsymbol{V} & \boldsymbol{F} \\ \boldsymbol{G} & \boldsymbol{0} \end{array}\right]\left[\begin{array}{c} \boldsymbol{p} \\ \boldsymbol{s} \end{array}\right] = \left[\begin{array}{c} \boldsymbol{d} \\ \boldsymbol{0} \end{array}\right] \tag{2.8}$$

where $\boldsymbol{G}$ contains for each triangle the coefficients that result from the constraint $\boldsymbol{\nabla}\times\boldsymbol{\nabla}\boldsymbol{v} = \boldsymbol{0}$, and $\boldsymbol{V}$ and $\boldsymbol{F}$ now contain extra path equations across faults.

2.4 Inversion

In practice equation 2.8 is inconsistent due to data errors. These include implicit data errors that may arise from the difference between true crustal deformation and our parameterized approximation assuming linear variation of $\boldsymbol{\nabla}\boldsymbol{v}$ in triangles and step-functions for $\Delta\boldsymbol{s}_k$. The implicit errors can be made small by taking sufficiently small triangles and fault segments. A detailed parameterization, however, will in general lead to a mixed-determined or underdetermined inverse problem because there will be an insufficient number of data to independently constrain all model parameters. Consequently, a solution will be non-unique. Further, inhomogeneous distribution of integration paths and near linear dependence between some equations in 2.8 will often lead to an ill-conditioned matrix. To deal with these problems we adopt an inversion procedure which selects a solution that fits the data best in a least squares sense and at the same time minimizes some model norm. For details see [e.g., Jackson, 1979; Menke, 1989; Scales et al., 1990] The following notation is used: $\boldsymbol{A}$ represents the coefficient matrix of equation 2.8, $\hat{\boldsymbol{d}} = [\boldsymbol{d}\,|\,\boldsymbol{0}]^T$, $\boldsymbol{m} = [\boldsymbol{p}\,|\,\boldsymbol{s}]^T$, $\boldsymbol{C}_d$ denotes

the data covariance matrix, and $\boldsymbol{D}$ stands for a damping or regularization operator that will be specified later. Assuming that the data and model are uncorrelated we choose to minimize the object function: $\Phi(\boldsymbol{m}) = (\boldsymbol{Am} - \hat{\boldsymbol{d}})^T \boldsymbol{C}_d^{-1}(\boldsymbol{Am} - \hat{\boldsymbol{d}}) + \alpha^2 \boldsymbol{m}^T \boldsymbol{D}^T \boldsymbol{Dm}$ where α controls the trade-off between fitting the data and minimizing the weighed model norm. The model $\boldsymbol{m}$ minimizing Φ is formally:

$$\boldsymbol{m} = (\boldsymbol{A}^T \boldsymbol{C}_d^{-1} \boldsymbol{A} + \alpha^2 \boldsymbol{D}^T \boldsymbol{D})^{-1} \boldsymbol{A}^T \boldsymbol{C}_d^{-1} \boldsymbol{d} \tag{2.9}$$

with a posteriori model covariance given by $\boldsymbol{C} = (\boldsymbol{A}^T \boldsymbol{C}_d^{-1} \boldsymbol{A} + \alpha^2 \boldsymbol{D}^T \boldsymbol{D})^{-1}$ and model resolution kernel $\boldsymbol{R} = \boldsymbol{C} \boldsymbol{A}^T \boldsymbol{C}_d^{-1} \boldsymbol{A}$.

The data covariance $\boldsymbol{C}_d$ incorporates, as a tuning parameter for inversion, variances for the exact equations $\boldsymbol{Gm} = \boldsymbol{0}$. The variances (row-weights) are chosen to make these equations at least as important as the data equations for determining the solution. In equation 2.9 it is assumed that $\boldsymbol{C}$ exists. If this proves not the case then either $\alpha^2 \boldsymbol{D}^T \boldsymbol{D}$ must be adapted or other strategies can be followed such as truncated Singular Value Decomposition. If for $\alpha = 0$ $\boldsymbol{C}$ exists then the ordinary least squares solution is obtained with $\boldsymbol{R} = \boldsymbol{I}$, the identity operator. This does not imply that the model covariance $\boldsymbol{C}$ is small. Data errors combined with ill-conditioning of the observation matrix will more than often result an unacceptably rough model and regularization is needed to further constrain the solution. Regularization will lower the model variance but also reduces the spatial resolution which is a well-known trade-off. A common choice for regularization is $\boldsymbol{D} = \boldsymbol{I}$ which leads to classical damped least squares penalizing the amplitudes of $\boldsymbol{m}$. Other possibilities are to take for $\boldsymbol{D}$ a first or second derivative operator which implies imposing spatial correlations between adjacent model parameters and which requires the model to be flat or smooth, respectively [e.g., Menke, 1989; Scales et al., 1990]. Because derivative operators have a non-empty null space, a combination with amplitude damping is necessary to fully regularize the inverse problem. In this thesis we will work with a combination of amplitude and second derivative regularization. This requires minimizing the object function $\Phi(\boldsymbol{m}) = (\boldsymbol{Am} - \hat{\boldsymbol{d}})^T \boldsymbol{C}_d^{-1}(\boldsymbol{Am} - \hat{\boldsymbol{d}}) + \alpha_a^2 \boldsymbol{m}^T \boldsymbol{m} + \alpha_d^2 \boldsymbol{m}^T \boldsymbol{D}_2^T \boldsymbol{D}_2 \boldsymbol{m}$ where $\boldsymbol{D}_2$ stands for a second derivative operator [Scales et al., 1990]. The solution that minimizes Φ is

$$\boldsymbol{m} = (\boldsymbol{A}^T \boldsymbol{C}_d^{-1} \boldsymbol{A} + \alpha_a^2 \boldsymbol{I} + \alpha_d^2 \boldsymbol{D}_2^T \boldsymbol{D}_2)^{-1} \boldsymbol{A}^T \boldsymbol{C}_d^{-1} \tag{2.10}$$

Inversion is now dependent on three tuning parameters: the weight attributed to the equations $\boldsymbol{Gp} = \boldsymbol{0}$, and α_a and α_d. Target of inversion is a model that can fit the data properly ($\chi^2 \approx 1$) and that has acceptable covariance $\boldsymbol{C}$ and resolution $\boldsymbol{R}$. This requires investigation of a range of solutions obtained for different combinations of the tuning parameters. Inevitably a model must selected on the trade-off curve between model variance and resolution.

Lastly, we note that our application involves parameters of different physical dimension and expectation value. In any data application, a Singular Value Decomposition of $\boldsymbol{A}$ will show that singular values associated with fault slip parameters are typically by a magnitude $10^4 - 10^6$ smaller than those associated with the elements of $\boldsymbol{\nabla v}$. This implies a large condition number which implicitly results from the large difference in size of coefficients in submatrices $\boldsymbol{V}$ and $\boldsymbol{F}$, respectively. A simple scaling between both sets of model parameters can be used to change the spectrum e.g., by multiplying the pertinent columns of $\boldsymbol{A}$ with

a priori standard deviations or expectations of parameter values. It is not difficult to show that column scaling is not necessary if $\boldsymbol{C}$ exists. However, if truncated Singular Value Decomposition is used as a means to solve the inverse problem care should be taken that the small but significant singular values associated with fault slip are not truncated. In this case column scaling is recommended.

2.5 Synthetic experiments

2.5.1 Synthetic experiment design

A forward finite element calculation is performed to obtain relative velocities which are consistent with a deformation field. The geometry of the synthetic model is defined in spherical coordinates. A $2^\circ \times 2^\circ$ model area is deformed by applying a plane shear stress at the top boundary. The lower boundary is kept fixed and the top, left and right boundaries are free to move. Elastic rheology is assumed and relative displacements are derived by solving the mechanical equilibrium equation using a finite element method [Govers, 1993]. Division of the displacements by an arbitrary time scale of one year determines the synthetic velocities, which become the data for our inverse modeling. We compute a velocity field for a model without faults (Model I; figure 2.2.Ia, Ib and Ic) and also for a model with two frictionless faults (Model II; figure 2.2.IIa, IIb and IIc).

Remarkably, at first sight the two velocity fields do not differ very much. Effects of slip on the two faults in model II, especially on the upper fault I, are not easily recognized in the velocity field. However, the patterns of the strain rate fields are quite different. The smooth strain rate field of model I shows strong shear strain rates at the top and dominant extension and contraction at the left and right sides, respectively, of the model. Although the above properties also characterize the strain rate field of model II, more striking are the relatively strong variations in strain rate due to the presence of the faults, especially around the fault tips. The slip on both faults reaches a maximum near the center of the fault traces and zero at the tips. The slip on the upper fault (fault I, figure 2.3) has a normal component, whereas the slip on the lower fault (fault II) has a strong thrusting component. Both faults also accommodate dextral strike-slip.

Some of the discontinuous transitions in the contouring of figures 2.2.Ib and IIb are due to our definition of the effective strain rate; we add a minus sign if contraction dominates. For instance, the principal strain rates (figures 2.2.Ic and IIc) show that the area located

Figure 2.2: Figure on next page: The two synthetic models each computed with 6238 finite elements. Both velocity fields are generated by the same shear stress applied to the top boundary. The bottom boundary is kept fixed and the top, left and right boundaries are free to deform. Model I: (Ia) Velocity field computed at 81 observation points; (Ib) Contoured effective strain rate field ($\pm\sqrt{\frac{1}{2}\dot{\boldsymbol{\epsilon}}\dot{\boldsymbol{\epsilon}}}$, with $\dot{\boldsymbol{\epsilon}} = \frac{1}{2}(\boldsymbol{\nabla v} + (\boldsymbol{\nabla v})^T)$); (Ic) Principal strain rates at 150 arbitrary locations. Model II: (IIa) Velocity field with the black line segments representing the faults; (IIb) and (IIc) similar to text at (Ib) and (Ic). The fault slip is shown in figure 2.3.

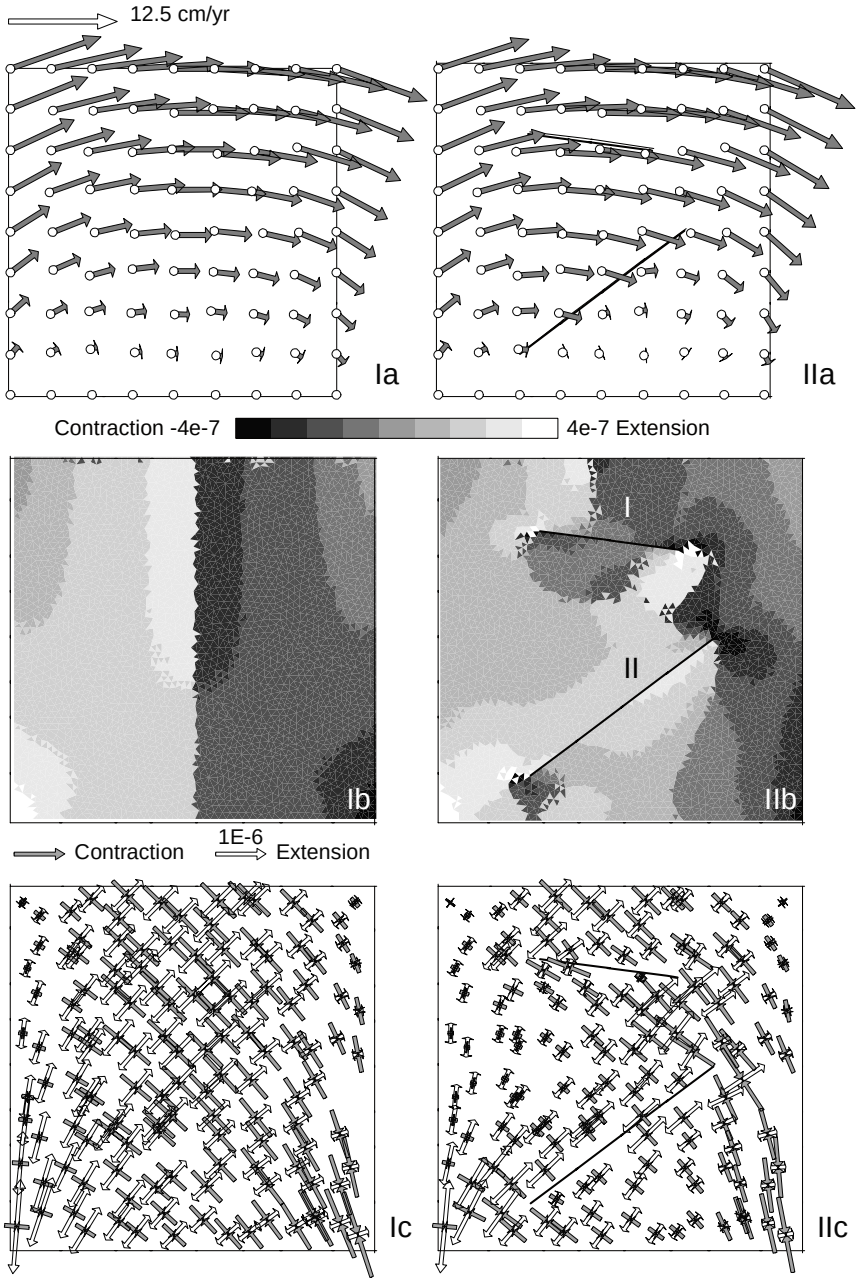

Figure 2.2: See caption on previous page.

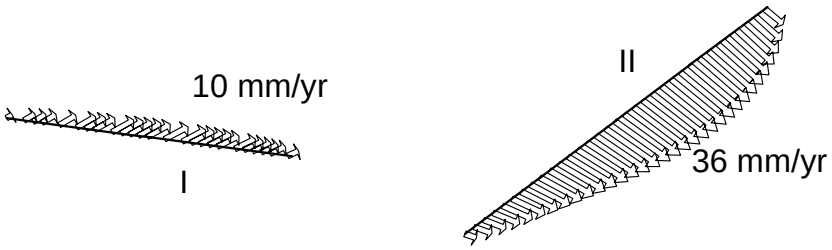

Figure 2.3: The distribution of fault motion, denoted by the arrows, on faults I and II of model II. Fault I accommodates dextral normal slip rates on 26 splitted nodes with a maximum of about 10 mm/yr at the center. Fault II is a dextral thrust with 32 splitted nodes and with a maximum slip rate of about 36 mm/yr.

along the north-south axis at the center of the model accommodates almost as much contraction as extension. A small preponderance of contraction over dilatation in one area and the reversed situation in a neighboring area is translated in a radical shift of sign of the effective strain rate, while the deformation field hardly changes.

2.5.2 Synthetic inverse problem

In the inversion we solve for the deformation field that generates the two lateral components of the synthetic velocity field $\boldsymbol{v} = (v_\theta, v_\phi)$ with units $[\frac{m}{yr}]$, which is determined by horizontal fault motion and the four components of the velocity gradient $\boldsymbol{\nabla v}$ that are purely associated with deformation in lateral directions. Our parameterization is restricted to linear variations of $\boldsymbol{\nabla v}$ within spherical triangles determined by T_n nodes spanning T_t triangles. Faults in the model area are parameterized by K great-circle line segments. We have a set of S observation sites. In the forward problem, defined by the linear matrix system 2.8, the data vector $\boldsymbol{d}$ contains the $S(S-1)$ velocity differences between all pairs of observation points and for the two velocity components. The model vector $\boldsymbol{s}$ contains for all fault segments the two components of the slip vector (s_θ, s_ϕ) with units $[\frac{m}{yr}]$ and consists of $2 \cdot K$ elements. The model vector $\boldsymbol{p}$ consists of $4 \cdot T_n$ elements and contains for all nodes the four components of $\boldsymbol{\nabla v}$, which in spherical geometry is denoted by

$$\boldsymbol{\nabla v} = \begin{bmatrix} v_{\theta\theta} & v_{\theta\phi} \\ v_{\phi\theta} & v_{\phi\phi} \end{bmatrix},$$

with units $[yr^{-1}]$. The symmetric part of $\boldsymbol{\nabla v}$, i.e., $\dot{\boldsymbol{\epsilon}} = \frac{1}{2}(\boldsymbol{\nabla v} + (\boldsymbol{\nabla v})^T)$, represents the strain rate tensor, and the antisymmetric part, i.e., $\dot{\boldsymbol{\omega}} = \frac{1}{2}(\boldsymbol{\nabla v} - (\boldsymbol{\nabla v})^T)$, the rotation rate tensor. Extensional strain and clockwise rotation are defined as positive and contractional strain and counterclockwise rotation as negative.

Weight factors α_a and α_d (equation 2.10) control the effect of amplitude damping of $\boldsymbol{\nabla v}$ on boundary nodes and second derivative regularization of $\boldsymbol{\nabla v}$ on all model nodes,

respectively. Besides data variances σ_d^2, the covariance $\boldsymbol{C}_d$ also contains variances σ_r^2 (with units $[\frac{1}{(m\,yr)^2}]$), as a tuning parameter for the weight of the extra $\boldsymbol{\nabla} \times \boldsymbol{\nabla v} = \boldsymbol{0}$ constraints (section 2.3). For determination of $(\boldsymbol{A}^T\boldsymbol{C}_d^{-1}\boldsymbol{A} + \alpha_a\boldsymbol{I} + \alpha_d^2\boldsymbol{D}_2^T\boldsymbol{D}_2)^{-1}$ (equation 2.10) we apply Cholesky decomposition [Press et al., 1992]. We use $\tilde{\sigma}_m = \frac{1}{M}\sum_{i=1}^{M}\sqrt{C_{ii}}$ as a general indication of the model error.

For the analysis of the inversion results we define a root-mean-square misfit function:

$$\Psi_P(\boldsymbol{x},\boldsymbol{y}) = \sqrt{\frac{\sum_{i=1}^{P}(x_i - y_i)^2}{\sum_{i=1}^{P} x_i^2}} \tag{2.11}$$

where $\boldsymbol{y} = (y_1, y_2, ..., y_P)$ is the vector that is to be compared to $\boldsymbol{x} = (x_1, x_2, ..., x_P)$. We compute model misfit $\Psi_M(\boldsymbol{\mu}, \tilde{\boldsymbol{m}})$ for inversion solution $\tilde{\boldsymbol{m}}$ with respect to the synthetic model $\boldsymbol{\mu}$, where $\tilde{\boldsymbol{m}}$ is an expansion of a solution $\boldsymbol{m}$ on the parameterization used in the finite element modeling. Similar to solution $\boldsymbol{m}$ the synthetic model consists of two parts; $\boldsymbol{\mu} = [\boldsymbol{p}_\mu \mid \boldsymbol{s}_\mu]^T$, with $\boldsymbol{p}_\mu$ the components of $(\boldsymbol{\nabla v})_\mu$ and $\boldsymbol{s}_\mu$ the components of fault slip. We separate the model misfit vector into $\boldsymbol{\delta p}_\mu = \boldsymbol{p}_\mu - \boldsymbol{p}_{\tilde{m}}$ and $\boldsymbol{\delta s}_\mu = \boldsymbol{s}_\mu - \boldsymbol{s}_{\tilde{m}}$. The number of model parameters of the synthetic model is $M = M_c + M_f$, with M_c the number of components of $\boldsymbol{\nabla v}$ at midpoints of finite elements and M_f the number of slip parameters at synthetic fault segments. Besides the root-mean-square model misfit $\boldsymbol{\Psi}_M(\boldsymbol{\mu}, \tilde{\boldsymbol{m}})$ we compute the usual model correlation coefficients $\boldsymbol{\rho}(\boldsymbol{\mu}, \tilde{\boldsymbol{m}}) = \boldsymbol{\mu}\cdot\tilde{\boldsymbol{m}}/(\|\boldsymbol{\mu}\| \cdot \|\tilde{\boldsymbol{m}}\|)$, which, however, will prove to be less sensitive to model differences than our Ψ measure.

We also use equation 2.11 to compute the data misfit $\Psi_N(\boldsymbol{d}, \boldsymbol{d}_m)$ with N the number of data, $\boldsymbol{d}$ the data vector and $\boldsymbol{d}_m = \boldsymbol{A}\boldsymbol{m}$. We note that the inversions are not noise free. Equation 2.8 is inconsistent because of implicit data errors. The data $\boldsymbol{d}$ result from the finite element modeling. A solution $\boldsymbol{m}$ however is based on the assumption that $\boldsymbol{\nabla v}$ varies linearly in triangles much larger than those used for computing $\boldsymbol{\mu}$. Any variation of $\boldsymbol{\mu}$ inside an 'inversion' triangle that cannot be matched by a linear trend will therefore cause data inconsistencies between the exact data $\boldsymbol{d}$ and those that can be ideally predicted from the left-hand side of equation 2.8.

2.5.3 Continuous deformation

In the first series of tests we apply our method to the velocity field of model I (figure 2.2.Ia) and solve for the components of $\boldsymbol{\nabla v}$ only. This reduces $\boldsymbol{m}$ and $\boldsymbol{A}$ of matrix system 2.9 to $\boldsymbol{p}$ and $[\boldsymbol{V}|\boldsymbol{G}]^T$, respectively. The number of model parameters is $M = M_c$. While the number and configuration of stations are kept constant, the triangulation is varied and we solve the problem on three grids (figure 2.4). For grid PII the nodes are placed at the 81 observation points. We take a uniform standard deviation $\sigma_d = 3$ mm/yr, which is of the order of the present accuracy obtained from repeated GPS campaigns.

Inversions are performed for a range of values of σ_r, α_a and α_d. Some numbers pertinent to inversions performed on each grid are listed in table 2.1. Figure 2.5 shows eigenvalue spectra of $\boldsymbol{C}^{-1}$ on grids PI (a), PII (b) and PIII (c). We plot the normalized spectrum $\boldsymbol{\lambda} = (\frac{\lambda_1}{\lambda_{min}}, \frac{\lambda_2}{\lambda_{min}}, \cdots, \frac{\lambda_M}{\lambda_{min}})$, with λ_{min} the smallest eigenvalue. Hence, the maximum value on the vertical axis (figures 2.5A, B' and C') is the condition number $\boldsymbol{\Lambda} = \lambda_{max}/\lambda_{min}$

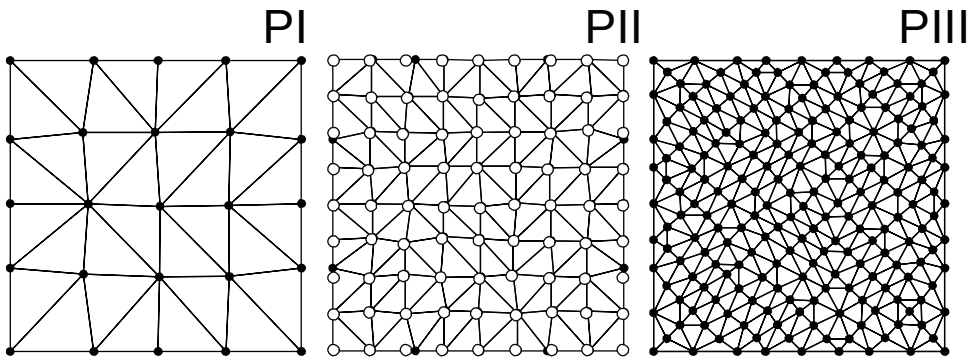

Figure 2.4: Three triangulation grids applied for inversion for $\boldsymbol{\nabla v}$ of the synthetic velocity field of model I (figure 2.2.I): (PI) 32 triangles; (PII) 128 triangles where the white dots indicate the (81) station configuration which is used for all experiments; (PIII) 384 triangles.

grid	T_n	T_t	$\triangle L$ $[m]$	σ_r^μ $[\frac{1}{myr}]$	$\tilde{\sigma}_m^\mu$ $[\frac{1}{yr}]$	Ψ_M %	Ψ_N %
PI	25	32	41657	-	$2{\cdot}10^{-8}$	4	2
PII	81	128	23987	$1.0{\cdot}10^{-11}$	$3{\cdot}10^{-8}$	5	0.3
PIII	209	384	12798	$2.1{\cdot}10^{-11}$	$1{\cdot}10^{-7}$	6	0.3

Table 2.1: Parameters for inversion for $\boldsymbol{\nabla v}$ on the grids PI, PII and PIII (see figure 2.4). Key for the input parameters: T_n, number of grid nodes; T_t, number of triangles; $\triangle L$, average length of path segments per triangle and σ_r^μ, the standard deviation for $\boldsymbol{G}$. Key for the output parameters: $\tilde{\sigma}_m^\mu$, the average model standard deviation; Ψ_M, the model misfit and Ψ_N the data misfit.

of $\boldsymbol{C}^{-1}$, with λ_{max} the largest eigenvalue. The difference between the dotted and dashed line represents the effect of $\boldsymbol{G}$ on the spectrum $\boldsymbol{\lambda}$. Including the $\boldsymbol{\nabla} \times \boldsymbol{\nabla v} = \boldsymbol{0}$ constraints has a strong positive effect on the conditioning of the inverse problem on grids PII and PIII. Besides reducing $\boldsymbol{\Lambda}$ on PII and PIII, $\boldsymbol{G}$ also considerably decreases the model misfit $\Psi_M(\boldsymbol{\mu}, \tilde{\boldsymbol{m}})$ on these grids (by about 10%). We define σ_r^μ as the standard deviation for which $\Psi_M(\boldsymbol{\mu}, \tilde{\boldsymbol{m}})$ is minimal (table 2.1). Regularization in the form of amplitude and second difference damping further smoothes the spectrum (solid line, figure 2.5a, b, c). Variation of σ_r and regularization have little effect on the inversion performed on grid PI. On this grid the data constrain the solution well.

The results for model misfit $\Psi_M(\boldsymbol{\mu}, \tilde{\boldsymbol{m}})$ and data misfit $\Psi_N(\boldsymbol{d}, \boldsymbol{d}_m)$ as functions of α_a, α_d and grid density, obtained for $\sigma_r = \sigma_r^\mu$, are shown in figure 2.6. In general, the synthetic deformation field is well recovered on all grids; minimal values of $\Psi_M(\boldsymbol{\mu}, \tilde{\boldsymbol{m}})$ are about 4% on PI, 5% on PII and 6% on PIII and the model correlation coefficient ranges between 0.96 and 0.98. On all grids $\Psi_N(\boldsymbol{d}, \boldsymbol{d}_m)$ and its variation as a function of α_d and α_a are small. On PI the data misfit is about 2%, somewhat larger than the 0.3% misfit on PII and PIII.

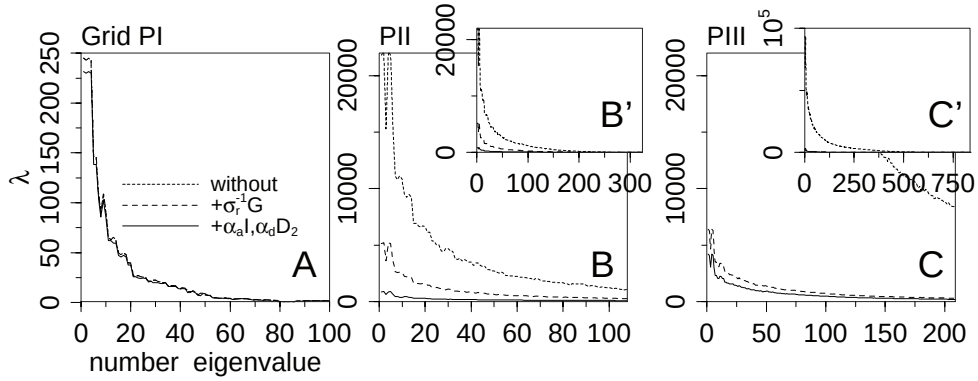

Figure 2.5: Spectra $\boldsymbol{\lambda} = (\frac{\lambda_1}{\lambda_{min}}, \frac{\lambda_2}{\lambda_{min}}, ..., \frac{\lambda_M}{\lambda_{min}})$ of $\boldsymbol{C}^{-1}$, obtained by singular value decomposition, of inversions for $\boldsymbol{\nabla v}$ on the grids PI, PII and PIII. Key: dotted line, $\sigma_r = \alpha_a = \alpha_d = 0$; dashed line, $\sigma_r = \sigma_r^\mu$, $\alpha_a = \alpha_d = 0$; solid line, $\sigma_r = \sigma_r^\mu$, $\alpha_a = \alpha_a^\mu$ and $\alpha_d = \alpha_d^\mu$; (A), (B') and (C') display the complete spectra (see table 2.1 for the values of σ_r^μ for which the spectra are computed) and (B) and (C) show the same spectra (B') and (C') for the first 100 to 200 eigenvalues, respectively.

We select the optimal solution to have minimal $\Psi_M(\boldsymbol{\mu}, \tilde{\boldsymbol{m}})$ and $\Psi_N(\boldsymbol{d}, \boldsymbol{d}_m)$ for $\sigma_r = \sigma_r^\mu$, $\alpha_a = \alpha_a^\mu$ and $\alpha_d = \alpha_d^\mu$ (see table 2.1). The regularized spectrum of $\boldsymbol{C}^{-1}$ of the optimal solution is shown with a solid line in figure 2.5.

Compared to the results obtained for grid PI the smaller values for $\Psi_N(\boldsymbol{d}, \boldsymbol{d}_m)$ obtained for PII and PIII may indicate a better fit of the model to small scale variations in $\boldsymbol{\mu}$. This is however not reflected in an improved model fit. The (small) increase of $\Psi_M(\boldsymbol{\mu}, \tilde{\boldsymbol{m}})$ with increasing grid density implies that the predominant part of the synthetic deformation field varies linearly on a scale of the order of or larger than $\triangle L$ on PI. Grid densification degrades the inverse problem conditioning, which independent of the application of the $\frac{1}{\sigma_r}\boldsymbol{Gp} = \boldsymbol{0}$ constraint requires stronger regularization to obtain acceptable solutions on PII and PIII. For illustration the optimal solution $\boldsymbol{m}$ on PII is given in figure 2.7. In general, the variation of the components of $\boldsymbol{\nabla v}$ (figure 2.7, panels (b)) agrees well with those of the synthetic solution (figure 2.7, panels (a)). Component $v_{\theta\theta}$ (figure 2.7.1a-1c) is relatively small and hardly contributes to the velocity field. Since the synthetic velocity field originates from the application of a plane shear stress it follows that the two components $v_{\theta\phi}$ and $v_{\phi\theta}$ (figure 2.7.2a-2c, 3a-3c) dominate the deformation field. The model misfit $\boldsymbol{\delta p}_\mu$ (figure 2.7, panels (c)) shows subsequent positive and negative misfits in longitude (θ) direction for $v_{\theta\theta}$ and $v_{\phi\theta}$ and in latitude (ϕ) direction for $v_{\theta\phi}$ and $v_{\phi\phi}$. These larger scale variations are responsible for the somewhat increased values of $\Psi_M(\boldsymbol{\mu}, \boldsymbol{m})$ on PII and PIII, compared to PI. Integration over these model misfit patterns yields (near) zero relative velocity, which demonstrates that this misfit pattern is in the null space of $\boldsymbol{A}$ and has not successfully been suppressed by regularization. The explanation of this lies in the symmetry of experiment design (i.e. symmetry in observation sites and thus in baseline sampling) which causes (near zero) eigenvalues (associated with near-null space eigenvectors) representing possible larger

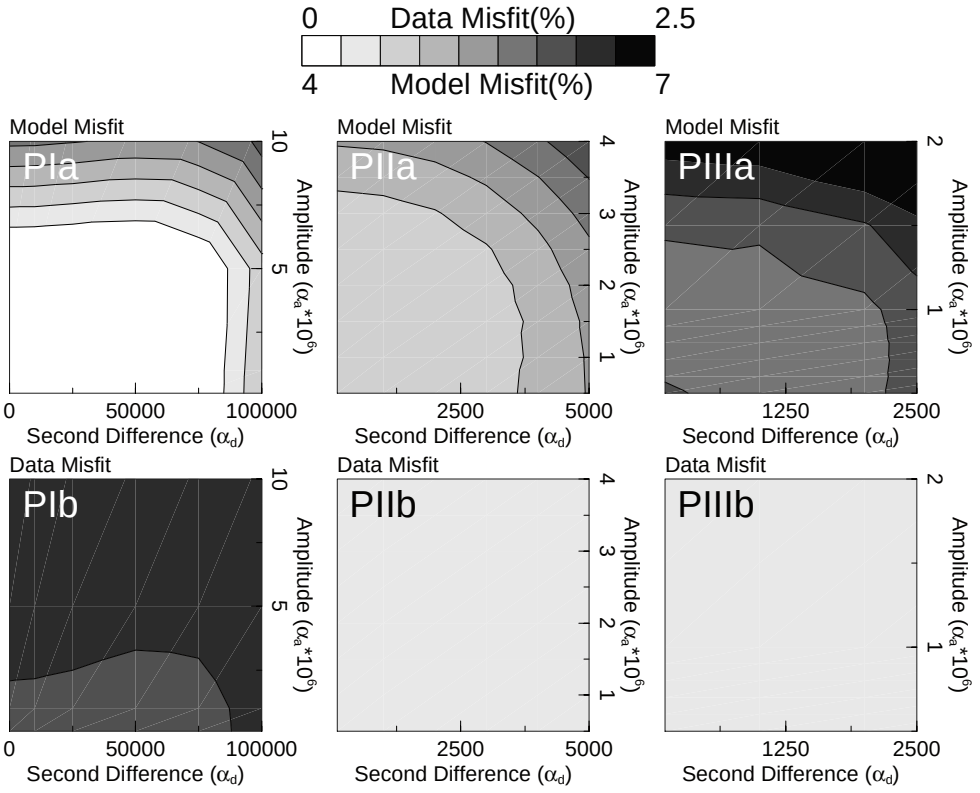

Figure 2.6: Influence of damping on data and model misfit of inversion for $\nabla \boldsymbol{v}$ on the grids PI, PII and PIII. The contouring denotes (a) $\Psi_M(\boldsymbol{\mu}, \boldsymbol{m})$ and (b) $\Psi_N(\boldsymbol{d}, \boldsymbol{d}_m)$ as functions of α_d for the second difference damping (horizontal axis) and of α_a for amplitude damping (vertical axis). In these computations the standard deviation for the $\nabla \times \nabla \boldsymbol{v} = \boldsymbol{0}$ constraints is $\sigma_r = \sigma_r^{\mu}$ (table 2.1).

scale variations in the model to which the data are insensitive. These effects are similar to those observed in synthetic travel time experiments [Lévêque et al., 1993].

2.5.4 Continuous deformation and fault motion

To solve for components of $\nabla \boldsymbol{v}$ and $\boldsymbol{s}$ simultaneously, we apply our method to synthetic velocity field II (figure 2.2), measured by the same 81 stations as in the previous experiments. Again, we consider three different grids; P1, P2 and P3 (figure 2.8) of which the triangulations are of similar density as of grids PI, PII and PIII (figure 2.4), respectively. On grid P1 and P2 fault I and II consist of 6 and 8 segments, respectively, and on P3 of 12 and 16 segments, respectively. We consider misfit functions for fault slip, $\Psi_{M_f}(\boldsymbol{s}_\mu, \boldsymbol{s}_{\tilde{m}})$, and for the velocity gradient, $\Psi_{M_c}(\boldsymbol{p}_\mu, \boldsymbol{p}_{\tilde{m}})$, separately. Again, we assume a uniform a priori data standard deviation σ_d of 3 mm/yr on all grids and scan the solution space for different

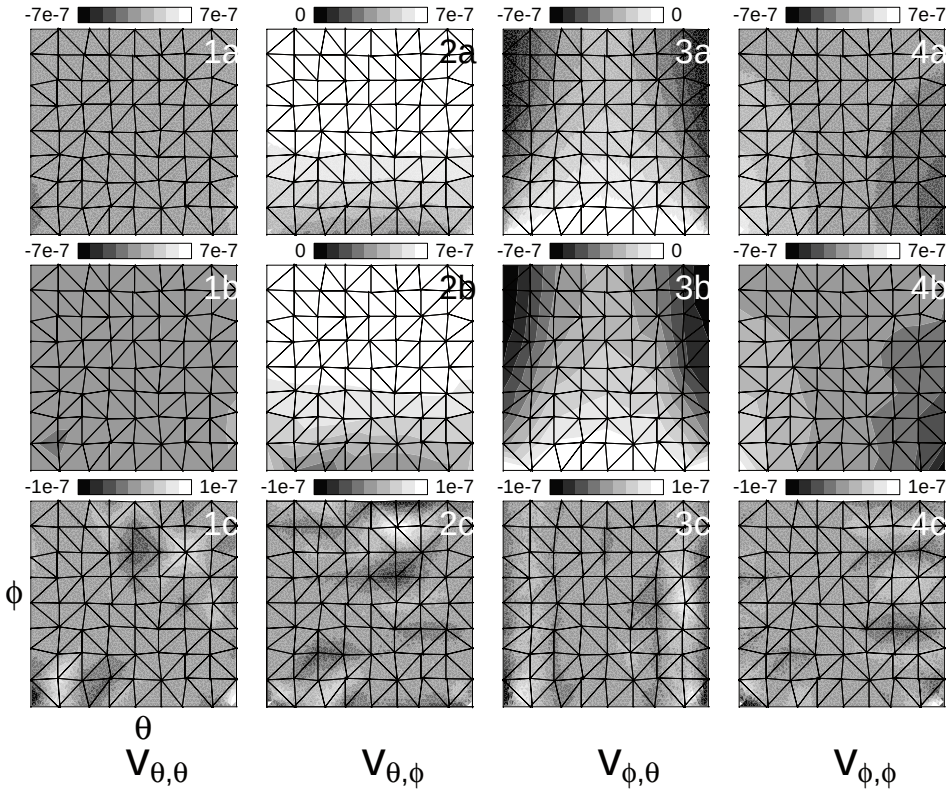

Figure 2.7: Optimal solution of inversion for $\boldsymbol{\nabla v}$ on grid PII; (a) synthetic model $\boldsymbol{p}_{\mu}$, (b) our solution $\boldsymbol{p}_{\tilde{m}}$ linearly interpolated over the finite element grid $\boldsymbol{p}_{\tilde{m}}$, (c) misfit $\boldsymbol{\delta p}$ with the synthetic deformation field, for (1) $v_{\theta\theta}$, (2) $v_{\theta\phi}$, (3) $v_{\phi\theta}$ and (4) $v_{\phi\phi}$. Note the different contouring limits.

combinations of σ_r, α_a and α_d.

2.5.5 Results of inversion for ∇v and s

Some aspects of the inversion parameterization and tuning parameters per grid are listed in table 2.2. The extra eigenvalues in the spectra of figure 2.9, compared to the spectra in section 2.5.3 (figure 2.5), are introduced by the fault parameters. Many of the small eigenvalues are associated with eigenvectors pertaining to fault slip and, as we will infer later, trade-off in the solution between fault slip and $\boldsymbol{\nabla v}$ as a result of lack of resolution (due to lack of data). The initial values of $\boldsymbol{\Lambda}$ on P1, P2 and P3 (dotted lines in figure 2.9) are much larger than on the respective equivalent grids PI, PII and PIII, indicating very small eigenvalues. The extra constraints represented by $\frac{1}{\sigma_r}\boldsymbol{Gp} = \boldsymbol{0}$ reduce $\boldsymbol{\Lambda}$ (dashed lines in figure 2.9 computed with $\sigma_r = \sigma_r^{\mu}$, defined as in section 2.5.3), by a factor of about 2, 20

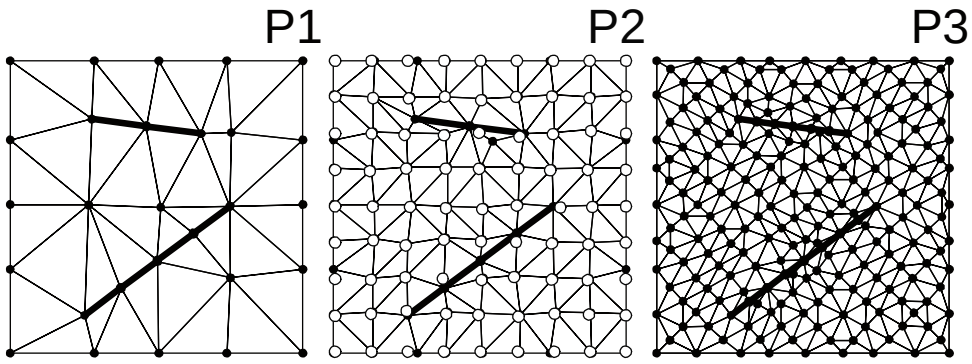

Figure 2.8: Three grids consisting of fault segmentation and triangulation of regions bounded by faults, applied for inversion for $\boldsymbol{\nabla v}$ and $\boldsymbol{s}$ of the synthetic velocity field of model II (figure 2.2): (P1) 38 triangles, 14 fault segments; (P2) 134 triangles, 14 segments, where the white dots indicate the (81) station configuration; (P3) 394 triangles, 28 fault segments

grid	T_n	T_t	$\triangle L$ $[m]$	σ_r^μ $\frac{1}{myr}$	$\tilde{\sigma}_p^\mu$ $[\frac{1}{yr}]$	$\tilde{\sigma}_s^\mu$ $[\frac{m}{yr}]$	Ψ_{M_c} %	Ψ_{M_f} %	Ψ_N %
P1	32	38	35392	$1.4{\cdot}10^{-12}$	$1{\cdot}10^{-8}$	0.004	23	30	3.5
P2	88	134	22222	$2.1{\cdot}10^{-12}$	$3{\cdot}10^{-8}$	0.001	21	26	2.5
P3	218	394	12575	$4.6{\cdot}10^{-12}$	$4{\cdot}10^{-8}$	0.0008	17	20	2

Table 2.2: Parameters for inversion for $\boldsymbol{\nabla v}$ and $\boldsymbol{s}$. Key for some of the output parameters: $\tilde{\sigma}_p^\mu$, $\tilde{\sigma}_s^\mu$ average model standard deviation for components of $\boldsymbol{\nabla v}$, $\boldsymbol{s}$, respectively, and Ψ_{M_f} model misfit for slip parameters. See the key of table 2.1 for the rest of the symbols.

and 200 on the grids P1, P2 and P3, respectively.

We find optimal values for σ_r and the damping parameters α_a and α_d which are comparable to the previous experiments in which we solved for $\boldsymbol{\nabla v}$ only. Figure 2.10 shows $\Psi_{M_f}(\boldsymbol{s}_\mu, \boldsymbol{s}_m)$ (2.10a), $\Psi_{M_c}(\boldsymbol{p}_\mu, \boldsymbol{p}_m)$ (2.10b) and $\Psi_N(\boldsymbol{d}, \boldsymbol{d}_m)$ (2.10c) as functions of α_d for second difference regularization and α_a for amplitude damping. In general we find improving model and data fit results for increasing density of the parameterization: $\Psi_{M_f}(\boldsymbol{s}_\mu, \boldsymbol{s}_m)$ decreases from above 30% on P1 to 20% on P3 and $\Psi_{M_c}(\boldsymbol{p}_\mu, \boldsymbol{p}_m)$ from 23% to 17%. $\Psi_N(\boldsymbol{d}, \boldsymbol{d}_m)$ has a minimal value of 3.5%, 2.5% and 2.0% on P1, P2 and P3, respectively. The model correlation coefficient ranges between 0.87 (P1) and 0.97 (P3) for $\boldsymbol{s}$ and between 0.95 (P1) and 0.98 (P3) for $\boldsymbol{\nabla v}$. On P3 we find minimal values of data and model misfit coinciding for similar values of α_a and α_d.

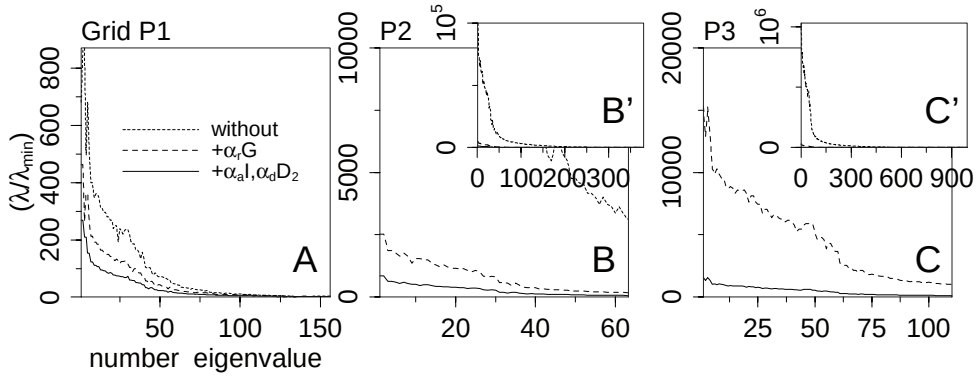

Figure 2.9: Spectra of $\boldsymbol{C}^{-1}$, obtained by singular value decomposition, of inversions for $\boldsymbol{\nabla v}$ and $\boldsymbol{s}$ on the grids P1, P2 and P3. See the caption of figure 2.5 for a complete explanation (see table 2.2 for the values of σ_r^μ for which the spectra are computed).

2.5.6 Analysis of one solution

We select the optimal solution on grid PIII for $\sigma_r = \sigma_r^\mu$, $\alpha_a = \alpha_a^\mu$ and $\alpha_d = \alpha_d^\mu$ (table 2.2), which leads to (nearly) coinciding minima of $\Psi_{M_c}(\boldsymbol{p}_\mu, \boldsymbol{p}_m)$, $\Psi_{M_f}(\boldsymbol{s}_\mu, \boldsymbol{s}_m)$ and $\Psi_N(\boldsymbol{d}, \boldsymbol{d}_m)$. In general, the properties of this solution (with $\Psi_{M_c}(\boldsymbol{p}_\mu, \boldsymbol{p}_m) = 17$ % and $\Psi_{M_f}(\boldsymbol{s}_\mu, \boldsymbol{s}_m) = 20$ % (panels (b), figure 2.11)) agree well with those of the synthetic solution (panels (a), figure 2.11). We can distinguish three different misfit patterns, that add up to $\boldsymbol{\delta p}_\mu$ (figure 2.11c) and $\Psi_{M_c}(\boldsymbol{p}_\mu, \boldsymbol{p}_m)$. The largest component of $\Psi_{M_c}(\boldsymbol{p}_\mu, \boldsymbol{p}_m)$ is determined by the small-scale, high-magnitude misfits near fault tips. Apparently, our model parameterization is, despite its large density compared to the station distribution, still too sparse to accommodate these variations. However, densification of the triangular grid proves of no use, because the small-scale, strong variations of the synthetic deformation field are also not fully detected by the observation station distribution adopted. Secondly, we find misfits of somewhat smaller magnitude surrounding the faults. Part of this model misfit signal varies linearly over the triangulation and correlates with the slip misfit vectors $\boldsymbol{\delta s}_\mu$ (figure 2.11.3c). For example the misfit slip vectors on fault I (of ≤ 3 mm/yr) are predominantly oriented in ϕ direction and correlate with the misfits of $v_{\phi\phi}$ surrounding this fault (figure 2.11.4c). The misfit slip vectors on fault II (of ≤ 1 cm/yr) that point in θ-direction change sign at the center of the fault trace and correlate with the misfit of $v_{\theta\theta}$ at both sides of this fault (figure 2.11.1c). The third source for misfit is represented by sequences of relatively long wavelength alternating positive and negative patterns (most prominent along the boundaries in ϕ-direction in figure 2.11.2c and in θ-direction in 2.11.3c) and are of the same origin as discussed at the end of section 2.5.3.

We find that the predominant part of the synthetic model is contained within the bounds imposed by the model errors for $\boldsymbol{\nabla v}$ (figure 2.12). Only at narrow zones along the model boundaries and the faults the model misfit for $\boldsymbol{\nabla v}$ exceeds the model errors. The model misfit for the fault slip vectors exceeds the model errors $\boldsymbol{\sigma}_m^f$ by on average 2 to 3 mm/yr,

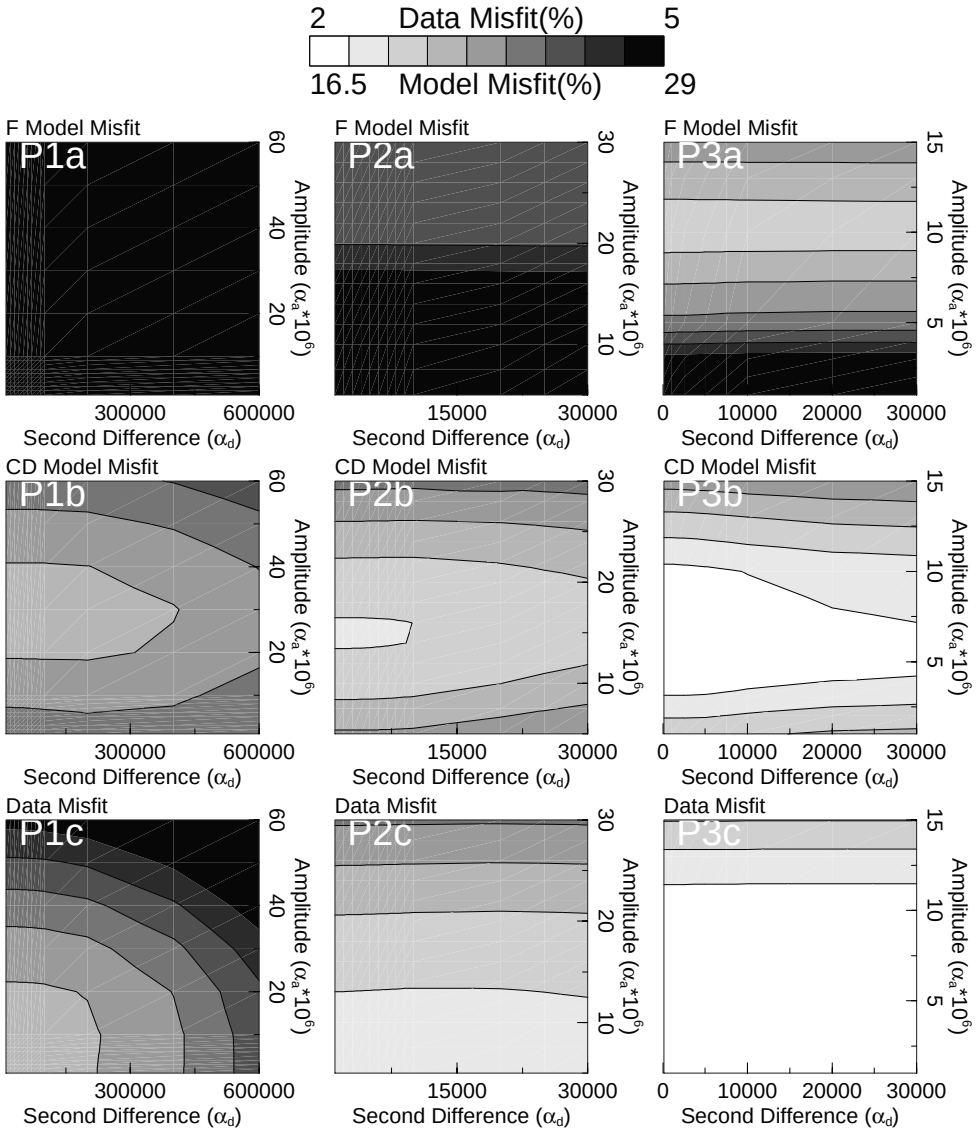

Figure 2.10: Influence of damping on data and model misfit of inversion for $\nabla \boldsymbol{v}$ and $\boldsymbol{s}$ on the grids P1, P2 and P3. Abbreviations CD and F in (a) and (b) denote the results for $\nabla \boldsymbol{v}$ and $\boldsymbol{s}$, respectively. The contouring denotes the model misfit for the (a) fault slip ($\Psi_{M_f}(\boldsymbol{s}_\mu, \boldsymbol{s}_m)$) and (b) $\nabla \boldsymbol{v}$ ($\Psi_{M_c}(\boldsymbol{p}_\mu, \boldsymbol{p}_m)$) and the (c) data misfit ($\Psi_N(\boldsymbol{d}, \boldsymbol{d}_m)$) as functions of α_d (horizontal axis) and α_a (vertical axis). In these computations the standard deviation for the $\nabla \times \nabla \boldsymbol{v} = \boldsymbol{0}$ constraints is $\sigma_r = \sigma_r^\mu$ (table 2.2).

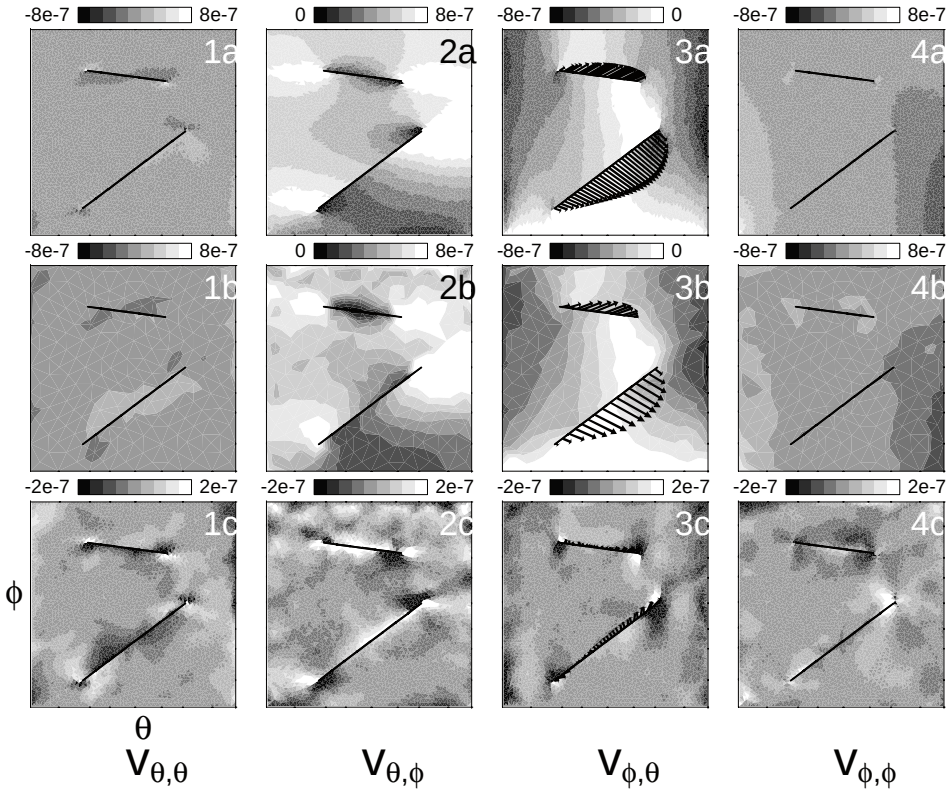

Figure 2.11: Optimal solution $\boldsymbol{m}$ of inversion for $\boldsymbol{\nabla v}$ and $\boldsymbol{s}$ on grid P3 (with $\Psi_{M_c}(\boldsymbol{p}_\mu, \boldsymbol{p}_{\tilde{m}}) = 17\%$, $\Psi_{M_f}(\boldsymbol{s}_\mu, \boldsymbol{s}_{\tilde{m}}) = 20\%$). See the caption of figure 2.7 for the components of $\boldsymbol{\nabla v}$, indicated by the contouring. For the slip solution $\boldsymbol{s}$: (3a) synthetic solution $\boldsymbol{s}_\mu$; (3b) our solution linearly interpolated over the finite fault elements $\boldsymbol{s}_{\tilde{m}}$ and (3c) misfit with the synthetic fault slip $\boldsymbol{\delta s}_\mu$. Note the different contouring limits.

which is, once again, indicative for trade-off between components of $\boldsymbol{\nabla v}$ and $\boldsymbol{s}$. An increase of the uniform data standard deviation σ_d of 3 mm/yr to about 6 mm/yr increases σ_m and consequently changes the formal status of most of the model misfits from significant to insignificant. However, it does not change the solution (figures 2.11b) and the misfit pattern (figures 2.11c).

Figure 2.13 shows the diagonal components R_{ii} and C_{ii} of the resolution $\boldsymbol{R}$ and covariance $\boldsymbol{C}$, respectively, pertaining to $\boldsymbol{\nabla v}$ of the optimal solution on grid P3 discussed in the previous section. In general the $v_{\theta\theta}$ and $v_{\phi\theta}$ components are better resolved than the $v_{\theta\phi}$ and $v_{\phi\phi}$ components and show smaller covariance. A similar observation is made for fault II with respect to fault I, of which the latter accommodates mostly ϕ-oriented fault slip. Corroborating inferences in the previous section, less well resolved model parameters

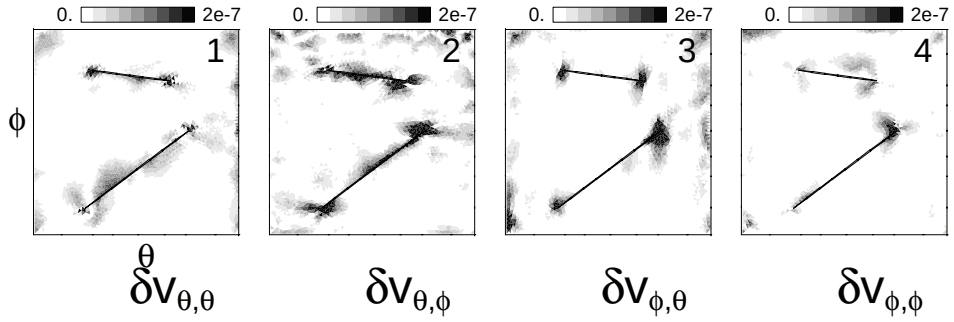

Figure 2.12: Difference between model misfit $\boldsymbol{\delta p}_m$ and model error $\boldsymbol{\sigma}_m$ of the optimal solution $\boldsymbol{m}$ of inversion for $\boldsymbol{\nabla v}$ and $\boldsymbol{s}$ on grid P3. The contouring denotes $\|\delta \boldsymbol{p}_\mu\| - \boldsymbol{\sigma}_m$, only if this difference is larger than zero. Otherwise the value plotted is set to zero. See the caption of figure 2.7 for the components of $\boldsymbol{\nabla v}$.

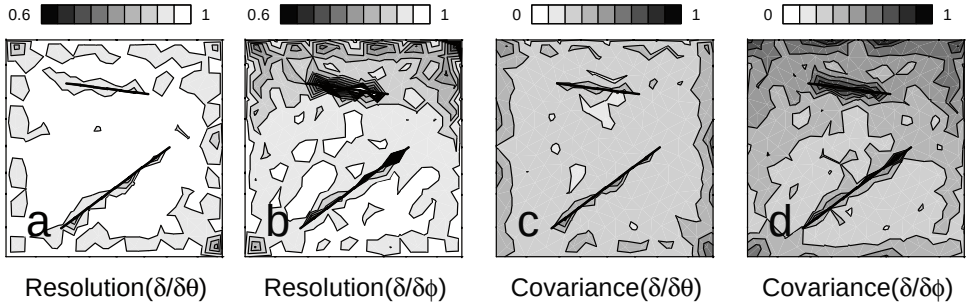

Figure 2.13: Contouring denotes the diagonal components R_{ii} of the resolution kernel $\boldsymbol{R}$ (a, b) and C_{ii} of the covariance $\boldsymbol{C}$ (c, d), respectively, interpolated between the nodes i of parameterization P3 and for components of $\boldsymbol{\nabla v}$ only; The spatial resolution for $v_{\theta\theta}$ and $v_{\phi\theta}$ (a) and for $v_{\theta\phi}$ and $v_{\phi,\phi}$ (b) are the same (similarly for the covariance (c) and (d)). The covariance is scaled by a factor of $1{\cdot}10^{-14}$.

with relatively large model errors are located along the faults and along the boundaries of the model area.

In the application of our method to real data, the choice for the best solution can only be based on data misfit, resolution and covariance characteristics for a range of solutions. The data misfit on P3 as a function of α_d and α_a (figure 2.10.P3c) varies smoothly and remains very small, even for significant changes in especially the model misfit for fault slip $\Psi_{M_f}(\boldsymbol{s}_\mu, \boldsymbol{s}_m)$ (figure 2.10.P3a). For the set of solutions found for grid P3 the trade-off between covariance and resolution becomes clear if we plot average estimates for standard deviations of $\boldsymbol{s}$ and $\boldsymbol{\nabla v}$, $\tilde{\sigma}^f_m = (1/M_f)\sum_{i=1}^{M_f}\sqrt{C_{ii}}$ and $\tilde{\sigma}^c_m = (1/M_c)\sum_{i=1}^{M_c}\sqrt{C_{ii}}$, respectively, and for the resolution $(1/M)\sum_{i=1}^{M} R_{ii}$ as functions of α_a and α_d (figure 2.14) in a similar way as in figure 2.10. In applications to real data somewhere within this trade-off

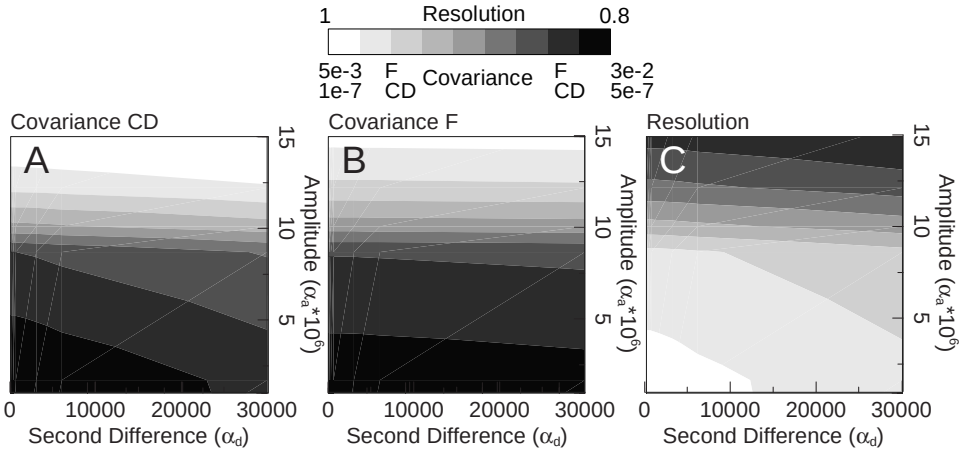

Figure 2.14: Influence of damping on average model error and resolution of inversion for $\boldsymbol{\nabla v}$ and $\boldsymbol{s}$ on grid P3. Abbreviations CD and F indicate $\boldsymbol{\nabla v}$ and $\boldsymbol{s}$, respectively. Contouring denotes average standard deviations of (A) $\boldsymbol{\nabla v}$: $\tilde{\sigma}_m^c = (1/M_c)\sum_{i=1}^{M_c}\sqrt{C_{ii}}$; (B) $\boldsymbol{s}$: $\tilde{\sigma}_m^f = (1/M_f)\sum_{i=1}^{M_f}\sqrt{C_{ii}}$ and (C) average resolution $(1/M)\sum_{i=1}^{M} R_{ii}$ as functions of α_d (horizontal axis) and α_a (vertical axis), similar as for the results shown in figure 2.10.

between resolution and covariance a model must be selected.

Of interest is to determine how sensitive the solution is to the exclusion of one observation site i. This is done by exclusion of all 80 observations involving i from $\boldsymbol{d} = \boldsymbol{Am}$, which gives equations $\boldsymbol{d}_{-i} = \boldsymbol{A}_{-i}\boldsymbol{m}_{-i}$, and comparison of the inversion results with those of an inversion with the full set of stations, hereafter the reference inversion. To analyze the sensitivity of the solution to all 81 stations we perform a succession of 81 inversions on grid P3 with $\sigma_r = \sigma_r^\mu$, $\alpha_a = \alpha_d^\mu$ and $\alpha_d = \alpha_d^\mu$. We define the sensitivity of a quantity ζ to the exclusion of data associated with site i as

$$\delta\zeta(i) = \tilde{\zeta} - \zeta(i), \tag{2.12}$$

with $\zeta(i)$ its value computed for the inversion of $\boldsymbol{d}_{-i} = \boldsymbol{A}_{-i}\boldsymbol{m}_{-i}$ and $\tilde{\zeta}$ its value for the reference inversion. Figure 2.15 represents the results of the sensitivity tests for 6 different quantities for ζ: The average model standard deviation of $\boldsymbol{\nabla v}$: $\tilde{\sigma}_m^c$ (2.15a), and of $\boldsymbol{s}$: $\tilde{\sigma}_m^f$ (2.15b), model misfit functions $\Psi_{M_c}(\boldsymbol{p}_\mu, \boldsymbol{p}_m)$ (2.15c) and $\Psi_{M_f}(\boldsymbol{s}_\mu, \boldsymbol{s}_m)$ (2.15d), average model resolution $\tilde{r}$ (2.15e) and data misfit $\Psi_N(\boldsymbol{d}, \boldsymbol{d}_m)$ (2.15f). In general, the inversion is not very sensitive to exclusion of any of the stations. The inversion results are most sensitive to exclusion of observation points located along the boundaries of the model area and close to the faults. The average model standard deviation of the slip parameters σ_m^f becomes worse if the faults are less well sampled, but this does not have significant influence on σ_m^c. We conclude that the partitioning of the solution over fault slip and velocity gradient is, as expected, sensitive to the presence of observation sites near the faults. This trade-off is primarily determined by lack of data and not by our interpretation method.

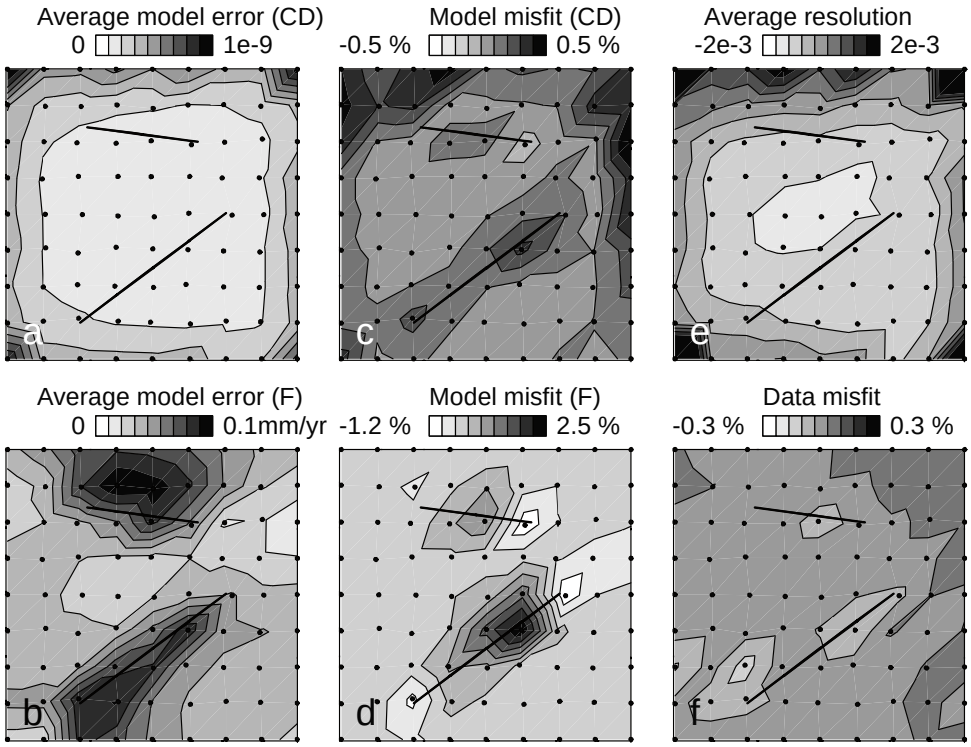

Figure 2.15: Results of the sensitivity of several characteristics of the optimal solution (presented in figure 2.11) to the exclusion of one station (black dots). The contouring denotes $\delta\zeta(i)$ at the location of station i (equation 2.12), with for ζ: (a) $\tilde{\sigma}_m^c$; (b) $\tilde{\sigma}_m^f$; (c) $\Psi_{M_c}(\boldsymbol{p}_\mu, \boldsymbol{p}_m)$; (d) $\Psi_{M_f}(\boldsymbol{s}_\mu, \boldsymbol{s}_m)$; (e) $(1/M)\sum_{i=1}^{M} R_{ii}$; (f) $\Psi_N(\boldsymbol{d}, \boldsymbol{d}_m)$. The reference values $\tilde{\zeta}$ are: (a) $2{\cdot}10^{-8}$; (b) 0.4 mm/yr; (c) 20 %; (d) 17 %; (e) 0.91; (f) 2%.

To further examine the trade-off between $\boldsymbol{s}$ and $\boldsymbol{\nabla v}$, we perform an inversion on P3 with a data set consisting of 100 stations with the additional 19 stations located closely along both sides of the fault traces. We do not add more stations at the fault tips, because this complexity can only be resolved by more sites and smaller triangles. Figure 2.16a shows the misfit between the 4 components of $\boldsymbol{\nabla v}$ of the synthetic deformation field and the 100-station solution. The misfits due to the trade-off between $\boldsymbol{s}$ and $\boldsymbol{\nabla v}$ have become smaller (compare to figure 2.11c). This becomes clear if we plot the difference between the 81- and the 100-station solution (figure 2.16b). Furthermore, the residual fault slip $\triangle \boldsymbol{s}$ is very small (on average less than 1 mm/yr). Model misfits for fault slip and continuous deformation have decreased to about 12%.

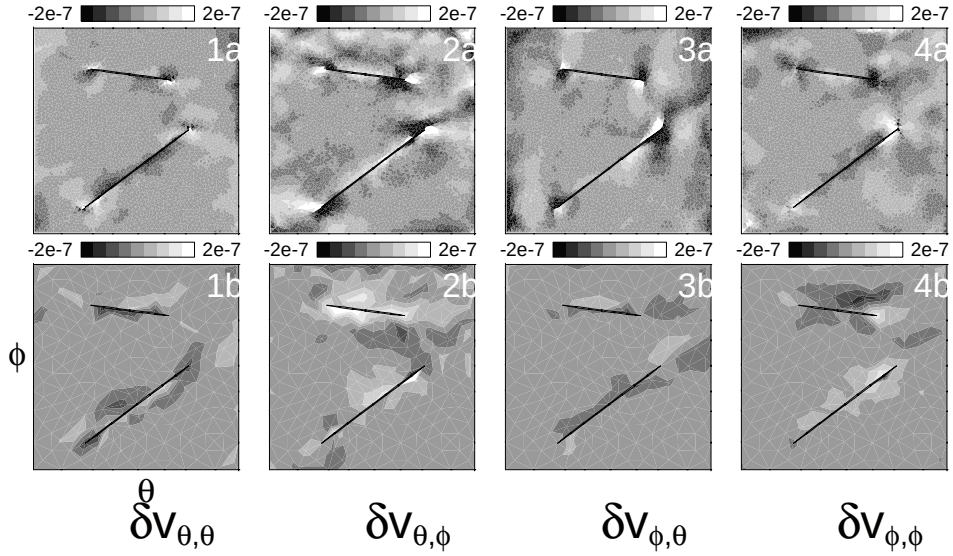

Figure 2.16: (a) Difference between synthetic deformation field II (figure 2.2.IIb) and $\nabla \boldsymbol{v}$ determined jointly with $\boldsymbol{s}$ on grid P3 for a data set with 100 observations, of which the extra stations (compared to the 81 used in the previous studies) are located closely around the fault traces. See the caption of figure 2.7c for explanation of the components. (b) Difference between the optimal solution for a data set with 81 stations (figure 2.11b) and the optimal solution for a data set with 100 stations, both on P3.

2.6 Discussion and conclusion

The synthetic data for our experiments where constructed to be internally consistent with the synthetic deformation field. Further, the synthetic model was constructed to possess more detail than could be resolved, i.e. nonlinear variation of the velocity gradient field within the triangles used for inversion, to mimic data complexities of real data sets. The synthetic experiments demonstrate that our proposed kinematic inversion method works well to obtain joint estimates of the velocity gradient field and slip on active faults. The data are fit within their error bounds for solutions which are well resolved and have acceptable covariance. Model misfit patterns could be sufficiently minimized and basically can be understood as a result of the imposed lack of data. Extra constraints imposed on the solution for $\nabla \boldsymbol{v}$ in the form of $\nabla \times \nabla \boldsymbol{v} = \mathbf{0}$ data equations improve the conditioning of the inverse problem and increase the model fit. Our adopted regularization strategy aimed at obtaining smooth models. Some small amplitude but spatially large-scale and smooth model variations prove to be associated to the model null space. Imposing an additional flatness constraint (first derivative damping) will probably suppress these effects.

Although our parameterization is based on linear variation of the velocity gradient within triangles this proves not particularly restrictive. Strong variations in the velocity

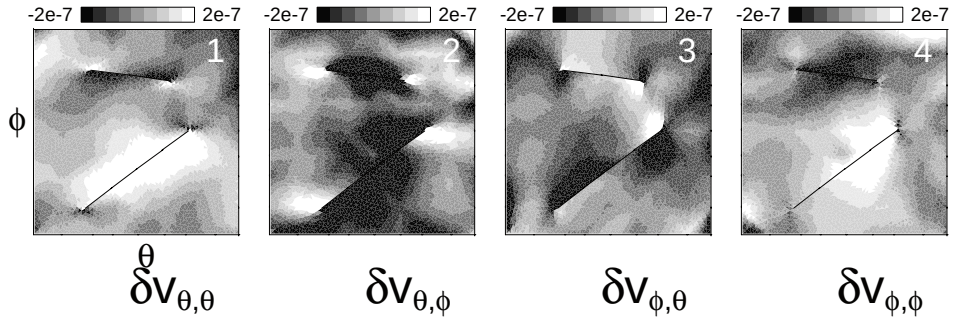

Figure 2.17: Difference between $\nabla \boldsymbol{v}$ determined jointly with $\boldsymbol{s}$ and $\nabla \boldsymbol{v}$ obtained in an inversion ignoring fault slip; 1-4 denote components of $\nabla \boldsymbol{v}$ (see caption of figure 2.7c.)

gradient field can be accommodated by using a denser parameterization with smaller triangles. The most basic problem we encountered is the trade-off between fault slip and the velocity gradient field. We stress that this effect is due to lack of data. Any inversion method of relative motions will one way or another encounter this problem and have to deal with it. Our method offers sufficient flexibility to study trade-off phenomena. For instance an inversion performed for data set I (no faults in the synthetic model) for both velocity gradient and fault slip yields insignificant fault slip. Conversely, an inversion of data set II restricted to solving for the velocity gradient only yields a solution with small data misfit and very large model misfit (figure 2.17 and compare to figure 2.7c). In general, ignoring fault contributions in the inversion would lead to a test of the hypothesis that all faults are essentially locked at the surface. Similarly one can test the hypothesis that the velocity gradient is zero and that fault slip purely reflects crustal block motion. In our synthetic experiments an inversion for fault slip only, although well resolved, cannot fit the data properly and this solution can therefore be rejected.

The trade-off may complicate the interpretation of estimated fault slip in inversions of real data. Parameterization of large faults only will render a continuous deformation solution that probably represents slip on non-parameterized faults combined with distributed deformation in the crust. If only observation sites are used far away from faults, the estimated fault slip will reflect predominantly (long term) crustal block motion, i.e. independent of fault locking. If sites are used close to faults, the actual fault motion will prevail in the estimate which includes obtaining zero motion if a fault has been locked during the observation period. Insignificant slip rates in combination with strong variations in the velocity gradient near the fault trace suggest fault locking and/or surface creep processes associated with fault activity at depth. Using observation sites close to faults is the only remedy (for any method) to break the trade-off.

One interesting extension of the method would seem to assume unknown fault location and include fault locations as additional model parameters. This is however doomed to fail because there is no kinematic coupling between fault position and velocity gradient field in our pure kinematic approach. In fact, this lack of coupling combined with lack of data

causes the trade-off between velocity gradient and fault slip. Solving for fault location could however be successful if crustal and fault rheology would enter the analysis, e.g., by invoking elastic dislocation models to create a relation between fault behavior and the velocity gradient field. Another interesting development would be to include time as an independent variable and invert time series obtained from permanent observation with GPS. We foresee no basic problems for this application because time is already included in the observation equation (equation 2.1). For this application of our method inclusion of earthquake related motions would not only cause no basic problems, it would even be highly desirable in order to map the kinematic response of the crust to preseismic loading, coseismic rupture and eventually postseismic relaxation processes. We leave this for future development.

For application of our method to deformation studies in areas with large variations in topography (e.g., volcano deformation) we note that the lateral components of relative velocity may also depend on the radial (depth) derivative component of the velocity gradient field and hence should be included in the forward problem. Our synthetic model was constructed from a plane stress finite element computation which implies that the radial derivative of the horizontal components of velocity are zero.

Basically our proposed method is independent of spatial scale. For instance it can also be applied to study global crustal deformation and plate motion. Further, because of its independence of crustal rheology the inversion results are useful as constraints or boundary conditions on crustal modeling, and for direct interpretation of strain and rotation fields, and fault slip, in the context of the tectonic evolution of a particular study region.

Chapter 3

Present-day crustal deformation of the Aegean

3.1 Introduction

The extensive monitoring of active crustal motion by means of satellite geodesy over the past 15 years has been an important contribution to the present knowledge of the surface kinematics of the Aegean region, one of the Earth's most seismically active and rapidly deforming continental regions. The recent integration of geodetic data of over 30 local campaigns has lead to a data set of more than 200 velocity vectors [Clarke et al., 1999; Cruddace et al., 1999] and is performed within the framework of the SING project (GPS Seismic hazard in Greece). This preliminary version of the final data set samples the area from longitude east 20.5° to 28° and from latitude north 35° to 41.5° and is especially dense at the Ionian islands, the Greek mainland and around the Gulf of Corinth.

In this chapter we apply our inversion method to the SING data set in two different versions. We invert for the velocity gradient only which would follow from the assumption that all faults in the Aegean were locked during the entire observation period. We compare results of this application with those of inversions for both velocity gradient and fault motion allowing for slip on some major faults in the region. Further, we compare the results of both solutions with seismic moment tensor information, other geodetic studies, both on regional and local spatial scales, and young paleomagnetic and geologic observations. Finally, in an attempt to contribute to a more detailed, kinematic picture of the present-day deformation of the Aegean, we propose a new view on the accommodation of deformation in the crust. For a full description and discussion of the method we refer to chapter 2.

3.2 Active tectonics

The tectonics of the Aegean region can be considered in a larger-scale framework of the interacting Eurasian, African and Arabian plates (figure 3.1). About 12 Myr ago (mid-

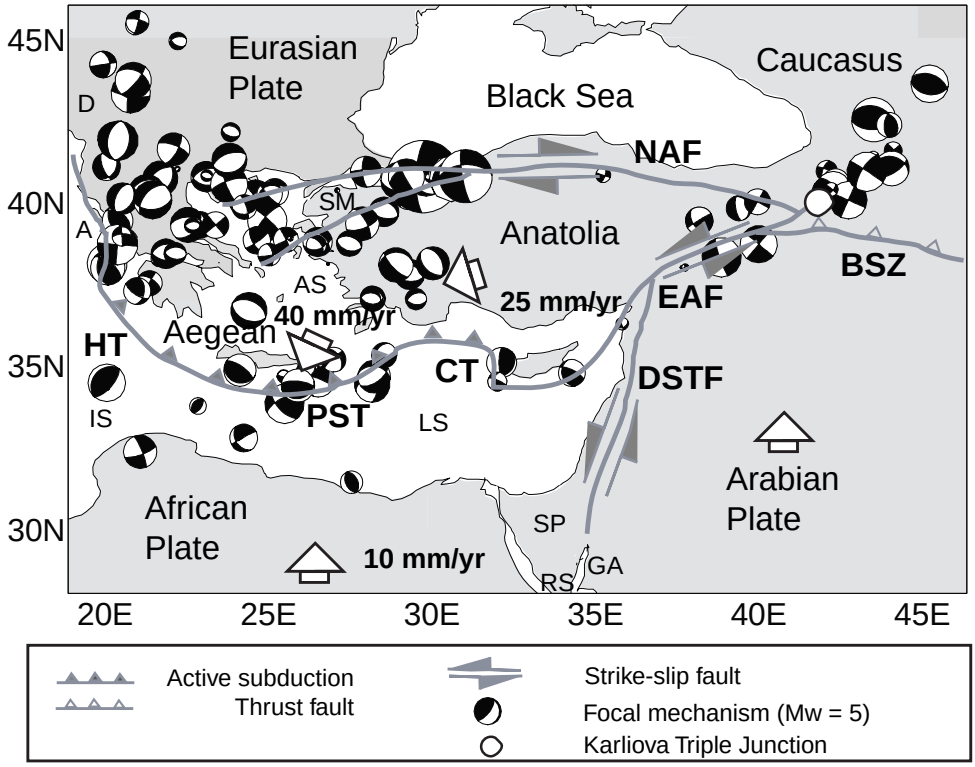

Figure 3.1: Simplified representation of the tectonics in the Eastern Mediterranean. The white arrows represent the motion relative to Eurasia fixed. The African plate can also be denoted as the Nubian plate. Key: A, Adriatic Sea; AS, Aegean Sea; BSZ, Bitlis suture zone; CT, Cyprus trench; D, Dinarides; DSR, Dead Sea Rift; EAF, East Anatolian fault; GA, Gulf of Aquaba; HT, Hellenic trench; IS, Ionian Sea; LS, Libyan Sea; NAF, North Anatolian fault; PST, Pliny-Strabo trench; RS, Red Sea; SM, Sea of Marmara; SP, Sinaï Peninsula.

Miocene), the Arabian plate reached the Eurasian plate borders, which closed the Bitlis suture and initiated the continental collision that is still continuing [e.g., Dewey et al., 1986; Armijo et al., 1999]. At the Caucasus and the region between the Black and the Caspian Seas, representing the northern rim of the broad boundary zones between the plates, Arabia is being overridden by Eurasia. The southern rim is marked by the Bitlis-Zagros fold and thrust belt. The release of gravitational potential energy due to the thickened crust in eastern Turkey has been proposed as the cause for the wrenching of Anatolia from Eurasia leading to the WSW directed motion of Anatolia along the North Anatolian fault with respect to Eurasia [e.g., McKenzie, 1972; Jackson and McKenzie, 1984, 1988]. The now nearly 2000-km-long North Anatolian fault has propagated through continental crust and lithosphere from the Karliova triple junction (Eurasia-Anatolia-Arabia) to the Aegean region [Armijo

Figure 3.2: Map of Greece with main topographic features.

et al., 1999]. Geological and space geodetic observations estimate the present-day slip rate at a 25 mm/yr [Armijo et al., 1999; Straub et al., 1997; Reilinger et al., 1997; McClusky et al., 2000]. Around the Sea of Marmara and the Dardanelles the North Anatolian fault enters the Aegean where it disperses along the North Aegean trough and other, more southernly located, NE-SW oriented fault branches. This style of faulting ends against NW-SE and E-W trending normal faults in central and northern Greece [Taymaz et al., 1991].

The boundary between the Aegean and Eurasia is unclear. Paleomagnetic observations [e.g., Kissel et al., 1986; Kissel and Laj, 1988], seismic moment tensors [e.g., Jackson and

McKenzie, 1988; Taymaz et al., 1991] and regional GPS studies [e.g., Reilinger et al., 1997; Straub et al., 1997; Kahle et al., 2000; McClusky et al., 2000] show that the NE-SW dextral shear crosses the central Aegean. At the western Aegean the Kephalonia fault zone represents the boundary between the Adriatic Sea and the Aegean region and marks the beginning of the Hellenic trench. North of the Kephalonia fault zone the Hellenic arc does not seem to accommodate any motion, while it shows rapid southwestward motion with respect to Europe south of it [Smith et al., 1990; Kahle et al., 1996; Noomen et al., 1996]. This may indicate that the westward motion of Turkey is being accommodated by shortening in the region north of the Kephalonia fault zone [McKenzie, 1972, 1978] and/or by motion on the Kephalonia fault zone and the western Hellenic trench [e.g., Kahle et al., 1995, 1996]. Whether the North Anatolian fault connects to the Gulf of Corinth is subject of debate [Le Pichon et al., 1995; Armijo et al., 1996; Papazachos, 1999; Papazachos et al., 2000].

A phase of extension of the Aegean was initiated about 12 Myr ago probably caused by the roll-back of African lithosphere beneath the Aegean along the Hellenic trench [e.g., Meijer and Wortel, 1997], where the Eastern Mediterranean Basin (African plate) is subducting in NNE direction. Wide-spread basin subsidence resulted in the formation of the Aegean Sea [e.g., Le Pichon and Angelier, 1979; Mueller and Kahle, 1993; Jackson, 1994]. At present, the central southern Aegean between the volcanic (latitude 37° to 38°) and non-volcanic Hellenic arc (latitude 35° to 36°) appears to be relatively aseismic and strain-free [e.g., Kahle et al., 2000], yet it must have undergone an increase in surface area by a factor of about two since extension began [Le Pichon et al., 1995]. Although the net effect of relative plate motion between Africa and Eurasia is convergence, the Aegean region must still be subject to large-scale extension evidenced by the present-day southwestward directed motion at a rate of about 40 mm/yr with respect to Europe of the eastern Aegean south of $\sim$40°N and the western Aegean south of $\sim$38°N [e.g., McKenzie, 1972; Jackson, 1994; Le Pichon et al., 1995; McClusky et al., 2000]. The localization and distribution in the Aegean of this motion relative to Eurasia is complex and not fully agreed upon. In the eastern Aegean region at western Turkey N-S extension is taken up by E-W trending graben structures [Taymaz et al., 1991; Straub et al., 1997; Kurt et al., 1999; Kahle et al., 2000]. In the central and western Aegean region N-S motion is accommodated by N-S extension in the North Aegean trough and on normal faults and graben structures in the Greek mainland [e.g., Taymaz et al., 1991; Jackson et al., 1992] and along the Gulf of Corinth [e.g., McKenzie, 1972, 1978; Le Pichon et al., 1995; Armijo et al., 1996], and by dextral motion along the Kephalonia fault system [e.g., Kahle et al., 1995, 1996; Cocard et al., 1999].

3.3 Data: the SING project

Since 1988 several regional GPS networks have been established in the Aegean area (marked by a ♡-symbol in table 3.1). Frequent occupation of these networks led to a GPS data archive that, together with SLR observations in the context of the Wegener project (♣-symbol, table 3.1) and 100-year old triangulation data from a network in central Greece (♠-symbol, table 3.1), samples the Greek mainland, the Peloponessos, the Ionian islands and the Aegean Sea. The integration of these data into one main data set, locally densified by smaller-scale GPS arrays obtained at seismically active areas or areas of expected seis-

	CG♡ [1,2]	I♡ [3,4]	A♡ [5,6,7]	C♡ [8,9]	T♠ [10,8,11]	W♣ [12,13,17]	Ai♢ [2,14,15]	G♢ [16]
1892					x			
1904					x			
1974					x			
1988			10					
1989	5	9	10		9			
1990		6		5				
1991	10	9		9				
1992			5		6	8		
1993	5	10		5				
1994		4,9				8		
1995				10			6,10	5,9
1996	5		9,10		6	6,10	5	5
1997	9-10							
1998								6

Table 3.1: Different data sets that constitute the SING data set. Symbols: ♡, regional networks; ♠, historic triangulation network; ♣, Mediterranean SLR network; ♢, local postseismic networks. Network keys: CG, Central Greece; T, historic triangulation; I, Ionian; A, Aegean; W, Wegener; C, Corinth; Ai, Aigion; G, Grevena. Numbers between straight brackets refer to publications in which the campaign and processing of the data set is described: 1 [Denys et al., 1995], 2 [Clarke et al., 1998], 3 [Kahle et al., 1995], 4 [Kahle et al., 1996], 5 [Kastens et al., 1989], 6 [Gilbert et al., 1994a], 7 [McClusky et al., 2000], 8 [Davies et al., 1997], 9 [Briole et al., 1996], 10 [Billiris et al., 1991], 11 [Veis et al., 1992], 12 [Noomen et al., 1993], 13 [Smith et al., 1994], 14 [Bernard et al., 1997], 15 [Clarke et al., 1997a], 16 [Clarke et al., 1997b], 17 [Zerbini et al., 1998]. The numbers in the table refer to the month during which the stations were occupied.

mic risk, is one of the subjects of the GPS Seismic Hazard in Greece (SING) project [e.g., Clarke et al., 1999; Cruddace et al., 1999]. Main objectives of the SING-project are the assessment of strain accumulation throughout Greece and the identification of areas of high seismic hazard. The data set used in this study constitutes a large subset of a preliminary version of the SING data with velocities measured up to 1998. In addition to the main data it contains data of two smaller-scale densification arrays (♢-symbol, table 3.1) and is especially dense in central and northern Greece, the Ionian islands and the eastern Peloponessos. Table 3.1 lists the time intervals of occupation per network.

The processing of the data and the integration of the different subsets is described by Clarke et al. [1998]; Cruddace et al. [1999] and Clarke et al. [1999]. We summarize the basic SING strategy. The GPS data are processed with the Bernese [Rothacher and Mervart, 1996] and the GIPSY-OASIS II [Webb and Zumberge, 1997] scientific software packages. With both methods an average position for the permanent station CG54 (also Dionysos, figure 3.3) over the period of observations is estimated in ITRF96, with respect to which the coordinate sets are transformed. The differences between the two solutions for the location of CG54 are small: 1 mm for the eastern, 8 mm for the northern and 0.6 mm for the vertical

component. Velocities are calculated under the assumption that short-term inter-seismic velocities are steady and therefore reference frame biases can be estimated. The errors in the velocities are scaled based on a combination of baseline repeatability measurements and formal χ^2-values computed by the processing software.

In 1992 the almost 100 year old Greek triangulation network was re-occupied by GPS. The orientation of the triangulation - GPS velocity estimates is constrained using 14 sites common to both the triangulation and the local GPS networks [Billiris et al., 1991; Davies et al., 1997; Clarke et al., 1998]. The results show a high compatibility between short-term and 100-year deformation estimates; the coordinate fit of the triangulation networks fits the model of steady state velocities well within 95% confidence limits.

Two earthquakes occurred during occupation of the stations between 1988 and 1998, that had significant, coseismic influence on the measurements: the M_s=6.2, June 15, 1995 Aigion (Gulf of Corinth, Aigion earthquake hereafter) and the M_s=6.6, May 13, 1995 Kozani-Grevena (northern Greece, Grevena earthquake hereafter) earthquakes, both associated with almost pure extension. Clarke et al. [1997a] subtracted the coseismic velocities due to the Aigion earthquake from the SING data, shown in figure 3.3C. Only those measurements done during the 4 campaigns in the Grevena area after the Kozani-Grevena earthquake are included [Clarke et al., 1997b] (table 3.1, figure 3.3B). The velocities, of which the first measurements were obtained 5 days after the Grevena earthquake, show SW to SSW directed motion southeast of the epicenter and of the NE-SW striking rupture plane [e.g., Clarke et al., 1997b]. Finally, we exclude those velocities computed from sites that were occupied only twice. The remaining set is sufficiently dense to represent the regional velocity field and consists of 175 vectors (figure 3.3).

3.4 Evidence for postseismic deformation?

Initial inversions of the 175 SING data set (figure 3.3) are targeted at fitting both the relative velocity data and the $\boldsymbol{\nabla} \times \boldsymbol{\nabla v} = \mathbf{0}$ constraints by solving for a continuous deformation field only. In this part of the analysis faults are ignored; parameterization is restricted to the velocity gradient field. This inversion is further described in appendix C and shows that acceptable model error can only be obtained for models with a poor data fit ($\chi^2 >> 1$). Inspection of the solution demonstrates that the region near the Gulf of Corinth is responsible for the large data misfit (figure C.3), this despite the much denser parameterization used here (figure C.1B). Linear variation of $\boldsymbol{\nabla v}$ in small triangles is apparently insufficient to fit the data, which show strong spatial variation over small distances (figure 3.3). The presence in the SING set of the data of the Grevena and Aigion networks (table 3.1) that were acquired almost immediately after the Grevena and Aigion earthquakes raises the question to what extent the data are influenced by postseismic deformation. We recall that the data have been corrected for coseismic deformation [Clarke et al., 1997a].

Postseismic deformation would constitute a time-dependent signal in GPS data which is not being modeled in our present approach. From geodetic studies of crustal deformation associated with large earthquakes either afterslip and/or viscoelastic relaxation of the lower crust (and perhaps upper mantle) have been proposed as main sources for postseismic deformation [e.g., Pollitz et al., 2000]. Because constraints on both horizontal and vertical

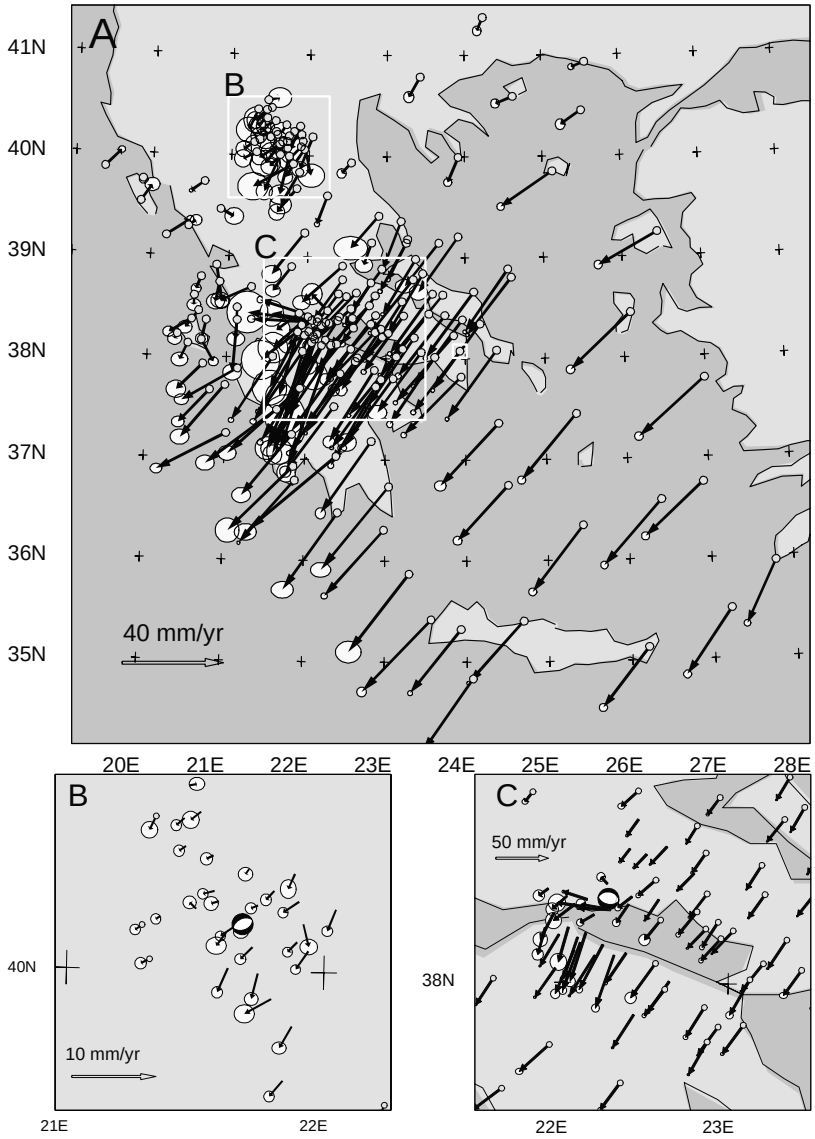

Figure 3.3: (A) The 175 velocity vectors of the SING data set, displayed with respect to a Eurasia fixed reference frame. The small open, white square at longitude 23.93°, latitude 38.08° indicates the fixed station CG54 (Dionysos). The two windows indicate the local areas that are enlarged in (B) the Grevena area, northern Greece, with the fault plane solution of [Clarke et al., 1997b] for the May 13, 1995, Kozani-Grevena earthquake; and in (C) the Gulf of Corinth, with the fault plane solution of Bernard et al. [1997] for the June 15, 1995, Aigion earthquake.

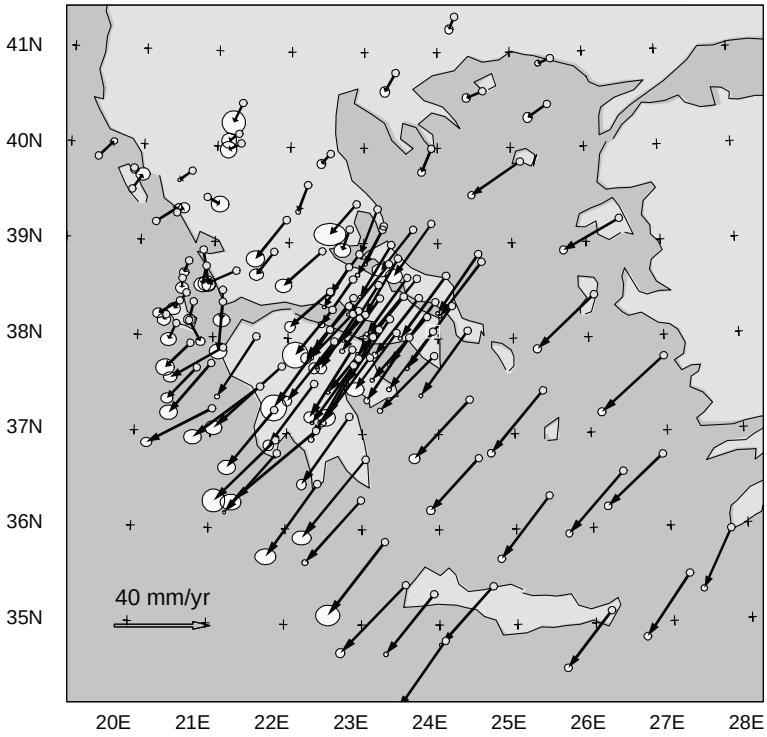

Figure 3.4: The 116 velocity vectors of the SING data set without the possibly post-seismically influenced stations. For further information see caption of figure 3.3

motions are critical for a unique estimate of the individual contributions of both processes, the assessment of possible postseismic deformation for the Grevena and Aigion earthquakes from our horizontal GPS velocities is not straightforward. Both visco-elastic relaxation and afterslip may have played a role in the postseismic deformation. Koukouvelas and Doutsos [1996] measured an afterslip throw of 3 cm within the first 10 weeks after the earthquake. Furthermore, from magneto-telluric profiles crossing the Aigion fault segment Pham et al. [2000] found evidence for a regional-scale, highly conductive layer, 5 to 10 km thick, at a depth of about 13 km, suggesting the presence of fluid enriched crustal rocks with a ductile rheology. Such a layer could play an important role in visco-elastic relaxation of the crust after a large earthquake. We do not know of detailed descriptions of observations of post-seismic deformation due to the Grevena earthquake. However, the short time-interval of 5 days between the actual earthquake and the first occupation of the Grevena network causes the possible presence of a considerable non-stationary postseismic signal in the data to be a complicating factor for our analysis.

In general, possible postseismic effects are most likely averaged out over the 100-year time interval between the first and last measurements at triangulation sites. This expectation

is confirmed by studies of Davies et al. [1997] and Clarke et al. [1998], who find a high compatibility between short-term and 100-year geodetic estimates of deformation, before the earthquakes occurred. However, since occupations of the Aigion, Corinth and Grevena networks took place within the first year after the earthquakes at the end of the time-interval that covers the complete data set (table 3.1), strong signals like the co- and postseismic velocities associated with the two earthquakes mentioned can cause anomalous velocity behavior compared to the rest of the data. To derive the regional-scale, steady velocity field we exclude all stations that may have been influenced by postseismic motions from the Aigion and Grevena earthquakes, which reduces the data set to 116 vectors. The remaining velocity data set (figure 3.4) contains only a few data at the Grevena area and no data directly along the north and south of the western part of the Gulf of Corinth. The procedure followed for the exclusion of data is described in appendix C. An attempt to separate interseismic from postseismic effects by comparing a solution obtained for the 175-vector data set with a solution for the 116-vector data set shows considerable difference in the deformation field at the Grevena and Aigion regions only. Finally, appendix C presents the results of a simple forward computation of the response of a visco-elastic half space [VISCO1D, Pollitz et al., 2000] to the stresses released by the Aigion earthquake. In the remainder of this chapter we will use the reduced data set of 116 velocity vectors.

3.5 Inversion

3.5.1 Model parameterization

The data are inverted for two different representations of the Aegean crustal deformation field; the first in terms of continuous deformation only, the second in terms of continuous deformation and fault motion. For both inversions we use the same triangular grid (figure 3.5). On the fault traces duplicate model nodes are used to allow decoupling across the fault in a joint inversion for the velocity gradient field and fault motion. In general, the local density of the stations is used as a guide for local densification of model nodes for the triangulation.

For the parameterization of faults we adopt the fault zones of the tectonic maps presented by Taymaz et al. [1991] and Jolivet et al. [1994]. The location and strike of the main faults of both studies are almost similar and the information on the smaller-scale structures is complementary. Information from local studies is used to define the location of the fault traces more precisely. We do not aim at a fault parameterization which is as complete as possible. Our modeling implies that slip that occurred on non-parameterized faults will be represented in our solution by local variation in the velocity gradient field.

At southern Albania and northwestern Greece (the Epirus region) we parameterize the boundary between the Adriatic Sea and the Aegean region. The fault system parallel to this boundary [Mantovani et al., 1992] is represented by one fault. We connect the segmentation of the southern strand of the N-S pull-apart basin of the Gulf of Arta to the segments of the sinistral Katouna fault striking in a NW-SE direction [Le Pichon et al., 1995; Haslinger et al., 1999]. The region immediately south and southeast of the southern termination of the Katouna fault north of the Gulf of Patras is characterized by small-scale N-S opening

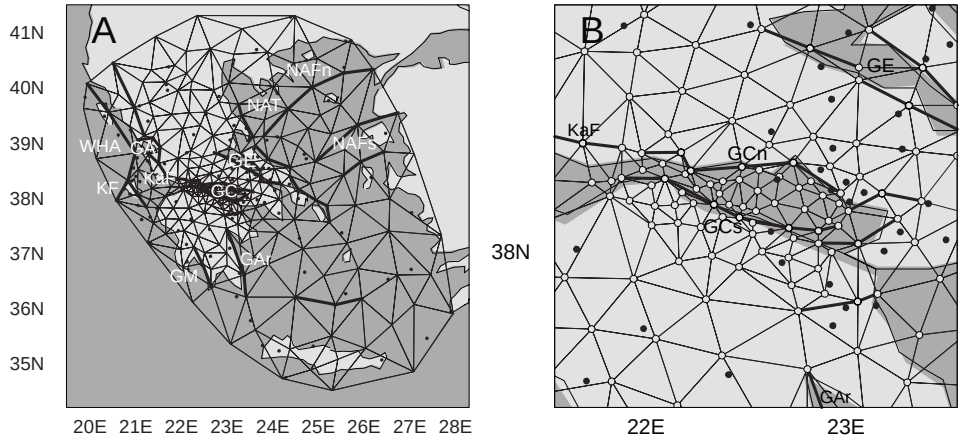

Figure 3.5: Model parameterization of the (A) Aegean. Key: GA, Gulf of Arta; GAr, Gulf of Argolis; GC, Gulf of Corinth; GE, Gulf of Evvia; GM, Gulf of Messinia; KaF, Katouna fault; KF, Kephalonia fault; NAFn, northern branch of North Anatolian fault; NAFs, southern branch of NAF; NAT, North Aegean Trough; WHA, West Hellenic arc. (B) Gulf of Corinth. Key: GCn, northern strand of the Gulf of Corinth; GCs, southern strand of Corinth. The black dots indicate the sites of the reduced data set of 166 velocity vectors.

graben structures, which we parameterize as the eastward continuation of the Katouna fault. The parameterization of the Kephalonia fault zone consists of the southern Kephalonia and the northern Lefkada segment [Louvari et al., 1999].

The Peloponessos is separated from the Greek mainland by the Gulf of Patras in the west prolongating into the Gulf of Corinth in the east. The location, orientation and activity of the faults in the proximity of the Gulf of Corinth are by no means certain. We parameterize this area by incorporating two main fault strands, the first along the north coast and the second along the south coast (figure 3.5)B. At the Peloponessos we incorporate the NW-SE trending graben structures at the Gulf of Messinia and the Gulf of Argolis. In a similar way as for the Gulf of Corinth we parameterize the Gulf of Evvia by two faults along both sides of the coasts. Along the east coasts of the mainland of Greece and the island of Evvia we include the NW-SE trending fault zone, which separates Greece from the northeastern part of the Aegean Sea [e.g., Taymaz et al., 1991].

East of 31°E the North Anatolian fault has a narrow and localized character. Before it enters the Aegean region its lateral motion is transferred across an active pull-apart basin at the Sea of Marmara, where the slip motion is partitioned over several subbranches [Straub, 1996; Armijo et al., 1999]. We parameterize three strands; the two northernmost main strands and a smaller subbranch. The northern strand enters the North Aegean trough, an ENE-trending depression zone. We omit parameterization of the extensional graben structures in western Turkey, because of the small number of data in this region.

i	T_n	T_t	K	σ_r $\left[\frac{10^{-10}}{myr}\right]$	α_a $[10^7]$	α_d $[10^6]$	χ^2	$\tilde{r}_m$	$\tilde{\sigma}^c_m$ $\left[\frac{10^{-8}}{yr}\right]$	$\tilde{\sigma}^f_m$ $\left[\frac{mm}{yr}\right]$
I	257	492	-	3.4	1.0	1.5	1.18	0.92	1.7	-
II	295	492	96	1.1	1.0	0.75	1.13	0.96	1.4	0.6

Table 3.2: Grid characteristics, a priori model parameters and average results for the inversion for $\boldsymbol{\nabla v}$ only (inversion I) and for joint estimates of $\boldsymbol{\nabla v}$ and $\boldsymbol{s}$ (inversion II). Key: i, inversion; T_n, number of model nodes; T_t, number of triangles; K, number of fault segments; σ_r; standard deviation of $\boldsymbol{\nabla} \times \boldsymbol{\nabla v} = \mathbf{0}$ data constraints; $\tilde{r}_m = \frac{1}{M}\sum_{i=1}^{M} R_{ii}$; the average model resolution, with R_{ii} the resolution matrix and M the number of model parameters; $\sigma^c_m = \frac{1}{M_c}\sum_{i=1}^{M_c}\sqrt{C_{ii}}$, the average standard deviation for the components of $\boldsymbol{\nabla v}$, with $M_c = 4T_n$ the number of components of $\boldsymbol{\nabla v}$; $\sigma^f_m = \frac{1}{M_f}\sum_{i=1}^{M_f}\sqrt{C_{ii}}$, the average standard deviation for the components of $\boldsymbol{s}$, with $M_f = 2K$ the number of slip components.

3.5.2 Regularization

In a first series of inversions (inversions I hereafter) we solve for the lateral components of $\boldsymbol{\nabla v}$ only. We represent $\boldsymbol{\nabla v}$ in spherical coordinates in a symbolic notation (chapter 2) by

$$\boldsymbol{\nabla v} = \begin{bmatrix} v_{\theta\theta} & v_{\theta\phi} \\ v_{\theta\phi} & v_{\phi\phi} \end{bmatrix},$$

where θ denotes longitude and ϕ denotes latitude. In a second series (inversions II) we also solve for the horizontal slip vector $\boldsymbol{s} = (s_\theta, s_\phi)$. While tuning the covariance factor σ_r for the extra $\boldsymbol{\nabla} \times \boldsymbol{\nabla v} = \mathbf{0}$ constraints and the regularization parameters α_a and α_d (chapter 2) we primarily focus on obtaining solutions (I and II for inversions I and II, respectively) that are comparably resolved. Furthermore, to certify that the solutions I and II accommodate about the same percentage of relative motion we also attempt to keep the data misfit values χ^2 for both solutions of the same order.

While performing inversions I and II separate computation of χ^2 for the data and the extra constraints shows that both data parts have a χ^2 of 1.0, which for the latter was obtained using a standard deviation of $\sigma_r^I = 3.4 \cdot 10^{-10}$(m yr)$^{-1}$ for inversions I and $\sigma_r^{II} = 1.1 \cdot 10^{-10}$(m yr)$^{-1}$ for inversions II. The fact that σ_r^I is larger than σ_r^{II} can be explained by the piece-wise continuous formulation of inverse problem II. The parameterization of fault zones creates a block-like structure across which the velocity gradient can vary discontinuously: the solution fits the extra equations within several sub-regions, instead of within the whole model area. Both resulting solutions still contain roughness possibly related to solution components pertaining to small eigenvalues. Regularization with amplitude damping on boundary nodes and second derivative damping on all nodes is imposed by constraining $\alpha_a \boldsymbol{I}\,\boldsymbol{p} = \mathbf{0}$ and $\alpha_d \boldsymbol{D}\,\boldsymbol{p} = \mathbf{0}$, respectively, where $\boldsymbol{p}$ contains the components of $\boldsymbol{\nabla v}$ (chapter 2). Mild amplitude damping reduces the large variances along the model boundaries somewhat. Additional second derivative damping reduces the roughness of solutions I and II at small spatial scales. Compared to inverse problem II inverse problem I is less well conditioned and needs stronger second derivative regularization to control the

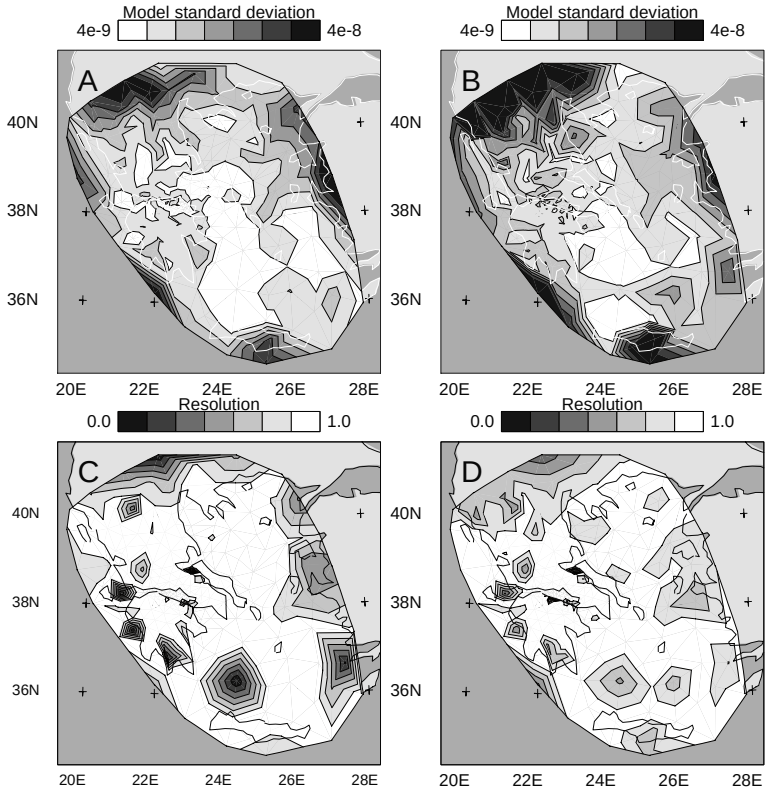

Figure 3.6: Model error and resolution of solution I with $\sigma_r = 3.4 \cdot 10^{-10}$(m yr)$^{-1}$, $\alpha_a = 1.0 \cdot 10^7$ and $\alpha_d = 1.5 \cdot 10^6$; Contouring of (A) $\sqrt{C_{ii}}$ and (B) R_{ii} pertaining to the $v_{\theta\theta}$ component; (C) and (D) see subscript for (A) and (B), respectively, pertaining to the $v_{\theta\phi}$ components.

model variance. The damping slightly impairs the spatial resolution, but still leads to an acceptable data misfit with $\chi^2 = 1.18$ for solution I and $\chi^2 = 1.13$ for solution II (table 3.2). The part of solution II belonging to fault slip is not subject to any form of damping. We accept the combinations of average resolution, model error and data fit listed in table 3.2 for further analysis of solutions I and II.

Figures 3.6 and 3.7 show results for model standard deviations $\sqrt{\boldsymbol{C}_{ii}}$ and diagonal components of the resolution matrix $\boldsymbol{R}_{ii}$ for the $v_{\theta\theta}$ and the $v_{\theta\phi}$ components of solutions I and II, respectively. In general, for both solutions the areas of relatively large standard deviation and relatively low resolution are located at the boundaries of the model. Furthermore, some individual nodes are less well resolved. Relatively large model errors on both components of solution II also occur along some faults; the North Anatolian fault branches, the fault at the central Aegean Sea and on the faults associated with the plate boundary between the Adriatic Sea and Eurasia. For both solutions, the model standard deviation of $v_{\theta\theta}$ is better

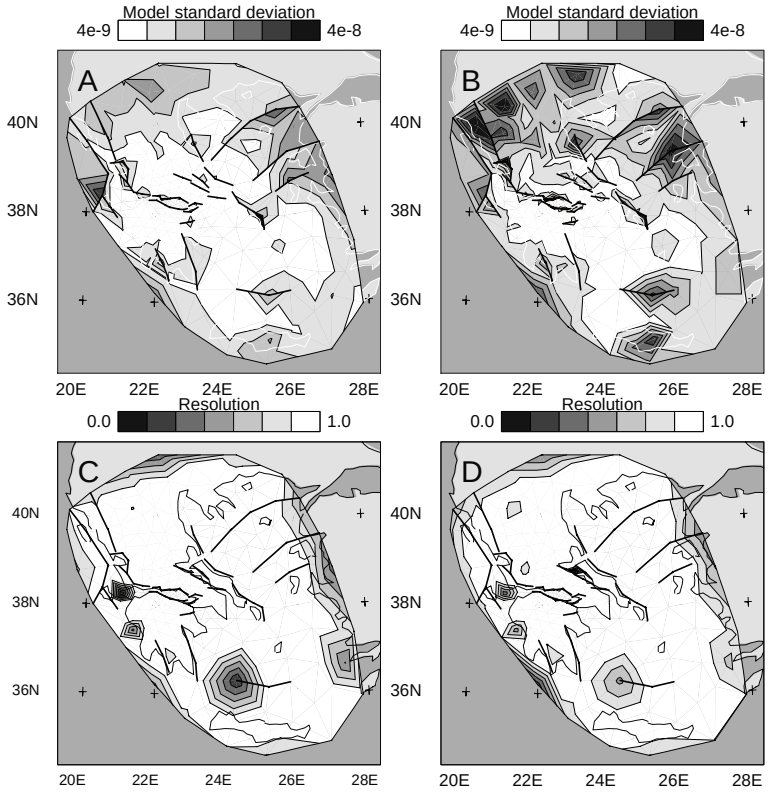

Figure 3.7: Model error and resolution of solution II with $\sigma_r = 1.1 \cdot 10^{-10}$(m yr)$^{-1}$, $\alpha_a = 1.0 \cdot 10^7$ and $\alpha_d = 1.5 \cdot 10^6$; See the caption of figure 3.6 (the resolution and model errors for the fault slip solution are listed in table 3.3).

determined than of $v_{\theta\phi}$, especially along the northern and northeastern model boundary. This difference can be explained by the distribution of stations. For example, there are no stations along the northernmost part of the model boundary, which means that this part is sampled by predominantly horizontal integral paths between stations located at the northeastern and northwestern corners of the model area. Model error and model resolution of solution II are better determined compared to solution I. This results from the parameterization of fault slip, which not only enables the accommodation of relative velocities by fault motion but also requires extra model nodes along fault traces. The fault slip model parameters are well resolved (R_{ii} all between 0.9 and 1.0) and the fault slip model errors are relatively small (all not larger than 2 mm/yr, table 3.3).

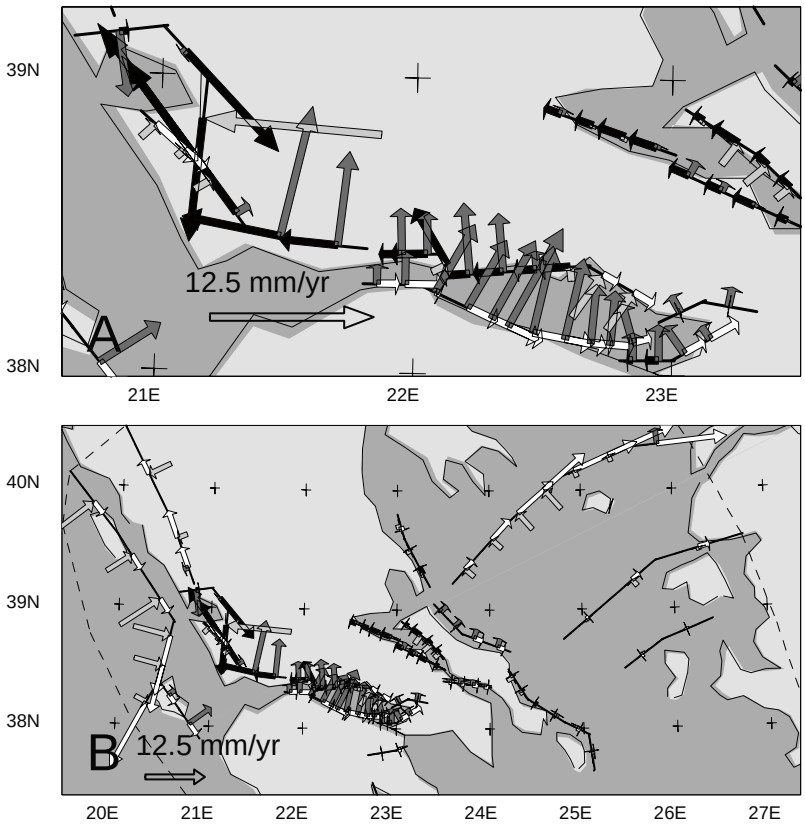

Figure 3.8: Fault slip rate vectors of solution II; the arrows denote the fault-parallel and fault-perpendicular components of the slip vector. Key for the colors: black arrows = sinistral strike-slip, white = dextral strike-slip, light-grey = thrusting, dark-grey = normal faulting. (A) Slip solution for the Katouna fault, the Gulf of Corinth and the Gulf of Evvia. The fault segmentation around the Gulf of Arta accommodates normal slip on the northern fault segment, sinistral slip on the eastern segment, sinistral slip with a relatively large thrust component on the southeastern segment, dextral slip with a relatively small thrust component on the southwestern segment. The NW-SE trending segment of the Katouna fault accommodates sinistral slip with relatively small normal and thrust components. The E-W trending segment of the Katouna fault accommodates sinistral slip with a relatively large normal component. (B) Northern part of model area (the slip solution for the faults at the southern part of the model are very small). Dashed lines indicate model boundaries.

3.6 Solution

3.6.1 Fault slip rate

Comparison of solutions I and II and discussion of the differences between the two is not straightforward because of the fundamentally different mechanisms applied to accommo-

	AEP	KF	GCn	GCs	NAF
$\perp$	5.1^r-8.3^r	2.7^r-6.7^r	4.8^n-3.4^r	1.3^n-7.4^n	4.2^r-2.8^n
$\sigma_\perp$	0.4-0.5	2.0-0.8	0.6-0.4	0.5-0.6	0.4-1.2
$\parallel$	2.3^d-2.9^d	8.4^d-12.7^d	4.3^s-1.5^d	0.3^d-3.8^d	1.9^d-12.3^d
$\sigma_\parallel$	0.4-0.5	0.9-1.8	0.5-0.2	0.4-0.6	0.4-0.7

Table 3.3: Fault slip rates of solution II. Key: $\perp$, $\parallel$: fault-perpendicular, fault-parallel slip component fault (in mm/yr); $\sigma_\perp$, $\sigma_\parallel$: fault-perpendicular, fault-parallel model error; ^{d} dextral; ^{s} sinistral; ^{r} reverse; ^{n} normal; AEP, Adriatic-Eurasia plate boundary; KF, Kephalonia and Lefkada fault segments; GCn, Gulf of Corinth (northern strand); GCs, Gulf of Corinth (southern strand); NAF, North Anatolian fault. The range of slip rates per fault denotes the maximum and minimum slip rates at this fault. If one fault accommodates both dextral and sinistral or both reverse and normal slip on different segments, then the maximum rate per slip orientation is given.

date relative velocities. Therefore, we describe the slip part of solution II first. In sections 3.6.2 and 3.6.3 we compare the velocity gradient fields of solution I and II and investigate the influence of inclusion of fault segmentation with respect to a model based on a continuous velocity gradient field.

We find that especially the parameterized fault zones on the mainland of Greece, the Gulf of Corinth, the Ionian region and in the northern Aegean Sea accommodate strong slip rates (table 3.3) compared to the parameterized faults south of the area shown in figure 3.8 that accommodate slip rates of the order of 0-1 mm/yr. We find strong thrusting at the northern segment of the plate boundary between Eurasia and the Adriatic Sea. Along the Lefkada segment towards the Kephalonia segment this slip gradually changes into predominant strike-slip. The fault zone parallel to the plate-boundary accommodates dextral strike-slip with a thrust component. The Gulf of Arta is subject to mainly sinistral strike-slip. The Katouna fault and the northern strands of the Gulf of Patras and the western Gulf of Corinth behave as sinistral, normal faults. Northeast of the Gulf of Corinth and on the southern strands of the Gulfs of Patras and Corinth we find dextral normal slip. The fault-perpendicular components of slip rate on the faults bounding the Gulf of Evvia at both sides are very small, the fault-parallel components are sinistral and of the order of a few mm/yr. The NW-SE trending fault structure just east of the coast of Greece and of the island of Evvia accommodates extension of a few mm/yr. The North Anatolian fault and the two southernly located subbranches accommodate dextral strike-slip. On the main branch this rate increases to a maximum of about 13 mm/yr from west to east, with components of thrust and extension on the western and eastern segments, respectively.

3.6.2 Strain rate

The strain rate tensor is the symmetric part of $\boldsymbol{\nabla v}$. Figures 3.9 and 3.10 display the principle strain rates of solutions I and II, respectively. Although with different amplitudes, solution I and II have in common several distinct strain rate patterns: The southern regions of Macedonia, Bulgaria and Albania, at the northern model boundary, shows relatively weak strain

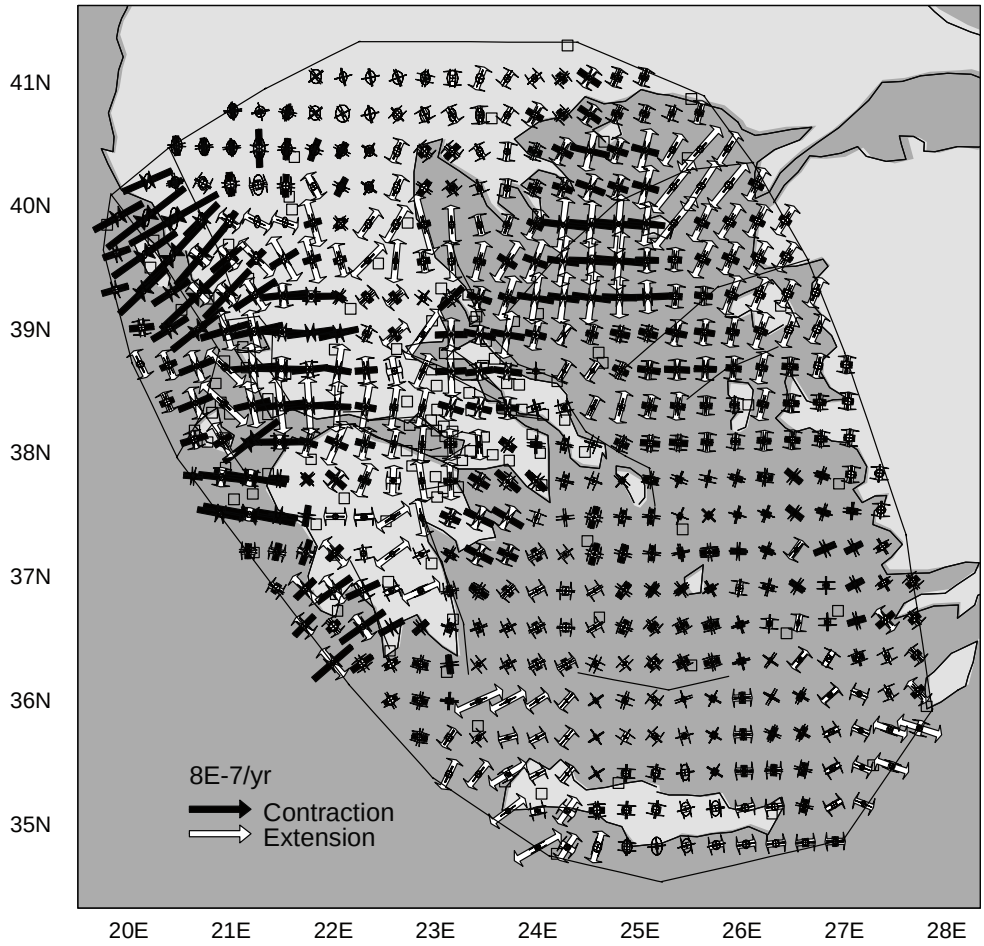

Figure 3.9: Principal strain rates and uncertainties computed on the nodes of a regular grid for solution I. This inversion is performed without parameterization of fault slip. However the fault segmentation of inversion II is indicated to facilitate comparison with the strain rate results of inversion II (figure 3.10). The open squares represent the station positions.

rates. Southwest of this area, a belt of relatively strong NE-SW oriented contraction dominates the coastline of Albania and northwestern Greece (between 20.5°E, 40°N and 21°E, 39°N). A transition zone can be traced from southern Albania/northwestern Greece and the region east of Corfu (21.5°E, 39.5°N) towards the region south of the island of Kephalonia (21°E, 38°N), separating the dominant the contraction from a more complex strain pattern at northern and central Greece and the western Peloponessos. A narrow E-W running zone of, on average, N-S extension is found between southern Albania/northwestern Greece and the North Aegean Trough at latitude 39.5°N. The orientation of the extension changes from

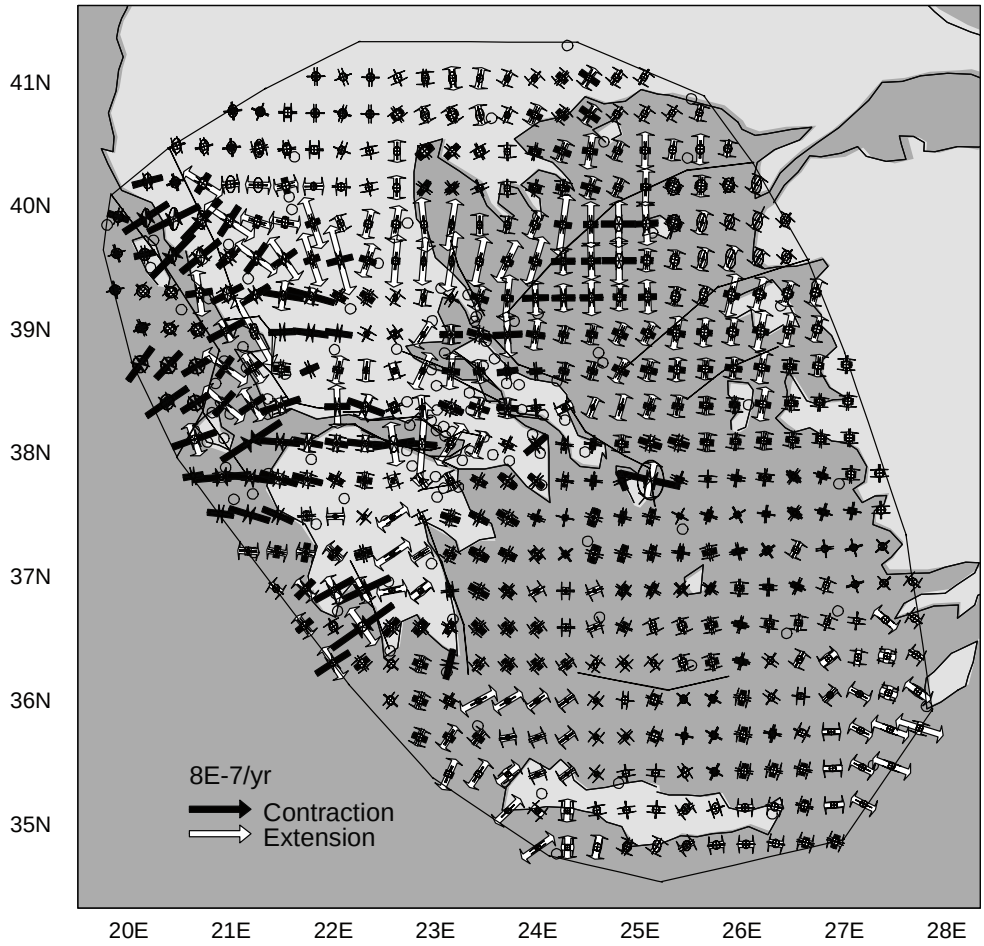

Figure 3.10: Principal strain rates and uncertainties computed on the nodes of a regular grid for solution II. The open circles represent the station positions.

NNW-SSE at northwestern Greece (22°E), where the strain rate field also contains a considerable contractional component, to NNE-SSW at the North Aegean trough (23.5°E), where strain rates indicate pure, uniaxial extension. In the northeastern Aegean Sea the almost pure extension of the North Aegean trough changes to shear strain rates at the region where the western termination of the North Anatolian fault zone plays a major role (between longitudes 24°E and 25°E). South of the North Aegean trough at the Gulf of Evvia and around the northern part of the island of Evvia shear strain of similar orientation are found. Extension at the islands of Lesbos and Chios and western Turkey has a NNE-SSW orientation. Central Greece clearly separates the N-S oriented, relatively strong extensional regime associated

with the Gulf of Corinth (between latitudes 38°N and 38.5°N) from the E-W trending zone of N-S extension at northwestern and northern Greece at latitude 39.5°. The region east of the Gulf of Arta exhibits E-W oriented contraction. The strain rate field of the Peloponessos shows large variation on relatively small spatial scales. Southeast of Kephalonia and at the northwestern Peloponessos E-W to NE-SW directed contraction prevails. The southwestern Peloponessos exhibits shear strain rates, while the central Peloponessos extends in NE-SW direction. In general, the Aegean Sea south of latitude 38° accommodates relatively weak strain rates. Exceptions are the areas under extension southwest of Crete and between Crete and Rhodes. Although, in general, the resolution along the model boundaries areas is relatively low, these particular areas are well resolved in both solutions (figures 3.6C, D and 3.7C, D).

The main differences between solution I and II are found at the areas, where faults accommodate strong slip rates in solution II (i.e., the northern Aegean Sea, the mainland of Greece, the Gulf of Corinth and the Ionian region). In general, compared to solution I the inclusion of faults in solution II reduces the magnitude of ∇v. Besides decrease of the average magnitude, the spatial distribution of ∇v of solution II is different from solution I, which can be observed from local changes in orientation of the principle strain rates.

In solution I contraction is distributed over the Adriatic Sea and the Albanian coast. The western part of the Greek mainland (between latitudes 38.5°N and 39°N) shows E-W contraction. The region west of the Kephalonia fault zone is characterized by shear strain rates and east of the fault by NW-SE extension. In solution II part of the contraction between the Adriatic Sea and Albania present in solution I is accommodated as slip on the plate boundary and on the fault parallel to the boundary (that runs from 20.5°E, 40.5°N to 21°E, 39°N). Contraction is concentrated in the Albanian coastal area, whereas shear strain rates with a WNW-ESE oriented extensional component prevail east of the boundary-parallel fault along the zone between 21°E, 40°N and 21.5°E, 39.5°N. In solution II the magnitude of the extension at latitudes 39.5°N is larger than in solution I and the orientation more uniformly N-S oriented. The strong E-W oriented thrust component on the fault southeast of the Gulf of Arta (21°E, 39°N, figure 3.8A) accommodates part of the E-W oriented contraction of the strain rate field of solution I. This results in solution II, together with strong sinistral slip on the faults that surround the Gulf of Arta, in pure NNW-SSE oriented extension in the Gulf of Arta and considerably weaker contraction at central Greece (around 22°E, 38.5°N). Accommodation of dextral thrust motion on the Kephalonia fault is found in combination with pure NE-SW oriented contraction west of the fault and relatively uniform shear strain rates east of the fault. Compared to solution I the shear strain rates in solution II at the southwestern Peloponessos (around 22.5°E, 36.5°N) are somewhat stronger.

In solution I a uniform shear strain rate regime is found along the Katouna fault zone (at latitude 38.5°N, between longitudes 21°E and 22°E; from the connection with the southern tip of the Gulf of Arta to the Gulf of Patras) and north (38.3°N) and south (38°N) of the Gulf of Patras. In solution II the accommodation of strike-slip motion on the Katouna fault structure almost completely replaces the shear strain rates in this region in solution I. Similarly, the normal fault component of the slip on the E-W trending segments of the Katouna fault structure accommodates most of the N-S extension between the western Peloponessos and western central Greece found in solution I (between latitudes 38°N and 38.5°N). The

concentration of discrete fault motion on the north and south coasts of the Gulf of Corinth and Patras reduces the rates of N-S extension across the western part of the Gulf (between 22°E and 22.5°E) and at the northern Peloponessos and increases the rates of N-S extension at the eastern part of the Gulf (between 22.5°E and 23°E) and of E-W oriented contraction along the south coast with respect to solution I.

In solution I the transition of extension in the North Aegean trough to shear strain rates at the region of the North Anatolian fault zone is diffuse. The Dardanelles show relatively strong NE-SW oriented extension. In solution II the western termination of the North Anatolian fault zone separates extension from shear strain rates. Extension at the Dardanelles (around 25.5°E, 39.5°N) is reduced compared to solution I due to a combination of dextral and normal slip on the easternmost segment of the parameterized part of the North Anatolian fault.

3.6.3 Rotation rate

The rotation rate tensor is obtained from the anti-symmetric part of $\nabla \boldsymbol{v}$. Figures 3.11A and B show the rotation rates in units of degrees/Myr for solution I and II, respectively. Again, the overall patterns are similar for both solutions: The southern regions of Albania, Bulgaria and Macedonia show relatively low rotation rates. We find a strong phase of counterclockwise rotation rates at the continental collision zone at northwestern Greece. The rotation rates at central Greece have a clockwise orientation. Relatively strong clockwise rotation rates are found in northern Evvia and the Parnassos region. In between the north and south coasts of the Gulfs of Patras and Corinth we find relatively moderate clockwise rotation rates of the order of a few degrees/Myr. Strong clockwise rotation rates dominate the central Ionian islands (Lefkas and Zakynthos) and the western Peloponessos. This clockwise rotation rate regime weakens towards the eastern and southeastern Peloponessos. Southwestern Turkey, Rhodes and Crete accommodate counterclockwise rotation rates of the order of a few degrees/Myr.

The main differences between the rotation rate fields of solution I and II can be found along the traces of the North Anatolian and Kephalonia faults and at the Adriatic Sea. In solution I the regions around the North Anatolian fault zone and North Aegean trough can be identified by a zone of clockwise rotation rates. Dextral slip on the North Anatolian fault almost completely replaces these rotation rates in solution II. In solution I the zone of strong clockwise rotation rates in the northwestern Peloponessos continues in northward direction until Corfu, while this zone in solution II is restricted to the western Peloponessos and the Ionian region bounded by the Kephalonia fault zone. In solution II the regimes of counterclockwise rotation rates at the Albanian coastal area and of clockwise rotation rates in Parnassos and Evvia are somewhat stronger than in solution I.

Figure 3.11: Figure on next page: Contoured geodetic rotation rates of (A) solution I and (B) solution II, scaled to degrees per Myr. The numbers refer to local averages of relatively strong rotation rates with 1-σ errors between brackets. The fault segmentation of inversion II is indicated in (A) to facilitate comparison with (B).

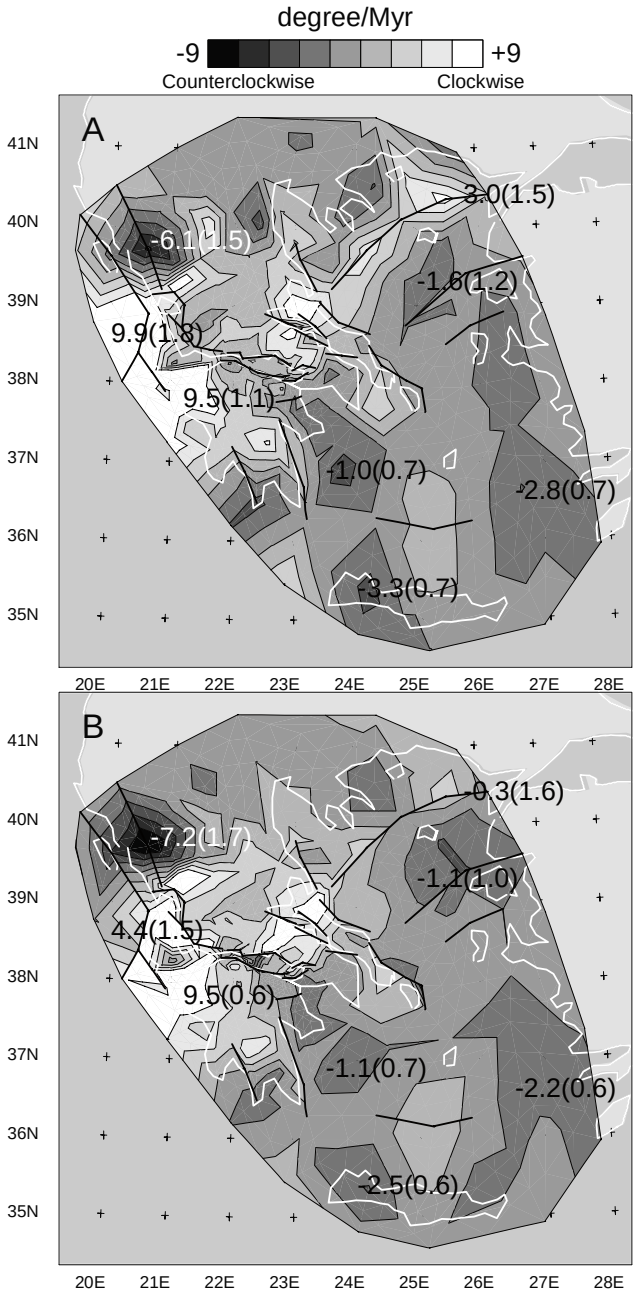

Figure 3.11: See caption on previous page

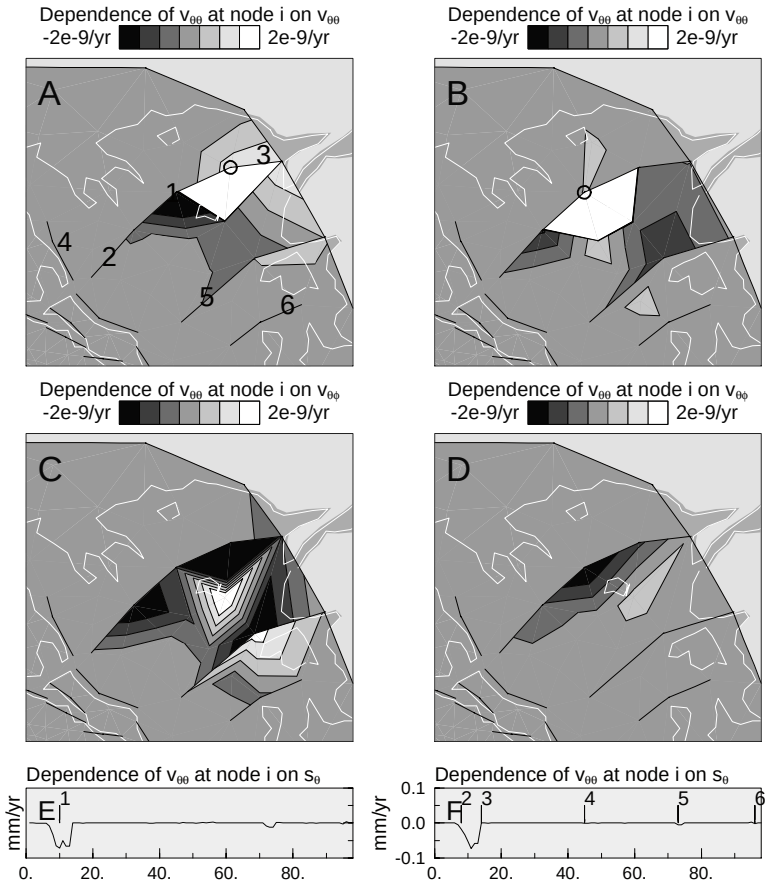

Figure 3.12: Two model estimates $\boldsymbol{m}_i$ at the North Anatolian fault zone, resulting from multiplication of resolution kernel $\boldsymbol{R}$ (solution II) with $a\boldsymbol{e}_i$: $\boldsymbol{m}_i = \boldsymbol{R} \cdot (a\boldsymbol{e}_i)$ for $v_{\theta\theta}$ with $a = 10^{-7}$/yr at node i (indicated by open circles in (A) and (B)). Contouring denotes (A), (B) $\boldsymbol{v}_{\theta\theta}$; (C), (D) $\boldsymbol{v}_{\theta\phi}$; and (E), (F) $\boldsymbol{s}_{\theta}$. For (E) and (F) the horizontal axis indicates the number of the slip parameters, [1,..,6] refer to slip parameters accommodated on segments indicated by corresponding numbers in (A) and (B). In (A) and (B) the values of $\boldsymbol{m}$ at node i exceed the contour limits and approach a.

3.6.4 Trade-off between ∇v and s

To investigate the extent to which components of slip rate and the velocity gradient field are resolved we inspect the columns of the resolution matrix $\boldsymbol{R}$. The i-th column of $\boldsymbol{R}$ represents how a certain amplitude a assigned to parameter i (with unit vector $\boldsymbol{e}_i$) is smeared over the solution, hence $\boldsymbol{m}_i = \boldsymbol{R} \cdot (a\boldsymbol{e}_i)$. This is investigated for selected model parameters associated with the North Anatolian fault system and the Gulf of Corinth. Figure 3.12 shows two model estimates $\boldsymbol{m}_i$ for the velocity gradient component $v_{\theta\theta}$ with $a = 10^{-7} yr^{-1}$ of

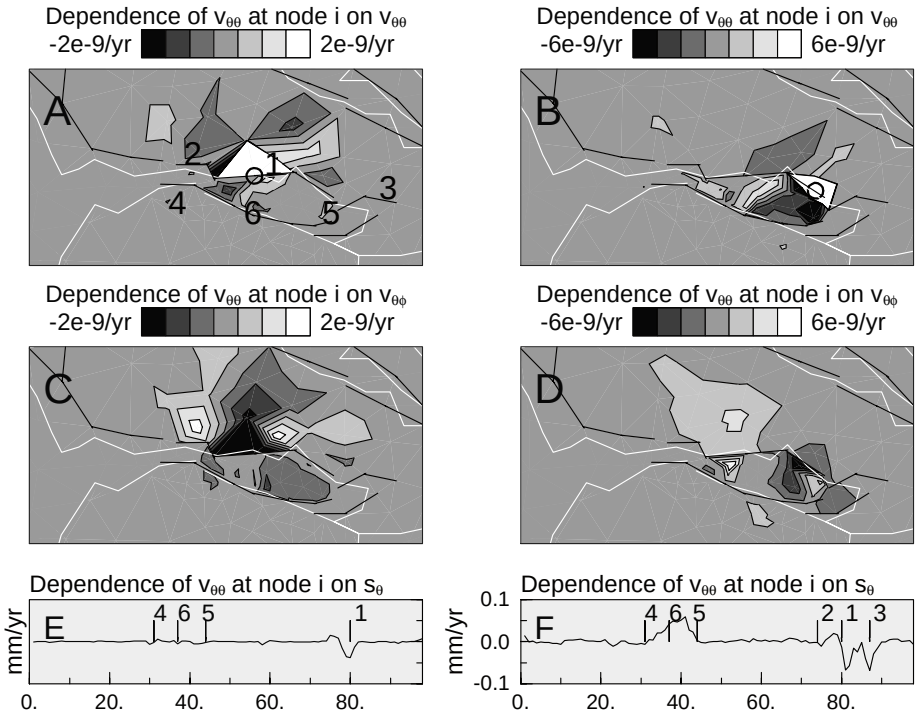

Figure 3.13: Two model estimates $\boldsymbol{m}_i$ at the Gulf of Corinth. See the caption of figure 3.12.

two neighboring nodes that are located directly at the south-side of a fault segment of the North Anatolian fault.

For both model estimates we find that the solution for $v_{\theta\theta}$ at the selected node weakly depends on the $v_{\theta\theta}$ (figure 3.12A, B) and $v_{\theta\phi}$ (figure 3.12C, D) components of surrounding nodes and on s_θ (figure 3.12E, F) on nearby fault segments. Note that, except for the amplitudes at the selected nodes, the values attained by $\boldsymbol{m}_i$ elsewhere in the model are by a factor of almost 100 smaller than the input amplitude a. We conclude that trade-off between $\boldsymbol{s}$ and $\boldsymbol{\nabla v}$ on these segments of the North Anatolian fault are not very strong. Similar results are found for one model estimate on a node that spans the triangulation delineating the bounds on the northern coast of the Gulf of Corinth (figure 3.13A, C, E). For a node on the same fault segmentation located more to the east the results are somewhat different (figure 3.13B, D, F). Although the values attained by $\boldsymbol{m}_i$ are still not very large compared to the input amplitude of a, the dependence of $v_{\theta\theta}$ at the selected node on the $v_{\theta\theta}$ (3.13B) and $v_{\theta\phi}$ (3.13D) components of surrounding nodes and on s_θ (3.13F) on nearby fault segments is stronger with respect to the former results (note the different contour limits in 3.13B, D and F). For all estimated models $\boldsymbol{m}_i$ shown here the values of $v_{\phi\phi}$, $v_{\phi\theta}$ and s_ϕ contain only zeros.

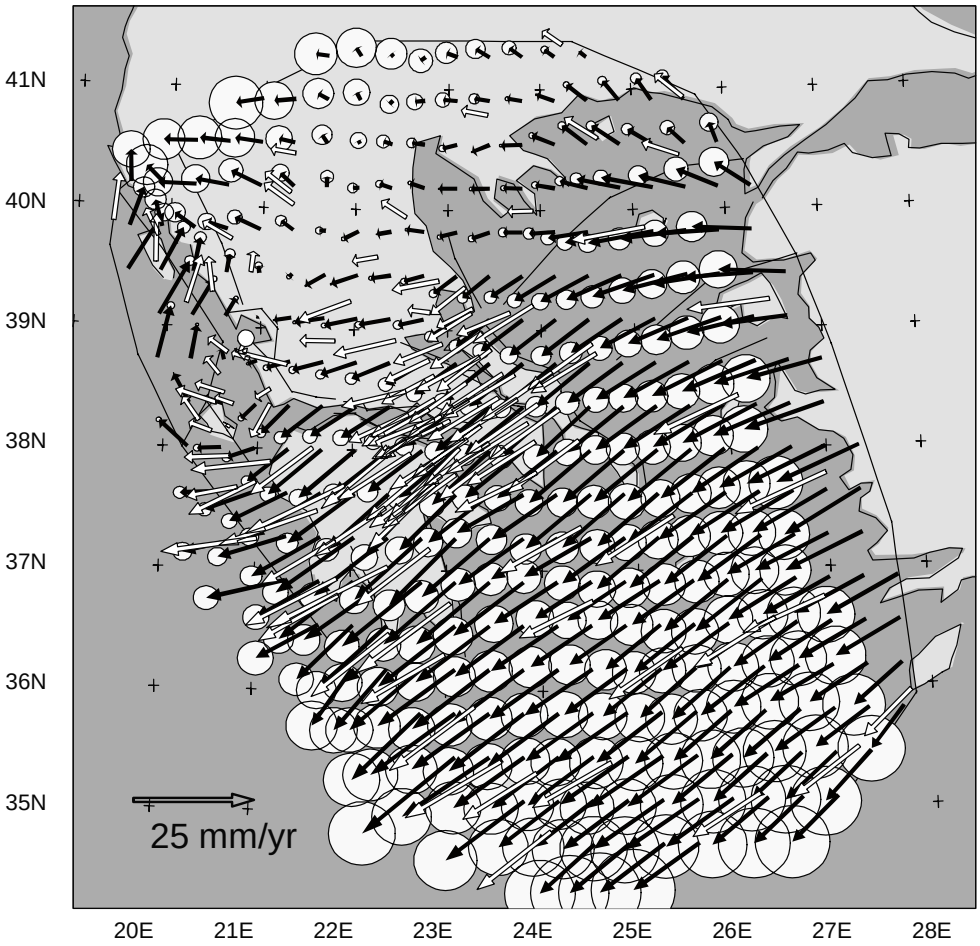

Figure 3.14: Black arrows indicate the predicted velocity field computed on a regular grid with solution I. The white vectors indicate the velocity data. The data and predictions are plotted with respect to a location at the Gulf of Arta, indicated by the white dot around 21°E, 39°N. The fault segmentation of inversion II is indicated here to facilitate comparison with figure 3.15.

3.7 Velocity field

Figures 3.14 and 3.15 display the velocity fields predicted by solution I and II, respectively, on a spatial regular grid. For this representation we perform a forward computation of the solution to determine the velocity vector at the nodes of the grid with respect to a reference point (at which the velocity is then zero). In general, the Aegean velocity field consists of three main regimes; the Aegean Sea and the Peloponessos, the Adriatic Sea and central and northern Greece (figure 3.3). These regimes can best be distinguished if the velocity is

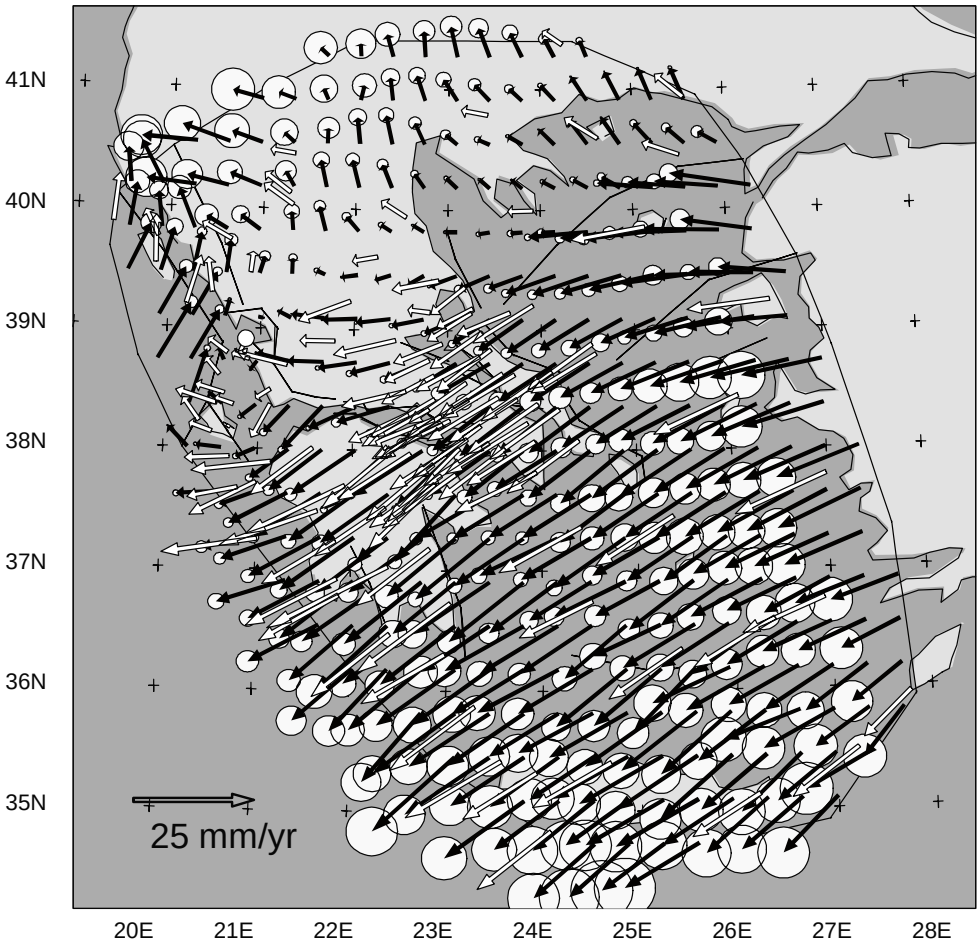

Figure 3.15: See caption of figure 3.14 for solution II.

represented with respect to the area around the Kephalonia fault zone and the Gulf of Arta, where the transition zones between the regimes meet. The velocity field of the Aegean Sea and the Peloponessos has a southwestward direction, increases towards the southwest and deviates towards the west across the Peloponessos, consistent with results of Le Pichon et al. [1995]. The velocity field of the small part of the Adriatic Sea has a NNE direction with respect to the Gulf of Arta. Collision is represented by the sudden transition from NNE to WNW directed velocities across the plate-boundary from west to east. The velocity field of central Greece has an westward direction with respect to the Gulf of Arta.

The main differences between the velocity fields predicted by solutions I and II occur at the northern model boundary and around the parameterized faults. The weak velocity

	KFZ(s)	GC(e)		NAF(s)	NAT(e)	WA(e)	SAS(e)
		west	east				
lo	20.3-20.8	22.3-23.3	21.8-22.3	23.0-26.0	22.3-23.5	26.3-28.0	26.3-28.0
la	38.1-39.2	38.0-38.4	38.0-38.5	39.0-40.5	39.4-40.3	38.0-39.5	35.3-37.3
1	77±14	103±9	88±9	94±16	85±19	16±19	27±14
2	133±14	162±7	137±8	173±18	239±21	91±23	119±18
3	150	120		180	150	70-85	90

Table 3.4: Average strain rates of solution I. Key: KFZ, Kephalonia Fault zone; GC, Gulf of Corinth; R, Rhodes; NAF, North Anatolian Fault; NAT, North Aegean Trough; WA, Western Anatolia; SAS, Southeast Agean Sea; s, strike-slip; e, extension. 1 magnitudes of the prevailing strain rate regime in the area of interest by averaging the strain rates over a rectangular local grid (lon and lat denote grid corners); 2 maximum principal strain rates (in 10^{-9}/yr); 3 maximum principal strain rates of the solution of [Kahle et al., 2000].

field at the southern regions of Albania, Macedonia and Bulgaria and northeastern Greece of solution I has ENE to E directions, whereas solution II predicts larger velocities at N to NNE directions with respect to the Gulf of Arta. Difference due to the fault slip is best observed along the trace of the North Anatolian fault zone. The magnitude and orientation of the velocity field predicted by solution I south of the main branch of the North Anatolian fault gradually change while following the velocity field across the fault, whereas this transition in solution II occurs more abruptly. Similar discontinuous transitions in the velocity field predicted by solution II can be observed at the Kephalonia fault zone and the Katouna fault zone.

3.8 Analysis of the solutions and comparison with related work

The results for the deformation rate field of solution I are compared with several other regional and local geodetic studies of the Aegean deformation field, all translating velocity data into a velocity gradient field. Solution II is not incorporated in this comparison, because these geodetic studies do not incorporate fault motion.

3.8.1 Comparison of ∇v with related work

In a recent study, Kahle et al. [2000] apply the collocation method [Kahle et al., 1995; Straub et al., 1997] to a GPS velocity set that samples the Aegean and Anatolian microplates and also contains several sites at Africa and Arabia [Cocard et al., 1999; McClusky et al., 2000]. On average, this data set is sparser than the data set from which solutions I and II are derived (figure 3.16). Table 3.4 lists the maximum magnitudes of the principal strain rates per area of Kahle et al. [2000](3) and of solution I (2). A first striking difference between both solutions is that at those areas where our data density is higher (Gulf of Corinth, North

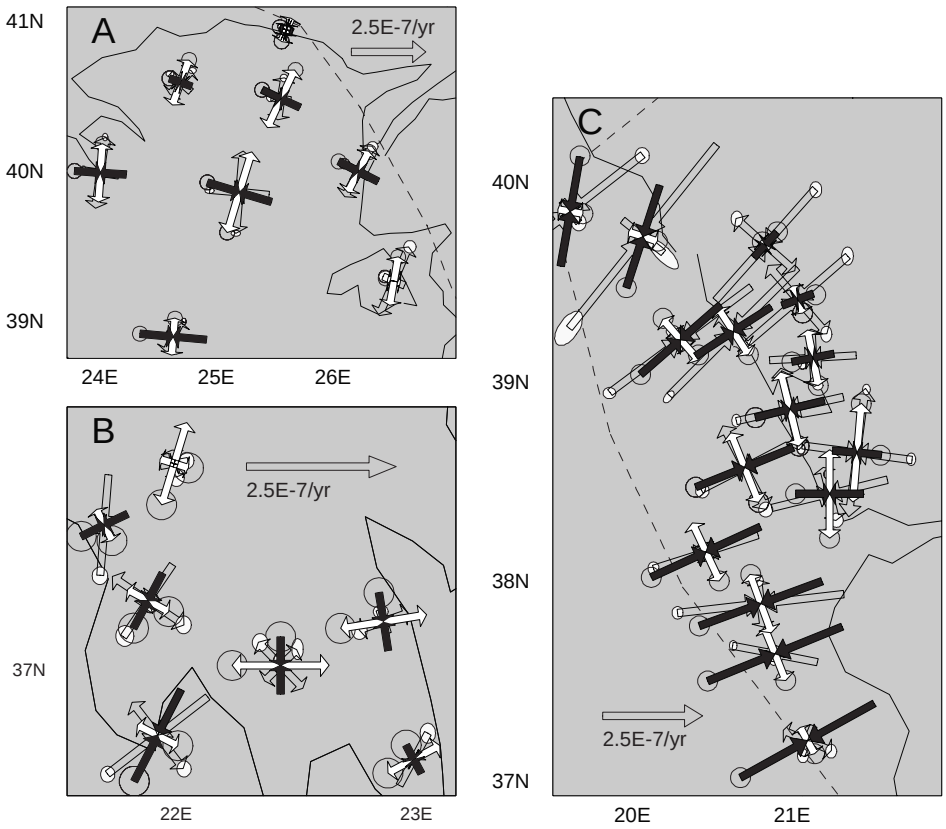

Figure 3.16: Comparison between the principle strain rates of solution I (open arrows with white error ellipses) and the principle strain rates of the solution of Kahle et al. [2000] (filled arrows, black indicating contraction and white extension, with open error ellipses), plotted at the coordinates of the Aegean GPS sites of the data used by Kahle et al. [2000]. Dashed lines indicate the model boundaries.

Aegean trough) our strain rates are higher as well. Maximum magnitudes more or less agree in those areas where the data coverage is of comparable density (Kephalonia fault, North Anatolian fault). This observation is consistent with observations by Kahle et al. [2000] who find highest strain rates at those areas along the North Anatolian Fault zone where the data density is highest. To characterize a regional strain rate regime we also list the magnitudes of strain rate averaged over a larger area that surrounds the particular fault zones (table 3.4(1)).

In figure 3.16 principle strain rates and uncertainties of solution I and of the Kahle et al. [2000] solution are shown together, both plotted at the station locations of the data set of Kahle et al. [2000]. The uncertainties of the strain rate solution of Kahle et al. [2000] are of the order of 20 to $30 \cdot 10^{-9}$/yr in Greece. In figure 3.16 we have plotted a uniform uncertainty of $25 \cdot 10^{-9}$/yr for their principal axes. North of Corfu our contraction is stronger than and

makes an angle with the principal axes of Kahle et al. [2000] (figure 3.16C). In general, orientations of principle strain rates along the coast of the Greek mainland show agreement. However, contraction of solution I is considerably stronger than contraction found by Kahle et al. [2000]. Orientation and magnitude of shear strain rates along the Kephalonia fault are consistent and agree within the margin of error. Directly south of the Kephalonia Fault zone the solution of Kahle et al. [2000] shows strong, ENE-WSW oriented contraction, where the contraction of solution I is weaker and has a more E-W to WNW-ESE direction. The NE-SW extension southwest of Crete present in solution I (figure 3.9) is not found by Kahle et al. [2000]. Principle strain rates of both solutions show further agreement in the region between Crete and Rhodes and at central Greece. Close agreement is found at the region of the North Anatolian fault, where differences are within the margin of error (figure 3.16A, table 3.4). Disagreement is found for the rates of extension in northern Greece and at Lesbos, Chios and western Turkey, being stronger in solution I. An explanation for the higher rates in northern Greece could be the higher density of our data set in this region. The inclusion of data on the Anatolian micro-plate of the set of Kahle et al. [2000] probably impose better constraints on northwestern Turkey and the islands of Lesbos and Chios. Differences in density of the data sets may also form the explanation for the, in general, inconsistent results at the Peloponessos (figure 3.16B); the SING set contains many stations around the Gulf of Corinth, where the data set of Kahle et al. [2000] contains none, that are of considerable influence on the strain rates of the Peloponessos.

In the geodetic study of Clarke et al. [1998] uniform strain and rotation rates are computed at points of a regular grid in central Greece using data from neighboring sites. For central Greece and the Peloponessos Davies et al. [1997] compute uniform strain and rotation rates within triangles spanned by the station positions. Clarke et al. [1997a] obtain strain estimates across the Gulf of Corinth by measuring along individual baselines between pairs of stations at opposite sides of the Gulfs of Patras and Corinth. Similar to the results of Clarke et al. [1997a, 1998] and Davies et al. [1997] our solution I accommodates stronger rates of extension across the western than across the eastern part of the Gulf of Corinth. However, even the maximum rate of extension in solution I is much smaller than the results of Clarke et al. [1998], who find extensional strain rates of $150 \pm 20 \cdot 10^{-9}$/yr and $1120 \pm 50 \cdot 10^{-9}$/yr for the eastern and western sides, respectively. These rates are computed from data from the Central Greece and Aigion Postseismic networks that form part of the original, complete SING data set (table 3.1, figure 3.3). We have filtered strong contractional and extensional signals by considering only part of the data (appendix C). Clarke et al. [1997a] assume that the postseismic displacements are small compared with coseismic displacements. Although this assumption is probably true, it does not automatically mean that postseismic deformation is small compared with the interseismic deformation field. The N-S extension of the Parnassos region, the Evvia island and the Gulf of Evvia are consistent with observations of Clarke et al. [1998]. Davies et al. [1997] does not find a uniform strain rate pattern in this region. Our results accord with the N-S extension and E-W contraction at the western part of central Greece, the transition in the northern Peloponessos from N-S extension at the Gulf to E-W extension at the central Peloponessos and the relatively low strain rates at the western Peloponessos and at the Aegean Sea east of the Peloponessos. Davies et al. [1997] find different results at the western Peloponessos, Parnassos and north-

ern Greece. Le Pichon et al. [1995] and Davies et al. [1997] have not detected significant N-S extension at northern Greece, possibly because the northernmost station in their data sets is located around 22.4° longitude, 39.8° latitude, which is within the E-W trending zone of N-S direction extension of solution I (and II). Extension of this magnitude and at this latitude is also not present in the solution of Kahle et al. [2000], which may be due to their sparse data coverage of central Greece.

The rotation rate field of solution I is consistent with the rotation rates computed by Clarke et al. [1998]. Rotation rates have clockwise orientations with relatively large magnitudes of the order of 10 degrees/Myr southwest of the Gulf of Patras changing in eastward direction south of the Gulf of Corinth to counterclockwise orientation with small magnitudes. Within the Gulf rotation is of negligible rate. The Parnassos region and Evvia accommodate relatively strong clockwise rotation rates.

We conclude that the main, qualitative deformation characteristics of solution I (i.e., N-S extension of the Gulf of Corinth and the North Aegean trough, dextral shearing along the Kephalonia fault and North Anatolian fault zones, E-W contraction of northwestern Greece and relatively low deformation of the Aegean Sea south of 38°N) have been found by earlier studies based on GPS data. It is difficult to say to what extent the discrepancies in results are caused by differences in methodology used by the different approaches. Most of the differences concerning magnitude and orientation of the strain rate fields can be explained by differences in distribution of the sites, origin and time of measurement of the data and possible postseismic influence incorporated in the data.

3.8.2 The significance of the slip solution

In chapter 2 we inferred that a basic trade-off may exist between fault slip and the velocity gradient field. The main cause for this trade-off is the lack of physical constraints that couple fault motion to continuous deformation in a pure kinematic inversion of the velocity data. The trade-off is best resolved in case relative motion observations exist close to the fault zones. If this is not the case then fault slip may also reflect relative crustal block rotations (geological fault slip), while the fault itself can be locked. An example of this is the North Anatolian fault. Baselines between stations intersecting the North Anatolian fault measure the far-field velocity, because the SING data do not densely sample the region close to fault. Average slip rates on the main branch and the southernly located subbranch of the North Anatolian fault of 11 ± 2 mm/yr and 2 ± 1 mm/yr, respectively, agree with geological estimates of Armijo et al. [1999], who also found that long-term kinematics of the North Anatolian fault appear to be similar to the present-day kinematics deduced from space geodesy. However, whether the fault is locked or accommodates slip motion will not become evident from application of our method to this data set.

An example of a densely sampled fault is the Kephalonia fault, accommodating smaller slip rates in our solution than predicted by geological observations of Louvari et al. [1999], who measure a dextral slip rate of 20-30 mm/yr with a thrust motion on the Lefkada and Kephalonia fault segments. The presence of strong dextral shear strain rates surrounding the near-field of the fault may suggest that the fault is locked. Evidence for present-day activity along the, densely sampled, Gulf of Arta and the Katouna fault zone, supporting the fault

motion found in our solution, comes from a tomographic study of the upper crustal layer revealing a low-velocity zone [Haslinger et al., 1999]. Sinistral slip has also been derived by Le Pichon et al. [1995].

Convergence associated with the collision at northwestern Greece is not concentrated as slip on the plate boundary, but also appears as broadly distributed, contractional strain rate. The fault zone parallel to the plate-boundary accommodates predominant dextral strike-slip with a thrust component, consistent with geological observations [Mantovani et al., 1992]. The transcurrent deformation can not solely be accommodated by the simple parameterization of only one boundary-parallel fault and also appears as distributed shear strain rate.

From geological observations Armijo et al. [1996] estimate a normal slip rate across the Gulf of Corinth of 11 ± 3 mm/yr in the west and 6 ± 2 mm/yr in the east (Xylokastro fault segment), accommodated on the southern strand of the Gulf. From GPS Clarke et al. [1997a] compute rates of 13 and 6 mm/yr across the western and eastern part of the Gulf, respectively, and Le Pichon et al. [1995] compute 15 mm/yr across the Gulf of Patras. The normal component of the slip rate in solution II at the western part of the Gulf of Corinth is almost equally divided between the north and south coasts. Because the data set contains only one velocity observation within the Gulf, the partitioning of slip over the northern and southern strands of the Gulf of Corinth and Patras is mainly determined by baselines between stations that cross the Gulf in an E-W direction. Nevertheless, resolution kernels of the slip component and dependence of ∇v on s (figure 3.13) show that separate contributions of slip on each strand are relatively well determined (although better in the west than in the east). Summed pairs of slip rates at the same longitudes accommodated at the northern and southern segments result in normal slip rates of 12 to 13 mm/yr at the western and 3 to 6 mm/yr at the eastern Gulf, accounting for geodetic predictions for motion across the Gulf.

Summarized, we find that the orientations of the slip vectors of solution II are in good agreement with geological observations and geodetic derivations. Trade-off between estimates for the velocity gradient field and slip motion require a careful interpretation of the magnitudes of the slip solution.

3.8.3 Comparison with earthquakes and stress indicators

In this section we compare solutions I and II with earthquake and stress data to examine to what extent our representation of the deformation field based on geodetic data obtained at the Earth's surface reflect deeper crustal deformation patterns. We compare the orientations

Figure 3.17: Figure on next page: (A) Shallow (depth $<$ 15 km) and strong (M $\geq$ 5) earthquakes for 426 BC to 2000: Principal (P and T) axes of the two-dimensional (lateral) moment tensors deduced from the fault plane solution parameters published by [Ekström and England, 1989; Ambraseys and Jackson, 1990; Taymaz et al., 1991; Jackson et al., 1992; Papazachos and Kiratzi, 1996; Papazachos et al., 1999, and references therein] and from the Harvard centroid moment tensor (CMT) solutions (1995-2000). Dashed lines indicate the model boundaries, straight lines indicate the fault parameterization of inversion II. (B) Detail of (A).

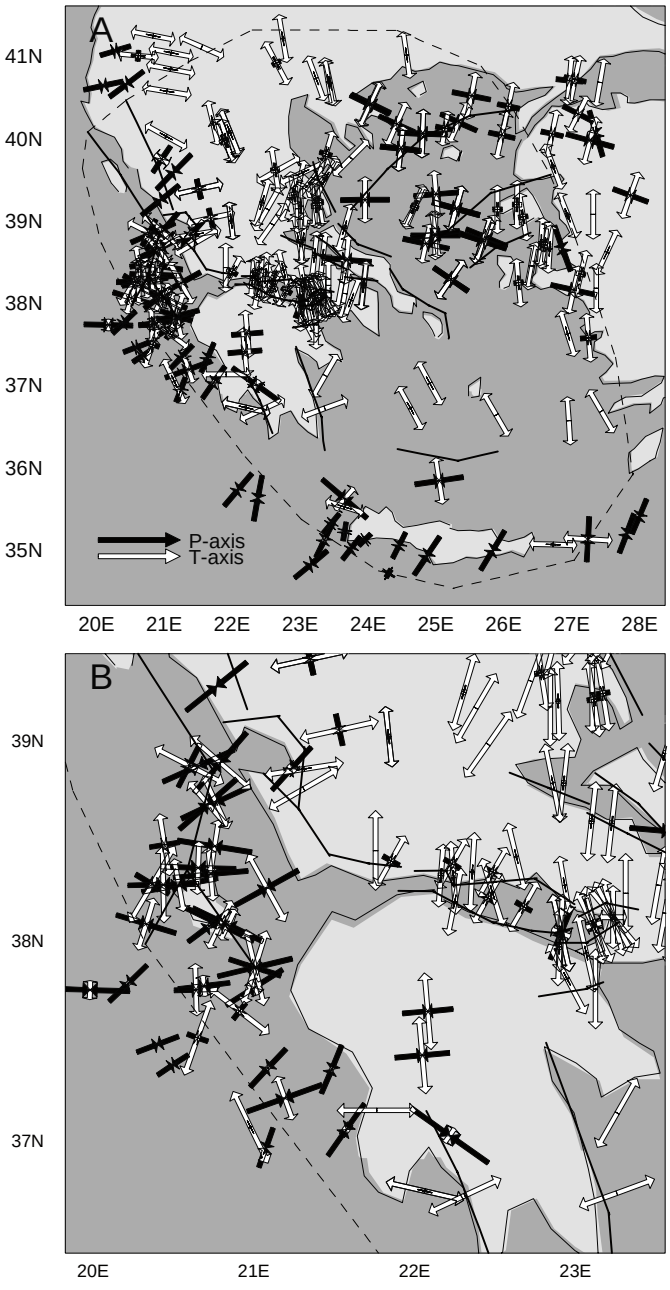

Figure 3.17: See caption on previous page.

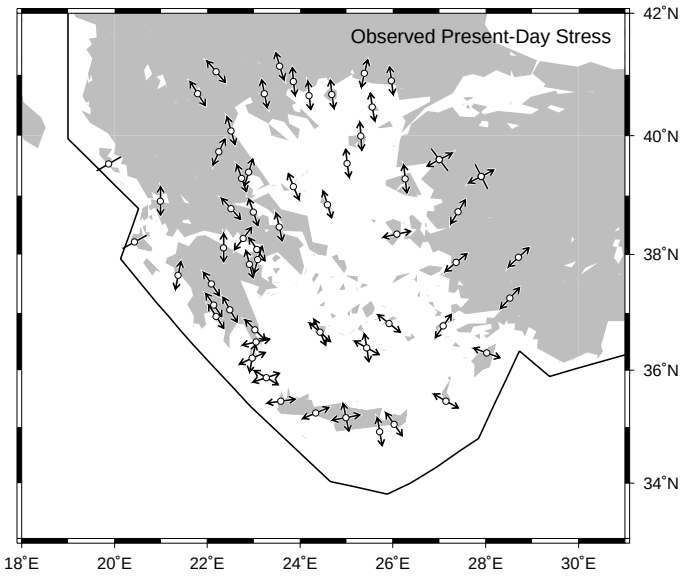

Figure 3.18: From Meijer and Wortel [1997]: compiled from geologic studies of Angelier et al. [1982] and Mercier et al. [1987] of the kinematics of faults that have been active from the middle Pleistocene until now. Double arrow: principal axis of tension, short line: principal axis of compression. Also shown is the Hellenic trench system (black lines) connecting with the NW Greece/Adriatic Sea collision zone.

of the slip rates of solution II (figure 3.8) and the derived strain rate fields of solutions I and II (figures 3.9 and 3.10) with P- and T-axes of a set of about 225 strong ($M_0 > 5$) and shallow (< 15 km) earthquakes (figure 3.17), of which 12 occurred before 1800 [Papazachos et al., 1999, and references therein] and around 20 between 1800 and 1900 [Ambraseys and Jackson, 1990; Papazachos et al., 1999]. Because our solution is based on the lateral components of the velocity field, figure 3.17 shows the principal axes of the lateral components of the seismic moment tensor. Furthermore, we compare the properties of solutions I and II with an average stress field, compiled by Meijer and Wortel [1997] from geologic studies of Angelier et al. [1982] and Mercier et al. [1987] of the kinematics of faults that have been active from the middle Pleistocene until now (figure 3.18).

Due to seismic quiescence, maybe indicative for a seismic gap, the orientation of principle strain rates around the island of Corfu (20.5°E, 39.5°N) cannot be compared with earthquakes. However, one stress indicator on Corfu and P-axes north (20.5°E, 40.5°N) and southwest (21°E, 39.5°N) of Corfu show ENE-WSW and NE-SW orientations, respectively, consistent with the average orientation of contraction along the Albanian coastal area in solutions I and II and with the thrust slip found on the plate boundary and the fault on the Albanian coast. East of this zone of contraction (at longitude 21°E, between latitudes 40°N and 41.5°N) T-axes have a distinct WNW-ESE orientation east of the fault. Location and orientation agree with the component of extension in solution II. The NNW-SSE extension

in northwestern Greece in solutions I and II encompasses the small cluster of NNW-SSE oriented T-axes, associated with the Grevena earthquake.

Strike-slip earthquakes, although with scattered moment tensor orientations, clearly delineate the Kephalonia fault zone (figure 3.17B), consistent with shear strain rates east of the fault (21°E, 38.5°N) and the dextral component of the slip of solution II. Solution I only shows shear strain rates west of the Kephalonia fault (20.5°E, 38.5°N). Although earthquakes with pure thrusting mechanisms are absent, stress data on the island of Kephalonia indicate NE-SW compression, which may suggest thrust fault motion as we find in solution II. Strain rates west of the Peloponessos (21°E, 37.5°N) of solution I and II accommodate very weak and no, respectively, N-S extension, with directions in agreement with earthquake moment tensors. Continuing in southward direction, the sudden change in orientation of the P-axes from E-W to NNE-SSW (21.5°E, 37.3°N) is detected by solutions I and II. While the patterns of strain rate, stress and P-and T-axes of earthquakes represent completely different types of deformation for the central Peloponessos, all suggest that the region between the Peloponessos and Crete is under ENE-WSW extension. The strain rates around Crete do not reflect any shortening associated with the frequent occurrence of compressional earthquakes below the Hellenic trench. This possibly reflects a difference between near surface deformation and deformation at larger depth. The orientations of the extensional pattern show some agreement with the stress indicators on western Crete.

The strong sinistral slip and shear strain rates found on the Katouna fault zone in solutions I and II are not confirmed by earthquake activity, nor is there any indication from seismicity and stress data that contraction plays a role in western central Greece (around 21.5°E, 38.5°N). The Gulfs of Corinth and Patras are characterized by extreme seismic activity of mainly (N-S) extensional earthquakes and by stress data with N-S tensional axes. Solution I reflects these observations by strong extension, solution II by extension and strong normal slip rates. No seismic or geological evidence exists for the thrusting at the eastern side of the north coast of the Gulf of Corinth and the strong strike-slip fault motion accommodated on the north and south coasts in solution II, but this thrusting agrees with relative block rotations as will be discussed in section 3.9.

Both solution I and II follow the average strain regime for the western Hellenic arc and the Peloponessos proposed by Mueller and Kahle [1993] and also found by other neotectonic studies based on microseismicity [Hatzfeld et al., 1990] or geodetic data [Davies et al., 1997]: The transition of predominantly N-S directed extension around the Gulf of Corinth into E-W extension of the Peloponessos takes place in the northern Peloponessos. A zone of extension connects the south coast of the Gulf of Corinth across the Peloponessos with western Crete (explained by backarc spreading in the Aegean Sea by Mueller and Kahle [1993]). Tension changes into compression at Kephalonia and the western Peloponessos due to the collision between the Adriatic Sea and the Aegean region. The small transition zone between both regimes runs from northern Greece across the Gulf of Patras to the southwestern Peloponessos.

In general, the orientation of the principal extension axes of solutions I and II at the northern Aegean Sea follow the orientation of the tensional stress and T-axes field, which gradually changes from NNW-SSE in central and northern Greece (22°E, 40°N) towards NNE-SSW in the eastern Aegean Sea (26°E, 40°N), at the islands Lesbos and Chios (26°E,

39°N) and western Turkey (27°E, 38°N). The strike-slip events delineate the regions of dextral slip associated with the branches of the North Anatolian fault as we find it in the slip component of solution II. The orientation of T-axes of normal faulting events characterizing the North Aegean trough (23.5°E, 39.5°N) agrees with the pure extension of both solutions. Earthquakes between the North Aegean trough and the Gulf of Corinth show N-S extension, where both solutions I and II only contain N-S extension at the Parnassos region (23°E, 38.5°N). The shear strain rates in solution I and II found at Evvia and the Gulf of Evvia (23.5°E, 38.5°N) are not confirmed by strike-slip mechanisms.

Only a few large earthquakes have been generated in the interior of the Aegean Sea, which is reflected in our solutions by a relatively weak strain rate field. However, we find no agreement between principle strain rates and P-axes or stress indicators. In the south-eastern Aegean Sea orientation of T-axes northwest of Rhodes are slightly different, but the orientation of the stress indicator on Rhodes agrees with the NW-SE orientation of extension of solution I and II at this region.

Style and orientation of the widespread earthquake activity along two parallel, E-W trending seismicity belts at the Gulf of Corinth and between central Greece mainland and the Gulf of Evvia show N-S extension. This region has been proposed to represent a pull-apart system [Armijo et al., 1996; Ambraseys and Jackson, 1990; Taymaz et al., 1991, e.g.,]. The epicenter of the Grevena earthquake (the NNW-SSE oriented T-axis at about longitude 22^o, latitude 40^o, figure 3.17) is located north of this zone. Prior to the Grevena earthquake northern Greece was regarded as an aseismic, rigid block based on the low instrumental seismicity during the last few decades to 100 years [Papazachos et al., 1989]. However, recent investigations of its seismic history, triggered by the unexpected appearance of the strong Grevena earthquake sequence, present evidence for large earthquakes that took place hundreds of years ago, suggesting recurrence periods of around 200 years [Stiros, 1998]. Our strain rate solutions (figures 3.9 and 3.10), the computed velocity fields (figure 3.14 and 3.15) and the Grevena earthquake sequence suggest that the zone of N-S extension is located or distributed more to the north than was formerly assumed. This was already noted by Kahle et al. [2000] from a joint consideration of the central and northern Greek neotectonic and seismotectonic patterns. The kinematic models of Taymaz et al. [1991] and Jackson et al. [1992] do not extension at this region either, because these models are based on earthquake data. The resulting strain rate field from inversion of the original data set (section C.1, figure C.2A) also contains the zone of extension at northern Greece, although of narrower width and lower magnitude. Future space geodetic studies at this area and north of it are necessary to provide more accurate boundary constraints on the wide-spread extension and pull-apart mechanisms in central and northern Greece.

In summary we infer both agreement and disagreement with principle directions of earthquake moment tensors. In part this may reflect errors in both our model and in the moment tensor estimates. But, we cannot exclude that disagreement may reflect a difference between the near surface and deeper crustal deformation. One cause can be that if near surface deformation is (isotropically) elastic the principle axes of strain rate will align with those of the near surface stress field. In particular, since the Earth's surface is stress free this requires that one principle axis is always perpendicular to the surface. At larger depth there is no such requirement and principle axes may rotate forced by deeper crustal

dynamics. This consideration would suggest that combining geodetic data with moment tensor solutions is not straightforward.

3.8.4 Rotation rates: comparison with paleomagnetism

The rotation rates of solution I and II, based on geodetic data, are representative for the period of observation (e.g., approximately 100 years), while paleomagnetic data are representative for the past million years. Furthermore, our computed rates refer to rotation about a vertical axis of a small rigid equidimensional element, while paleomagnetic rotations may represent rotations of considerable crustal blocks [McKenzie and Jackson, 1983]. To determine the extent to which the present-day pattern may be representative for the past few million years and reflects larger-scale crustal block rotation we compare the rotation rates of solution I and II with young paleomagnetic observations obtained in the Aegean region.

From paleomagnetic observations Kissel and Laj [1988] proposed a Neogene evolution for the Aegean arc, starting from an E-W trending configuration. During the middle Miocene, the western (NW Greece) and eastern (SW Turkey) Aegean Arc started a clockwise and counterclockwise rotation, respectively. A second phase of rotation was thought to have occurred only in the western Aegean arc (Ionian islands) during the last 5 Myr. However, from paleomagnetic data Duermeijer et al. [2000] found evidence for a young (< 0.8 Myr) and rapid clockwise rotation phase in the western Aegean arc and a young (presumably < 2 Myr) counterclockwise rotation phase in the eastern arc, of which the latter has been proposed earlier by Le Pichon and Angelier [1979]. Paleomagnetic and neotectonic observations suggest that the region inside the Aegean arc consists of two major blocks with an opposite sense of rotation. The islands Naxos and Milos exhibit counterclockwise, Mykonos and Tinos clockwise rotations [Kondopoulo and Pavlides, 1990; Avigad et al., 1998; Walcott and White, 1998], the latter being consistent with areas to the northwest on the Greek mainland [Kissel et al., 1986]. This implies that the boundary between the two rotation phases lies north of Naxos, and probably also north of Kythira [Duermeijer et al., 2000].

Solutions I and II show large parts of the Aegean rotating in the same manner of which the orientation is consistent with the paleomagnetic observations obtained by Duermeijer et al. [2000], which suggests that the rotation rates represent longer-term, larger-scale crustal block rotation. The dominant features of our rotation rate solution (i.e. the presence of two regions with an opposite rotational orientation and strong extension at central Greece) agree with the results from a geodetic study of Le Pichon et al. [1995]. According to their results the area north of the Gulf of Corinth and western Peloponessos are subject to a clockwise rotation and the area south of the Gulf of Corinth and the Aegean Sea to a counterclockwise rotation. In the rotation rate fields of solutions I and II the boundary between clockwise and counterclockwise rotation rates is located somewhat different, since we find the whole Peloponessos participating in the clockwise rotation phase. Le Pichon et al. [1995] propose the North Anatolian fault as the northern boundary of the counterclockwise rotation phase of the Aegean Sea. This is consistent with the results of solution II, in which the clockwise rotation rates around the North Anatolian fault of solution I are replaced by dextral slip motion. The continuation of the boundary between the regions of clockwise and

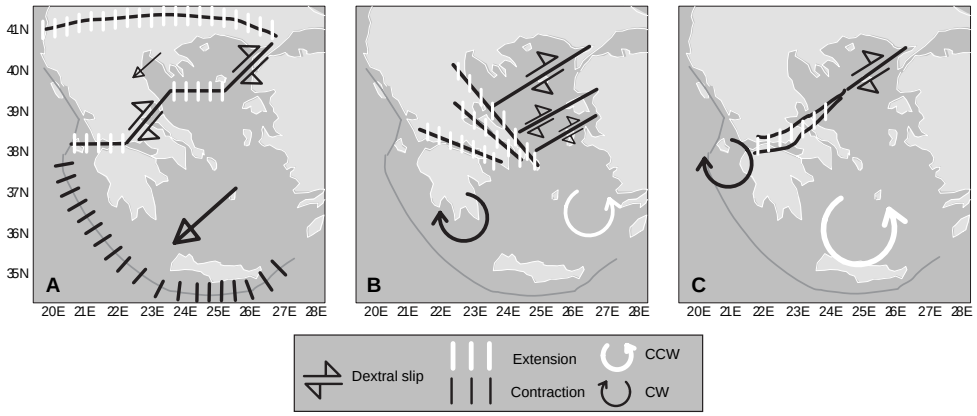

Figure 3.19: Three kinematic models of the present-day surface deformation of the Aegean described in the text. The grey line indicates the Hellenic arc. The cartoons represent the models of (A) McKenzie [1972, 1978]; (B) Taymaz et al. [1991] and Jackson et al. [1992]; (C) Le Pichon et al. [1995].

counterclockwise rotation rates agrees very well with paleomagnetic studies [Kondopoulo and Pavlides, 1990; Avigad et al., 1998; Walcott and White, 1998; Duermeijer et al., 2000]: Tinos and Mykonos are part of the clockwise rotation phase of Greece, while Naxos, Milos, Kythira and the southern tip of the Peloponessos exhibit counterclockwise rotation together with the predominant part of the Aegean Sea.

3.9 A detailed view on crustal deformation of the Aegean region

The agreement in orientation between the slip vectors of solution II and geological observations and the consistency found between rotation rate results and paleomagnetic observations suggests that the deformation field of solution II reflects larger-scale crustal block motion. We use this solution to propose a model of the kinematics of the (present-day) deformation of the brittle upper-layer of the Aegean crust and compare it with other kinematic models of the Aegean. For an overview of the kinematic models of Aegean tectonics we refer to Jackson [1994]. In general, three basic kinematic concepts can be extracted from the literature:

1. The model proposed by McKenzie [1972, 1978] is based on the distribution of focal mechanisms and consists of three interacting micro-blocks (figure 3.19). Assuming that the colliding continental blocks at northwestern Greece and the Hellenic trench must accommodate the SW-directed motion of Anatolia, NE-SW oriented dextral strike slip across the island of Evvia, the Parnassos region and the central Gulf of Corinth, connecting to the Kephalonia fault zone separates the southwestward moving

southern Aegean from northwestern Greece. N-S directed extension on EW-trending graben structures at western Turkey characterizes the boundary between the southern Aegean and northeastern Aegean fixed to Anatolia. This model is supported by the kinematic interpretation based on GPS velocities presented by McClusky et al. [2000].

2. Taymaz et al. [1991] use the wide-spread intraplate seismicity to develop a floating-block continuum model (i.e. the 'broken slat model'). In this model NE-oriented dextral strike-slip faults at the eastern Aegean Sea, associated with the western termination of the North Anatolian fault, end against NW-SE and E-W trending normal faults in central and northern Greece. This would explain the simultaneous processes of dextral slip in the east and N-S oriented extension in the west across the Gulf of Corinth and central Greece. The velocity model of Jackson et al. [1992], also based on the information from earthquakes, agrees with the model of Taymaz et al. [1991] and predicts clockwise rotation rates throughout the central Aegean and counterclockwise rotation rate at the eastern Aegean and western Turkey. Further, the absence of seismicity in the Aegean Sea suggests that this region moves to the southwest as a rigid unit at present.

3. According to the model of Le Pichon et al. [1995] the area north of the Gulf of Corinth and the western Peloponessos are subject to a clockwise, the area south of the Gulf of Corinth and the Aegean Sea, part of Anatolia, to a counterclockwise rotation, thus producing a N-S extending Gulf of Corinth, that represents the boundary between both regions. This zone of extension initiates as a narrow zone extension at the North Aegean trough and widens towards the western Aegean.

Recent studies on the present-day crustal deformation of the Aegean region based on paleomagnetic and geodetic data indicate that especially the relative rotations of individual blocks play an important role [Le Pichon et al., 1995; Duermeijer et al., 2000]. The relation between rotating blocks and fault slip are visualized, in a highly simplified representation, in figure 3.20. In cartoon 3.20A two individual blocks with a relative counterclockwise rotation are separated by a fault zone. If a data set would densely sample the velocity field related to the motion depicted in figure 3.20A application of our method will characterize both blocks and the fault zone in between by counterclockwise rotation rates and dextral slip, respectively. If the relative motion of the blocks can not be completely accommodated by slip, due to for example locking of the fault or data acquired within the fault zone, this results in distributed deformation, which will show up in our solution as clockwise rotation rates and NW-SE directed extensional and NE-SW directed contractional strain rates concentrated around the fault zone. Cartoon 3.20B displays the same deformation parameters for two blocks rotating with a clockwise orientation.

Naturally, in practice, interpretation based on these highly schematic relations strongly depends on data density and the location of incorporated faults. Furthermore, the rotation of an independently moving block will rarely be completely rigid and probably be subject to strongly varying deformation phases on small spatial scales. Nevertheless, we assume that we have parameterized the main faults (and thus delineated the main crustal blocks)

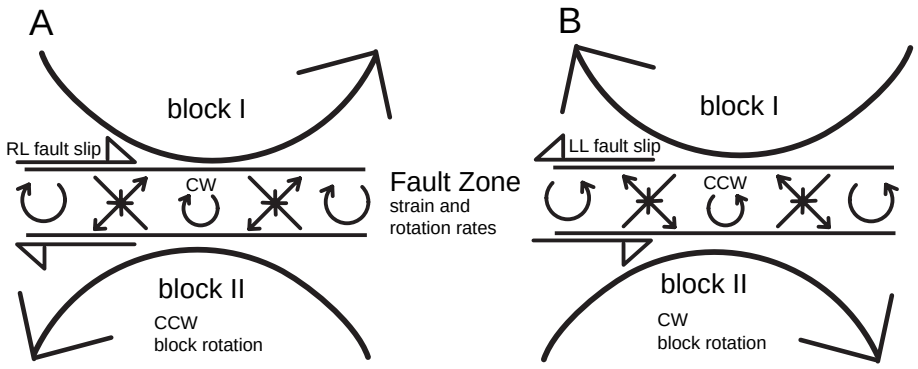

Figure 3.20: Relative block rotations: (A) Block I and II both rotate with a counterclockwise orientation. Dextral slip, clockwise rotation rates and shear strain rates characterize the fault zone. (B) The same deformation parameters as shown in (A) for two blocks, rotating clockwise. In this case the fault zone is characterized by sinistral slip rates, counterclockwise rotation rates and shear strain rates; (C) One block with a counterclockwise rotation rate is intersected by a fault. The fault zone is characterized by sinistral slip rates; (D) One block with a clockwise rotation rate is intersected by a fault. The fault zone is characterized by dextral slip rates. See the text for further information.

and that our solution therefore reveals whether blocks move independently and if so, what the orientation of their relative motion on average is.

The main results for strain, rotation and slip rates of solution II are summarized in figure 3.21 and discussed per region. In the remainder of this section reference to figures 3.8 (slip rates of solution II), 3.10 (strain rates) and 3.11B (rotation rates) is done by only using the figure numbers.

North Anatolian fault and North Aegean trough

The models of Taymaz et al. [1991]; McKenzie [1972] and Le Pichon et al. [1995] agree upon a dextral North Anatolian fault and an extending North Aegean trough, also found in our results (3.8 and 3.10). The deformation pattern found around the North Anatolian fault zone can be represented by cartoon 3.20A. Dextral slip motion on the North Anatolian fault separates two counterclockwise rotating regions of northeast Greece and the northeast Aegean Sea (3.11B). In solution I the region around the North Anatolian fault is wider than in solution II and characterized by clockwise rotation and shear strain rates, as depicted in cartoon 3.20A in the zone between the two rotating blocks. The region south of the main trace of the North Anatolian fault is subject to distributed continuous deformation in the form of strong shear strain rates (3.10). To what extent this deformation is accommodated by the many, not parameterized, subbranches of the North Anatolian fault is not clear. Projection of the orientation of the principle strain rates onto the average NE-SW orientation of the strikes of these small faults suggests dextral slip.

In contrast to Taymaz et al. [1991], both McKenzie [1972] and Le Pichon et al. [1995]

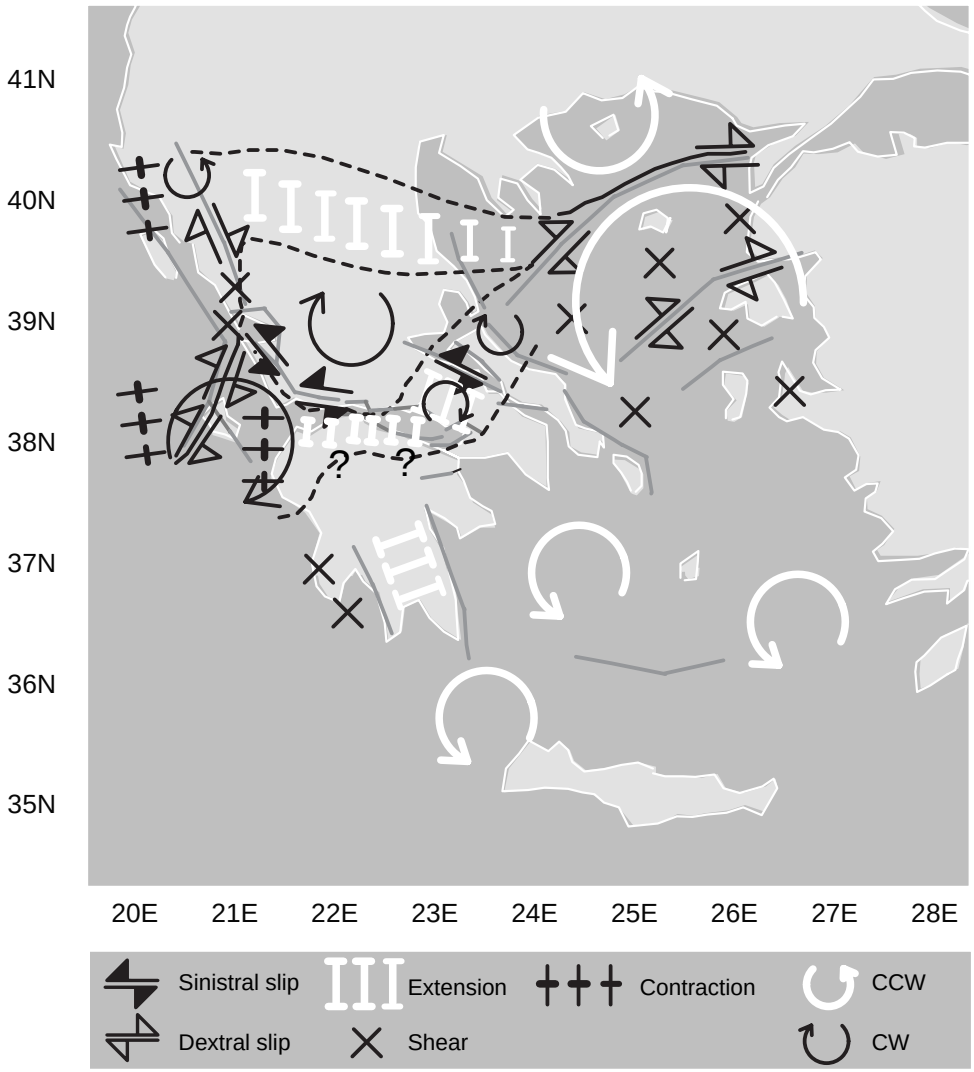

Figure 3.21: Straight grey lines represent parameterized faults or plate boundaries. Straight black lines indicate deformation zone on which common agreement exists. Dashed lines represent deformation zones inferred from solution II. The symbols in the figure, explained in the legend, indicate the main features of solution II in a highly schematic manner. Abbreviations CW and CCW in the legend denote clockwise and counterclockwise, respectively. The size of the symbol refers to the size of the region for which it represents the deformation mechanism.

propose a continuation of the North Anatolian fault zone in southwestward direction towards

the Gulf of Corinth in the form of a continuation of strike-slip and widening of the boundary zone from the North Aegean trough, respectively. We find clockwise rotation rates at the island of Evvia and the Parnassos region (3.11B), separated by sinistral slip along the coast of the Gulf of Evvia (3.8). This pattern suggests a connection of the North Anatolian fault to the Gulf of Corinth occurring by clockwise rotation rates of small blocks and sinistral slip on the faults bounding the Gulf of Evvia. This type of deformation can be viewed as the deformation within a fault zone between blocks that perform a counterclockwise rotation with respect to each other, as indicated by figure 3.20A. It is interesting to note here, that the interpretation of the deformation field largely depends on the scale at which we consider the results; clockwise rotation rates at Evvia and the Parnassos region, separated by sinistral slip, can also be viewed as the representation of cartoon 3.20B. The E-W trending zone of N-S extension at northwestern and northern Greece (3.10), connecting the North Aegean trough to the transcurrent, dextral fault system east of the collision zone between the Adriatic Sea and the Aegean region, has been discussed in section 3.8.3.

Connection of the Kephalonia fault zone with the transcurrent fault system at the Albanian coast and projection of the uniform shear strain rates, with NW-SE oriented extension and NE-SW oriented contraction, onto this imaginary fault, would result in dextral fault motion that transfers the northern Greek extension to the Kephalonia fault zone. The combination of clockwise rotation and dextral slip around the Kephalonia fault zone implies that this region does not consist of different crustal blocks, but constitutes one block, the dextral slip of the Kephalonia fault a manifestation of clockwise rotation (like clockwise rotation rates in solution I indicate the dextral slip regime of the North Anatolian fault zone).

Gulf of Corinth and Gulf of Patras

The deformation pattern around the Gulfs of Corinth and Patras (the Gulf hereafter) is complex. Consistent with results of Le Pichon et al. [1995] and discussed in section 3.8.2, our solution shows an increase of widening in the form of normal slip motion across the Gulf from east to west. We find dextral slip on the northeastern segment and all southern segments of the Gulf (3.8) and clockwise rotation rates north of, within and southwest of the Gulf (3.11B). Following the relations between rotation and slip proposed in figure 3.20 this suggests that the Parnassos region, the eastern part of the Gulf and the northern and northwestern Peloponessos are part of the same clockwise rotation regime. The strong sinistral strike-slip motion along the northwestern coast of the Gulf continuing along the Katouna fault zone into the Gulf of Arta (3.8) in combination with clockwise rotation rates at central Greece (3.11B) implies that central Greece represents an individual subregion. The existence of these differently behaving, neighboring regions requires two transitional boundaries; the first between the eastern and western part of the northern Gulf coast and the second between the northwestern part and the rest of the Gulf. In figure 3.21 we have interpreted both transitions as part of the same continuation of the northwestern boundary of the widened deformation zone associated with the North Anatolian fault. The derived deformation zone connects the North Anatolian fault across the Gulf with the Kephalonia fault zone. The location of its trace agrees with the location of the boundary zone across the Aegean proposed by McKenzie [1972, 1978] (figure 3.19A). Several studies based on different types of observations also suggest different deformation mechanisms at the eastern

and western part of the Gulf. GPS data show that N-S oriented extension across the east is considerably weaker than across the west [Briole et al., 1996; Davies et al., 1997; Clarke et al., 1997a, 1998]. Evidence for shallow, high conductivity is found only in the western part of the Gulf [Pham et al., 2000]. Fault plane solutions suggest a low-dip angle ($\leq 30^\circ$) fault for the west, in which the steeper faults that reach the surface at the south-side of the Gulf root [Rigo et al., 1996], and on average 45° dipping nodal planes at the east [Rietbrock et al., 1996; Bernard et al., 1997]. A teleseismic tomography study of Tiberi et al. [2000] images a NW-SE trending, narrow zone of thinned crust under Parnassos and Attica. This zone is overlapped by the northeastern part of the Gulf. Because the Gulf trends in a more E-W direction, a maximum lateral offset of about 20 km between the thinned crust and the Gulf is reached at the western part of the Gulf. Tiberi et al. [2000] suggest that a low-angle normal fault would explain why extension takes place within the Gulf, while the thinned crust is located more to the north. This rift geometry would suggest a gradual transition from extension on a common graben structure in the east to extension due to a low-angle normal fault in the west. Furthermore, the implicit westward propagation of the Gulf, in our model resulting from the dextral slip along its southern coast and the sinistral slip along the boundary crossing the Gulf, has also been observed or inferred by others [Le Pichon et al., 1995; Armijo et al., 1996; Clarke et al., 1998; Tiberi et al., 2000]. Whether our results are influenced by the low data density at the western side of the Gulf is difficult to say; future GPS campaigns will most likely provide further constraints on this.

Peloponessos

Le Pichon et al. [1995] argue that extension between the Aegean Sea, being part of the Anatolian microplate, and northern Greece, due to the opposite rotations of these regions, is distributed along the coastal plains of the mainland of Greece and the Peloponessos. Our results agree with their conclusions that extension east of the Gulf of Patras must be concentrated within the Gulf of Corinth and extension west and north of Patras is accommodated as extension at the pull-apart basin of the Gulf of Arta and as sinistral slip on the N-S trending segment of the Katouna fault system. However, they derive N-S directed extension within northwestern Peloponessos, where we find a distribution of deformation that can be explained by two blocks rotating in a clockwise manner (central Greece and the Ionian-western Peloponessos region) separated by a sinistral strike-slip fault (the Katouna fault) as shown in figure 3.20B.

3.10 Conclusions

We have analyzed a preliminary version of the SING geodetic velocity data set, which densely samples the Aegean area [Clarke et al., 1999; Cruddace et al., 1999]. We reduce the data set by removing the velocities that have been computed from only two station occupations and those that may have been influenced by two large seismic events, the 1995 Grevena and Aigion earthquakes that took place at the end of the time interval of station occupation. We assume that for the reduced data set remaining seismic motions are averaged out over the time interval between the first and last measurements at these sites.

We perform two series of inversions to derive the crustal deformation field from the data. In the first we invert for the lateral velocity gradient field (∇v) only (I) and in the second for the lateral velocity gradient field and horizontal fault motion (s) simultaneously (II). In inversion II the main fault zones and plate-boundaries are incorporated. Per inversion procedure a solution (I and II for inversion procedures I and II, respectively) is selected with reasonably well covariance, data fit and resolution properties. The main differences between solution I and II are found at the areas, where faults accommodate strong slip rates in solution II (i.e., the northern Aegean Sea, the mainland of Greece, the Gulf of Corinth and the Ionian region). Besides decrease of the average magnitude, the spatial distribution of ∇v of solution II is different from solution I, which can be observed from local changes in orientation of the principle strain rates.

In general, the properties of solution I are in good agreement with results from earlier geodetic studies solving for the lateral velocity gradient field on regional and local scale [Davies et al., 1997; Clarke et al., 1997a, 1998; Kahle et al., 2000; Le Pichon et al., 1995]. Most of the differences between our results and results from these studies can be explained by differences in density, origin and time of measurement of the data and possible postseismic influence incorporated in the data. From comparison of solutions I and II with P- and T-axes of shallow earthquakes and with stress data we find both patterns of agreement and disagreement. Possible causes for these discrepancies are errors in our model, errors in the moment tensor estimates or differences between the near surface and deeper crustal deformation, the latter suggesting that combining geodetic data with moment tensor solutions is not straightforward. The orientations of the slip vectors of solution II are generally in good agreement with geological observations and geodetic derivations. The consistency found between rotation rate results and young ($\approx$ 1Myr) paleomagnetic observations suggests that our deformation field reflects larger-scale crustal block rotation.

We present a new, detailed view on the present-day kinematics of the Aegean crustal deformation field assuming that solution II identifies possible large scale upper-crustal block motion. Consistent with results of Le Pichon et al. [1995] the clockwise rotation of central and western Greece and the counterclockwise rotation of the Aegean Sea, represented by individual zones of counterclockwise rotation rates, are separated by the dextral North Anatolian fault zone in the east. In westward direction the deformation zone associated with the North Anatolian fault continues as N-S extension into the North Aegean trough and crosses northern Greece. In southwestward direction the deformation associated with the North Anatolian fault is transferred by clockwise rotation of small blocks to the Gulf of Corinth. The location of the inferred fault zone associated with the North Anatolian fault and its continuation into the Gulf of Corinth agree with the boundary zone between the Aegean and the Anatolian micro-plates, proposed by McKenzie [1972, 1978]. In the Gulf of Corinth and the Gulf of Patras N-S oriented extension and E-W oriented dextral slip motion dominate the deformation field. Active tectonics in the Ionian region result from a strong dextral shear strain regime at the Kephalonia fault zone caused by the relative motion between the Aegean and the Adriatic Sea to the north and the fast southwestward moving Aegean microblock.

Chapter 4

Crustal deformation of Southeast Asia

4.1 Introduction

The kinematics of Southeast Asia are determined by the convergence of the Eurasian, Indo-Australian, Philippine Sea and Caroline plates (figure 4.2B). Global plate motion models [e.g., DeMets et al., 1990, 1994] describe the rigid motion of plates, but can not be applied to derive the deformation field within the plates and boundary zones. Since the beginning of the 90's complementary information on the velocity field has been provided for by space geodetic measurement campaigns, held in different parts of Southeast Asia. An ever increasing collection of (mainly) GPS data sets consists of regional studies [e.g., Wilson et al., 1998; Kato et al., 1998b; PCGIAP Working Group 1, 1998; Bock et al., 2001; Michel et al., 2001] and more local studies sampling the velocity field within plate-boundary zones (e.g., Java [Tregoning et al., 1994]; New Guinea [Puntodewo et al., 1994; Tregoning et al., 1998]; Sumatra [Prawirodirdjo et al., 1996, 2000; Genrich et al., 2000]; Taiwan [Yu et al., 1999]; Sulawesi [Walpersdorf et al., 1998; Simons et al., 1999; Stevens et al., 1999]; and the Banda region [Genrich et al., 1996]).

In this study we apply our inverse method, discussed in chapter 2, to an integrated data set, consisting of several regional and local GPS data sets obtained in Southeast Asia. Our main objective is to determine the spatial variation in the surface deformation field by inverting the data into (1) discrete slip motion on major fault zones in the plate boundary regions and (2) the velocity gradient field in the crustal blocks and plate interiors.

4.2 Tectonic setting

Southeast Asia is considered as the area that is bounded in the west by Laos, Thailand and the Malaysian peninsula, in the south by the Indonesian archipelago (Sumatra, Java, Sumba, Timor), in the east by Irian Jaya (Indonesia) and the Philippines and in the north by Taiwan

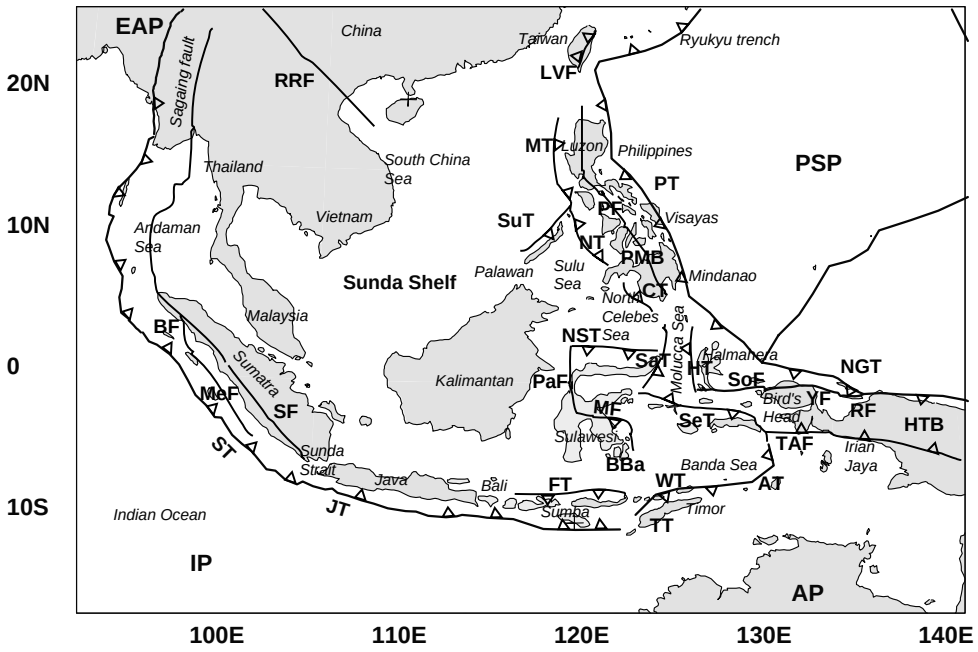

Figure 4.1: Southeast Asia, with lines indicating the plate boundaries and main faulting structures; Key: Plates: IP, Indian; AP, Australian; PSP, Philippine Sea; EAP, Eurasian. Trenches: ST, Sumatra; JT, Java; NGT, New Guinea, NST, North Sulawesi; PT, Philippine; SaT, Sangihe; HT, Halmahera; SuT, Sulu; CT, Cotabato; NT, Negros; MT, Manila. Troughs: TT, Timor; SeT, Seram; AT, Aru. Fault zones: SF, Semangko; BF, Batee; MeF, Mentawai; MF, Matano; PaF, Palu; YF, Yapen; RF, Ransiki; SoF, Sorong; TAF, Tarera-Aiduna; PF, Philippine; LVF, Longitudinal Valley. Backarc thrusts: FT, Flores; WT, Wetar. NCS, North Celebes Sea; SS, Sunda Strait; BBa, Banda backarc; HTB, Highlands Thrust Belt; PMB, Philippine Mobile Belt.

and Vietnam (figure 4.1).

Interaction between local, relatively rigid blocks and broad zones of distributed deformation characterizes the regional tectonics of Southeast Asia. Although Southeast Asia is formally considered to be part of the Eurasian continent, evidence for deformation within

Figure 4.2: Figures on next page: Tectonics of SEA. (A) Contours denote age of oceanic lithosphere (unknown in the area without contouring). Dots denote earthquakes from the Harvard CMT catalogue; from light-grey to darker denotes shallow (60 km) to deep (700 km) events. Key: IP, Indian plate; AP, Australian plate; CP, Caroline plate; PSP, Philippine Sea plate; EAP, Eurasian plate; SCS South China Sea. (B) Arrows denote the NUVEL-1a plate velocities relative to a stable Eurasia [DeMets et al., 1994]; dark-grey: Indian plate, grey: Australian plate, white: Pacific/Caroline plate, light-grey: Philippine Sea plate. Focal mechanisms of shallow earthquakes (to a depth of 30 km).

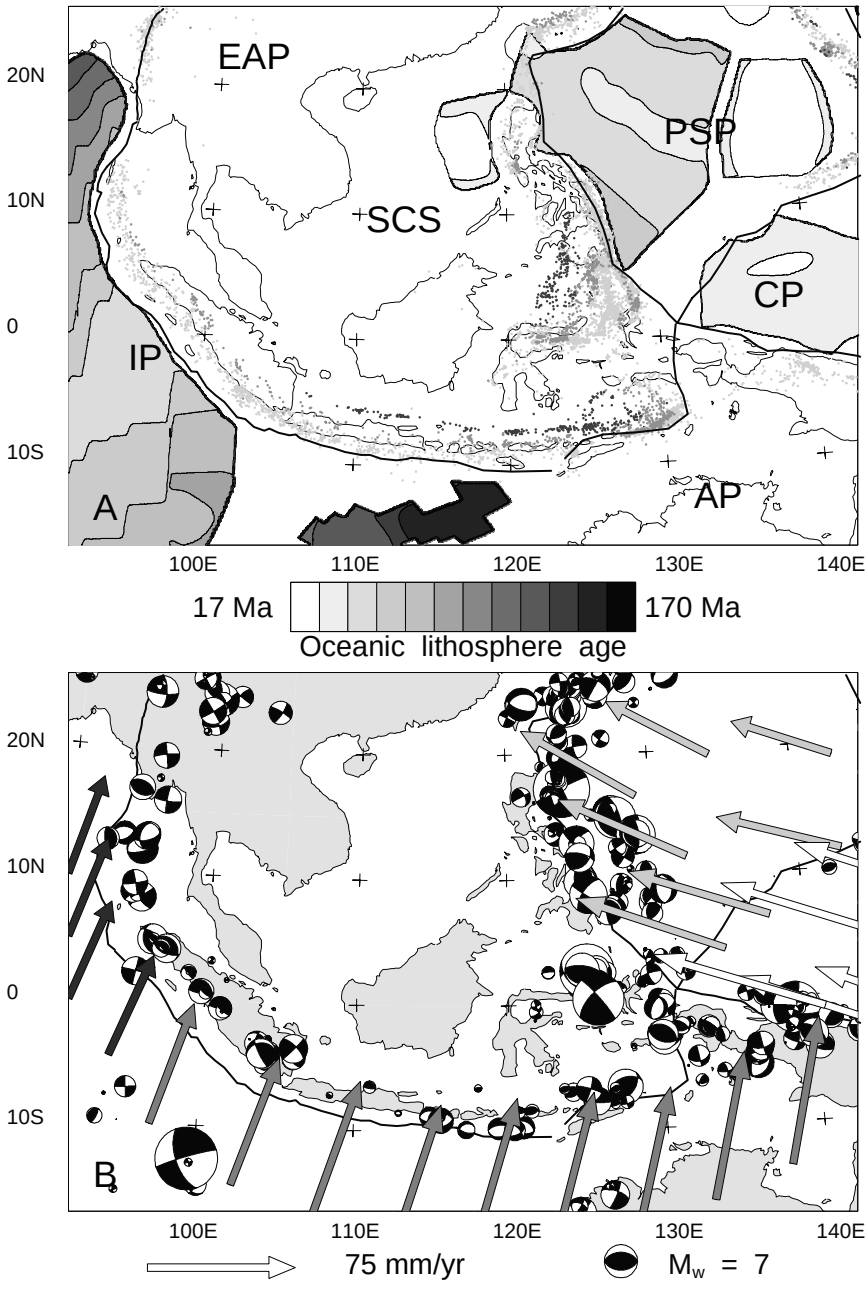

Figure 4.2: See caption on previous page

the Asian plate suggests independent motion of Sundaland, i.e. the stable interior of Southeast Asia [e.g., Cardwell and Isacks, 1978; Tapponnier et al., 1986]. Recently, three independent studies based on GPS measurements and focal mechanisms found a small north to northeast motion of Sundaland relative to Eurasia [Tregoning et al., 1994; Simons et al., 1999; Kreemer et al., 2000].

Along the Sunda arc-trench system, extending from the Eastern Himalayan Syntaxis to Sumba, the Indo-Australian plate moves with a rate of about 70-75 mm/yr in average N25°E direction relative to Eurasia [DeMets et al., 1990] (figure 4.2B). At Sumatra relatively young ($\approx$ 50 Myr) oceanic lithosphere (figure 4.2A) subducts in a direction obliquely to the trench. The seismic history of the Sunda Arc during the last 300 years reveals 2 large ($M_w > 8$) interplate earthquakes with thrust mechanisms at Sumatra, suggesting that a significant percentage of motion perpendicular to the plate boundary occurs seismically [Newcomb and McCann, 1987]. The Java trench remained relatively calm, probably as a result of the old age (of $\approx$ 150 Myr) of the subducting oceanic lithosphere [Hamilton, 1979] (figure 4.2A) and the sub-perpendicular direction of plate convergence (figure 4.2B). The Banda arc connects to the Sunda arc in the west at Sumba and extends along the Timor, Aru and Seram troughs in a horseshoe-shape to the east and north. Along the southern Banda arc continental lithosphere of Australia reached the trough about 3 Myr ago and initiated the accretion of the forearc to the subducting plate [Hamilton, 1979]. The seismic history of the Timor forearc does not reveal major thrust earthquakes. The occurrence of large ($M_w > 7$) earthquakes in the backarc [McCaffrey, 1988] supports the view that continental collision probably caused transfer of deformation from the forearc to the Flores and Wetar backarc thrusts as a result of Quaternary uplift and crustal thickening of the forearc [e.g., Audley-Charles, 1975; Silver et al., 1983b, 1986].

Oblique shortening between the Pacific (Caroline) and Australia plates at an azimuth of 248° and rate of 110 mm/yr [DeMets et al., 1990] is accommodated in the Irian Jaya province of Indonesia (western part of New Guinea). Geological structure and the motion of the northern part of the Bird's Head suggest that at present the Sorong-Yapen-Ransiki fault zone constitutes the main boundary between Australia and the Pacific [Hamilton, 1979; Abers and McCaffrey, 1988; McCaffrey and Abers, 1991]. The Palu-Koro and Matano faults at Sulawesi form the boundary between Sundaland to the west and the zone of convergence between Australia and the Pacific to the east. E-W shortening in this collisional setting is accommodated by clockwise rotation of the Sulawesi block along the Palu-Koro-Matano fault system [Hamilton, 1979; Silver et al., 1983a; Surmont et al., 1994].

The motion of the Philippine Sea plate is not well constrained due to lack of spreading boundaries [e.g. Ranken et al., 1984; DeMets et al., 1990]. However, recently obtained GPS measurements [Kato et al., 1998b; Yu et al., 1999] agree with plate motion models [Seno et al., 1993; DeMets et al., 1994]. Along the western boundary of the Philippine Mobile Belt eastward subduction of marginal basins (South China Sea, Sulu Sea and Celebes Sea) at the Manila, Negros and Cotabato trenches continues very slowly due to collision of the Palawan continental block [Rangin, 1989; Barrier et al., 1991]. After the initiation of this collision (8 to 9 Ma) subduction changed from west to east of the Philippines. Here, oceanic material of the Philippine Sea plate subducts northwestward at the Luzon trough and Philippine trench. South of 3°N and north of 15°N evidence for an active Philippine trench disappears [Nichols

et al., 1990]]. At the Molucca Sea plate convergence is taken up by the doubly subducting Molucca plate; eastward beneath Halmahera (part of the Philippine Sea plate) and westward beneath the Sangihe trench (an Eurasian margin) [Quebral et al., 1996; Lallemand et al., 1998; Rangin et al., 1999]. Northward translation along the Philippine fault and subduction along the Manila trench of the North Luzon arc resulted in collision with the Eurasian continental margin at Taiwan [Suppe, 1981; Lee and Lawver, 1994]. Near Taiwan, the Philippine Sea plate moves toward Eurasia at a rate of 86 mm/yr with an azimuth of 307° [Seno et al., 1993; DeMets et al., 1994].

4.3 Data

Four GPS data sets with epochs ranging between 1989 and 1997 provide most of the horizontal velocities for our application (figure 4.3): (1) The GPS data set of Matheussen [2000] completely covering the Southeast Asian region, (2) the GPS data set of Bock et al. [2001] sampling the Indonesian island arc, (3) the GPS data set of Yu et al. [1999] sampling Taiwan and Luzon and (4) five velocity measurements of the GPS data set of Kato et al. [1998b] (WING-data set) located at the Philippine Sea Plate, Taiwan and Southeast China. We assume that the velocity field has remained stationary during the overall period of observation.

4.3.1 Main data set

We define the data set of Matheussen [2000] as the main data set in the inversion, since it covers the whole model area and can serve as a reference, with respect to which the other data sets are defined. The GPS data set of Matheussen [2000] contains the GEODYSSEA data, the Sulawesi data and the APRGP data. The GEODYSSEA data set covers the whole region of Southeast Asia and consists of about 40 sites. Incorporated are the GEODYSSEA data that have been obtained during 2 campaigns in 1994 and 1996 [Simons et al., 1999; Wilson et al., 1998] and the Indonesian sites only of the GEODYSSEA 1998 campaign [Michel et al., 2001]. The Sulawesi data set consists of about 45 stations and has been obtained during campaigns in 1997 and 1998 [Simons et al., 1999]. The APRGP data [PCGIAP Working Group 1, 1998] have been obtained during campaigns in 1997 and 1998 and cover a broad area; besides Southeast Asia, also Australia, Japan and Iran. Matheussen [2000] analyzed the raw data with the GAMIT [King and Bock, 1999] and GLOBK [Herring, 1999] software packages. By applying the fiducial network approach, based on about fifty sites of the International GPS service for Geodynamics (IGS) network [Beutler et al., 1994], the different data sets were combined within the International Terrestrial Reference Frame (ITRF97) [Sillard et al., 1998; Boucher et al., 1999]. For our inversion we use about 20 vectors of the Sulawesi data set by excluding the data that densely sample the Palu-Koro fault transect (figure 4.4C). We only use the southeast Asian part of the APRGP set, which is densest at Malaysia, Thailand, Vietnam and Laos, but also contains sites at Java, Sumatra, Sulawesi, the Philippines and Irian Jaya. The final subset of the Matheussen [2000] data in the inversion consists of 59 velocities, with an average formal standard deviation of 1.0 mm/yr.

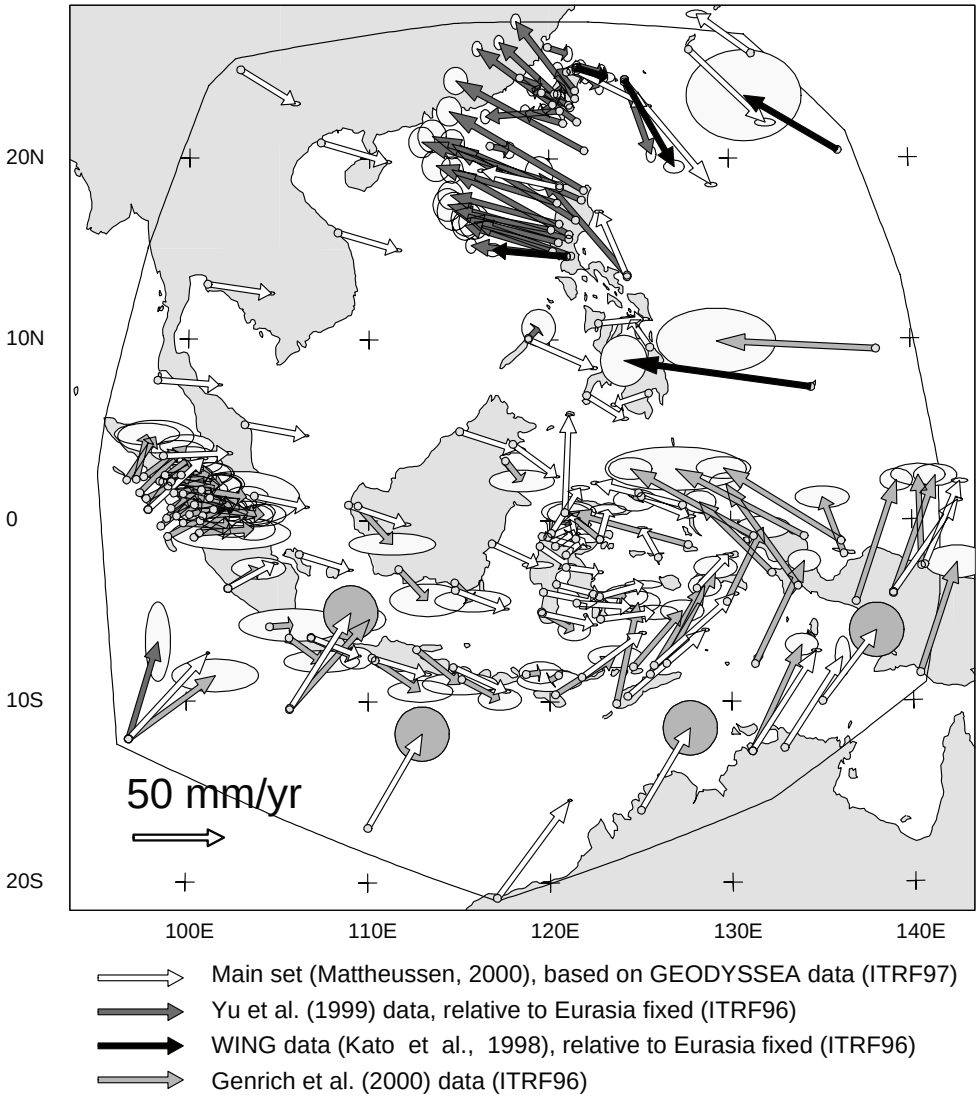

Figure 4.3: The GPS velocity data sets, used in this study, are plotted in the coordinate systems in which they originally were defined. The four velocity vectors with shaded ellipses are the extra Australia vectors discussed in section 4.3.3.

4.3.2 Other data sets

The Indonesia GPS data set of Bock et al. [2001] results from GPS geodetic surveys in 1989-1994 [Puntodewo et al., 1994; Tregoning et al., 1994; Genrich et al., 1996; Prawirodirdjo

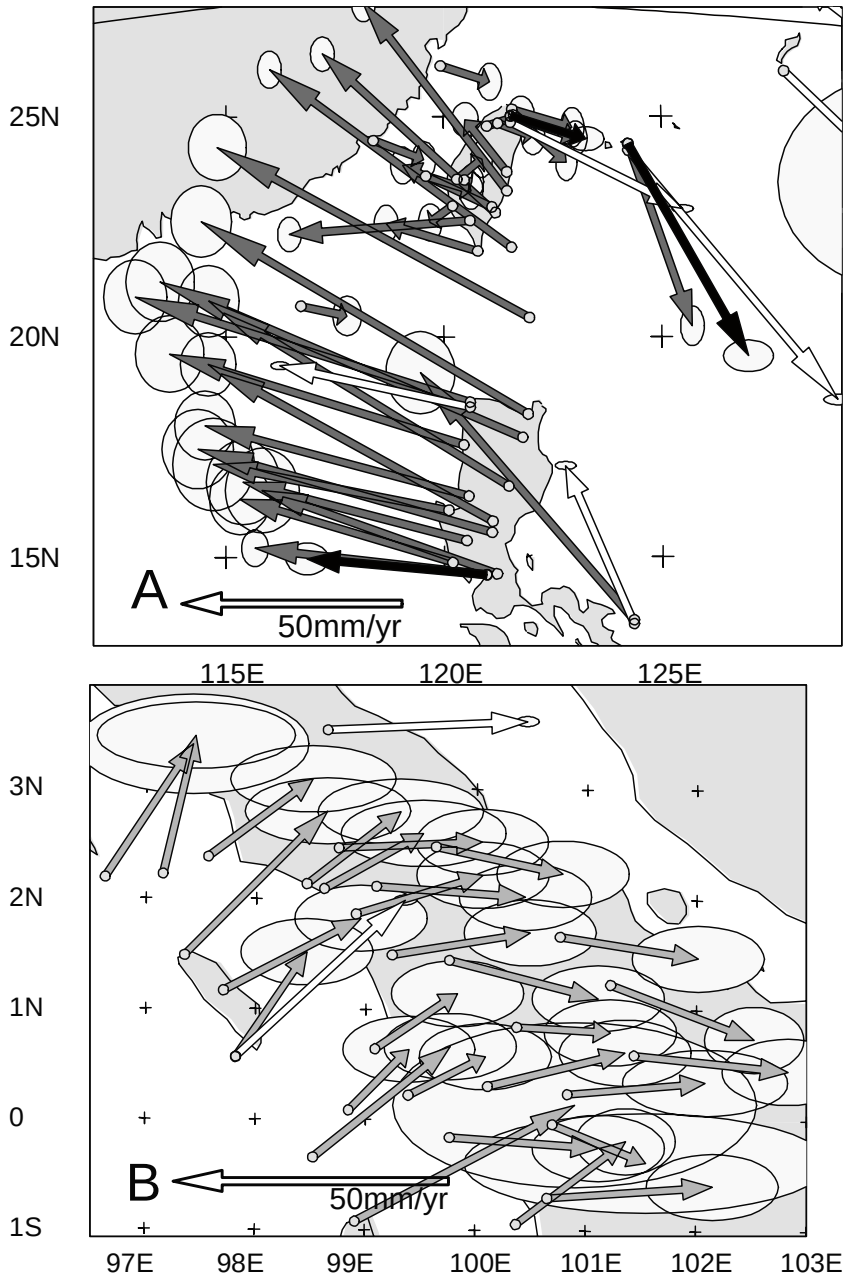

Figure 4.4: See caption on next page.

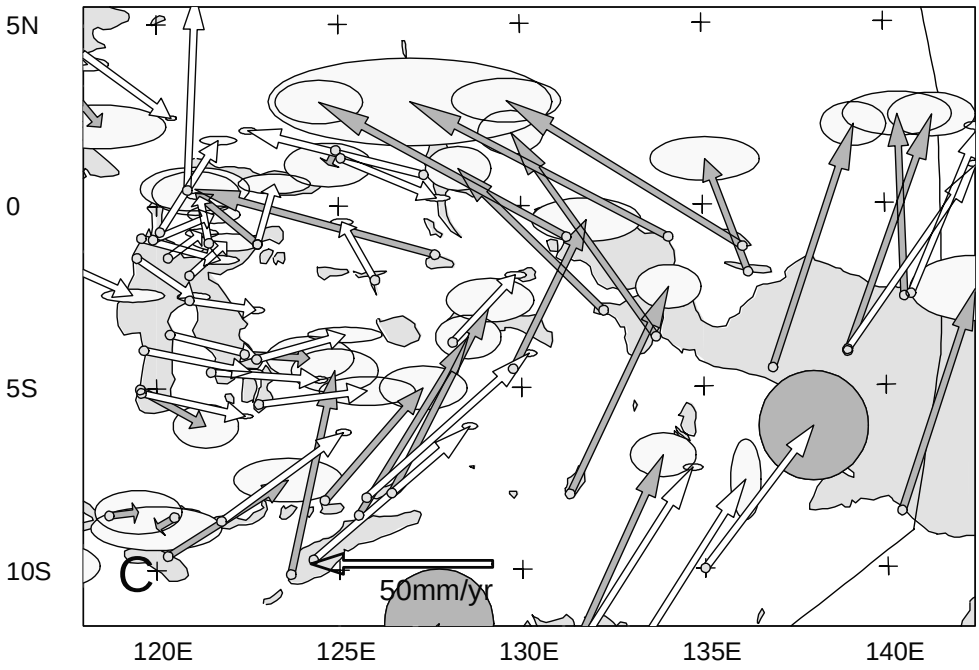

Figure 4.4: Details of figure 4.3; (A) (on previous page) Taiwan and the northern Philippines (Luzon); (B) (on previous page) Sumatra; (C) the Banda region, Sulawesi, Halmahera and Irian Jaya. The color code of the vectors and ellipses corresponds to the color code used in figure 4.3.

et al., 1996; Stevens et al., 1999; McCaffrey et al., 2000]. The data comprise over 150 sites. More than half of these velocities is located in Sumatra (figure 4.4B) along both sides of both the Mentawai and the Semangko fault, covering a large part of the Sumatra fore- and backarc (figure 4.4B). This part of the data set is described by Prawirodirdjo et al. [2000] and Genrich et al. [2000]. The remaining part of the data covers all major islands of Indonesia (figures 4.3 and 4.4C). We exclude the GPS data that are part of local arrays and densely sample transects over the Semangko fault zone [Genrich et al., 2000], which finally leaves us with 68 velocities of the original set. In general, the data processing is similar as described for the Matheussen [2000] data; the daily solutions for each survey year were estimated by application of the programs GAMIT [King and Bock, 1999] and GLOBK [Herring, 1999], merged in a single Kalman filter solution and combined within the International Terrestrial Reference Frame (ITRF96) [Boucher et al., 1999]. The formal standard deviations on the velocity measurements are on average 2 mm/yr for the north and 5 mm/yr for the east component, based on a white noise stochastic model for site coordinates [Zhang et al., 1997]. However, it has been suggested that GPS position estimates are significantly influenced by colored noise [Bock et al., 1997; Zhang et al., 1997], which would result in formal errors that are 2 to 4 times larger [Genrich et al., 2000].

Source	lo	la	ω (°/Ma)
DeMets et al. [1994]	-112.4°E	50.6°N	0.23
Larson et al. [1997]	-102.8°E±4.1	56.3°N±4.3	0.26±0.02
Sillard et al. [1998]	-120.5°E±2.8	48.6°N±3.2	0.21±0.01
This study	-101.9°E±2.3	55.8°N±1.5	0.24±0.01

Table 4.1: Eurasia-ITRF Euler poles. Key: lo, longitude; la, latitude; ω, rotation rate.

To better constrain the Philippine Sea Plate we add 5 vectors of the Western Pacific Integrated Network of GPS (WING) data set [Kato et al., 1998b], a continuous GPS tracking network. The velocities were estimated during the time-interval 1995-1997 and defined with respect to Eurasia fixed in the ITRF96 reference frame (figure 4.4A). The definition of stable Eurasia is based on a study of Heki [1996] who used VLBI data to compute the residual motion of sites near plate boundaries. Heki [1996] estimated the motion of Tsukuba at Japan under the assumption that VLBI sites on the Eurasian cratons represent the motion of the rigid plate. As Tsukuba is also incorporated in the WING data, Kato et al. [1998b] assign it the estimate of Heki [1996] and define the rest of the velocities with respect to this site. Although they only fix Tsukuba site, they find consistency between their GPS velocity and the VLBI velocity of Heki [1996] at Shanghai. The data have an average standard deviation of 3.6 mm/yr.

We include 37 velocity measurements of the Taiwan GPS data set of Yu et al. [1999], defined with respect to stable Eurasia (in ITRF96) (figure 4.4A). Fifteen newly established stations at Taiwan and Luzon were occupied three times during 1996-1998. The full data set also contains velocities from continuous GPS sites at Taiwan and of the WING network. The data are defined in a similar manner as described by Kato et al. [1998b] for the WING data, only now Shanghai represents the reference station and is the difference between the Tsukuba velocity of this data set and the estimate of Heki [1996] insignificant. The data have an average standard deviation of 1.9 mm/yr.

To define the velocities of the data sets of Kato et al. [1998b] and Yu et al. [1999] with respect to the main data set we compute the Euler pole for the Eurasian plate from 6 stations on stable Eurasia from the data set of Matheussen [2000], most of which are located in Europe. Comparison with other studies shows good agreement between our pole and the resulting pole of Larson et al. [1997] (see table 4.1). We rotate the Eurasia fixed data with respect to the ITRF97 data and find in general a good match between the velocity vectors of different data sets at the same sites (figure 4.5).

Although we transformed the Eurasia fixed data with respect to the main set, we still leave two residual rigid rotation vectors to be determined in the inversion (section 2.2), one for the set of Bock et al. [2001] and one for the combined data sets of Kato et al. [1998b] and Yu et al. [1999]. Since the boundaries of our model encompass only 5 velocity vectors of the WING data set [Kato et al., 1998b], we can not determine an individual residual rotation vector for this set. Relative rotations between the networks might still be present due to differences in network geometry, number of data or formal error distribution. Naturally, these factors not only produce uniform rotations of one network with respect to another, but

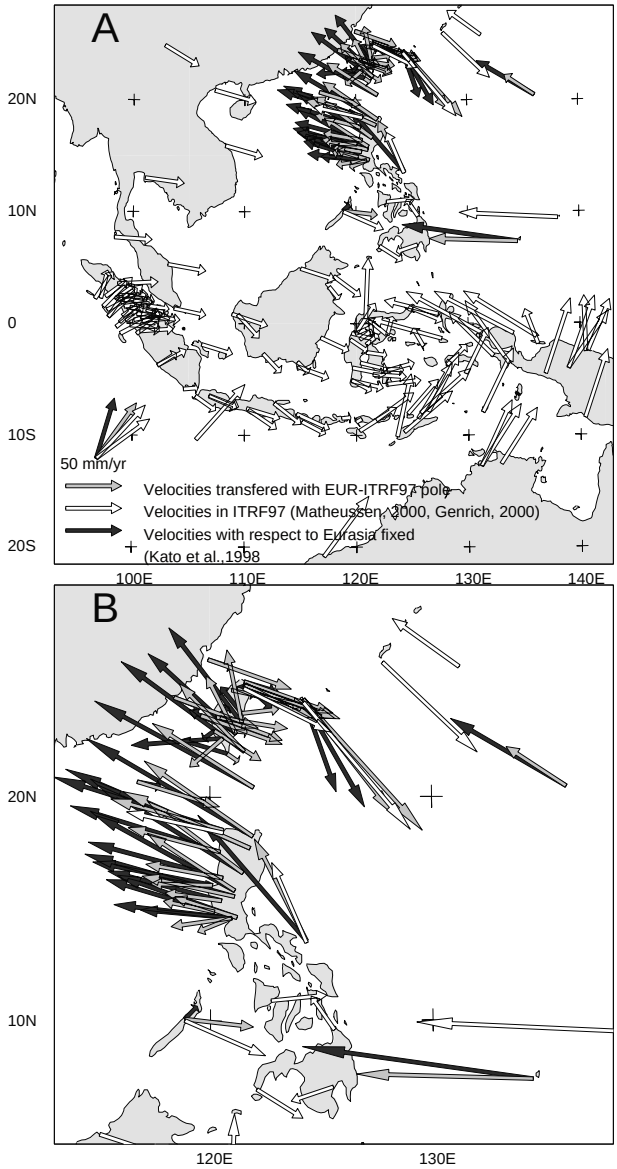

Figure 4.5: Rotation of the data of Kato et al. [1998b] and Yu et al. [1999]. Key for arrows: white, data of Matheussen [2000] and Bock et al. [2001]; black, data of Kato et al. [1998b] and Yu et al. [1999] in a Eurasia fixed reference frame; grey, data of Kato et al. [1998b] and Yu et al. [1999] after multiplication with the Eurasia-ITRF Euler pole (table 4.1) for (A) the whole model area, (B) Taiwan and the Philippines (detail of (A)).

Source	lo	la	ω (°/Ma)
Argus and Gordon [1991]	33.2°E	33.8°N	0.68
DeMets et al. [1994]	33.2°E	33.8°N	0.65
Larson et al. [1997]	40.7°E±2.8	31.4°N±1.7	0.61±0.01
Sillard et al. [1998]	38.8°E±1.4	32.0°N±0.5	0.61±0.01
This study	37.5°E±0.3	32.9°N±0.1	0.60±0.01

Table 4.2: Australia-ITRF Euler poles. Key: lo, longitude; la, latitude; ω, rotation rate.

most likely also induce internal, non-uniform deformation. However, the latter can only be dealt with by combining the field data and processing them simultaneously. In this study we assume that relative differences between networks can be modeled by uniform rotations with respect to the main set.

Figure 4.4A shows that differences exist between velocity vectors measured at the same site of the data of Kato et al. [1998b] and of Yu et al. [1999]. This could be due to the different time-intervals during which the sites of both networks have been occupied but, since both data sets are defined with respect to only one station, may also be caused by the inconsistent definition of the networks with respect to Eurasia fixed. For these data sets a difference in a velocity measurement at the same site automatically becomes part of the misfit after the inversion. Our treatment of the underestimation of formal errors in GPS velocities is similar to what is described in Kreemer et al. [2000]. They multiply published standard errors by a factor of 2 and use a factor of 10 for the IGS station in Singapore. However, instead of a factor of 2 we use a factor of 3, as suggested by Genrich et al. [2000].

4.3.3 Extra Australia constraints

To provide better constraints along the southern boundary of our model area, we add four velocity vectors at the Australian plate. We do not add extra data at the Philippine Sea plate, because the motion of this plate is uncertain [Ranken et al., 1984; DeMets et al., 1990] and our main data set does not sample this area densely enough to constitute a proper reference with respect to which extra Philippine Sea plate data can be defined. We determine the Euler pole from the 12 velocity vectors on the Australian plate in the data set of Matheussen [2000] (figure 4.6) at 32.9°N, 37.5°E with a rate of 0.60°/Myr. Again, this pole agrees with the Australia-ITRF pole of [Larson et al., 1997] for the Australian plate (see table 4.2). With our pole we calculate four extra velocity vectors along the Sunda and Banda arcs (indicated in figure 4.3 by shaded ellipses). We do not calculate a velocity vector west of 105° longitude, because of the transition to a different deformation regime south of the Sumatra trench [e.g., Cloetingh and Wortel, 1986; Coblentz et al., 1998]. The added rigid plate velocity vectors keep a minimal distance of 400 km from the plate boundaries, except for the vector at Christmas Island near the Java trench. Recent GPS measurements [Tregoning et al., 1994] reveal a relative velocity across the Java trench that matches the NUVEL-1a vector within 1 cm/yr [McCaffrey, 1996], suggesting that the motion is close to the rigid plate motion. In total the data set for inversion consists of 173 motion vectors.

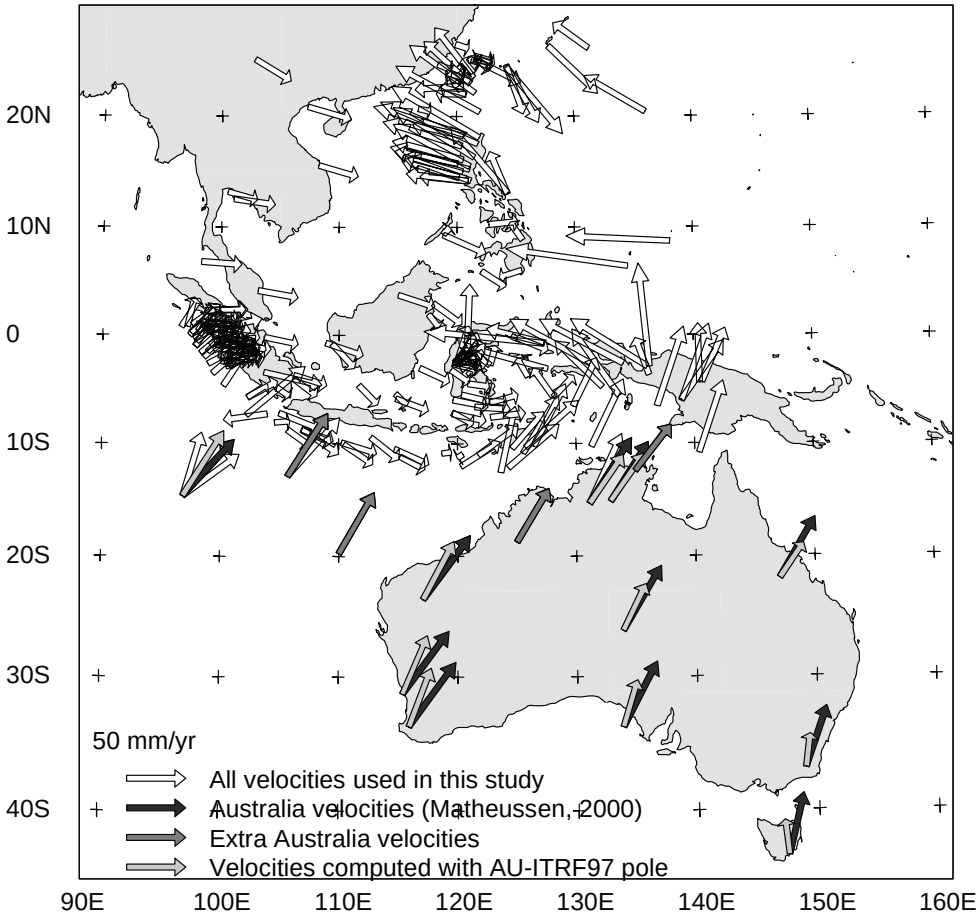

Figure 4.6: The velocity data used in this study. Arrows indicate: white, data sets of Matheussen [2000]; Bock et al. [2001]; Yu et al. [1999]; Kato et al. [1998b]; black, data at Australian plate of Matheussen [2000] used for the computation of the Australia-ITRF97 Euler pole (table 4.2); light-grey, velocities computed with Euler pole determined by Australia data; dark-grey, four velocities that are added to the data set used for the inversion as extra constraints on the southern model boundary.

4.4 Model parameterization and inversion

The data are inverted for two different representations of the Southeast-Asian crustal deformation field; the first in terms of continuous deformation only (inversion I), the second in terms of continuous deformation and fault motion (inversion II). Continuous deformation is parameterized in terms of linear variation of the velocity gradient field over spherical triangles. We apply the Delaunay triangulation method of Shewchuk [1996], which is based on the Delaunay refinement algorithm for quality triangular mesh generation of Ruppert

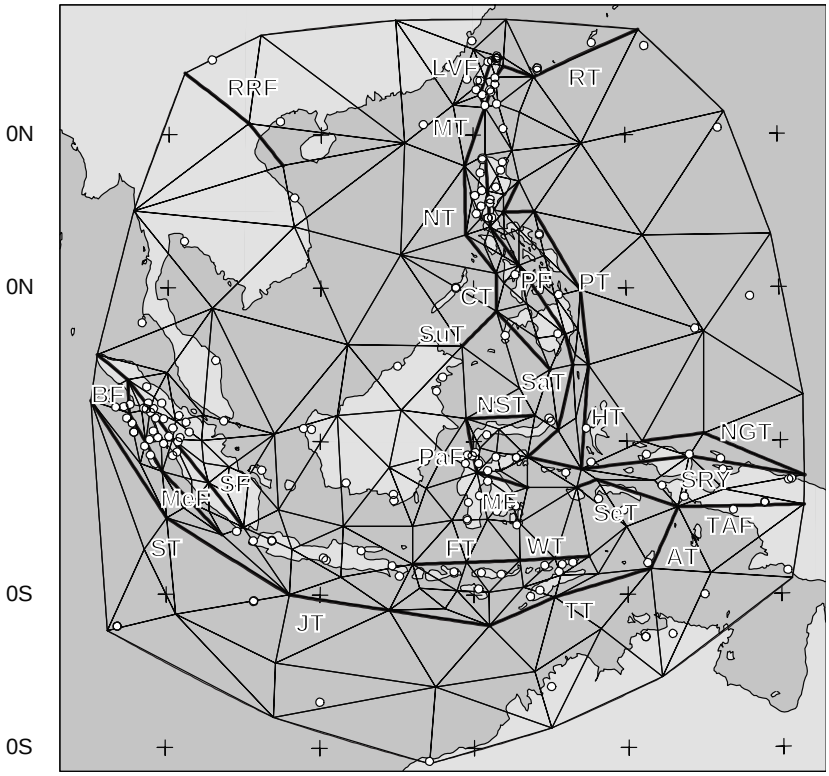

Figure 4.7: Parameterization of the model area. Thick lines indicate fault segmentation. Key: AT, Aru trough; BF, Batee fault; CT, Cotabato trench; FT, Flores thrust; HT, Halmahera trench; JT, Java trench; LVF, Longitudinal Valley fault; MeF, Mentawai fault; MF, Matano fault; MT, Manila trench; NGT, New Guinea trench; NST, North Sulawesi trench; NT, Negros trench; PaF, Palu-Koro fault; PF, Philippine fault; PT, Philippine trench; RRF, Red River fault, SaT Sangihe trench; SeT, Seram trough; SF, Semangko fault; ST, Sumatra trench; SuT, Sulu trench; SYR, Sorong-Yapen-Ransiki fault; TAF, Tarera-Aiduna fault; TT, Timor trough; WT, Wetar trench. White dots indicate the site positions. Note that in our choice for the triangle nodes we are not restricted to the locations of the observation sites.

[1985]. We use the same triangular grid for inversions I and II (figure 4.7). For inversion II on the fault traces duplicate model nodes are used to allow decoupling of the velocity gradient field across the fault.

The limited density of the data set and our aim to model the regional deformation field only restrict the estimation of the velocity gradient and fault slip to sizeable areas and fault segments, respectively. In general, the local density of the stations is used as a guide for local densification of model nodes for the triangulation. The main active faults of the regional study of Lee and Lawver [1995] constitute the basis for fault selection. We choose to rep-

i	T_n	T_t	K	σ_r $\left[\frac{10^{-10}}{myr}\right]$	α_a $[10^7]$	α_d $[10^6]$	χ^2	$\tilde{r}_m$	$\tilde{\sigma}^c_m$ $\left[\frac{10^{-9}}{yr}\right]$	$\tilde{\sigma}^f_m$ $\left[\frac{mm}{yr}\right]$
I	163	305	-	3.3	5.0	3.0	2.4	0.80	5.8	-
II	211	305	64	0.2	5.0	1.0	1.4	0.88	5.3	1.4

Table 4.3: Some quantities characterizing results for the inversion for $\boldsymbol{\nabla v}$ only (inversion I) and for joint estimates of $\boldsymbol{\nabla v}$ and $\boldsymbol{s}$ (inversion II). Key: i, inversion; T_n, number of model nodes; T_t, number of triangles; K, number of fault segments; σ_r; standard deviation of $\boldsymbol{\nabla} \times \boldsymbol{\nabla v} = \mathbf{0}$ data constraints; $\tilde{r}_m = \frac{1}{M}\sum_{i=1}^{M} R_{ii}$; the average model resolution, with R_{ii} the resolution matrix and M the number of model parameters; $\sigma^c_m = \frac{1}{M_c}\sum_{i=1}^{M_c}\sqrt{C_{ii}}$, the average standard deviation for the components of $\boldsymbol{\nabla v}$, with $M_c = 4T_n$ the number of components of $\boldsymbol{\nabla v}$; $\sigma^f_m = \frac{1}{M_f}\sum_{i=1}^{M_f}\sqrt{C_{ii}}$, the average standard deviation for the components of $\boldsymbol{s}$, with $M_f = 2K$ the number of slip components.

resent complex fault systems in wide deformation zones by one single fault. For instance, one fault segment with the coordinates of the main fault branch represents distributed fault systems for the Semangko fault zone and Philippine fault zone. Some stations are located between the subbranches of the actual fault zone and their motion may be influenced by slip on the subbranches. Deformation at these stations and other deformation due to the omission of smaller faults are in the inversion converted into estimates of the local velocity gradient field.

Information from local studies is used to define the location of the fault traces more precisely. The Semangko fault in Sumatra, the almost 2000-km long fault structure that connects the Sunda Strait in the southeast to the Andaman Sea in the northwest, and the Mentawai fault off the coast of Sumatra are implemented according to Bellier and Sébrier [1995] and Diament et al. [1992], respectively. The GPS study of Puntodewo et al. [1994] is used to define the E-W trending Sorong, Yapen and Ransiki faults (as one sequence of segments). Parameterization of the Philippines consists of three elongated, N-S trending fault structures [Barrier et al., 1991]. West of the Philippines the Manila and Cotabato trenches are connected by the Negros trench. We connect the Philippine fault to the Sangihe trench [Quebral et al., 1996]. The southern tips of the Sangihe and Halmahera trench segments end in the segment that prolongs the Sorong fault in the west and represents the E-W trending fault zone north and south of the Sula Islands. We parameterize the North Sulawesi trench and the Palu-Koro-Matano fault system in Sulawesi according to Silver et al. [1983a] and the Longitudinal Valley fault in Taiwan according to Yu et al. [1999].

For details of our inversion procedure we refer to chapter 2. In the first series of inversions (I) we solve for the lateral components of $\boldsymbol{\nabla v}$ only. We represent $\boldsymbol{\nabla v}$ in spherical coordinates in a symbolic notation by

$$\boldsymbol{\nabla v} = \begin{bmatrix} v_{\theta\theta} & v_{\theta\phi} \\ v_{\theta\phi} & v_{\phi\phi} \end{bmatrix},$$

where θ denotes longitude and ϕ latitude. For each component we estimate the linear variation within triangles. In the second series (inversions II) we also solve for the horizontal

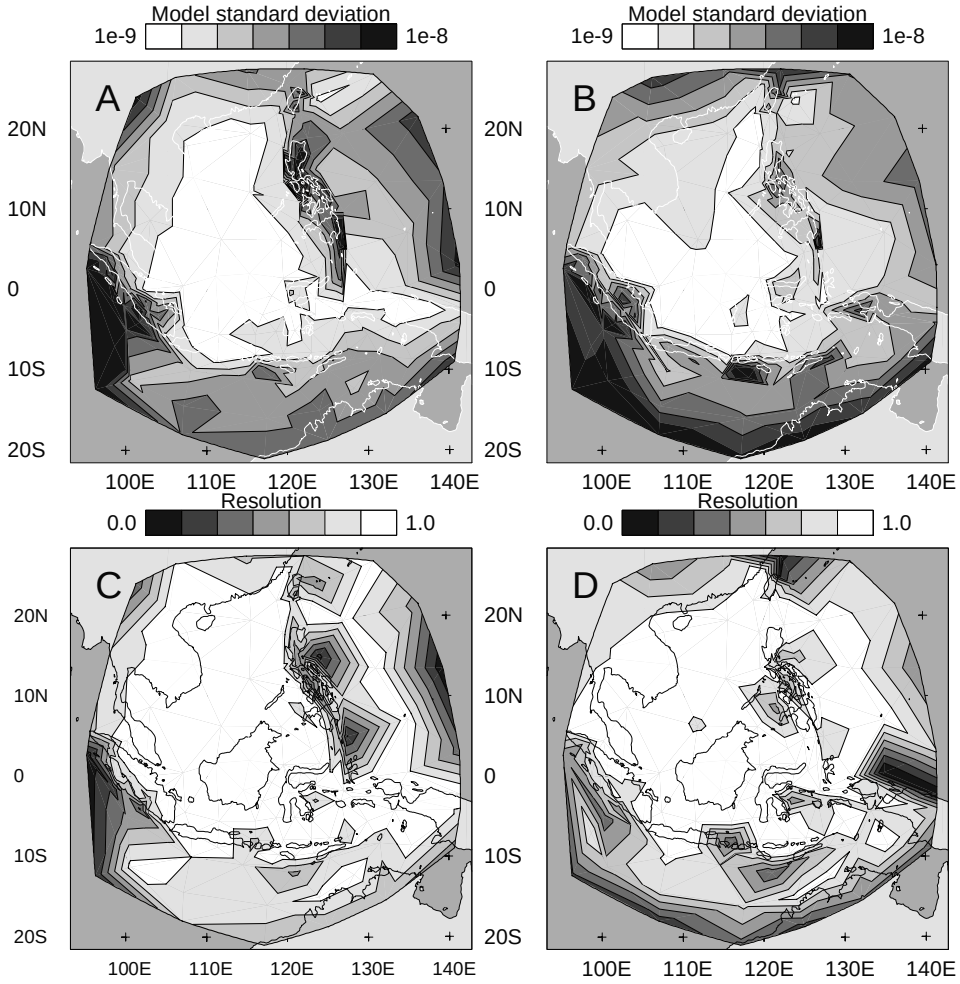

Figure 4.8: Model error and resolution of solution I with $\sigma_r = 3.3 \cdot 10^{-10}$(m yr)$^{-1}$, $\alpha_a = 5.0 \cdot 10^7$ and $\alpha_d = 3.0 \cdot 10^6$; Contouring of (A) $\sqrt{C_{ii}}$ and (B) R_{ii} pertaining to the $v_{\theta\theta}$ component; (C) and (D) see subscript for (A) and (B), respectively, pertaining to the $v_{\theta\phi}$ components.

slip vector $\boldsymbol{s} = (s_\theta, s_\phi)$. While tuning the variance factor σ_r for the extra $\boldsymbol{\nabla} \times \boldsymbol{\nabla v} = \mathbf{0}$ constraints and the regularization parameters α_a and α_d we primarily focus on obtaining solutions that are well resolved in combination with acceptable model errors and a small data misfit ($\chi^2 \approx 1.0$.)

While performing inversions I and II, without application of any form of regularization, separate computation of χ^2 for the data and the $\boldsymbol{\nabla} \times \boldsymbol{\nabla v} = \mathbf{0}$ constraints shows that both data parts have a χ^2 of 1.0, which for the latter was obtained using a standard deviation of

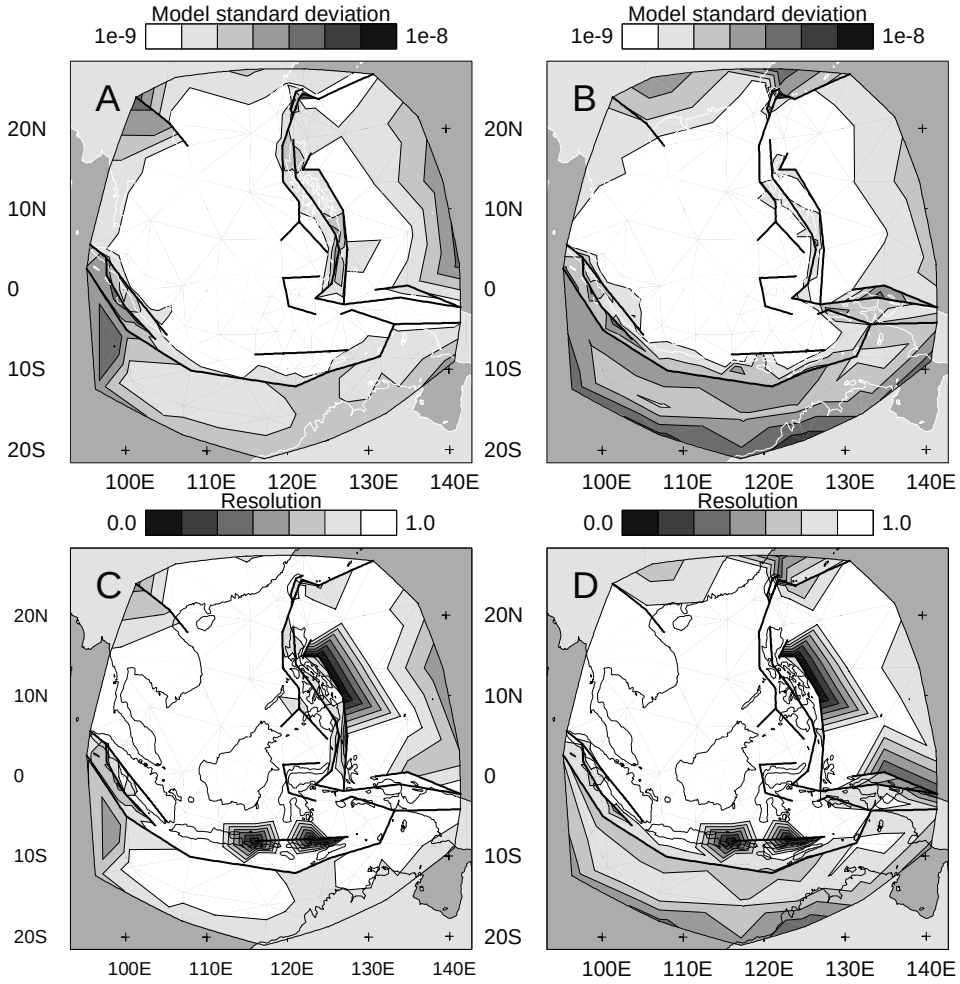

Figure 4.9: Model error and resolution of solution II with $\sigma_r = 0.2 \cdot 10^{-10}$(m yr)$^{-1}$, $\alpha_a = 5.0 \cdot 10^7$ and $\alpha_d = 1.0 \cdot 10^6$; See the caption of figure 4.8.

$\sigma_r = 3.3 \cdot 10^{-10}$(m yr)$^{-1}$ for inversion I and $\sigma_r = 0.2 \cdot 10^{-10}$(m yr)$^{-1}$ for inversion II. Both resulting solutions still contain roughness possibly related to solution components pertaining to small eigenvalues. Regularization with amplitude damping and second derivative damping on all nodes is imposed by constraining $\alpha_a \boldsymbol{I}\boldsymbol{p} = \boldsymbol{0}$ and $\alpha_d \boldsymbol{D}\boldsymbol{p} = \boldsymbol{0}$, respectively, with $\boldsymbol{p}$ the model vector with the components of $\boldsymbol{\nabla v}$. Mild amplitude damping already reduces the larger variances. Additional second derivative damping reduces the roughness of solutions I and II at small spatial scales. Compared to inverse problem II inverse problem I requires stronger second derivative regularization to control the model variance. The

Data	Solution	lo	la	ω (°/Ma)
Bock et al. [2001]	I	121.3°E±0.1	26.3°S±1.0	0.21±0.01
	II	119.4°E±0.2	24.8°S±1.0	0.21±0.01
Kato et al. [1998b]&	I	57.0°W±0.1	18.9°S±0.2	0.22±0.01
Yu et al. [1999]	II	58.7°W±0.1	22.4°S±0.1	0.20±0.01

Table 4.4: Residual rotation vectors of the extra data sets with respect to the main set of Matheussen [2000] for solutions I and II. Key: lo, longitude; la, latitude; ω, rotation rate.

damping slightly impairs the spatial resolution, but still leads to an acceptable data misfit with $\chi^2 = 2.4$ for solution I and $\chi^2 = 1.5$ for solution II (table 4.4). The part of solution II belonging to fault slip is not subject to any form of damping.

Figures 4.8 and 4.9 show results for model standard deviations $\sqrt{\boldsymbol{C}_{ii}}$ and diagonal components of the resolution matrix $\boldsymbol{R}_{ii}$ (see chapter 2) for the $v_{\theta\theta}$ and the $v_{\theta\phi}$ components of solutions I and II, respectively. In general, for both solutions the areas of relatively large standard deviation and relatively low resolution are mainly located at the boundaries of the model. Model error and model resolution of solution II are better compared to solution I. This results from the parameterization of fault slip, which not only enables the a larger degree of freedom to fit relative velocities by fault motion but also requires extra model nodes along fault traces. However, both $v_{\theta\theta}$ and $v_{\theta\phi}$ components of solution II at some individual nodes along the Philippine trench and along the Flores and Wetar backarc thrusts are less well resolved. The resolution of the fault slip model parameters is acceptable (table E.2). The standard deviations for the fault slip solution reach a maximum at the western extension of the Semangko fault of 5 and 12 mm/yr in longitude and latitude direction, respectively. For the remaining part of the slip solution model errors range between 1 and 3 mm/yr and are listed in table E.2 per fault segment.

The misfit vectors shown in figure 4.10 result from subtracting the velocity data from the velocities predicted by solutions I and II, respectively, at the sites of observation. Relatively large misfits at Sumatra and Taiwan are mainly due to the high data density compared to the size of the triangles (figures 4.10B and D).

Local misfit vectors exceeding the data error ellipses demonstrate that our parameterization is occasionally too coarse for modeling local detail. We set out for modeling regional scale variation in $\boldsymbol{\nabla v}$ and $\boldsymbol{s}$. The consequence of this somewhat conservative approach is a data misfit which is slightly larger than $\chi^2 = 1$.

The results of solution I and II for the residual rotation vectors between different velocity data sets, given as Euler poles in table 4.4, are slightly different. In solution I the rotation vector found for the data set of Bock et al. [2001] produces residual velocities between 7 mm/yr at Christmas Island and 14 mm/yr at the westernmost site on Sumatra. The rotation vector found for the data of Kato et al. [1998b]; Yu et al. [1999] produces residual velocities between 2 mm/yr at and 4 mm/yr at Taiwan and Luzon, 5 mm/yr at Palawan, 6 mm/yr at the Philippine Sea plate with a maximum of 16 mm/yr at Cocos island. For solution II these rates differ on average less than a mm/yr with a maximum of 1 mm/yr at Cocos Island. The remaining velocities of solution II (i. e. the velocities that determine the deformation field)

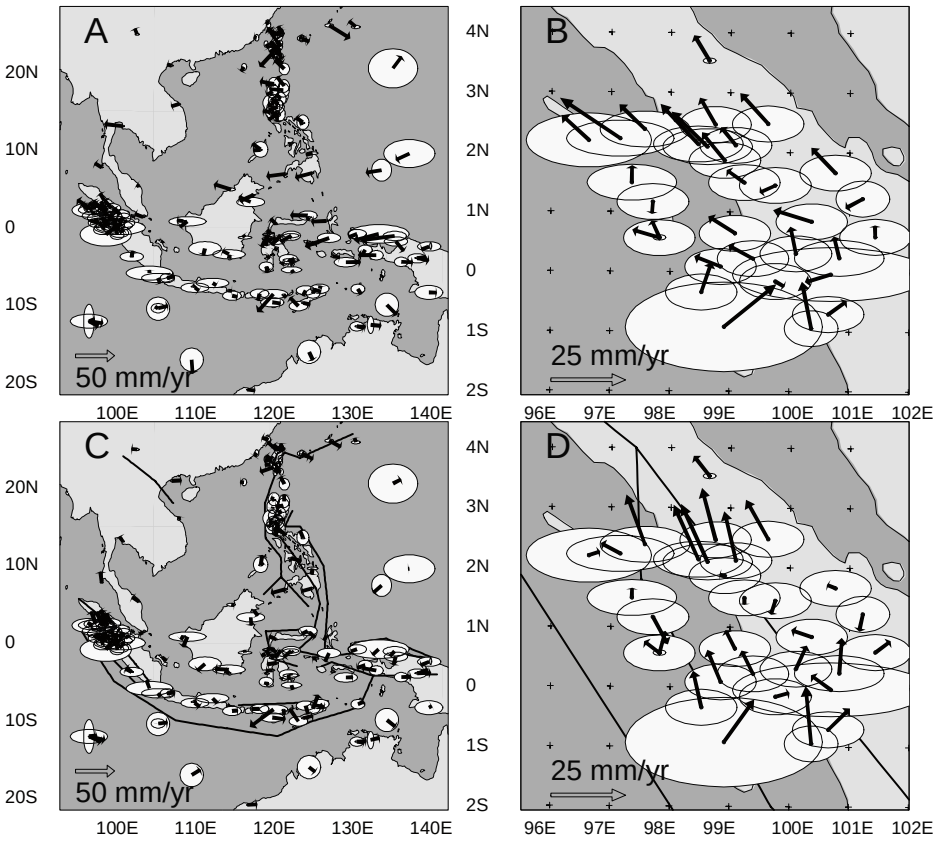

Figure 4.10: Misfits between data and velocity vectors predicted by solution I for (A) the whole model area and (B) Sumatra. Figures (C) and (D) show the misfits predicted by solution II. The ellipses indicate the 3σ-errors of the data. The straight lines in (C) and (D) indicate the fault segmentation of solution II.

are listed in table D.1.

4.5 Solutions

4.5.1 Fault motion

Comparison of solutions I and II and discussion of the differences between the two is not straightforward because of the fundamentally different mechanisms applied to accommodate relative velocities. Therefore, we describe the slip part of solution II before we discuss the solutions for the velocity gradient field of solution I and II to investigate the influence of inclusion of fault segmentation. The fault slip solution is shown in figure 4.11. The

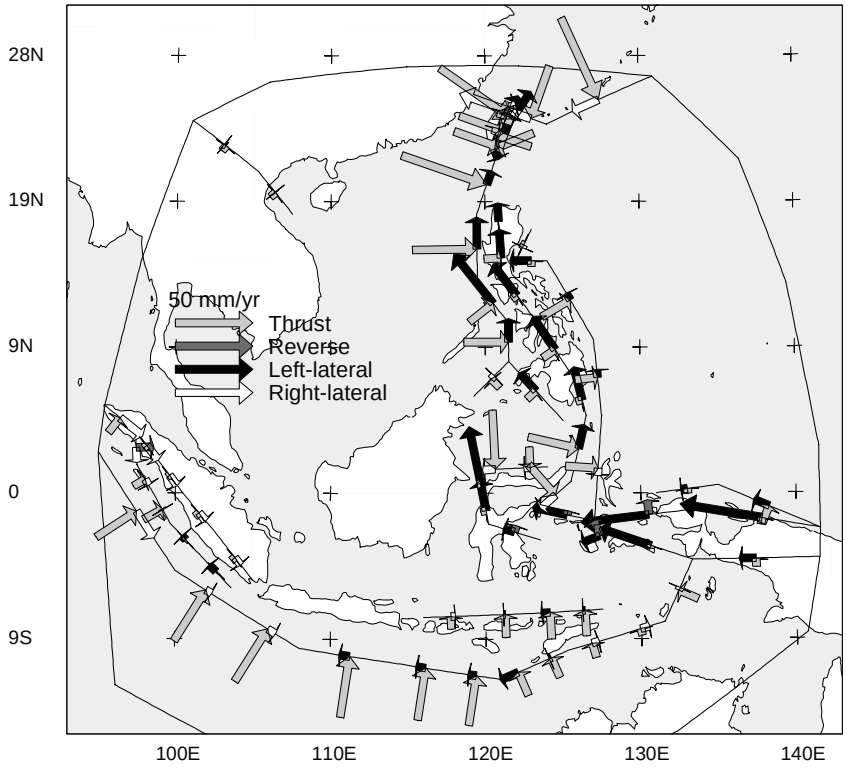

Figure 4.11: Fault slip rate vectors of solution II; the arrows denote the fault-parallel and fault-perpendicular components of the slip vector.

quantitative fault slip rates are listed in table E.2.

At Sumatra part of the arc-perpendicular component of plate motion is accommodated as thrusting on the plate interface of the Sunda arc and on the northern segments of the Mentawai fault. Part of the arc-parallel component of relative plate motion is taken up on the plate boundary, along the Semangko and Batee faults in the form of dextral slip motion and along the Mentawai fault as sinistral slip motion. The Java trench accommodates shortening with relatively small dextral and sinistral components. The thrust component decreases in eastward direction on the Timor and Aru troughs. Along the Banda arc part of the oblique component of relative plate motion appears as sinistral shearing on the plate interface. Shortening is also manifested at the Flores and Wetar backarc segments.

Irian Jaya is dominated by strike-slip regimes. Sinistral motion on the New Guinea trench, Sorong-Yapen-Ransiki fault zone, Seram trough and Tarera-Aiduna fault zone accommodates a large amount of relative motion between the Philippine Sea plate and Australia. Relatively small components of thrust motion are found on the New Guinea trench and on the Yapen-Ransiki segments. We find small normal slip contributions on the Sorong

segment and the Seram trough. The Palu-Koro-Matano fault system in Sulawesi behaves as a purely sinistral fault. Thrusting on the North Sulawesi trench decreases from west to east.

The part of relative plate motion between the Philippine Sea plate and Eurasia that is accommodated as discrete motion at the Molucca Sea is distributed between the Halmahera and Sangihe trench. Thrusting at the Philippine trench remains relatively uniform from south to north, while thrust motion at the Cotabato-Negros-Manila trench system gradually increases from south to north. Part of the oblique component of relative plate motion is taken up by the Philippine fault system and at the Cotabato-Negros-Manila trench system. This sinistral and contractional fault motion regime continues northward into Taiwan, where it is transferred onto the Longitudinal Valley fault and the plate interface between the Philippine Sea plate and Eurasia. The Ryukyu trench is characterized by dextral thrust motion.

4.5.2 Strain and rotation rates

The symmetric part of ∇v represents the strain rate tensor, the anti-symmetric part represents the rotation rate tensor. In figures 4.12 and 4.13 we plot the principal axes of the strain rate tensor of solution I and II, respectively. Figures 4.14A and B show the rotation rates of solution I and II, respectively.

In solution I the Sunda arc appears as a broad zone of strong contraction especially around the trench south of Java. Strong contraction continues to the northwest along the Sumatra trench and affects some parts of the Sumatran fore- and backarc region. The Sumatra region is subject to a clockwise rotation rate regime. The continuation of the zone of contraction to the east is characterized by a gradual shift from the forearc at the Java trench to the backarc Banda basin east and north of Timor. The western Timor forearc, the northern part of the Banda arc curvature, western Sulawesi and western Irian Jaya rotate in a counterclockwise direction. In Sulawesi we find a predominantly extensional regime and a zone of clockwise rotation rates north and northeast of the North Sulawesi trench. The strong shortening in E-W direction just south of the Philippines, present in the velocity data (figure 4.4A), appears as contraction concentrated at the Halmahera and Sangihe trench system. West of Luzon the Manila trench is represented by contraction. The Philippine Sea plate shows significant internal deformation. Besides contraction and clockwise rotation of its northern part, a counterclockwise rotation rate regime dominates the southern part.

Differences between solution I and II can immediately be recognized from comparing 4.12 with 4.13 and 4.14A with 4.14B. The accommodation of discrete fault motion in solution II considerably decreases the magnitude of the strain and rotation rates with respect to solution I. Strain and rotation rates of solution I show a relatively strong velocity gradient field at the interiors of the plates, whereas the main deformation features in solution II are located in the plate boundary zones.

The relation between fault motion and strain rates follows from comparison between figures 4.12 and 4.13. A large part of the contraction south of the Sumatra and Java trenches in solution I is taken up by discrete thrust motion on the Sunda arc in solution II. Relatively strong contraction at the Celebes and Molucca Seas, the southern Philippines and west of the Negros and Manila trenches in solution I has diminished in solution II due to the accommodation of thrust motion on the parameterized fault and plate boundary zones. Furthermore,

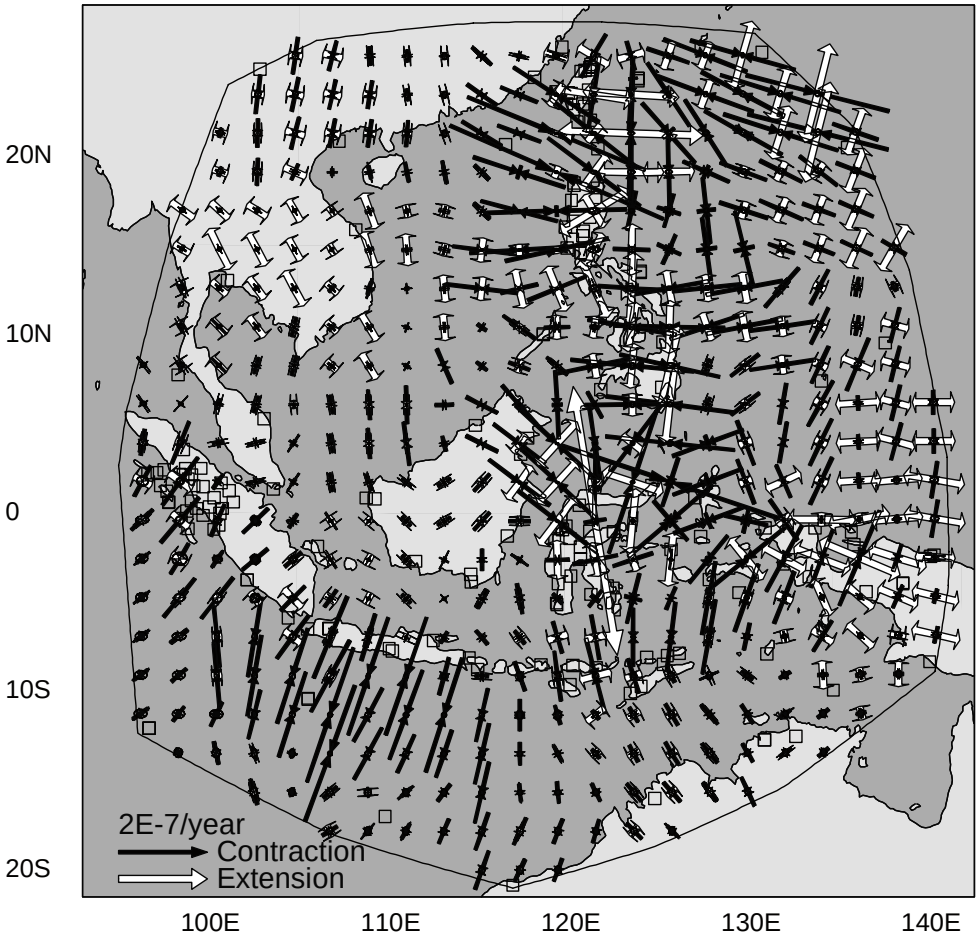

Figure 4.12: Principal strain rates of solution I computed on a regular grid. The open squares represent the station positions.

strike-slip on the Palu-Koro fault in Sulawesi, the Philippine fault and the Sorong-Yapen-Ransiki fault in solution II considerably reduce the shear strain rates found at these regions in solution I.

The relation between fault motion and rotation rates becomes apparent from comparing figures 4.14A and B. The accommodation of dextral slip on the Semangko fault reduces the magnitude of the clockwise rotation phase in Sumatra in solution I (figure 4.14B). The relatively strong counterclockwise rotation rate regimes at Irian Jaya and along the Palu-Koro fault system in solution I have disappeared in solution II due to the sinistral fault motion accommodated by the fault systems in these regions. The counterclockwise rotation rates at the southern part of the Philippine Sea plate in solution I are minimized in solution II,

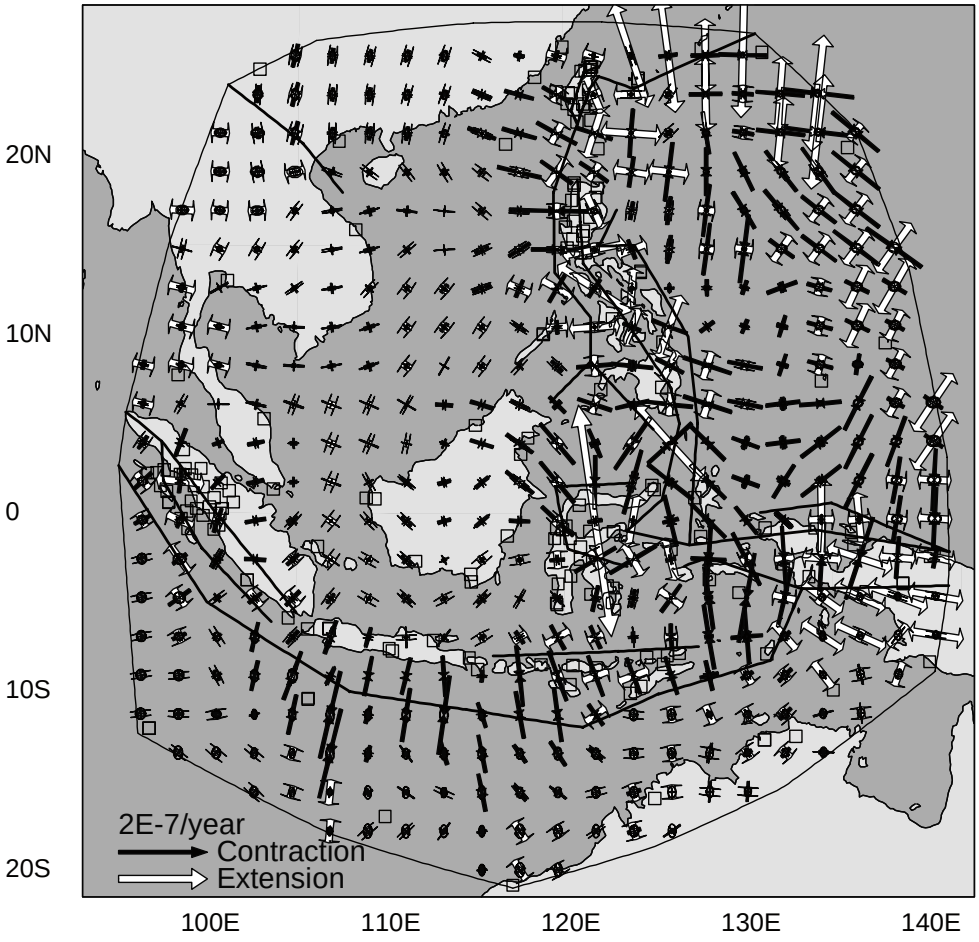

Figure 4.13: Principal strain rates of solution II computed on a regular grid. The open squares represent the station positions.

because of plate rotation by the sinistral motion along the New Guinea trench, the Sorong-Yapen-Ransiki and Philippine fault systems.

Solution I does not provide information about the partitioning of relative plate motion between discrete fault motion, strain and rotation rates at the plate boundaries. Rotation rate regimes in a continuous ∇v field are either indicative for strike-slip motion in broad fault zones or for rotations of (micro-)blocks. Furthermore, whether contraction and extension in solution I are localized on faults or plate boundaries or distributed over larger-scale regions does not become evident. This relates directly to the spatial sparseness (except for some regions) of the data set. Inversion for ∇v and s, on the other hand, enables the accommodation of localized motion on faults or plate boundaries and offers insight in the distribution

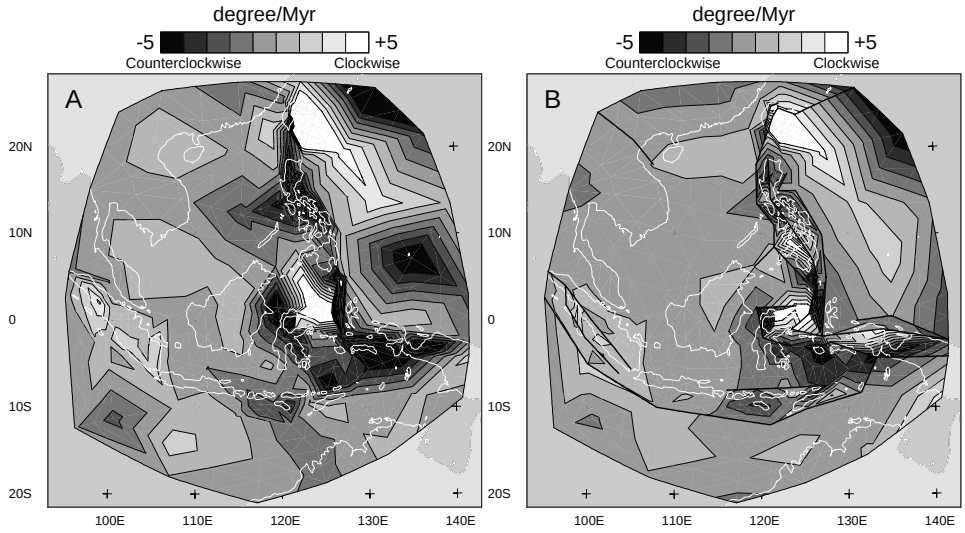

Figure 4.14: Rotation rates of solution (A) I and (B) II, scaled to degrees per Myr.

of deformation in terms of slip, (micro-)block rotation and strain rates. Whether this fault motion has taken place during the time interval of the measurements, will not become evident. In general, distinguishing fault locking from fault slip is difficult, because the velocity data set is spatially sparse and most observations are obtained in the far-field of fault zones. Solution I would be closest to a deformation field in which all faults are locked whereas in solution II faults are free to slip. In particular, fault slip in solution II can result from relative crustal block motion projected on faults as slip (which may not have occurred in actuality because of fault locking). In the remainder of this chapter we will concentrate on solution II.

4.5.3 Trade-off between ∇v and s

To investigate the extent to which components of slip rate and the velocity gradient field are independently resolved in solution II we inspect the columns of the resolution matrix $\boldsymbol{R}$. The i-th column of $\boldsymbol{R}$ indicates how a certain amplitude a assigned to parameter i (with unit vector $\boldsymbol{e}_i$) is smeared over the solution $\boldsymbol{m}_i$, hence $\boldsymbol{m}_i = \boldsymbol{R} \cdot a\boldsymbol{e}_i$. This is investigated for selected model parameters associated with the Flores backarc thrust, where we find relatively low model resolution (figures 4.9C and D). Figures 4.15A, C and E show model estimate $\boldsymbol{m}_i$ for the velocity gradient component $v_{\theta\theta}$ with amplitude $a = 10^{-7}$/yr at a node located directly at the north-side of the Flores thrust.

Figures 4.15B, D and F show $\boldsymbol{m}_i$ for the velocity gradient component $v_{\theta\theta}$ with amplitude $a = 10^{-7}$ m/yr at a node along the Philippine trench in the Philippine Sea plate, which is weakly resolved according to figures 4.9C and D. Note the difference in contour and y-

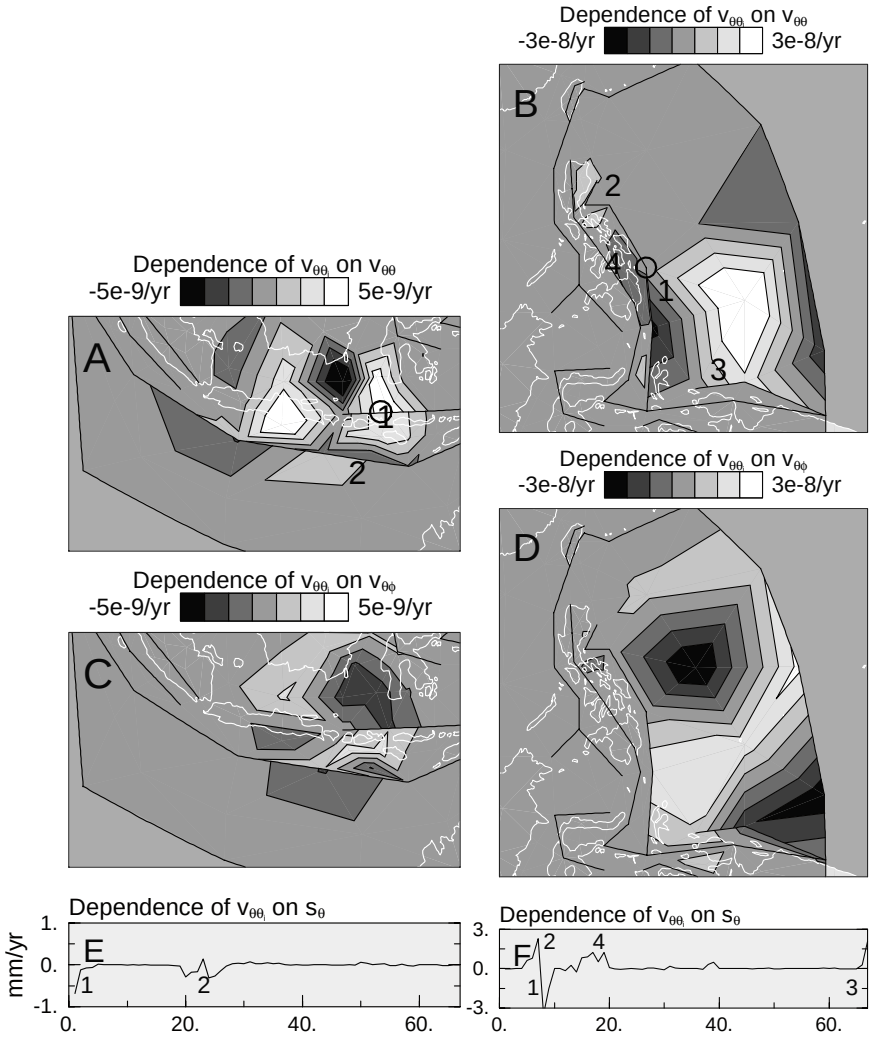

Figure 4.15: Two model estimates $\boldsymbol{m}_i$ at the Flores and Wetar back arc thrust zone (A, C, E) and at the Philippine Sea Plate (B, D, F) resulting from multiplication of the resolution kernel $\boldsymbol{R}$ of solution II with $a\boldsymbol{e}_i$: $\boldsymbol{m}_i = \boldsymbol{R} \cdot a\boldsymbol{e}_i$, with $a = 10^{-7}$/yr on node i, indicated by the open circle in (A) and (B). The contouring denotes (A) and (B) $\boldsymbol{v}_{\theta\theta}$; (C) and (D) $\boldsymbol{v}_{\theta\phi}$; and (E) and (F) $\boldsymbol{s}_\theta$. In figure (A) the value of $\boldsymbol{m}$ at the location of node i exceeds the limits imposed by the plots and approaches the value of a. For (E) and (F) the horizontal axis indicates the number of the slip parameters. The numbers in (E) and (F) refer to slip parameters associated with fault segments indicated by corresponding numbers in (A) and (B).

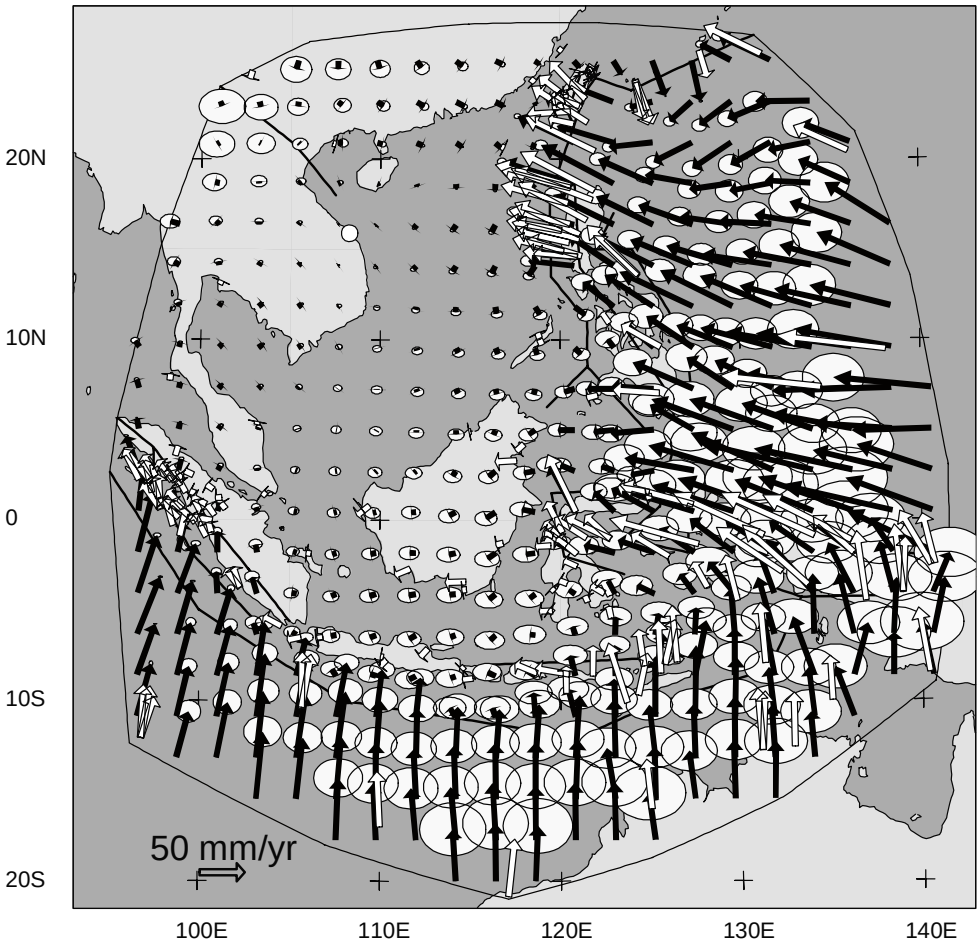

Figure 4.16: The black arrows indicate the velocity field predicted by solution II on a regular grid, with respect to a station (white dot at approximately 108°E, 17°N) in Sundaland. The white arrows indicate the velocity data used in the inversions.

axis limits between A, C, E and B, D, F. For this $v_{\theta\theta}$ component we find a strong trade-off between $v_{\theta\theta}$ and $v_{\theta\phi}$ components on the Philippine Sea plate and s_θ components on the Philippine trench, the Philippine fault and the New Guinea trench. Similar results are found for the two, weakly resolved nodes located more to the north along the Philippine trench on the Philippine Sea plate (figure 4.9C).

4.5.4 Velocity field

Figure 4.16 represents the velocity field predicted with respect to a station in Sundaland. For this representation we perform a forward computation of the solution to determine the velocity vector on the nodes of the grid with respect to a reference station (where the velocity is zero). We find that relatively small velocities delineate Sundaland including the southern part of Sulawesi. The velocity field across the Sunda arc at Java shows an abrupt transition from predominantly north directed velocities to relatively small WSW directed velocities, whereas the forearc of Sumatra, between the Sumatra trench and the Semangko fault still accommodates a considerable N-S component. The magnitude of the velocity field north of the Semangko fault is of the order of the velocities in Sundaland. At the transition from the Sunda to the Banda arc, at the island of Sumba ($\sim$120°E), the character of the plate boundary between Sundaland and Australia changes. The N-S component of the velocity field at the forearc increases from Sumba to the eastern Banda Sea, where its magnitude is of the order of the northern Australia velocity field. The predominant amount of relative plate motion between Australia and Sundaland at the longitude of Timor ($\sim$125°E) is now mainly accommodated by the Wetar backarc thrust fault. Across the Tarera-Aiduna fault system and the Seram trough in Irian Jaya the westward component of the velocity field increases from south to north, reflecting accommodation of the predominantly E-W directed motion of the Philippine Sea plate with respect to Sundaland. The velocity field of Sulawesi shows an increase of NNW directed motion from south to north, until it reaches a maximum just south of the North Sulawesi trench.

The velocity field of the Philippine Sea plate shows large spatial variations, which we attribute to the poor data constraints on its internal deformation. We note that, although the spatial resolution for the interior of the Philippine Sea plate is relatively good (figures 4.9C and D), one should realize that this results from the relatively large triangles used here. Hence, solution and predicted velocity field can only be trusted, if the actual velocity gradient field of the real crust would vary linearly over the triangles adopted in our parameterization. A parameterization with smaller triangles would readily lead to severe lack of resolution in the interior of the Philippine Sea plate, because of lack of data, and allow for an alternative flow pattern.

The E-W shortening between the Philippine Sea plate and Sundaland at the Molucca Sea is almost completely accommodated at the relatively narrow Halmahera and Sangihe trench systems. Across the islands of Mindanao and Visayas the predominant amount of E-W shortening is accommodated east of and within the Philippine Mobile Belt, whereas at Luzon its E-W component is absorbed west of the Philippines at the Manila trench system. The transition between the velocity fields of the Philippine Sea and Eurasian plates at the Taiwan region is spread out over a large area south of the Ryukyu trench.

4.6 Discussion of the solution per region

In the next sections we discuss the results for the Southeast Asian deformation field of solution II per region. Table E.1 gives an quantitative overview of estimates for strain and rotation rates and motion accommodated by faults and plate boundaries found in the litera-

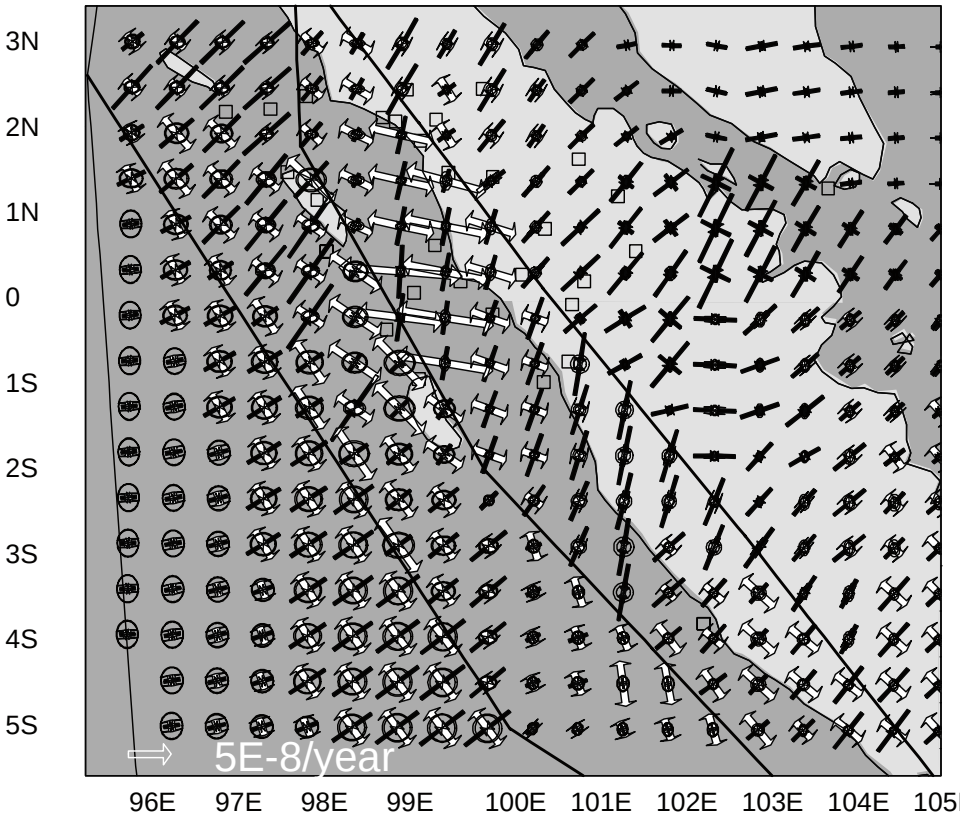

Figure 4.17: Principal strain rates with error ellipses of solution II computed on a regular grid at Sumatra. White arrows indicate extension, black arrows indicate contraction. The open squares represent the station positions.

ture on Southeast Asia. Slip rates of solution II are listed in table E.2. Although for some regions we compare our results with results of studies based on the same GPS data as are incorporated in our data set, the difference in methodology applied makes a comparison worthwile.

4.6.1 Western Sunda arc

West of Thailand we find E-W extension, which is consistent with the direction and the presumed present-day activity of the opening of the Andaman Sea [e.g., Curray et al., 1979; Guzmán-Speziale and Ni, 1996].

The recent release of a dense Sumatra GPS data set [Genrich et al., 2000; Prawirodirdjo et al., 2000] has led to a series of detailed studies of the deformation field of Sumatra between 3°S and 3°N [Genrich et al., 2000; McCaffrey et al., 2000; Sieh and Natawidjaja,

2000]. The results of these studies and the inclusion of the Bock et al. [2001] data set, in which a reduced version of the Sumatra data set is incorporated, in this study enables to compare the Sumatra deformation field resulting from the application of our inversion method in somewhat more detail.

McCaffrey et al. [2000] use a finite element model to produce a continuous $\nabla \boldsymbol{v}$ field of the Sumatran fore- and backarc. They find that the arc-normal component of relative plate motion between Australia and Eurasia is distributed over the forearc between the trench and the Semangko fault in the form of arc-normal contraction. In our solution a large component of shortening is accommodated on the plate interface. Thrust slip motion on the northern segments of the Mentawai fault, not incorporated in the study of McCaffrey et al. [2000], concentrates arc-normal contraction to the region around the trench and between the trench and the northern part of the Mentawai fault (between 3°S and 3°N; figure 4.17). The small variation around 0.5°S in the orientation of the principal axes in the forearc will be discussed later in this section. The southern part of the Mentawai fault does not accommodate thrust slip motion, resulting in arc-normal contraction between the southern segments of the Mentawai and the Semangko faults. The different distribution of strain at this part of Sumatra may be due to the sparser data density with respect to northern Sumatra (figure 4.4B). Furthermore, we also find a significant component of arc-normal contraction in the backarc east of the Semangko fault, in contradiction with the results of Genrich et al. [2000] and McCaffrey et al. [2000], who predict very small deformation rates for this region. This discrepancy may be explained by the more regional approach of this study, in which the Sumatra deformation field is constrained by data throughout the whole Southeast Asian region.

Geological, seismic and geodetic data suggest that dextral strike-slip on the Semangko fault accommodates a considerable percentage of the arc-parallel component of relative plate motion between Australia and Eurasia [e.g., Fitch, 1972; Jarrard, 1986; McCaffrey, 1991; Bellier and Sébrier, 1995]. Estimates of its slip based on GPS measurements and interplate earthquake slip vectors differ from estimates based on geology. An elastic dislocation model of the Semangko fault [Genrich et al., 2000] (with a locking depth of 15 km) and a kinematic analysis of interplate earthquake slip vectors [McCaffrey et al., 2000] estimate relatively uniform slip rates of the order of 25 mm/yr between 1°S and 3°N. Geological observations reveal a slip rate increasing from 6 mm/yr just west of the Sunda Strait, ∼11 mm/yr at 1°S to ∼25 mm/yr at northern Sumatra [Sieh et al., 1991, 1994; Bellier and Sébrier, 1995]. The discrepancy between geodetic and geological estimates is explained by the different time-intervals for which the data are representative; an increase of slip along the southern segments of the Semangko fault system must then have taken place within the last few Myr [Sieh and Natawidjaja, 2000]. As the orientations of earthquake slip vectors are not exactly normal to the Sumatra trench, displacement along the thrust plate interface and within the forearc must take up part of the arc-parallel component [Fitch, 1972; Jarrard, 1986]. McCaffrey et al. [2000] infer that the slip rate on the Semangko fault is ∼2/3 of the full trench-parallel component of relative plate motion and assign the missing arc-parallel shear to extension of the forearc region. Both arc-parallel extension in the forearc and the geological estimate of a varying strike-slip component on the Semangko fault have been associated with the northward increasing obliquity of convergence. Increase of obliquity in

combination with coupling between the forearc and the subducting slab forces the forearc to stretch in a direction parallel to the margin and increases the forearc motion relative to the subducting plate [McCaffrey, 1992, 1996]. On the other hand, the recent discovery of the Mentawai fault at the outer-arc ridge off Sumatra [Diament et al., 1992] provides an entirely rigid alternative to the extension of the Sumatran forearc. If this fault is moving in a dextral sense, the Sumatra sliver plate can be seen as decomposed of several strips [Diament et al., 1992; Bellier and Sébrier, 1995; Malod and Kemal, 1996]. However, it remains questionable whether the Mentawai fault plays a major role in accommodating dextral slip, since a variety of surface deformation data reveal recent subduction-driven contraction at the outer margin of the forearc [Samuel and Harbury, 1996; Genrich et al., 2000]. This observation is also found in our solution.

The arc-parallel component of relative plate motion is accommodated by several types of deformation in solution II. The slip rate of 10 ± 1 mm/yr on the Batee fault agrees with estimates of Bellier and Sébrier [1995] and Malod and Kemal [1996]. We find an increase of the slip rate accommodated by the Semangko fault system of 6 ± 1 mm/yr on southern segments (5°S) via 10 ± 3 mm/yr on central segments (1°S - 1°N) to 20 ± 5 mm/yr on the northern segment (3°N). The rates are consistent with geological estimates [Sieh et al., 1991, 1994; Bellier and Sébrier, 1995], however lower than the geodetic estimates for slip at depth based on elastic dislocation modeling. An explanation for the latter disagreement could be the high data density closely around the Semangko fault (the distance between fault trace and nearest stations is of the order of a few km), which in our solution reduces the trade-off between fault slip and the velocity gradient to represent the actual, present-day deformation field at the Earth's surface. Indicative for a (partly) locked fault is the shear strain rate regime near the fault trace north of 0.5°S, which can associated with elastic loading effects. The absence of extension along the central segments of the Semangko fault (between 3°S and 0.5°S), also found by McCaffrey et al. [2000]; Genrich et al. [2000] and Sieh and Natawidjaja [2000], shows that the fault takes up a large part of the arc-parallel component here.

In contradiction with the derivation of McCaffrey et al. [2000] we find that only an average of 25% of arc-parallel relative plate motion is accommodated by the Semangko fault system. The remaining part of arc-parallel plate motion is accommodated by dextral slip motion on the plate interface and extension in the forearc. The dextral slip motion on the plate interface increases from 7 ± 1 to 25 ± 2 mm/yr from south to north. These rates are within the margins imposed by predictions of arc-parallel slip on the plate interface based on deflection angles of earthquake slip vectors and estimates of the arc-parallel component of relative plate motion [McCaffrey, 1996; McCaffrey et al., 2000]. North of 3°S the predominant amount of arc-parallel extension occurs in the forearc sliver plate, as predicted by Bellier and Sébrier [1995]. South of 3°S arc-parallel extension is accommodated east of the Mentawai fault on the Sumatran mainland. Finally, we find a clockwise rotation rate of a few degrees/Myr of the Sumatran fore- and backarc (figure 4.14D). Clockwise rotation of the Sumatra region has also been proposed by Bellier and Sébrier [1995] as a mechanism for the accommodation of arc-parallel relative plate motion.

Strain rates across the Sumatra trench west of the Mentawai fault between 3°S and 0.5°S do not show a change in orientation; extension and contraction have arc-parallel and

arc-normal orientations, respectively. North of 0.5°S the orientations of contraction and extension in the forearc show a small angular change to NNE-SSW and WNW-ESE, respectively. This difference between the northern and southern parts of the Sumatra trench is also found by Prawirodirdjo et al. [1996], who explain this observation by almost complete coupling of the forearc to the subducting plate south of 0.5°S and half as much to the north.

The deformation field of solution II shows arc-normal contraction at the Java trench and thrust motion of ∼45 mm/yr. The sinistral slip component of a maximum of 9 mm/yr accommodated on the Java trench is within the estimate of McCaffrey [1996], based on deflection angles of earthquake slip vectors. The Java forearc does not show significant arc-parallel extension, which suggests that the arc-parallel component of relative plate motion is entirely taken up by the plate interface.

4.6.2 Eastern Sunda arc and Banda arc

We find that the predominant amount of relative plate motion is accommodated north of the Timor trough, at the Timor forearc and the Flores and Wetar backarc thrusts. Deformation of the Timor backarc is relatively weak. Although the slip motion accommodated at the Banda arc south of Timor is reduced considerably with respect to the western segments of the Banda arc (figure 4.11), our solution suggests that there is still shortening occurring between Australia and the Timor forearc. This contradicts the conclusion of Audley-Charles [1986] and Snyder et al. [1996], based on seismic reflection profiles, of Kreemer et al. [2000], based on a combination of GPS and earthquake moment tensors (see section 4.7), and of geological studies by Johnston and Bowin [1981] and Charlton [1986], that the Timor forearc has become part of the Australia plate. However, it confirms the conclusion of Karig et al. [1987], also based on seismic reflection profiles, that accretion of Timor island arc terrain to the northern margin of the Australia plate has not yet been entirely completed. Our average rate of ∼10 mm/yr of shortening is only slightly higher than the careful limit of $<$10 mm/yr posed by Genrich et al. [1996] based on GPS. Internal deformation of the Timor forearc is also represented by sinistral slip motion on the western margin of the Banda arc and shear strain rates (although relatively poorly resolved, figures 4.9C and D). These types of deformation together with counterclockwise rotation rates found at Sumba and Timor (figure 4.14D) were also recognized from earthquake slip vectors [McCaffrey, 1988] and GPS [Genrich et al., 1996] and may be indicative for the interacting sinistral NE oriented strike-slip faults in the Timor forearc described by Breen et al. [1989].

The counterclockwise rotation rates, found in the eastern Banda Sea, could indicate block-like motion of this region. Although the orientation of rotation agrees with young paleomagnetic data of Haile [1978] on Seram, we have to be careful using this result as a verification of our solution, since it is based on one site only and may be a very local rotation (*Robert Hall, 2001, personal communication*).

4.6.3 Irian Jaya

According to Abers and McCaffrey [1988] and McCaffrey and Abers [1991] the Sorong-Yapen-Ransiki and the Tarera-Aiduna fault systems almost completely accommodate the

arc-parallel component of Australia-Pacific relative motion of a total of about 100 mm/yr in the form of sinistral slip divided over both systems at a ratio of 80 and 20 mm/yr, respectively. These are averaged, long-term slip rates. We find sinistral slip at rates of 53 mm/yr on the Sorong-Yapen-Ransiki fault zone and 10 mm/yr on the Tarera-Aiduna fault system. The relatively strong shear strain rates in the New Guinea Highlands account for the remaining part of the arc-parallel relative plate motion [Abers and McCaffrey, 1988]. In our solution the Seram trough, parameterized as the westward continuation of the Tarera-Aiduna fault zone, takes up part of the relative plate motion as sinistral slip at a rate of 36 mm/yr.

We find thrust motion of the order of 12 mm/yr on the eastern segment of the New Guinea trench and almost no arc-perpendicular motion on the western segment. These slip results agree with the conclusion of Ekström and England [1989] and Milsom et al. [1992], that the western side of the New Guinea trench is inactive, and with the conclusion of Hamilton [1979] and Puntodewo et al. [1994], that at the eastern side of the New Guinea trench subduction is taking place in southward direction. However, resolution of the $v_{\theta\phi}$ component (figure 4.9) shows that the N-S component of deformation at the New Guinea trench and at northern Irian Jaya is relatively poorly determined. Similarly, the resolution of slip motion on the New Guinea trench is relatively poor. This provides an explanation for the extension between the trench and the Sorong-Yapen-Ransiki fault, which then may be considered as a compensation for the thrust motion on the New Guinea trench.

We find a clockwise rotation rate regime around the Sorong-Yapen-Ransiki fault system in northern Irian Jaya, where paleomagnetic observations along the Sorong-Yapen-Ransiki fault system do not agree on one uniform rotation pattern [Ali and Hall, 1995].

4.6.4 Sulawesi

At the east relative to the west of the North Sulawesi trench a smaller amount of thrust motion is accommodated, because of the clockwise rotation of the north arm of Sulawesi [Silver et al., 1983a; Surmont et al., 1994]. Accordingly, at the North Sulawesi trench we find clockwise rotation rates in northern Sulawesi (figure 4.14B) and pure thrust motion on the North Sulawesi trench with magnitudes of 13 mm/yr in the east and 38 mm/yr in the west. These rates closely agree with estimates of Stevens et al. [1999]. The maximum rate lies between the predictions of average long-term shortening across the trench system of 30 and 50 mm/yr of Jarrard [1986] and Silver et al. [1983a], respectively. We find purely sinistral slip on the Palu-Koro and Matano faults, consistent with geologic and geodetic observations [Silver et al., 1983a; Walpersdorf et al., 1998; Stevens et al., 1999]. Rates range between 8 on the Matano and 38 mm/yr on the Palu-Koro fault. Like the Semangko fault, the Palu-Koro fault is densely sampled by stations (with on average only a few km distance between fault trace and nearest stations). However, unlike the results for the Semangko fault, slip rates for the Palu-Koro fault in solution II closely agree with predictions based on elastic dislocation models [Stevens et al., 1999; Walpersdorf et al., 1998]. This may be explained by the difference in locking depths inferred for both faults, i.e. 15 km for the Semangko fault [Genrich et al., 2000] and 4.5 km [Stevens et al., 1999] or 12 km [Walpersdorf et al., 1998] for the Palu-Koro fault. In elastic dislocation models the width of the zone, that is influenced by elastic loading effects induced by slip at depth, determines the magnitude of

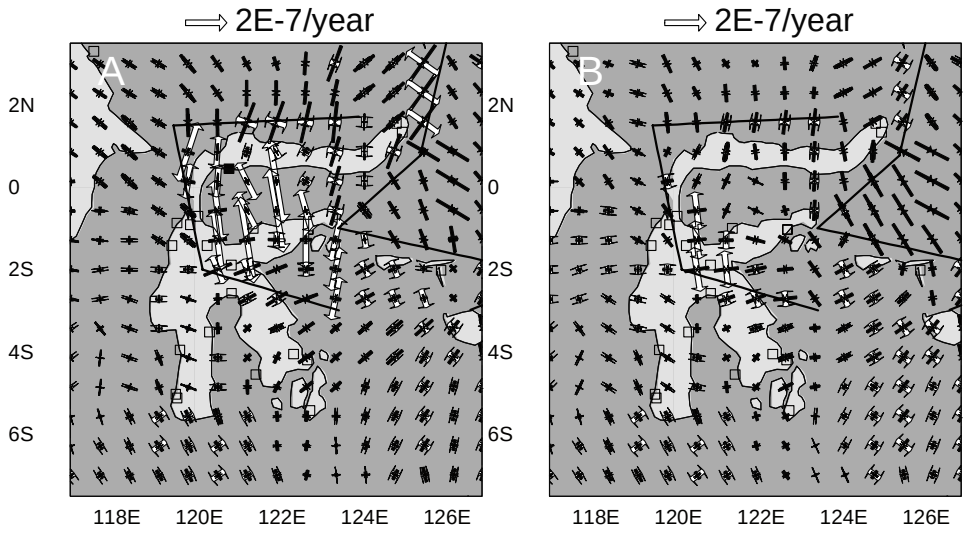

Figure 4.18: Principal strain rates with error ellipses computed on a regular grid at Sulawesi of (A) solution II and (B) the solution resulting from inversion of the data set without the Tomini station (indicated by a black square in (A)). White arrows indicate extension, black arrows indicate contraction. The open squares represent the other station positions.

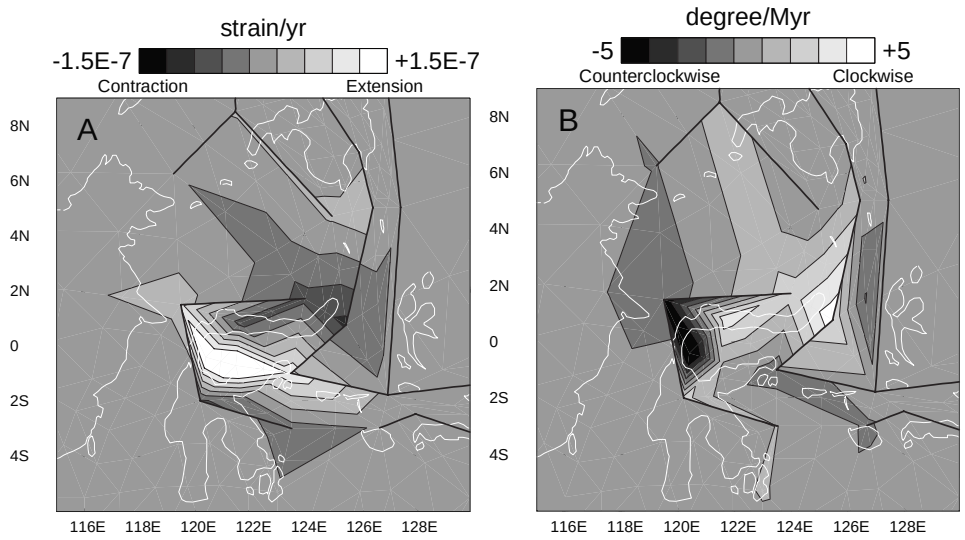

Figure 4.19: The difference between the velocity gradient field of solution II and the solution resulting from inversion of the data set without the Tomini station ($\triangle \nabla \boldsymbol{v}$); (A) effective strain rates, (B) rotation rates. The components of $\triangle \nabla \boldsymbol{v}$ outside the area shown in (A) and (B) are insignificant.

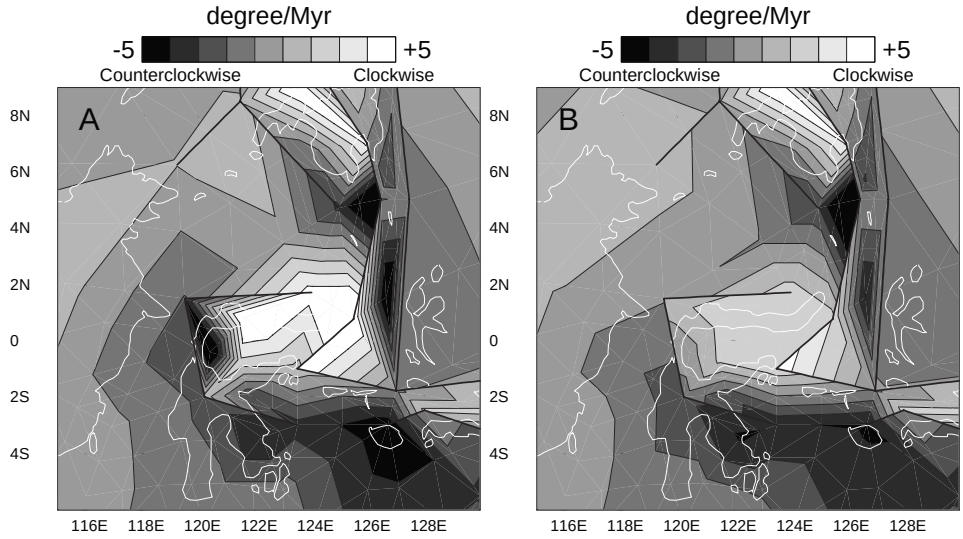

Figure 4.20: Rotation rates at Sulawesi of (A) solution II (this plot is a detail of figure 4.14B) and (B) the solution resulting from inversion of the data set without the Tomini station (figure 4.18A).

the locking depth [Savage and Burford, 1973]. If the locking depth is found to be relatively shallow, as for the Palu-Koro fault, estimates from elastic dislocation models will probably be close to estimates from our method. Relatively weak shear strain rates along the Palu-Koro fault (figure 4.18) confirm that most sinistral motion is accommodated on the fault.

Additionally, the strain rate field shows relatively strong N-S extension. This is caused by fitting the north directed, relatively large velocity at the Tomini station just south of the North Sulawesi trench (figure 4.4C, indicated by a black square in figure 4.18A and a † in table D.1). This velocity vector is probably still contaminated by co- and postseismic motion due to the M_w=7.9, January 1, 1996 and M_w=7.0, July 22, 1996 earthquakes that occurred in the western part of the north arm of Sulawesi [Walpersdorf et al., 1998].

If we remove the Tomini station from the velocity set and perform a joint inversion under the same conditions (in terms of regularization) as chosen for solution II the strong N-S oriented extension in Sulawesi disappears almost completely (figure 4.18B). The difference between the velocity gradient fields of solution II and the solution without the Tomini station is characterized by extensional strain rates that are strongest south of the north arm of Sulawesi (figure 4.19A) and counterclockwise rotation rates along the Palu-Koro fault (figure 4.19B). The rotation rate field in Sulawesi of the solution without the Tomini station has a pure clockwise orientation and an on average smaller magnitude compared to solution II (figure 4.20). In general, the slip rates on the Sulawesi faults decrease due to the removal of the Tomini station (table E.2).

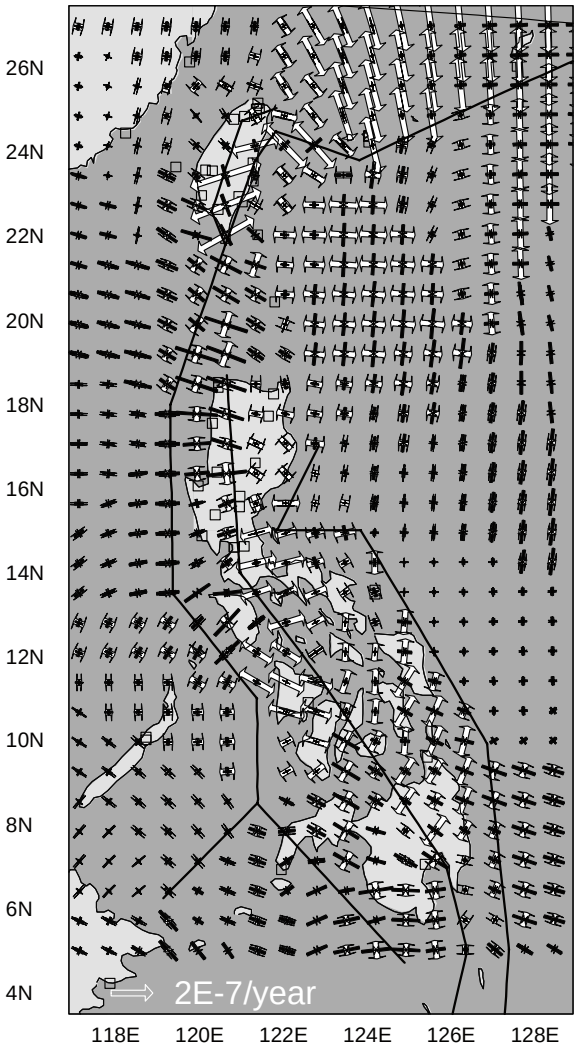

Figure 4.21: Principal strain rates of solution II computed on a regular grid at the Philippines. White arrows indicate extension, black arrows indicate contraction. Open squares represent the station positions.

4.6.5 Philippines and Taiwan

Sinistral slip on the Philippine fault system and arc-parallel extension of the forearc consume the trench parallel component of plate convergence between the Philippine Sea plate and Sundaland [e.g., Fitch, 1972; Barrier et al., 1991; Duquesnoy et al., 1994; McCaffrey, 1996]. Our slip rate solution predicts pure sinistral slip rates of, on average, 20 to 25 mm/yr on the Philippine fault, which agrees with results from different studies: Duquesnoy et al.

[1994] induce 26±10 mm/yr on the central segments of the Philippine fault (around 13°N) from geodetic observations (trilateration and GPS). From GPS data Yu et al. [1999] predicts 24±7 mm/yr for the northern and central segments. From a kinematic modeling study Barrier et al. [1991] predicts 19 mm/yr on central and 25 mm/yr on southern segments of the fault. Lee and Lawver [1994] derive a sinistral translation along the Philippine fault up to about 21 mm/yr, assuming that the Philippine Sea plate performs a rigid rotation and that the arc-parallel component is accommodated solely on the Philippine fault. Besides as sinistral slip on the Philippine fault arc-parallel plate motion in our solution is accommodated in the form of a (spatially varying) shear strain rate regime across the Philippines and as relatively strong sinistral slip on the Cotabato-Negros-Manila trench system. Since neither geologic, geodetic nor seismic studies provide evidence for a strike-slip component on this trench system, this may be due to trade-off between ∇v and s in the Philippine region. Patterns of an extending fore- and back arc can be recognized, but do not reveal a uniform arc-parallel orientation, as proposed by McCaffrey [1996].

To which extent the shortening between the Philippine Sea plate and the Eurasian plate is partitioned over the trench systems east and west of the Philippines is not agreed upon [Rangin, 1989; Nichols et al., 1990; Barrier et al., 1991; Quebral et al., 1996; Lallemand et al., 1998; Rangin et al., 1999]. Our solution shows that east of the Philippines a relatively small part of the convergence between the Philippine Sea plate and the Eurasian plate is accommodated at the Philippine trench, where the Philippine Sea plate subducts in a northwest direction. West of the Philippines a larger part of the convergence is taken up by the eastward subducting Negros and Cotabato trenches. The Manila trench accommodates a large part of the shortening, which agrees with the (GPS) study of Rangin et al. [1999]. South of Mindanao the strike-slip dominated regime changes to convergence across the Sangihe trench [Quebral et al., 1996; Lallemand et al., 1998]. Our maximum thrust rates of 34 and 21 mm/yr for the Sangihe and Halmahera trenches, respectively, are only slightly lower than the estimates of 40 and 30 mm/yr of Lallemand et al. [1998]. Possibly, in solution II the remaining part of convergence between the Philippine Sea plate and Sundaland is accommodated in the form of contractional strain rates at the Molucca Sea.

The orientation of the sinistral, thrust slip vectors of solution II on the Longitudinal Valley fault in Taiwan agrees with geologic, seismic and geodetic observations, [e.g., Barrier and Angelier, 1986; Yu et al., 1990; Hu et al., 1997]. The thrust component ranges between a few and 27 mm/yr, slightly higher than results of Yu et al. [1990] who predict rates between 10 and 23 mm/yr, based on trilateration and leveling data. The sinistral component, ranging between 5 and 7 mm/yr, is considerably lower than the rates of 23 to 30 mm/yr of Yu et al. [1990] and more in agreement with Barrier and Angelier [1986], who find a minor sinistral component. The high shear strain rates found at Taiwan (figure 4.21) probably partly represent shearing on the major, non-parameterized shear zones on the island of Taiwan, running parallel to and west of the Longitudinal Valley fault [Hu et al., 1997].

4.7 Seismicity and GPS

We compare orientations of principal strain rates, derived from solution II (figure 4.13) with the principal axes of the strain rate field of a study by Kreemer et al. [2000], in which

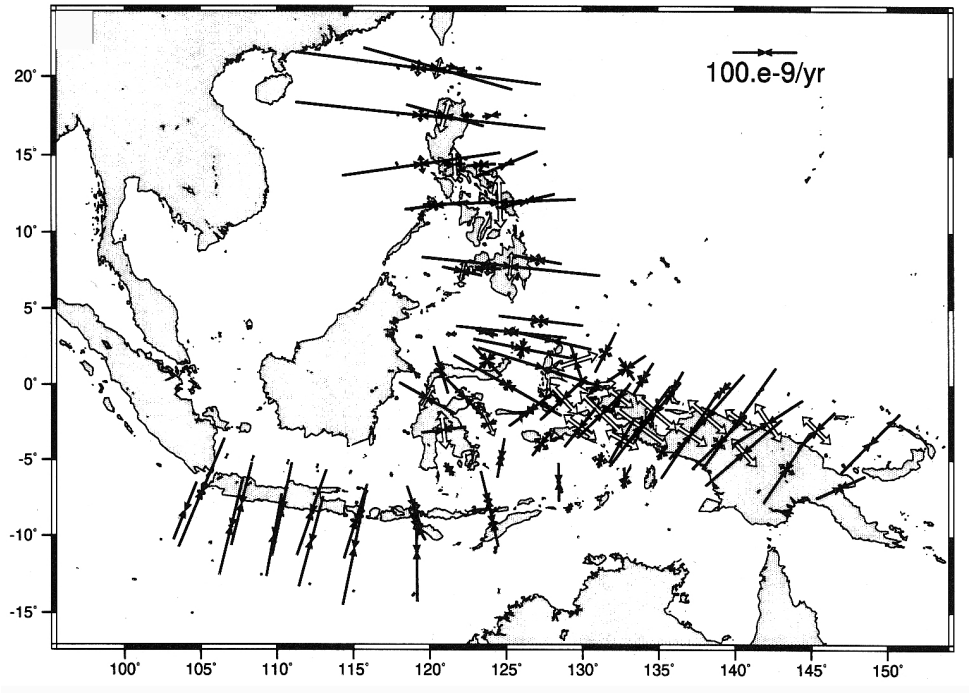

Figure 4.22: From Kreemer et al. [2000]: Principal axes of the strain rate field obtained from fitting GPS velocities. Open arrows indicate extensional strain rates, and solid arrows correspond to compressional strain rates. Directional information of the principal strain rates ($\pm 10^{\circ}$ uncertainty) is inferred from the seismic strain rate tensor field associated with events for which $M_0 < 1 \times 10^{20}$N m.

GPS data and focal mechanisms of earthquakes are combined within one model of the deformation field of the Philippines and Indonesia (figure 4.22). Their GPS data are taken from several individual studies by Puntodewo et al. [1994]; Genrich et al. [1996]; Kato et al. [1998b]; Tregoning et al. [1998]; Simons et al. [1999]; Stevens et al. [1999]; Yu et al. [1999]. The data of Genrich et al. [1996]; Puntodewo et al. [1994]; Stevens et al. [1999] are incorporated in the data set of Bock et al. [2001], used in this study. The data of Simons et al. [1999] are incorporated in the data set of Matheussen [2000].

The orientation of contraction along the Sunda arc west of the island of Sumba and the almost pure thrust motion accommodated on the plate interface of solution II agree with the strain rates of Kreemer et al. [2000]. The change in orientation and localization of contraction from NNE-SSW in the Java forearc to NNW-SSE in the Timor and Banda backarc regions is present in both solutions. However, our solution also contains a significant arc-parallel component of extension within the Timor forearc. The shear strain rates of the solution of Kreemer et al. [2000] reveal a uniform strike-slip regime in Irian Jaya with an

additional NE-SW oriented contractional component north of the New Guinea trench, evidence for strain partitioning due to the oblique relative plate motion between the Australia and Philippine Sea plates. These features are consistent with the relatively strong sinistral slip component on the Sorong-Yapen-Ransiki and Tarera-Aiduna fault systems and the contraction north of the New Guinea trench in solution II. However, solution II also contains an additional on average arc-parallel extensional component in Irian Jaya, predominantly WNW-ESE oriented extension south of the Tarera-Aiduna fault system and a change in orientation of contraction from NNE-SSW in eastern to NNW-SSE in western Irian Jaya. Kreemer et al. [2000] find contraction across the North Sulawesi trench, consistent with the thrust fault motion of solution II. Their shear strain rates in Sulawesi agree with the sinistral slip component on the Palu-Koro-Matano fault system, but do not show the relatively strong N-S extension, present in our solution. Although their GPS data set contains the relatively large velocity at northern Sulawesi (section 4.6.4), the smoothing procedure applied prevents the solution from fitting it. The contraction along the Halmahera and Philippine trench system and along the Sangihe, Cotabato, Negros and Manila trench system in the solution of Kreemer et al. [2000] is present as discrete thrust motion on these segments and as contraction west of the Manila trench in solution II. Likewise, we find significantly higher convergence rates west of the Philippine trench than east of it. Shear strain rates in the Philippines show an increase from Mindanao to Visayas and a decrease from Visayas towards the Manila trench in the solution of Kreemer et al. [2000]. This information comes from GPS data, since magnitudes of strike-slip earthquakes in the Philippines are too weak to significantly contribute to the strain rate field. Strike-slip rates accommodated by the Philippine fault and the Manila trench in our solution are probably associated with these shear strain rates and reveal a similar pattern of subsequent northward increase and decrease. The component of sinistral slip found on the Cotabato and Negros trench systems is only weakly present in the solution of Kreemer et al. [2000].

The model of Kreemer et al. [2000] results from a relatively smooth interpolation of GPS vectors, using the method described in Haines [1982]; Holt and Haines [1993]. This interpolation is further constrained by incorporating local strain rate representations of earthquake moment tensors in the analysis, but does not explicitly include fault motion. Our approach is purely based on surface data and allows, through its parameterization, for more spatial variability in the strain rate fields. We consider the differences in data types used and methodological approach as the cause for the discrepancies noted.

4.8 Final discussion and general conclusions

The tectonics of Southeast Asia are determined by a complex pattern of interacting plates and micro-plates, separated by fault systems or zones of widely distributed deformation. GPS observations can provide information about the style of the present-day deformation and the distribution of relative plate motion at the plate boundary zones. In this chapter we apply the inversion method, presented and tested in chapter 2, to a combination of GPS data sets obtained in Southeast Asia between 1989 and 1998 and discuss the quantitative and qualitative aspects of the results. The data density is highest at some parts of the plate boundary zones (i.e., Sumatra, Sulawesi, the northern Philippines) and lowest at the interiors

of Sundaland, the Australian, Philippine Sea and Caroline plates.

We perform two series of inversions to derive the crustal deformation field. In the first we invert for the lateral velocity gradient field (∇v) only (I) and in the second for the lateral velocity gradient field and horizontal fault motion (s) simultaneously (II). In inversion II the main fault zones and plate-boundaries are incorporated. Per inversion procedure a solution (I and II for inversion procedures I and II, respectively) is selected with acceptable covariance, data fit and resolution properties. The accommodation of discrete fault motion in solution II considerably decreases the magnitude of the strain and rotation rates with respect to solution I. Strain and rotation rates of solution I are relatively strong at the plate interiors, whereas the main deformation features in solution II are located in the plate boundary zones. Strike-slip fault motion in solution II replaces or reduces rotation rate regimes in solution I. Thrust, normal and strike-slip motion in solution II replace or reduce wider distributed contractional, extensional and shear strain rate regimes, respectively. Inversion for ∇v and s enables the accommodation of localized motion on faults or plate boundaries and offers insight in the distribution of relative plate motion in plate boundary zones in terms of slip, (micro-)block rotation and strain rates.

Comparison of the components of solution II with other studies based on geologic, seismic, paleomagnetic and geodetic data shows a mixed pattern of both agreement and disagreement. In general, the qualitative aspects of the strain, rotation and fault slip rate components of solution II agree with existing observations and derivations. Orientations of fault slip vectors reflect orientations of long-term fault motion as they are derived from geologic and geodetic observations and plate tectonics. Further, the solution reflects main features as rigid plate motion, continental collision and rotation of crustal blocks and the partitioning of relative plate motion in plate boundary zones. The plate motion components perpendicular to the boundary are partitioned in thrust fault motion and contraction of fore-and backarcs. The oblique components are partitioned in strike-slip fault motion, shear strain rates and arc-parallel extension of the forearc.

Quantitative aspects of the results are more difficult to interpret. In general, we find that slip rates of solution II do not exceed fault slip rates estimated from geological observations or plate tectonic models. This suggests that possible remnant deformation is accommodated in our solution as strain or rotation rates, waiting to be released by earthquakes or as creep on faults.

We compare the strain rate field of solution II with the resulting strain rate field of the study of Kreemer et al. [2000] based on GPS and seismic moment tensors. We find agreement in main styles of deformation, i.e. distribution of contraction within the plate boundaries of converging plates and shear-strain rate regimes along major strike-slip fault zones. Due to the parameterization of faults in solution II convergence across plate boundary zones is reflected by a combination of thrust motion on faults or plate boundaries and contraction in fore-and backarc regions, shearing along faults by a combination of strike-slip motion on faults and shear strain rate regimes around the fault. Basically different results in our study are arc-parallel extension of forearc regions in plate-boundary zones that are dominated by shortening between two plates and a more spatially variable strain rate field.

Appendix A

Fault motion and fault parameterization

Consider an arbitrary integration path L_{ij} crossing a fault in an arbitrarily deforming medium. We parameterize L_{ij} with the arc-length parameter l and take $l = 0$ at the intersection of L_{ij} with the fault. The integration 2.3 is split into three parts:

$$\begin{aligned} \Delta \boldsymbol{v}_{ij}(t) &= \int_{L_{ij}} \boldsymbol{\nabla v}(\boldsymbol{r}, t) \cdot \mathrm{d}\boldsymbol{r} \\ &= \int_{l_i}^{-\epsilon} \boldsymbol{\nabla v} \cdot \frac{d\boldsymbol{r}}{dl} \mathrm{d}l + \int_{-\epsilon}^{+\epsilon} \frac{d\boldsymbol{v}}{dl} \mathrm{d}l + \int_{-\epsilon}^{l_j} \boldsymbol{\nabla v} \cdot \frac{d\boldsymbol{r}}{dl} \mathrm{d}l \end{aligned} \tag{A.1}$$

where ϵ is a small arc distance. The second term on the right hand side reduces to $\boldsymbol{v}(+\epsilon) + \boldsymbol{v}(-\epsilon)$ which is the difference in velocity across the fault over an interval 2ϵ. If the fault is locked and $\epsilon \to 0$ this term vanishes because of the continuity of $\boldsymbol{v}$. To simulate a slip rate on the fault we let $\boldsymbol{v}$ depend on ϵ and generate a sequence of velocity functions $\boldsymbol{v}_\epsilon(l)$ which converges to $\boldsymbol{v}$ when $\epsilon \to 0$. Since the fault is slipping the velocity profiles $\boldsymbol{v}_\epsilon$ converge to a step function at the fault with $\boldsymbol{v}(-\epsilon) \to \boldsymbol{v}(0^-)$ and $\boldsymbol{v}(+\epsilon) \to \boldsymbol{v}(0^+)$. Substituting $\boldsymbol{v}_\epsilon$ for $\boldsymbol{v}$ in equation A.1 and letting $\epsilon \to 0$ then $\boldsymbol{v}_\epsilon(+\epsilon) + \boldsymbol{v}_\epsilon(-\epsilon) \to \boldsymbol{v}(0^+) - \boldsymbol{v}(0^-)$ which reduces the second term on the right hand side to non-vanishing fault slip rate while integration in the first term ends at the fault at $l = 0^-$ and in the last term integration starts at $l = 0^+$. This leads to the addition of path integration and faults slip terms which, after defining sign conventions, leads to equation 2.5.

The sign of the fault slip term depends on the direction of integration. To develop a consistent way of adding fault slip terms we first define the parameterization of fault geometry and relative sense of fault motion. Fault geometry is parameterized on the Earth surface as straight (or great circle) fault segments connected by support points $\boldsymbol{r}_k, k = 1, 2, ..$ (figure A.1a, b). Let $\boldsymbol{T}_k = (\boldsymbol{r}_{k+1} - \boldsymbol{r}_k)/|\boldsymbol{r}_{k+1} - \boldsymbol{r}_k|$ denote the tangential unit vector of a segment, then the unit normal $\boldsymbol{N}_k$ on the segment is taken at 90 degrees counterclockwise from $\boldsymbol{T}_k$. The upward pointing unit vector is denoted by $\boldsymbol{B}_k$. We label the two crustal blocks separated by a fault segment as block 1 and block 2 where $\boldsymbol{N}_i$ always points into block 1. Let $\Delta \boldsymbol{s}_k^1$ and $\Delta \boldsymbol{s}_k^2$ represent the absolute 3-D block displacement of block 1 and 2, respectively. We define the relative fault slip as: $\Delta \boldsymbol{s}_k = \Delta \boldsymbol{s}_k^1 - \Delta \boldsymbol{s}_k^2$ which gives the relative displace-

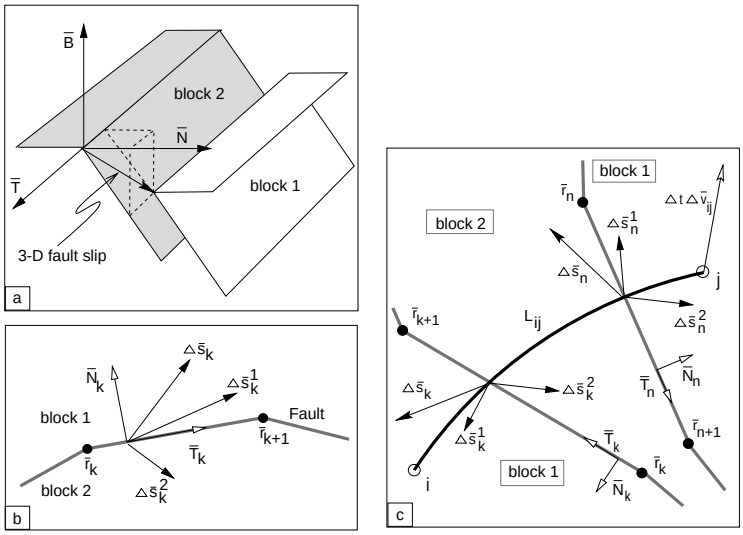

Figure A.1: Illustration of the parameterization of 3-D fault slip; a) Two crustal blocks that have experienced a 3-D relative displacement and the triad of unit vectors $\boldsymbol{T}$, $\boldsymbol{N}$, $\boldsymbol{B}$ used for the definition of fault segments, b) Map view of a fault between 'block 1' and 'block 2' at fault segment k and horizontal unit vectors indicated. Denoted are the absolute (horizontal) block displacements $\Delta \boldsymbol{s}_k^1$, and $\Delta \boldsymbol{s}_k^1$, and the relative displacement $\Delta \boldsymbol{s}_k$, c) Integration path L_{ij} crossing two fault segments k and n with relative and absolute fault displacements indicated. See text for further explanation.

ment of block 1 with respect to block 2. This definition is completely determined by $\boldsymbol{T}_k$ and changes sign if $\boldsymbol{T}_k$ is reversed in direction. However, the sense of relative displacement is preserved independent of the direction of $\boldsymbol{T}_k$. Let Δs_k^T, Δs_k^N and Δs_k^B denote the projections of $\Delta \boldsymbol{s}_k$ on the three unit vectors. Right lateral displacement is given by $\Delta s_k^T > 0$, left lateral displacement by $\Delta s_k^T < 0$, normal faulting by $\Delta s_k^N > 0$, and thrusting by $\Delta s_k^N < 0$. Note that $\Delta \boldsymbol{s}_k$ also fixes the fault dip.

Figure A.1c illustrates fault slip rate contributions averaged over time interval Δt to an integration path L_{ij} crossing fault segments k and n. For simplicity pure translational motion is assumed and rigid blocks, hence $\boldsymbol{\nabla v} = 0$. Absolute motions give: $\Delta t\, \Delta \boldsymbol{v}_{ij} = \Delta \boldsymbol{s}_n^1 - \Delta \boldsymbol{s}_k^1$, which can be rewritten as $\Delta t\, \Delta \boldsymbol{v}_{ij} = (\Delta \boldsymbol{s}_n^1 - \Delta \boldsymbol{s}_n^2) - (\Delta \boldsymbol{s}_k^1 - \Delta \boldsymbol{s}_n^2)$. Noting that $\Delta \boldsymbol{s}_n^2 = \Delta \boldsymbol{s}_k^2$ we get $\Delta \boldsymbol{v}_{ij} = (-\Delta \boldsymbol{s}_k + \Delta \boldsymbol{s}_n)/\Delta t$. The $+$ and $-$ sign result from the definition of relative fault slip and the direction of stepping over a fault segment. When going from site i to j segment k is crossed from a "1-block" to a "2-block" hence the change in relative motion is $-\Delta \boldsymbol{s}_k$. In general these signs are given by $\alpha_k = sign(\boldsymbol{N}_k \cdot \boldsymbol{l}_{ij})$ where $\boldsymbol{l}_{ij}$ is the local tangent to L_{ij} in the direction of integration. In case block 2 is not rigid and/or rotating about some axis a relative motion $\Delta \boldsymbol{s}_n^2 - \Delta \boldsymbol{s}_k^2$ may exist across block 2. This gives $\Delta \boldsymbol{v}_{ij} = (-\Delta \boldsymbol{s}_k + \Delta \boldsymbol{s}_n)/\Delta t + (\Delta \boldsymbol{s}_n^2 - \Delta \boldsymbol{s}_k^2)/\Delta t$. The last term, however, is accounted for by equation 2.3. Only the jump in velocity across a fault matters for pure fault contributions to $\Delta \boldsymbol{v}_{ij}$ which we derived at the start of this appendix. When a path crosses K faults the total slip contribution to relative motion generalizes to equation 2.4.

Appendix B

Parameterization of ∇v

The parameterization of $\boldsymbol{\nabla v}$ is restricted to specifying its spatial behavior for each single triangle T^τ by shape functions. Let L^τ denote the path segment in T^τ of an integration path L (where we dropped the subscript ij to save on notation). Then equation 2.3 can be written as:

$$\Delta \boldsymbol{v} = \sum_\tau (\Delta \boldsymbol{v})^\tau = \sum_\tau \int_{L^\tau} \boldsymbol{\nabla v}(\boldsymbol{r}) \cdot \mathrm{d}\boldsymbol{r} \tag{B.1}$$

Now we need only concentrate on the contribution to $\Delta \boldsymbol{v}$ from one triangle T^τ. The vertices of T^τ correspond to model nodes with position vectors $\boldsymbol{r}^\tau_m, m = 1, 2, 3$. At each vertex m we have 9 model parameters assembled in $\boldsymbol{\nabla v}(\boldsymbol{r}^\tau_m)$. We denote the kl-component (row index k) of $\boldsymbol{\nabla v}(\boldsymbol{r}^\tau_m)$ by $p^{\tau m}_{kl}$, hence in cartesian geometry $p^{\tau m}_{kl} = (\partial v_k / \partial x_l)(\boldsymbol{r}^\tau_m)$. For each component of $\boldsymbol{\nabla v}(\boldsymbol{r})$ the spatial variation in triangle T^τ is determined by:

$$[\boldsymbol{\nabla v}(\boldsymbol{r})]_{kl} = \sum_{m=1}^{3} p^{\tau m}_{kl} g^\tau_m(\boldsymbol{r}) \tag{B.2}$$

where $g^\tau_m(\boldsymbol{r})$ are known functions that interpolate between the unknown model parameters $p^{\tau m}_{kl}$. Substituting this parameterization in the path integral for T^τ gives for the k-th component of $(\Delta \boldsymbol{v})^\tau$:

$$\begin{aligned} &(\Delta \boldsymbol{v})^\tau_k = \textstyle\int_{L^\tau} [\boldsymbol{\nabla v}(\boldsymbol{r}) \cdot \mathrm{d}\boldsymbol{r}]_k = \sum_{m=1}^3 \sum_{l=1}^3 p^{\tau m}_{kl} G^{\tau m}_l \\ &\text{with } G^{\tau m}_l = \textstyle\int_{\lambda_1}^{\lambda_2} g^\tau_m(\boldsymbol{r}(\lambda)) \frac{(\mathrm{d}\boldsymbol{r}^\tau(\lambda)}{\mathrm{d}\lambda} \cdot \boldsymbol{q}_l) \mathrm{d}\lambda \end{aligned} \tag{B.3}$$

where $\boldsymbol{r}^\tau(\lambda) = r_1(\lambda)\boldsymbol{q}_1 + r_2(\lambda)\boldsymbol{q}_2 + r_3(\lambda)\boldsymbol{q}_3$, $(\lambda_1 < \lambda < \lambda_2)$ parameterizes L^τ with arc length λ. The $\boldsymbol{q}_i$ are unit axis-vectors in the coordinate frame adopted. Except for cartesian geometry, the $\boldsymbol{q}_i$ may depend on the arc-length λ. Substituting B.3 in B.1 gives:

$$(\Delta \boldsymbol{v})_k = \sum_\tau \sum_{m=1}^{3} \sum_{l=1}^{3} p^{\tau m}_{kl} G^{\tau m}_l \tag{B.4}$$

In the summation over τ, the coefficients $G_l^{\tau m}$ are zero for all triangles T^τ not intersected by path L. Equation B.4 can be simplified by noting that certain combinations of τ and m relate to the same node number n because one node is usually at the vertex of more than one triangle. Therefore, the summation over τ and m can be replaced by a summation over model nodes n yielding

$$(\Delta \boldsymbol{v})_k = \sum_{n=1}^{N} \sum_{l=1}^{3} p_{kl}^n H_l^n \quad \text{with} \quad H_l^n = \sum_{for"\tau m"=n} G_l^{\tau m} \tag{B.5}$$

In order to arrive at a set of linear equations incorporating all relative motion data we assemble all model parameters into one linear vector $\boldsymbol{p}$ of length $9N$ with $p_j = p_{kl}^n$, $j = l + 3(k-1) + 9(n-1)$. Label the set of M relative motion vectors as $\Delta_\nu \boldsymbol{v}$, $\nu = 1, 2, .., M$ and assemble these into one data vector $\boldsymbol{d}$ of length $3M$ with $d_i = (\Delta_\nu \boldsymbol{v})_k$, $i = k + 3(\nu - 1)$. Equation B.5 becomes for all data:

$$d_i = \sum_{j=1}^{9N} V_{ij} p_j \quad i = 1, .., M \quad \text{with} \quad V_{ij} = H_l^n \quad \text{or} \quad \boldsymbol{d} = \boldsymbol{V}\boldsymbol{p} \tag{B.6}$$

Next, we present some computation details with respect to applications in cartesian and spherical geometry. In flat geometry, for a given integration path L, we first calculate all intersection points with triangle edges and adopt straight line connections $\boldsymbol{r}^\tau(\lambda)$ between intersection points. We use linear interpolation functions $g_m^\tau(\boldsymbol{r})$ as for instance given by [Cook et al., 1989, p. 153]. The integration of B.3 for each triangle can be performed analytically leading to the coefficients $G_l^{\tau m}$.

In spherical (r, θ, ϕ) coordinates the velocity field is denoted by $\boldsymbol{v}(r, \theta, \phi) = v_r \hat{\boldsymbol{r}} + v_\theta \hat{\theta} + v_\phi \hat{\phi}$ where $\hat{\boldsymbol{r}}, \hat{\theta}, \hat{\phi}$ are unit vectors along the coordinates directions. A study region is triangulated with spherical triangles with edges along great circles. Intersections of L with triangle edges are computed and we adopt great circle segments $\boldsymbol{r}(\lambda)$ between intersection points given by $\boldsymbol{r}(\lambda) = a[\cos(\lambda/a)\hat{\boldsymbol{r}}_1 + \sin(\lambda/a)\hat{\boldsymbol{r}}_2]$, where a is the Earth radius, and $\hat{\boldsymbol{r}}_1$ and $\hat{\boldsymbol{r}}_2$ are two radial unit vectors in the great circle plane and at right angles to each other.

For a representation of the velocity gradient field in spherical coordinates it is economic to change notation: with x_l, ($l = 1, 2, 3$) we denote the coordinates r, θ, and ϕ, respectively, and similarly rename the corresponding unit vectors to $\boldsymbol{e}_l$. Then, the physical component kl of $\boldsymbol{\nabla v}$ is in spherical coordinates:

$$[\boldsymbol{\nabla v}(\boldsymbol{r})]_{kl} = \frac{1}{h_l(r, \theta)} \frac{\partial \boldsymbol{v}}{\partial x_l} \cdot \boldsymbol{e}_k \tag{B.7}$$

where the scale factors are $h_l(r, \theta) = 1, r, r \sin\theta$ for $l = 1, 2, 3$, respectively. Equation B.7 can be derived as follows. The tensor coordinate transformation from cartesian to spherical coordinates for one spherical component kl is: $\boldsymbol{\nabla v}_{kl} = \boldsymbol{e}_k \cdot \boldsymbol{\nabla v} \cdot \boldsymbol{e}_l$ where $\boldsymbol{\nabla v}$ on the right hand side is the cartesian tensor. This expression equals $\boldsymbol{e}_k \cdot (\nabla v_1 \cdot \boldsymbol{e}_l, \nabla v_2 \cdot \boldsymbol{e}_l, \nabla v_3 \cdot \boldsymbol{e}_l)^T$ which after taking the gradient in spherical coordinates, i.e. $\nabla v_i = \sum (1/h_j) \partial v_i / \partial x_j \boldsymbol{e}_j$, and re-arranging terms leads to the generic form B.7. We want to interpolate the physical

components of the velocity gradient field in triangles therefore we identify $p_{kl}^{\tau m}$ in B.2 entirely with $\boldsymbol{\nabla v}(\boldsymbol{r}_m^\tau)$ of equation B.7. The only thing left is to define interpolation functions g_m^τ. We have adopted (weakly nonlinear) interpolation functions defined by

$$g_m^\tau(\boldsymbol{r}) = [1 - \frac{\text{arc}(\boldsymbol{r}, \boldsymbol{r}_m^\tau)}{\text{arc}(\boldsymbol{r}_m^\tau, \boldsymbol{R}_m^\tau)}] \tag{B.8}$$

where $\text{arc}(\boldsymbol{r}, \boldsymbol{r}_m^\tau)$ is the arc distance between $\boldsymbol{r}$ and $\boldsymbol{r}_m^\tau$. The point $\boldsymbol{R}_m^\tau$ is located at the triangle side facing node $\boldsymbol{r}_m^\tau$ at the intersection with the great circle arc spanned by $\boldsymbol{r}_m^\tau$ and $\boldsymbol{r}$.

We remark that all numbers 3 and 9 in this appendix change to 2 and 4, respectively, if we would consider a two-dimensional problem.

Appendix C

Modeling postseismic deformation

C.1 Influence of data exclusion

In an attempt to assess the effect of postseismic deformation we define a subset of all stations that were occupied in the period after the Aigion and Grevena earthquakes and have likely experienced postseismic motion (hereafter 'postseismic subset'). To certify that this subset encompasses all stations affected we assume that every station that experienced coseismic deformation also moved by postseismic motion. It becomes part of the postseismic subset if its coseismic velocity is larger than the formal error of its measurement. To identify these stations we calculate the coseismic deformation by modeling the ground motion caused by uniform slip on a rectangular dislocation in an elastic half space [Okada, 1985]. The source parameters of the earthquakes, used in this calculation and listed in table C.1, are inverted from a combination of seismic (local, regional and teleseismic records of the mainshock and of aftershocks), GPS and InSAR data [Bernard et al., 1997] and from GPS data [Clarke et al., 1997b], which were also used to correct the SING data for coseismic displacements. The postseismic subset consists of 59 stations and the 175-vector set minus this postseismic subset is shown in figure 3.4.

We compare solutions that result from application of the inverse method to four subsets

	lon	lat	z [km]	strike	dip	rake	M_0 [$\cdot 10^{25}$Nm]	length [km]	d_{min} [km]	d_{max} [km]
G	21.63	40.02	11	252°	41°	-87°	16.3	27.1	2.8	13.5
A	22.12	38.21	10	277°	33°	-77°	3.4	15	4.5	9.7

Table C.1: Source parameters of the M_s=6.6, May 13, 1995 Kozani-Grevena [Clarke et al., 1997b] (G) and the M_s=6.2, June 15, 1995 Aigion (Gulf of Corinth) [Bernard et al., 1997] (A) earthquakes. d_{min} and d_{max} denote the depth of the upper and deeper edge of the fault, respectively.

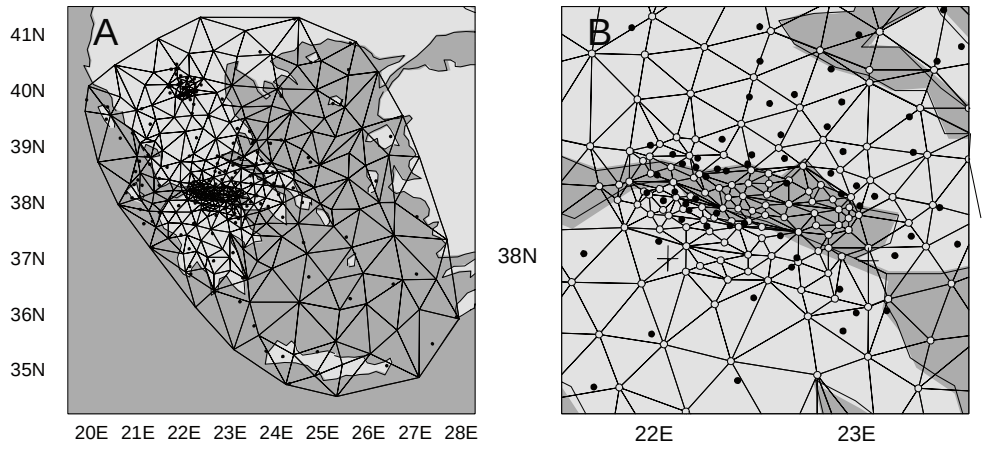

Figure C.1: Parameterization of the (A) model area, (B) Gulf of Corinth. The black dots represent the sites of observation.

of the SING data set to investigate the influence of the presence of stations that may have been influenced by postseismic deformation (section 3.4). The data sets are: (d1) the data set of 175 vectors, displayed in figure 3.3; (d2) the d1-set without the possibly influenced stations in the Aigion region; (d3) the d1-set without the possibly influenced stations in the Grevena area and (d4) the data set of 116 vectors (i.e. without the postseismic subset).

The inversions of the four data sets are targeted at fitting both the velocity data and the $\boldsymbol{\nabla} \times \boldsymbol{\nabla} \boldsymbol{v} = \mathbf{0}$ constraints by solving for a continuous velocity gradient field. In this analysis faults are ignored. We compare the solutions by determining the residual deformation fields of inversions of the d2-, d3- and d4- sets with respect to the 'reference solution', which is the deformation field computed from the d1-set. Consequently, parameterization is adjusted for inversion of the d1-set and then also applied to the d2-, d3- and d4-sets. In general, the local density of the stations is used as a guide for local densification of model nodes which determines the triangulation of the Aegean region. Due to the high station density and observed large velocity variations in the d1-set at the Corinth and Grevena epicentral areas the triangulation of these areas is made considerably denser than elsewhere (figure C.1). The solution is weakly regularized, but the focus remains primarily on data fit (expressed by the usual χ^2-measure). Table C.1 lists the results of the accepted solution per data set. Significant differences in resolution and model error between the solutions only occur around the two epicenters. The data fit is especially sensitive to the velocity data at the Aigion epicenter.

Figure C.2 depicts the residual effective strain ($\dot{\boldsymbol{\epsilon}}_{eff} = \frac{1}{2}\sqrt{\dot{\boldsymbol{\epsilon}}\dot{\boldsymbol{\epsilon}}}$, with $\dot{\boldsymbol{\epsilon}}$ the strain rate tensor) and rotation rate field that result from subtracting the solution for the d1-set from the solution for the d4-set. Outside the areas surrounding the two epicenters the solutions are practically equal, suggesting absence of far-field effects associated with motion in the epicentral region. The maximum principal extension rates occur at the epicenters of both earthquakes and coincide with T-axes derived from the focal mechanism solutions (figure

i	number of data	χ^2	$\tilde{r}_m$	$\tilde{\sigma}^c_m$ $\left[\frac{10^{-8}}{yr}\right]$	i	number of data	χ^2	$\tilde{r}_m$	$\tilde{\sigma}^c_m$ $\left[\frac{10^{-8}}{yr}\right]$
d1	175	3.6	0.96	1.0	d3	143	4.3	0.95	1.2
d2	146	1.2	0.96	1.1	d4	116	1.3	0.95	1.2

Table C.2: Results of inversions of four different subsets of the SING data set. See the caption of table 3.2 for an explanation of the symbols.

3.17).

A χ^2-value of 3.6 indicates that a large part of the d1-set can still not be fit. The maximum of the misfit vectors after inversion of the complete data set is about 25 mm/yr (figure C.3B). The maximum difference between observed velocities at the Aigion region and velocities predicted by the model which was computed from the d4-set is about 30 mm/yr (figure C.3A). These residuals indicate strong, extra extension restricted to a narrow zone within the Gulf, which is not modeled by the solution shown in figures C.2A and B.

C.2 Visco-elastic response

The observations of a complex pattern of strong postseismic signals right after the Aigion earthquake [Koukouvelas and Doutsos, 1996] suggest that the residual deformation field at the Gulf of Corinth (figure C.3A) may be, at least partly, the result from postseismic deformation. The Aigion earthquake was a pure normal faulting event and occurred on the north-dipping E-W oriented Aigion fault segment, which is part of the segmented faulting system at the south coast of the Gulf of Corinth. Average afterslip rates varied between 0.48 mm/day along the central part of the ruptured fault segment, adding up to a maximum of 3 cm afterslip throw, and 0.16 mm/yr at the eastern part during the first 10 weeks after the earthquake. Simultaneously, the foot-wall block showed uplift and the hanging-wall warp-like subsidence (folding). The western end of the fault segment showed general subsidence of the whole area during the first weeks after the earthquake, followed by uplift of the whole area without afterslip.

The presence of a regional-scale, highly conductive layer, 5 to 10 km thick, below about 10 to 15 km [Pham et al., 2000, section 3.4] may produce substantial transient surface deformation in a relatively short period of time after a large earthquake. To study the general character of postseismic deformation we use the VISCO1D model of Pollitz et al. [2000] which allows a first order estimate of the elastic motions at the Earth's surface. VISCO1D describes the response of a spherically stratified elastic- visco-elastic medium to the stresses generated by an earthquake occurring in one of the elastic layers in terms of a spherical harmonic expansion of spheroidal and toroidal motion components. We compute the visco-elastic response averaged over the first year immediately after the event, because the 'post-seismic' measurements at the Gulf of Corinth took place during three campaigns within the first year after the earthquake (table 3.1). Besides to the magnitude of the earthquake, the strength of the postseismic deformation computed by the VISCO1D model is especially

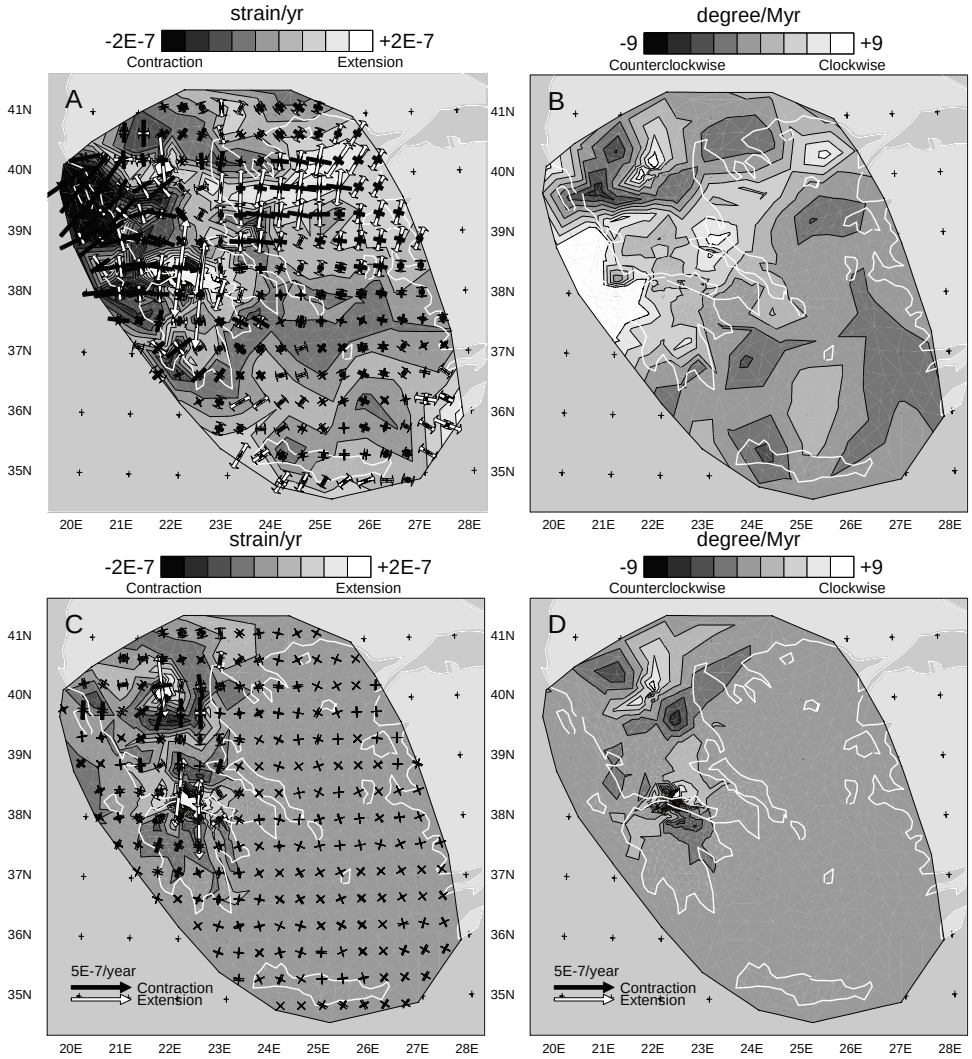

Figure C.2: (A) Effective strain rate and (B) rotation rate field of the solution for inversion of the d1-set; (C) residual effective strain rate and (D) residual rotation rate field after subtracting the solution for the d4-set (with the same parameterization and regularization as the solution for the d4-set) from the solution for the d1-set.

sensitive to the viscosity, thickness and depth of the seismogenic layer. For these input parameters we take realistic values leading to the most conservative estimate of visco-elastic relaxation. The stratification of crust and lithosphere are modeled according to the magneto-telluric observations of Pham et al. [2000]

The upper crust of the spherically stratified half space model is an elastic layer of 13 km

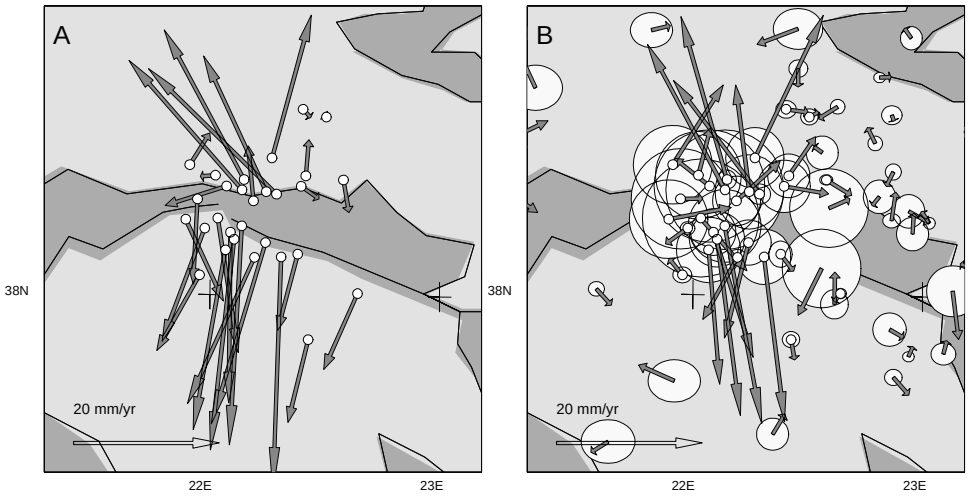

Figure C.3: (A) Residual velocity vectors at the sites that were excluded from the d1-set at the area of the Aigion epicenter after subtraction of the velocity vector that is predicted by the solution for the d4-set; (B) misfit vectors after inversion of the d1-set.

with average values for density ($\tilde{\rho}$), bulk modulus ($\tilde{\kappa}$) and shear modulus ($\tilde{\mu}$) of 3.0 g/cm^3, $7.0{\cdot}10^{10}$ Pa and $3.8{\cdot}10^{10}$ Pa, respectively. The ductile layer ($\tilde{\rho}$ =3.4 g/cm^3, $\tilde{\kappa}$ =$9.5{\cdot}10^{10}$ Pa, $\tilde{\mu}$ =$5.3{\cdot}10^{10}$ Pa), with a viscosity of $1.0{\cdot}10^{18}$ Pa s and thickness of 4 km, is followed by elastic material ($\tilde{\rho}$ =4.0 g/cm^3, $\tilde{\kappa}$ =$15{\cdot}10^{10}$ Pa, $\tilde{\mu}$ =$7.0{\cdot}10^{10}$ Pa), throughout the rest of the half space. Although Pham et al. [2000] propose the upper limit of the mantle to be positioned at a depth of 30 km, we do not include it in the half space model that leads to the results shown in figure C.4, because its contribution to the surface motions during the first year after an earthquake is insignificant. For the source parameters of the earthquake we take the fault plane solution that was also used to compute the coseismic motions due to the Aigion earthquake [Bernard et al., 1997, table C.1, section 3.4]. The resulting effective strain rates and principal axes are shown in figures C.4B and D, next to the effective strain rates (figure C.4A) and principal axes (figure C.4C) of the residual deformation field after subtracting the solution for the reduced data set from the solution for the complete data set.

A brief comparison of inversion results (figure C.4A, C) with predicted surface motion due to visco-elastic relaxation (figure C.4B, D) shows a general agreement in character of both solutions: (1) N-S directed contraction north and south of the Gulf of Corinth, followed towards the epicenter by (2) a zone of weaker extension, (3) a thin zone of strong contraction (although the contours of the contractional zone are somewhat irregular in our solution) and (4) strong N-S directed extension confined to a narrow zone within the Gulf. The main differences are (1) an orientation mismatch in the general pattern (compare figure C.4A and B), (2) an amplitude mismatch in the vicinity of the earthquake (compare figure C.4C and D) and (3) absence of local compression in the event region, which are predicted by the visco-elastic modeling, but not found in the inversion results. These differences can be

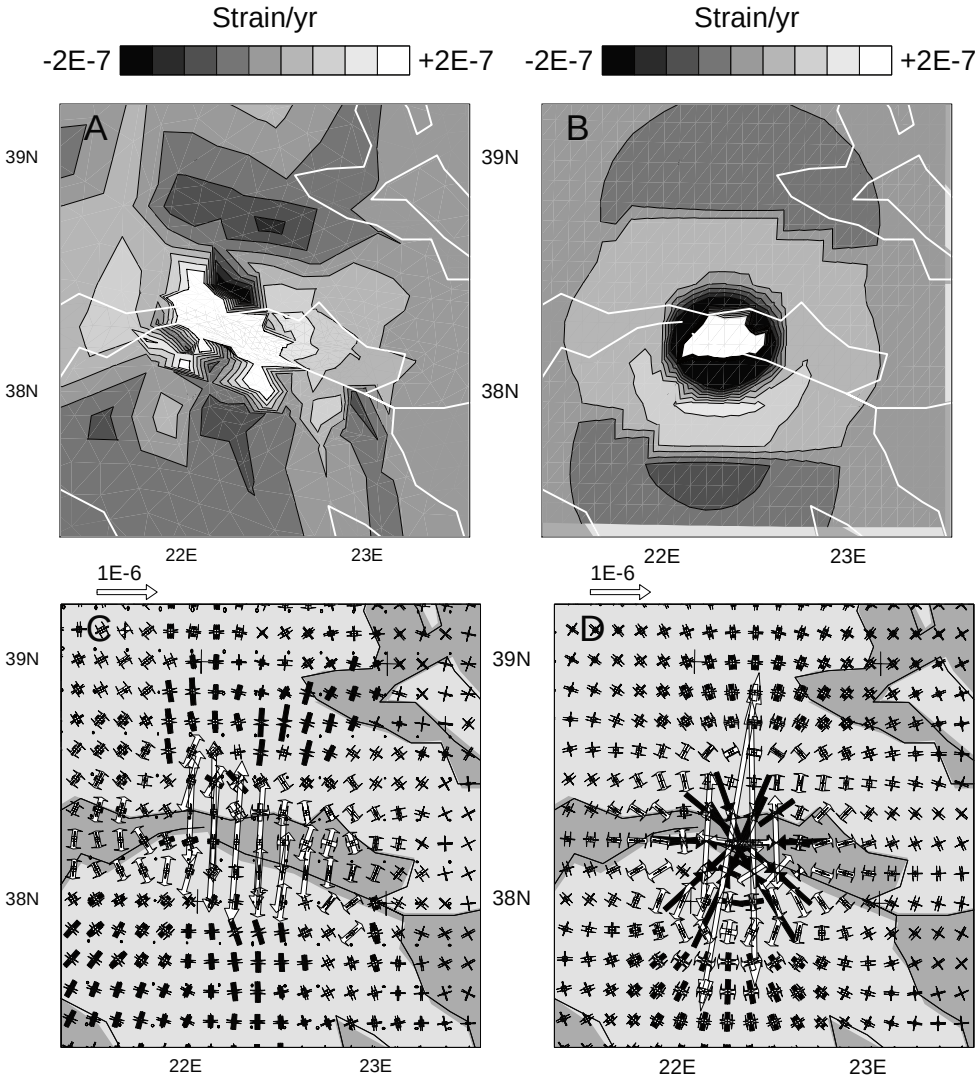

Figure C.4: (A) Detail of figure C.2C: Residual effective strain rate field at the Gulf of Corinth, (B) effective strain rate field averaged over one year due to visco-elastic relaxation (for model description, see text), (C) principal axes of residual strain rate field, belonging to (A), (D) principal axes of visco-elastic strain rate field belonging to (B).

caused by an orientation error in the fault plane solution, lateral heterogeneity in rheological properties of the crust (which has been proposed to exist [Pham et al., 2000]) and a wrong depth profile of rheological properties used for the visco-elastic modeling.

Appendix D

Velocity data for Southeast Asia

Table D.1: The complete velocity data set of solution II (section 4.4), after subtracting the residual rotation vectors resulting from the inversion. The number between brackets indicates the 3-σ error of the velocity component. Key: v_θ, longitudinal; v_ϕ, latitudinal component of velocity vector; † Tomini velocity vector.

#	position		velocity ($\frac{mm}{yr}$)		#	position		velocity ($\frac{mm}{yr}$)	
	(°E)	(°N)	v_θ	v_ϕ		(°E)	(°N)	v_θ	v_ϕ
Main data [Matheussen, 2000]									
1	140.7	-2.5	19 (4)	46 (1)	2	139.0	-4.0	35 (3)	51 (1)
3	131.3	25.8	-30 (6)	22 (2)	4	131.1	-12.8	35 (3)	56 (1)
5	128.1	-3.8	17 (3)	18 (1)	6	127.8	26.0	42 (6)	-40 (2)
7	127.3	0.9	-48 (2)	12 (1)	8	126.0	-2.0	-9 (3)	16 (1)
9	125.7	-8.0	45 (2)	40 (1)	10	125.6	9.6	-10 (7)	15 (2)
11	125.5	7.0	-19 (2)	-6 (1)	12	125.1	1.3	26 (4)	-11 (1)
13	124.3	13.5	-16 (2)	36 (1)	14	124.3	-9.7	43 (2)	37 (1)
15	124.2	24.2	48 (3)	-57 (1)	16	122.8	-5.4	30 (13)	4 (4)
17	122.8	-1.0	5 (10)	17 (3)	18	122.7	-4.2	24 (10)	7 (2)
19	122.7	10.9	25 (3)	2 (1)	20	122.1	6.9	21 (2)	-13 (1)
21	121.8	-8.6	34 (2)	24 (1)	22	121.5	24.9	39 (2)	-20 (1)
23	121.5	-4.6	30 (2)	-2 (1)	24	121.4	-1.0	-2 (4)	13 (1)
25	120.9	-2.6	18 (2)	-3 (1)	26	120.9	-1.9	10 (10)	9 (2)
27†	120.9	0.5	2 (2)	54 (1)	28	120.6	18.4	-43 (2)	9 (1)
29	120.4	-3.5	24 (3)	-6 (1)	30	120.3	-1.4	9 (4)	7 (1)
31	120.1	-0.7	16 (5)	25 (1)	32	119.9	-0.9	17 (7)	7 (2)
33	119.7	-4.0	30 (3)	-6 (1)	34	119.6	-0.9	22 (5)	-6 (1)
35	119.6	-5.1	28 (2)	-6 (1)	36	119.5	-1.4	16 (4)	-11 (1)
37	118.9	10.0	36 (2)	-16 (1)	38	118.0	4.2	24 (2)	-18 (1)
39	117.1	-20.9	40 (1)	54 (1)	40	116.8	-1.3	25 (9)	-12 (2)

Table D.1: continued

#	position		velocity ($\frac{mm}{yr}$)		#	position		velocity ($\frac{mm}{yr}$)	
	(°E)	(°N)	v_θ	v_ϕ		(°E)	(°N)	v_θ	v_ϕ
41	115.0	4.9	31 (6)	-10 (2)	42	114.8	-3.8	28 (2)	-10 (1)
43	114.7	-8.1	29 (2)	-13 (1)	44	110.2	-7.6	30 (3)	-9 (1)
45	108.9	0.9	32 (3)	-11 (1)	46	108.3	15.9	33 (2)	-10 (1)
47	107.3	20.9	37 (2)	-11 (1)	48	106.8	-6.4	27 (1)	-10 (1)
49	106.2	-1.9	28 (2)	-9 (1)	50	103.7	1.3	29 (2)	-6 (1)
51	103.1	5.3	34 (2)	-6 (1)	52	102.8	24.9	30 (3)	-19 (1)
53	102.3	-3.8	26 (2)	14 (1)	54	101.0	13.0	35 (2)	-5 (1)
55	98.6	3.5	36 (2)	2 (1)	56	98.3	7.7	34 (2)	-2 (1)
57	97.8	0.6	31 (2)	28 (1)	58	96.8	-12.1	44 (1)	47 (1)
59	132.9	-12.6	42 (4)	56 (11)					
Sumatra data [Bock et al., 2001]									
60	99.4	0.2	24 (12)	13 (6)	61	99.8	-0.2	34 (12)	-11 (6)
62	140.4	-8.5	28 (18)	64 (9)	63	106.8	-6.5	34 (9)	-11 (6)
64	114.8	-3.4	18 (21)	-15 (6)	65	129.8	-4.5	30 (15)	34 (6)
66	136.1	-1.2	-58 (15)	39 (6)	67	118.7	-8.5	19 (12)	7 (6)
68	99.8	1.4	38 (12)	-1 (6)	69	100.8	1.7	33 (12)	0 (6)
70	105.6	-6.5	26 (21)	-9 (6)	71	104.6	-5.9	19 (30)	8 (9)
72	96.8	-12.1	58 (24)	41 (9)	73	98.5	-0.3	35 (12)	26 (6)
74	98.8	0.1	21 (12)	18 (6)	75	97.8	0.6	24 (12)	26 (6)
76	97.7	1.2	36 (12)	20 (6)	77	97.4	1.5	37 (15)	33 (6)
78	97.6	2.4	32 (15)	6 (6)	79	138.1	9.4	-83 (33)	-2 (18)
80	131.1	-12.8	38 (9)	65 (6)	81	99.6	2.5	30 (12)	-5 (6)
82	115.2	-8.8	28 (12)	-15 (6)	83	125.5	-8.5	41 (9)	55 (6)
84	98.7	2.5	37 (12)	6 (6)	85	101.2	1.2	35 (9)	-16 (6)
86	132.3	-2.9	-29 (9)	45 (6)	87	98.5	2.1	27 (15)	19 (6)
88	100.7	-0.7	39 (12)	-5 (6)	89	133.7	-3.6	-33 (9)	53 (6)
90	124.6	-8.1	37 (12)	33 (6)	91	109.4	0.8	28 (24)	-23 (6)
92	122.4	-4.1	27 (12)	4 (6)	93	102.3	-3.8	23 (15)	8 (6)
94	123.7	-10.1	22 (12)	53 (6)	95	122.8	-1.0	-6 (12)	11 (6)
96	124.9	1.5	8 (12)	-11 (6)	97	134.1	-0.9	-61 (39)	43 (12)
98	98.9	-0.9	50 (33)	17 (15)	99	127.6	-1.3	-56 (15)	24 (6)
100	100.4	-0.9	29 (9)	17 (6)	101	111.7	-2.7	26 (21)	-11 (9)
102	100.4	0.8	27 (12)	5 (6)	103	100.8	0.2	35 (15)	8 (6)
104	100.1	0.3	36 (12)	12 (6)	105	98.9	1.9	33 (12)	12 (6)
106	101.4	0.6	35 (12)	-5 (6)	107	120.5	-8.5	2 (18)	-9 (6)
108	131.3	-7.9	36 (9)	48 (6)	109	140.5	-2.6	9 (15)	56 (6)
110	99.2	1.5	36 (12)	10 (6)	111	98.6	2.1	28 (15)	16 (6)
112	99.1	0.6	26 (12)	16 (6)	113	99.1	2.1	37 (12)	-8 (6)
114	131.3	-0.9	-61 (12)	38 (6)	115	112.7	-7.1	35 (21)	-20 (6)
116	117.6	3.3	18 (18)	-19 (6)	117	136.9	-4.5	30 (9)	66 (6)
118	119.5	-5.0	28 (9)	-4 (6)	119	100.7	0.0	23 (33)	-9 (9)

Table D.1: continued

#	position		velocity ($\frac{mm}{yr}$)		#	position		velocity ($\frac{mm}{yr}$)	
	(°E)	(°N)	v_θ	v_ϕ		(°E)	(°N)	v_θ	v_ϕ
120	120.3	-9.6	42 (15)	13 (6)	121	138.9	-4.1	30 (12)	61 (6)
122	126.4	-7.9	33 (12)	57 (6)	123	105.7	-10.4	54 (9)	42 (6)
124	136.2	-1.9	-1 (15)	38 (6)	125	97.2	2.2	17 (18)	32 (6)
126	96.6	2.2	23 (21)	26 (9)	127	110.4	-7.7	31 (18)	-13 (6)
Taiwan and Philippines data [Yu et al., 1999]									
128	134.5	7.3	-76 (13)	1 (14)	129	121.0	14.6	-16 (5)	-7 (4)
130	121.5	25.0	42 (4)	-15 (3)	131	124.2	24.4	54 (6)	-55 (4)
132	136.1	20.4	-28 (32)	16 (25)	133	119.9	26.2	36 (3)	-14 (4)
134	121.6	25.2	39 (3)	-15 (4)	135	121.6	25.0	37 (2)	-22 (4)
136	121.5	25.0	40 (3)	-16 (4)	137	121.2	24.9	33 (3)	-14 (4)
138	121.0	24.8	33 (3)	-9 (4)	139	118.4	24.5	37 (3)	-14 (4)
140	124.2	24.4	40 (3)	-53 (4)	141	121.5	23.7	16 (3)	0 (4)
142	119.6	23.7	36 (3)	-14 (4)	143	120.3	23.6	31 (2)	-6 (4)
144	120.5	23.6	28 (3)	-12 (4)	145	120.2	23.0	21 (3)	-15 (4)
146	121.1	23.0	6 (3)	-2 (4)	147	120.6	22.6	-15 (3)	-14 (4)
148	120.8	21.9	6 (3)	-6 (4)	149	116.7	20.7	41 (3)	-13 (4)
150	118.9	10.1	30 (9)	-5 (10)	151	121.5	23.3	-7 (3)	32 (4)
152	121.2	22.8	-13 (3)	25 (4)	153	121.6	22.0	-28 (3)	29 (4)
154	122.0	20.4	-43 (7)	27 (8)	155	120.6	18.5	-49 (7)	13 (8)
156	121.9	18.2	-47 (7)	33 (8)	157	121.8	17.7	-55 (8)	24 (9)
158	120.5	17.6	-39 (8)	10 (9)	159	121.5	16.6	-40 (7)	31 (8)
160	120.6	16.4	-32 (7)	5 (8)	161	120.1	16.1	-25 (9)	0 (11)
162	121.1	15.8	-36 (6)	25 (7)	163	121.1	15.6	-38 (8)	8 (9)
164	120.5	15.4	-22 (8)	2 (10)					
WING data [Kato et al., 1998b]									
165	120.2	14.9	-20 (7)	4 (8)	166	121.2	14.6	-25 (8	8 (10)
167	121.0	14.6	-24 (3)	-4 (4)	168	124.3	13.6	-11 (8	36 (9)
169	96.8	-12.1	36 (7)	49 (22)					
Extra Australia data									
170	105.7	-10.4	34 (15)	53 (15)	171	110.0	-17.0	30 (15)	52 (15)
172	125.0	-16.0	27(15)	45(15)	173	135.0	-10.0	30 (15)	39(15)

Appendix E

Quantitative deformation data of Southeast Asia

E.1 Literature

Table E.1: Slip, strain and rotation rate data and estimates of the crustal deformation in Southeast Asia: * slip denotes the arc-parallel component of relative plate motion derived from the angles of earthquake slip vectors, the strain rate denotes the arc-parallel strain rate (i.e., the slip divided by the length of the fore-arc). [1] based on the NUVEL-1A Euler pole for Eurasia - Australia of DeMets et al. [1994], [2] based on the pole of Larson et al. [1997]. Abbreviations: D, type of data referenced; d, dextral; s, sinistral; t, thrust; n, normal; G, geology; g, GPS; Q, earthquakes; P, plate tectonics; p, paleomagnetism. Positive, negative strain rates are arc-parallel extension, arc-normal contraction, respectively. Rotations come from young paleomagnetic data (Plio-pleistocene); positive, negative denote clockwise, counterclockwise rotation rates, respectively.

location	slip (mm/yr)	strain (10^{-8}/yr)	rotation (°/Myr)	reference	D
Sumatra					
SF 5°S	6d±4			Bellier and Sébrier [1995]	G
SF 1°S	17d±6			Bellier and Sébrier [1995]	G
SF 1°S	11d			Sieh et al. [1991, 1994]	G
SF 1°S	23d±3			Genrich et al. [2000]	g
SF 2°N	23d±2			Bellier and Sébrier [1995]	G
SF 2°N	27d			Sieh et al. [1991, 1994]	G
SF 3°N	26d±2			Genrich et al. [2000]	g
MeF	≤19d			Bellier and Sébrier [1995]	G
MeF	inactive			Sieh and Natawidjaja [2000]	G
MeF	≤5d			Genrich et al. [2000]	G

Table E.1: continued

location	slip (mm/yr)	strain (10^{-8}/yr)	rotation (°/Myr)	reference	D
BF 4°N	12d±5			Bellier and Sébrier [1995]	G
BF 4°N	11d±2			Malod and Kemal [1996]	G
BF 4°N	5d±2			Genrich et al. [2000]	g
forearc*	23d±15	1.7±0.4		McCaffrey [1996]	Q,P
forearc*	24d±4[1]			McCaffrey et al. [2000]	Q,P
forearc*	26d±3[2]			McCaffrey et al. [2000]	Q,P
forearc		8±5		Genrich et al. [2000]	g
Java					
forearc*	17s±10	0.0±0.4		[McCaffrey, 1996]	Q,P
Timor					
forearc		-6.3, 3.0		[Genrich et al., 1996]	g
Irian Jaya					
SYF	80s			[McCaffrey and Abers, 1991]	Q,P
SYF			-2.6±0.7	[Ali and Hall, 1995]	p
SYF			1.7±0.3	[Ali and Hall, 1995]	p
Seram			7-14	[Haile, 1978]	p
TAF	5-25s, 1-9t			[Abers and McCaffrey, 1988]	Q
TAF	20s			[McCaffrey and Abers, 1991]	Q,P
Sulawesi					
North Arm			4.0±0.5	[Surmont et al., 1994]	p
NST west	41t			[Stevens et al., 1999]	g
NST east	10t			[Stevens et al., 1999]	g
NST	50t			[Silver et al., 1983a]	G
NST	30t			[Jarrard, 1986]	G
PaF	38s±8, 8t			[Stevens et al., 1999]	g
PaF	34s, 4t			[Walpersdorf et al., 1998]	g
MF	33s, 15n			[Stevens et al., 1999]	g
Philippines					
PF 11°N:	26s±10			[Duquesnoy et al., 1994]	g
PF	20-25s			[Barrier et al., 1991]	G
PF	17-31s			[Yu et al., 1999]	g
PF	21s			[Lee and Lawver, 1994]	p
PT 10°N:	30t			[Lallemand et al., 1998]	G,P
PT 5°N:	<30t			[Lallemand et al., 1998]	G,P
SaT	40t			[Lallemand et al., 1998]	G,P
HT	30t			[Lallemand et al., 1998]	G,P

Table E.1: continued

location	slip (mm/yr)	strain (10^{-8}/yr)	rotation ($^\circ$/Myr)	reference	D
forearc*	50s±14	1.9±1.5		[McCaffrey, 1996]	Q,P
Taiwan					
LVF north	23s±2			[Yu et al., 1990]	g
LVF north	10t±1			[Yu et al., 1990]	g
LVF south	30s±3			[Yu et al., 1990]	g
LVF south	23t±3			[Yu et al., 1990]	g

E.2 Inversion results

F	Slip rate ($\frac{mm}{yr}$) $\perp$	Slip rate ($\frac{mm}{yr}$) $\parallel$	$\tilde{r}$	F	Slip rate ($\frac{mm}{yr}$) $\perp$	Slip rate ($\frac{mm}{yr}$) $\parallel$	$\tilde{r}$
	Sunda arc				**Banda arc**		
ST	$33^t(4)$-$42^t(2)$	$7^d(3)$-$25^d(6)$	.8	TT	$4^t(1)$-$16^t(2)$	$10^d(2)$-$17^s(1)$	.8
SF	$2^t(1)$-$13^t(12)$	$6^d(1)$-$20^d(5)$	1.	FT	$8^t(1)$-$15^t(1)$	$1^d(1)$-$3^d(1)$	.9
MeF	$1^n(1)$-$14^t(2)$	$4^d(1)$-$6^s(1)$	.7	WT	$16^t(1)$-$17^t(1)$	$2^s(1)$-$6^s(1)$	.9
BF	$11^n(1)$	$10^d(1)$	.7	AT	$16^t(2)$-$20^t(2)$	$1^d(1)$-$10^d(2)$	.6
JT	$43^t(3)$-$46^t(3)$	$5^d(2)$-$9^s(2)$	.9	SeT	$1^t(1)$-$11^t(1)$	$13^s(1)$-$36^s(1)$	1.
	Irian Jaya				**Taiwan**		
SYR	$5^t(1)$-$10^n(1)$	$23^s(1)$-$53^s(2)$	.8	MT	$31^t(1)$-$58^t(1)$	$10^s(1)$-$25^s(1)$	.8
TAF	$6^t(1)$	$10^s(1)$	.6	RT	$36^t(1)$-$58^t(1)$	$22^s(1)$-$49^d(1)$	.9
NGT	$3^t(2)$-$12^t(1)$	$5^s(1)$-$11^s(1)$	.5	LVF	$1^t(1)$-$27^t(1)$	$7^s(1)$-$5^d(1)$	.6
	Molucca Sea				**Sulawesi**		
SaT	$4^t(1)$-$34^t(1)$	$13^d(1)$-$22^s(1)$	.9	PaF	$3^t(1)$-$4^n(1)$	$8^s(1)$-$38^s(1)$	.7
HT	$21^t(1)$	$4^d(1)$	1.	PaF†	$2^t(1)$-$5^n(1)$	$8^s(1)$-$22^s(1)$	.7
				NST	$13^t(1)$-$38^t(1)$	$4^d(1)$-$8^d(1)$	.8
				NST†	$7^t(1)$-$14^t(1)$	$4^d(1)$-$6^d(1)$	.8
	Philippines				**Philippines**		
NT	$19^t(1)$	$41^s(1)$	.9	PT	$2^t(1)$-$21^t(1)$	$2^d(1)$-$14^s(1)$	.9
PF	$1^t(1)$-$11^t(1)$	$12^d(1)$-$26^s(1)$	.9	CT	$8^t(1)$-$29^t(1)$	$15^s(1)$-$16^s(1)$	.9
SuT	$8^t(1)$	$3^s(1)$	.9				

Table E.2: Slip rates of solution II; the model error is put between brackets. Key: F, fault; $\perp$, slip component perpendicular to fault segment; $\parallel$, parallel to fault segment, $\tilde{r}$, average resolution of the slip rates on the particular fault segments. ^{d}, dextral; ^{s}, sinistral; ^{n}, normal; ^{t}, thrust; †, the slip rates on the Sulawesi faults after removal of the Tomini velocity vector from the data set (table D.1). For the key on abbreviations indicating fault segments, see figure 4.7.

Bibliography

Abers, G. A. and McCaffrey, R. (1988). Active deformation in the New Guinea fold-and-thrust belt: Seismological evidence for strike-slip faulting and basement-involved thrusting. *J. Geophys. Res.*, 93:13,332–13,354.

Ali, J. R. and Hall, R. (1995). Evolution of the boundary between the Philippine Sea Plate and Australia: paleomagnetic evidence from eastern Indonesia. *Tectonophysics*, 251:251–275.

Ambraseys, N. N. and Jackson, J. A. (1990). Seismicity and associated strain of central Greece between 1890 and 1988. *Geophys. J. Int.*, 101(3):663–708.

Angelier, J., Lybéris, N., Le Pichon, X., Barrier, E., and Huchon, P. (1982). The tectonic development of the Hellenic arc and the Sea of Crete: a synthesis. *Tectonophysics*, 86:159–196.

Argus, D. F. and Gordon, R. G. (1991). No-net-rotation model of current plate velocities incorporating plate motion model NUVEL-1. *Geophys. Res. Lett.*, 18:2039–2042.

Armijo, R., Meyer, B., Hubert, A., and Barka, A. (1999). Westward propagation of the North Anatolian fault into the northern Aegean: Timing and kinematics. *Geology*, 27(3):267–270.

Armijo, R., Meyer, B., King, G., Rigo, A., and Papanastassiou, D. (1996). Quaternary evolution of the Corinth Rift and its implications for the Late Cenozoic evolution of the Aegean. *Geophys. J. Int.*, 126:11–53.

Audley-Charles, M. G. (1975). The Sumba fracture: a major discontinuity between eastern and western Indonesia. *Tectonophysics*, 26:213–228.

Audley-Charles, M. G. (1986). Rates of Neogene and Quaternary tectonic movements in the southern Banda Arc based on micropaleontology. *J. Geol. Soc. Lond.*, 143:161–175.

Avigad, D., Baer, G., and Heimann, A. (1998). Block rotations and continental extension in the central Aegean Sea: paleomagnetic and structural evidence from Tinos and Mykonos (Cyclades, Greece. *Earth Planet. Sci. Lett.*, 157:23–40.

Avouac, J. P. and Tapponnier, P. (1993). Kinematic model of active deformation in Central Asia. *Geophys. Res. Lett.*, 20:895–898.

Barrier, E. and Angelier, J. (1986). Active collision in eastern Taiwan: the Coastal Range. *Tectonophysics*, 125:39–72.

Barrier, E., Huchon, P., and Aurelio, M. (1991). Philippine Fault: A key for Philippine kinematics. *Geology*, 19:32–35.

Beavan, J. and Haines, J. (2001). Contemporary horizontal velocity and strain rate fields of the Pacific-Australian plate boundary zone through New Zealand. *J. Geophys. Res.*, 106(1):741–770.

Bellier, O. and Sébrier, M. (1995). Is the slip rate variation on the Great Sumatran Fault accomodated by fore-arc stretching? *Geophys. Res. Lett.*, 22(15):1969–1972.

Bennett, R. A., Rodi, W., and Reilinger, R. E. (1996). Global Positioning System constraints on fault slip rates in southern California and northern Baja, Mexico. *J. Geophys. Res.*, 101(10):21,943–21,960.

Bernard, P., Briole, P., Meyer, B., Lyon-Caen, H., Gomez, J.-M., Tiberi, C., Berge, C., Cattin, R., Hatzfeld, D., Lachet, C., Lebrun, B., Deschamps, A., Courboulex, F., Larroque, C., Rigo, A., Massonnet, D., Papadimitriou, P., Kassaras, J., Diagourtas, D., Makropoulos, K., Veis, G., Papazisi, E., Mitsakaki, C., Karakostas, V., Papadimitriou, E., Papanastassiou, D., Chouliaras, G., and Stavrakakis, G. (1997). The M_s = 6.2, June 15, 1995 Aigion earthquake (Greece): evidence for low angle normal faulting in the Corinth rift. *J. Seismol.*, 1:131–150.

Beutler, G., Mueller, I. I., and Neilan, R. E. (1994). The International GPS Service for Geodynamics (IGS): Development and start of official service on Januari 1. *Bull. Geod.*, 68:39–70.

Billiris, H., Paradissis, D., England, P., Featherstone, W., Parsons, B., Cross, P., Rands, P., Rayson, M., Sellers, P., Ashkenazi, V., Davison, M., Jackson, J., and Ambraseys, N. (1991). Geodetic determination of tectonic deformation in central Greece from 1900 to 1988. *Nature*, 350:124–129.

Bird, P. and Piper, K. (1980). Plane-stress finite element models of tectonic flow in southern California. *Phys. Earth Planet. Inter.*, 21:158–175.

Bock, Y., Prawirodirdjo, L., Genrich, J. F., McCaffrey, R., Stevens, C. W., Subarya, C., and Calais, E. (2001). GPS-derived microplate tectonics of Indonesia. *In preparation.*

Bock, Y., Wdowinski, S., Fang, P., Zhang, J., Willians, S., Johnson, H., Behr, J., Genrich, J., Dean, J., van Domselaar, M., Agnew, D., Wyatt, F., Stark, K., Oral, B., Hudnut, K., King, R., Herring, T., Dinardo, S., Young, W., Jackson, D., and Gurner, W. (1997). Southern California permanent GPS geodetic array: Continuous measurements of regional crustal deformation between the 1992 Landers and 1994 Northridge earthquakes. *J. Geophys. Res.*, 102:18013–18033.

Boucher, C., Altamimi, Z., and Sillard, P. (1999). The 1997 International Terrestial Reference Frame (ITRF97). Iers technical note no. 27, Observatoire de Paris, France.

Bourne, S. J. (1996). *Distributed deformation of the South Island of New Zealand*. D. Philos. thesis, Fac. of Phys. Sci., Univ. of Oxford, Oxford, England.

Bourne, S. J., Árnadóttir, T., Beavan, J., Darby, D. J., England, P. C., Parsons, B., Walcott, R. I., and Wood, P. R. (1998a). Crustal deformation of the Marlborough fault zone in the South Island of New Zealand: Geodetic constraints over the interval 1982-1994. *J. Geophys. Res.*, 103(12):30,147–30,165.

Bourne, S. J., England, P. C., and Parsons, B. (1998b). The motion of crustal blocks driven by flow of the lower lithosphere and implications for slip rates of continental strike-slip faults. *Nature*, 391:655–659.

Breen, N. A., Silver, E. A., and Roof, S. (1989). The Wetar back arc thrust belt, eastern Indonesia: the effect of accretion against an irregularly shaped arc. *Tectonophysics*, 8(1):85–98.

Briole, P., Rigo, A., Lyon-Caen, H., Ruegg, J. C., Hatzfeld, D., Deschamps, A., Papazissi, K., Mitsakaki, C., Agatza-Balodimou, A. M., and Veis, G. (1996). Active deformation of the Gulf of Corinth, Greece; results from repeated GPS surveys between 1990 and 1995. *Suppl., Eos, Trans. AGU*, 77.

Cardwell, R. K. and Isacks, B. L. (1978). Geometry of the subducted lithosphere beneath the banda sea in eastern Indonesia from seismicity and fault plane solutions. *J. Geophys. Res.*, 83:2825–2838.

Charlton, C. (1986). A plate tectonic model of the eastern Indonesia collision zone. *Nature*, 319:394–396.

Clarke, P., England, P., Parsons, B., Davies, R., Billiris, H., Galanis, J., Paradissis, D., Veis, G., Cross, P., Cruddace, P., Briole, P., Lyon-Caen, H., Kahle, H.-G., and Ambrosius, B. (1999). Some aspects of Aegean continental dynamics inferred from a decade of GPS measurements and a century of triangulation. *IUGG Abstracts B (1)*, 78.

Clarke, P. J., Davies, R. R., England, P. C., Parsons, B., Billiris, H., Paradissis, D., Veis, G., Cross, P. A., Denys, P. H., Ashkenazi, V., Bingley, R., Kahle, H.-G., Müller, M.-V., and Briole, P. (1998). Crustal strain in central Greece from repeated GPS measurements in the interval 1988-1997. *Geophys. J. Int.*, 135:195–214.

Clarke, P. J., Davies, R. R., England, P. C., Parsons, B. E., Billiris, H., Paradissis, D., Veis, G., Denys, P. H., Cross, P. A., Ashkenazi, V., and Bingley, R. (1997a). Geodetic estimate of seismic hazard in the Gulf of Korinthos. *Geophys. Res. Lett.*, 24:1303–1306.

Clarke, P. J., Paradissis, D., England, P., Parsons, B., Billiris, H., Briole, P., and Ruegg, J.-C. (1997b). Geodetic investigation of the 13 May 1995 Kozani-Grevena (Greece) earthquake. *Geophys. Res. Lett.*, 24(6):707–712.

Cloetingh, S. and Wortel, R. (1986). Stress in the Indo-Australian plate. *Tectonophysics*, 132(1):49–67.

Coblentz, D. D., Zhou, S., Hillis, R. R., Richardson, R. M., and Sandiford, M. (1998). Topography, boundary forces, and the Indo-Australian intraplate stress field. *J. Geophys. Res.*, 103(1):919–931.

Cocard, M., Kahle, H.-G., Peter, Y., Geiger, A., Veis, G., Felekis, S., Billiris, H., and Paradissis, D. (1999). New constraints on the rapid crustal motion of the Aegean region: Recent results inferred from GPS measurements (1993-1996) across the West Hellenic Arc. *Earth Planet. Sci. Lett.*, 172:39–47.

Cook, D. C., Malkus, D. S., and Plesha, M. E. (1989). *Concepts and applications of finite element analysis*. John Wiley & Sons, New York.

Coward, M. P. and Ries, A. C., editors (1986). *Collision tectonics*. Number 19 in Spec. Publ. geol. Soc. London. Blackwell Scientific Publications, Oxford.

Cruddace, P. R., Cross, P. A., Veis, G., Billiris, H., Paradissis, D., Galanis, J., Lyon-Caen, H., Briole, P., Ambrosius, B. A. C., Simons, W. J. F., Roegies, E., Parsons, B., England, P., Kahle, H.-G., Cocard, M., Yannick, P., Stavrakakis, G., Clarke, P., and Lilje, M. (1999). An interdisciplinary approach to studying seismic hazard throughout Greece. *IUGG Abstracts B (1)*, 78.

Curray, J. R., Moore, D. G., Lawver, L. A., Emmel, F. J., Raitt, R. W., Henry, M., and Kieckhefer, R. (1979). Tectonics of the andaman sea and burma. In Watkins, J. S., Montadert, L., and Dickerson, P., editors, *Geological and Geophysical Investigations of Continental Margins*, volume 29, pages 189–198. Mem. A. Assoc. Pet. Geol.

Davies, R. R., England, P., Parsons, B., Billiris, H., Paradissis, D., and Veis, G. (1997). Geodetic strain of Greece in the interval 1892-1992. *J. Geophys. Res.*, 102(11):24,571–24,588.

DeMets, C., Gordon, R. G., Argus, D. F., and Stein, S. (1990). Current plate motions. *Geophys. J. Int.*, 101:425–478.

DeMets, C., Gordon, R. G., Argus, D. F., and Stein, S. (1994). Effects of recent revisions to the geomagnetic reversal time scale on estimates of current plate motions. *Geophys. Res. Lett.*, 21:2191–2194.

Denys, P., Cross, P., Veis, G., Billiris, H., Paradissis, D., Ashkenazi, V., Bingley, R., England, P., Clarke, P., Kahle, H.-G., and Mller, M. V. (1995). GPS networks for determinig the accumulation of current crustal strain in Central Greece. *Proc. of the 1^{st} International Symposium on Deformation in Turkey, Ankara, TMMOB-HKMO*, 2:748–758.

Dewey, J. F., Hempton, M. R., Kidd, W. S. F., Saroğlu, F., and Sengör, A. M. C. (1986). Shortening of continental lithosphere: the neotectonics of Eastern Anatolia - a young collision zone. In Coward and Ries [1986], pages 3–36.

Diament, M., Harjano, H., Karta, K., Deplus, C., Dahrin, D., Jr., M. T. Z., Gérard, M., Lassal, O., Martin, A., and Malod, J. (1992). Mentawai fault zone off Sumatra: A new key to the geodynamics of western Indonesia. *Geology*, 20:259–262.

Duermeijer, C. E., Nyst, M., P. Th. Meijer, C. G. L., and Spakman, W. (2000). Neogene evolution of the Aegean arc: paleomagnetic and geodetic evidence for a rapid and young rotation phase. *Earth. Planet. Sci. Lett.*, 176:509–525.

Duquesnoy, T., Barrier, E., Kasser, M., Aurelio, M., Gaulon, R., Punongbayan, R. S., Rangin, C., and the French-Philippine Cooperation Team (1994). Detection of creep along the Philippine Fault: First results of geodetic measurements on Leyte island, central Philippine. *Geophys. Res. Lett.*, 21(11):975–978.

Dziewonski, A. M., Chou, T.-A., and Woodhouse, J. H. (1981). Determination of earthquake source parameters from waveform data for studies of global and regional seismicity. *J. Geophys. Res.*, 86:2825–2852.

Ekström, G. and England, P. (1989). Seismic strain rates in regions of distributed continental deformation. *J. Geophys. Res.*, 94(8):10,231–10,257.

England, P. and Jackson, J. (1989). Active deformation of the continents. *Ann. Rev. Earth Planet. Sci.*, 17:197–226.

England, P. and McKenzie, D. (1982). A thin viscous sheet model for continental deformation. *Geophys. J. R. astr. Soc.*, 70:295–321.

England, P. C. and Houseman, G. A. (1985). Role of lithospheric strength heterogeneities in the tectonics of Tibet and neighbouring regions. *Nature*, 315:297–301.

England, P. C. and Molnar, P. (1997). The field of crustal velocity in Asia calculated from Quaternary rates of slip on faults. *Geophys. J. Int.*, 130:551–582.

Feigl, K. L., Agnew, D. C., Bock, Y., Dong, D., Donnellan, A., Hager, B. H., Herring, T. A., Jackson, D. D., Jordan, T. H., King, R. W., Larsen, S., Larson, K. M., Murray, J. H., Shen, Z., and Webb, F. H. (1993). Space geodetic measurement of crustal deformation in central and southern california, 1984-1992. *J. Geophys. Res.*, 98:21,677–21,712.

Fitch, T. J. (1972). Plate convergence, transcurrent faults, and internal deformation adjacent to Southeast Asia and the Western Pacific. *J. Geophys. Res.*, 77:4432–4460.

Frank, F. C. (1966). Deduction of Earth strains from survey data. *Bull. Seismol. Soc. Am.*, 56:35–42.

Freund, L. B. and Barnett, D. M. (1976). A two-dimensional analysis of surface deformation due to dip-slip faulting. *Bull. Seism. Soc. Am.*, 66:667–675.

Freund, R. (1970). Rotation of strike-slip faults in Sistan, Southeastern Iran. *J. Geol.*, 78:188–200.

Genrich, J. F., Bock, Y., McCaffrey, R., Calais, E., Stevens, C. W., and Subarya, C. (1996). Accretion of the southern Banda Arc to the Australian Plate margin determined by Global Positioning System measurements. *Tectonics*, 15(2):288–295.

Genrich, J. F., Bock, Y., McCaffrey, R., Prawirodirdjo, L., Stevens, C. W., Puntodewo, S. S. O., Subarya, C., and Wdowiski, S. (2000). Distribution of slip at the northern Sumatran fault system. *J. Geophys. Res.*, 105(12):28,327–28,341.

Gilbert, L., Kastens, K., Hurst, K., Paradissis, D., Veis, G., Billiris, H., Höppe, W., and Schlüter, W. (1994a). Strain results and tectonics form the Aegean GPS experiment. *Suppl., Eos, Trans. AGU*, 67.

Gilbert, L. E., Scholz, C. H., and Beavan, J. (1994b). Strain localization along the San Andreas Fault: Consequences for loading mechanisms. *J. Geophys. Res.*, 99(12):23,975–23,984.

Gordon, R. G. and Stein, S. (1992). Global tectonics and space geodesy. *Science*, 256:333–342.

Govers, R. M. A. (1993). *Dynamics of lithospheric extension: A modeling study*. Number 105 in PhD Dissertation, Geologica Ultraiectina. Utrecht University, The Netherlands.

Guzmán-Speziale, M. and Ni, J. F. (1996). Seismicity and active tectonics of the Western Sunda Arc. In Yin, A. and Harrison, M., editors, *Tectonic evolution of Asia*, pages 63–84. Cambridge University Press, Cambridge, UK.

Haile, N. S. (1978). Paleomagnetic evidence for the rotation of Seram, Indonesia. *J. Phys. Earth*, 26:191–198. Supplement.

Haines, A. J. (1982). Calculating velocity fields across plate boundaries from observed shear rates. *Geophys. J. R. astr. Soc.*, 68:203–209.

Haines, A. J. and Holt, W. E. (1993). A procedure for obtaining the complete horizontal motions within zones of distributed deformation from the inversion of strain rate data. *Geophys. J. R. astr. Soc.*, 98:12,057–12,082.

Haines, A. J., Jackson, J. A., Holt, W. E., and Agnew, D. C. (1998). Representing distributed deformation by continuous velocity fields. Sci. rep., Inst. of Geol. and Nucl. Sci., Lower Hutt, New Zealand. 110 pp.

Hall, R. and Blundell, D., editors (1996). *Tectonic evolution of Southeast Asia*. Number 106 in Geological Society Special Publication. The Geological Society Publishing House, Bath, UK.

Hamilton, W. (1979). Tectonics of the Indonesian region. Prof. paper 1078, U.S.G.S.

Haslinger, F., Kissling, E., Ansorge, J., Hatzfeld, D., Papadimitriou, E., Karalostas, V., Makropoulos, K., Kahle, H.-G., and Peter, Y. (1999). 3D crustal structure from local earthquake tomography around the Gulf of Arta (Ionian region, NW Greece). *Tectonophysics*, 304:201–218.

Hatzfeld, D., Pedotti, G., Hatzidimitriou, P., and Makropoulos, K. (1990). The strain pattern in the western Hellenic arc deduced from a microearthquake survey. *Geophys. J. Int.*, 101:181–202.

Heki, K. (1996). Horizontal and vertical crustal movements from three-dimensional very long baseline interferometry kinematic reference frame: Implication for the reversal timescale revision. *J. Geophys. Res.*, 101:3187–3198.

Herring, T. A. (1999). Global Kalman filter VLBI and GPS analysis program. Version 5.0, Department of Earth, Atmospheric, and Planetary Sciences, Massachussetts Institute of technology and Scripps Institution of Oceanography, University of California at San Diego, USA.

Holt, W. E. and Haines, A. J. (1993). Velocity fields in deforming Asia from the inversion of earthquake-released strains. *Tectonics*, 12(1):1–20.

Holt, W. E. and Haines, A. J. (1995). The kinematics of nortern South Island, New Zealand, determined from geologic strain rates. *J. Geophys. Res.*, 100(9):17,991–18,010.

Houseman, G. A. and England, P. C. (1986). Finite strain calculations of continental deformation 1. Method and general results for convergent zones. *J. Geophys. Res.*, 91:3651–3663.

Hu, J.-C., Angelier, J., and Yu, S.-B. (1997). An interpretation of the active deformation of southern Taiwan based on numerical simulation and GPS studies. *Tectonophysics*, 274:145–169.

Jackson, D. D. (1979). The use of a priori data to resolve non-uniqueness in linear inversion. *Geophys. J. R. Astron. Soc.*, 57:137–157.

Jackson, J. (1994). Active tectonics of the Aegean Region. *Annu. Rev. Earth Planet. Sci.*, 22:239–271.

Jackson, J., Haines, J., and Holt, W. (1992). The horizontal velocity field in the deforming Aegean Sea Region determined from the moment tensors of earthquakes. *J. Geophys. Res.*, 97:17,657–17,684.

Jackson, J. and McKenzie, D. (1988). The relationship between plate motions and seismic tremors, and the rates of active deformation in the Mediterranean and Middle East. *Geophys. J. R. Astron. Soc.*, 93:45–73.

Jackson, J. and McKenzie, D. P. (1984). Active tectonics of the Alpine-Himalayan Belt between western Turkey and Pakistan. *Geophys. J.*, 77:185–246.

Jarrard, R. D. (1986). Relations among subduction parameters. *Rev. of Geophys.*, 24(2):217–284.

Johnson, H. O., Agnew, D. C., and Wyatt, F. K. (1994). Present-day crustal deformation in southern California. *J. Geophys. Res.*, 99(12):23,951–23,974.

Johnston, C. and Bowin, C. (1981). Crustal reactions resulting from the mid-pliocene to recent continent-island arc collision in the Timor region. *BMR J. Aust. Geol. Geophys.*, 6:223–243.

Jolivet, L., Brun, J.-P., Gautier, P., Lallemant, S., and Patriat, M. (1994). 3d-kinematics of extension in the Aegean region from the early Miocene to the Present, insights from the ductile crust. *Bull. Soc. géol. France*, 165(3):195–209.

Kahle, H.-G., Cocard, M., Peter, Y., Geiger, A., Reilinger, R., Barka, A., and Veis, G. (2000). GPS-derived strain rate field within the boundary zones of the Eurasian, African, and Arabian Plates. *J. Geophys. Res.*, 105:23,353–23,370.

Kahle, H.-G., Müller, M. V., Geiger, A., Danuser, G., Mueller, S., Veis, G., Billiris, H., and Paradissis, D. (1995). The strain field in northwestern Greece and Ionian Islands: results inferred from GPS measurements. *Tectonophysics*, 249:41–52.

Kahle, H.-G., Müller, M. V., and Veis, G. (1996). Trajectories of crustal deformation of western Greece from GPS observations, 1989-1994. *Geophys. Res. Lett.*, 23(6):677–680.

Karig, D. E., Barber, A. J., Charlton, T. R., Klemperer, S., and Hussong, D. M. (1987). Nature and distribution of deformation across the Banda arc-australia collision zone at Timor. *Geol. Soc. Am. Bull.*, 98:18–32.

Kastens, K. A., Balis, V., Billiris, H., Chayes, D., Elsner, C., Friedhoff, H., Habrich, H., Hurst, K., Koczynski, T., Milas, P., Mueller, A., Mueller, W., Papafitsorou, A., Paradissis, D., Raymond, C., Riecken, J., Sorge, B., Stephens, B., Stowell, J., Tsolakis, D., Tziotzis, J., Veis, G., and Vlachos, C. (1989). The Aegean GPS Project; 1988 results and 1989 plans. *Eos, Trans. AGU*, 70.

Kato, T., El-Fiky, G. S., Oware, E. N., and Miyazaki, S. (1998a). Crustal strains in the Japanese island as deduced from dense GPS arrays. *Geophys. Res. Lett.*, 25:3445–3449.

Kato, T., Kotake, Y., Nakao, S., Beavan, J., Hirahara, K., Okada, M., Hoshiba, M., Kamigaichi, O., Feir, R. B., Park, P. H., Gerasimenko, M. D., and Kasahara, M. (1998b). Initial results from WING, the continuous GPS network in the western Pacific area. *Geophys. Res. Lett.*, 25(3):369–372.

King, G. and Cisternas, A. (1991). Do little things matter? *Nature*, 351:350.

King, G., Oppenheimer, D., and Amelung, F. (1994). Block versus continuum deformation in the Western United States. *Earth planet. Sci. Lett.*, 128:55–64.

King, R. W. and Bock, Y. (1999). Documentation for the GAMIT GPS Analysis Software. Release 9.7, Department of Earth, Atmospheric, and Planetary Sciences, Massachussetts Institute of technology and Scripps Institution of Oceanography, University of California at San Diego, USA.

Kissel, C. and Laj, C. (1988). The Tertiary geodynamical evolution of the Aegean arc: a paleomagnetic reconstruction. *Tectonophysics*, 146:183–201.

Kissel, C., Laj, C., and Mazaud, A. (1986). First paleomagnetic results from Neogene formations in Evia, Skyros, and the Volos region, and the deformation of Central Aegean. *Geophys. Res. Lett.*, 13:1446–1449.

Kondopoulo, D. P. and Pavlides, S. B. (1990). Paleomagnetic and neotectonic evidence for different deformation patterns in the south Aegean volcanic arc: the case of Melos island. *Intern. Earth Sci. Congres on Aegean Regions, Proceedings*, 1:210–223.

Kostrov, V. V. (1974). Seismic moment and energy of earthquakes, and seismic flow of rocks. *Izv. Acad. Sci. USSR Phys. Solid Earth*, 1:23–44.

Koukouvelas, I. K. and Doutsos, T. T. (1996). Implications of structural segmentation during earthquakes: the 1995 Egion earthquake, Gulf of Corinth, Greece. *J. Struct. Geol.*, 18(12):1381–1388.

Kreemer, C., Holt, W. E., Goes, S., and Govers, R. (2000). Active deformation in eastern Indonesia and the Philippines from GPS and seismicity data. *J. Geophys. Res.*, 105:663–680.

Kurt, H., Demirbağ, E., and Kuşçu, I. (1999). Investigation of the submarine active tectonism in the Gulf of Gökova, southwest Anatolia - southeast Aegean Sea, by multi-channel seismic reflection data. *Tectonophysics*, 305:477–496.

Lallemand, S. E., Popoff, M., Cadet, J.-P., Bader, A.-G., Pubellier, M., Rangin, C., and Deffontaines, B. (1998). Genetic relations between the central and southern Philippine Trench and the Sangihe Trench. *J. Geophys. Res.*, 103(1):933–950.

Lamb, S. H. (1987). A model for tectonic rotations about a vertical axis. *Earth planet. Sci. Lett.*, 84:75–86.

Lamb, S. H. (1994). Behavior of the brittle crust in wide plate boundary zones. *J. Geophys. Res.*, 99(3):4457–4483.

Larsen, S. and Reilinger, R. (1992). Global Positioning System measurements of strain accumulation across the Imperial Valley, California: 1986-1989. *J. Geophys. Res.*, 97:8865–8876.

Larson, K. M. (1993). Application of the Global Positioning System to crustal deformation measurements, 3. result from the Southern California Borderlands. *J. Geophys. Res.*, 98:21,713–21,726.

Larson, K. M., Freymuller, J. T., and Philipsen, S. (1997). Global plate velocities from the Global Positioning System. *J. Geophys. Res.*, 102:9961–9981.

Le Pichon, X. and Angelier, J. (1979). The Hellenic Arc and trench system: A key to the neotectonic evolution of the eastern Mediterranean area. *Tectonophysics*, 60:1–42.

Le Pichon, X., Chamot-Rooke, N., Lallemant, S., Noomen, R., and Veis, G. (1995). Geodetic determination of the kinematics of central Greece with respect to Europe: Implications for eastern Mediterranean tectonics. *J. Geophys. Res.*, 100:12,675–12,690.

Lee, T.-Y. and Lawver, L. A. (1994). Cenozoic plate reconstruction of South China Sea region. *Tectonophysics*, 235:149–180.

Lee, T.-Y. and Lawver, L. A. (1995). Cenozoic plate reconstruction of Southeast Asia. *Tectonophysics*, 251:85–138.

Lévêque, J.-J., Rivera, L., and Wittlinger, G. (1993). On the use of the checker-board test to assess the resolution of tomographic inversions. *Geophys. J. Int.*, 115:313–318.

Louvari, E., Kiratzi, A. A., and Papazachos, B. C. (1999). The Cephalonia Transform Fault and its extension to western Lefkada Island (Greece). *Tectonophysics*, 308:223–236.

Lundgren, P., Saucier, F., Palmer, R., and Langon, M. (1995). Alaska crustal deformation: Finite element modeling constrained by geologic and VLBI data. *J. Geophys. Res.*, 100:22,303–22,045.

Malod, J. A. and Kemal, B. M. (1996). The Sumatra margin: oblique subduction and lateral displacement of the accretionary prism. In Hall and Blundell [1996], pages 19–28.

Mantovani, E., Albarello, D., Babbucci, D., and Tamborelli, C. (1992). Recent geodynamic evolution of the central Mediterranean region (Tortonian to Present). Technical report, Dep. of Earth Sci. Univ. of Siena, Siena, Italy.

Matheussen, S. (2000). Exploring the limits of GPS for geo-kinematic applications: A case study of crustal motions in South-East Asia. MSc. thesis, Delft Institute for Earth-Oriented Space Research, Delft University of Technology, Delft, The Netherlands.

Matsu'ura, M., Jackson, D. D., and Cheng, A. (1986). Dislocation model for aseismic crustal deformation at Hollister, California. *J. Geophys. Res.*, 91:12,661–12,674.

McCaffrey, R. (1988). Active tectonics of the eastern Sunda and Banda arcs. *J. Geophys. Res.*, 93:15,163–15,182.

McCaffrey, R. (1991). Slip vectors and stretching of the Sumatran forearc. *Geology*, 19:881–884.

McCaffrey, R. (1992). Oblique plate convergence, slip vectors, and fore-arc deformation. *J. Geophys. Res.*, 97:8905–8915.

McCaffrey, R. (1996). Estimates of modern arc-parallel strain rates in fore arcs. *Geology*, 24(1):27–30.

McCaffrey, R. and Abers, G. A. (1991). Orogeny in arc-continent collision: The Banda arc and western New Guinea. *Geology*, 19:563–566.

McCaffrey, R., Zwick, P. C., Bock, Y., Prawirodirdjo, L., Genrich, J. F., Stevens, C. W., Puntodewo,

S. S. O., and Subarya, C. (2000). Strain partitioning during oblique plate convergence in northern Sumatra: Geodetic and seismologic constraints and numerical modeling. *J. Geophys. Res.*, 105(12):28,363–28,376.

McClusky, S., Balassanian, S., Barka, A., Demir, C., Georgiev, S. E. I., Gurkan, O., Hamburger, M., Hurst, K., Kahle, H., Kastens, K., Kekelidze, G., King, R., Kotzev, V., Lenk, O., Mahmoud, S., Mishin, A., Nadariya, M., Ouzounis, A., Paradissis, D., Peter, Y., Prilepin, M., Reilinger, R., Sanli, I., Seeger, H., Tealeb, A., Toksöz, M. N., and Veis, G. (2000). Global Positioning System constraints on plate kinematics and dynamics in the eastern Mediterranean and Caucasus. *J. Geophys. Res.*, 105:5695–5719.

McKenzie, D. (1978). Active tectonics of the Alpine Himalayan Belt, the Aegean Sea and surrounding regions. *Geophys. J. R. astr. Soc.*, 55:217–254.

McKenzie, D. and Jackson, J. (1983). The relationship between strain rates, crustal thickening, paleomagnetism, finite strain and fault movements within a deforming zone. *Earth. Plan. Sci. Lett.*, 65:182–202.

McKenzie, D. and Jackson, J. (1986). A block model of distributed deformation by faulting. *J. Geol. Soc. London*, 143:349–353.

McKenzie, D. P. (1972). Active tectonics of the Mediterranean Sea. *Geophys. J. R. astr. Soc.*, 30:109–185.

Meijer, P. T. and Wortel, M. J. R. (1997). Present-day dynamics of the Aegean region: A model analysis of the horizontal pattern of stress and deformation. *Tectonics*, 16:879–895.

Menke, W. (1989). *Geophysical Data Analysis: Discrete Inverse Theory (revised edition)*, volume 45 of *International Geophysics Series*. Academic Press, Inc, San Diego, California.

Mercier, J. L., Sorel, D., and Simeakis, K. (1987). Changes in the overriding plate of a subduction zone: the Aegean arc from the Pliocene to the present. *Annales Tectonicae*, 1:20–39.

Michel, G., Reigber, C., Becker, M., Seeger, H., Simons, W., Vigny, C., Chamot-Rooke, N., Pichon, X. L., and P. Morgan, S. M. (2001). Crustal motion and block behaviour in SE-Asia from GPS measurements. *Earth Planet. Sci. Lett.*, 187:289–244.

Milsom, J., Masson, D., Nichols, G., Sikumbang, N., Dwiyanti, B., Parson, L., and Kallagher, H. (1992). The Manokwari trough and the western end of the New Guinea trench. *Tectonics*, 11:145–153.

Molnar, P. (1988). Continental tectonics in the aftermath of plate tectonics. *Nature*, 335:131–137.

Mueller, S. and Kahle, H.-G. (1993). Crust-mantle evolution, sturcture and dynamics of the Mediterranean-Alpine region. In Smith and Turcotte [1993], pages 249–298.

Newcomb, K. R. and McCann, W. R. (1987). Seismic history and seismotectonics of the Sunda Arc. *J. Geophys. Res.*, 92(1):421–439.

Nichols, G., Hall, R., Milsom, J., Masson, D., Parson, L., Sikumbang, N., Dwiyanto, B., and Kallagher, H. (1990). The southern termination of the Philippine trench. *Tectonophysics*, 183:289–303.

Noomen, R., Ambrosius, B. A. C., and F.Wakker, K. (1993). Crustal Motions in the Mediterranean Region Determined from Laser Ranging to LAGEOS. In Smith and Turcotte [1993], pages 331–346.

Noomen, R., Springer, T. A., Ambrosius, B. A. C., Herzberger, K., Kuijper, D. C., Mets, G.-J., Overgaauw, B., and Wakker, K. F. (1996). Crustal deformations in the Mediterranean area computed from SLR and GPS observations. *J. Geodynamics*, 21:73–96.

Okada, Y. (1985). Surface deformation due to shear and tensile faults in a half-space. *Bull. seism. Soc. A.*, 75:1135–1154.

Pacheco, J. F. and Sykes, L. R. (1992). Seismic moment catalog of large shallow earthquakes, 1900 to 1989. *Bull. Seis. Soc. A.*, 82(3):1306–1349.

Papazachos, B. C., , and Papazachos, C. B. (1989). *The earthquakes of Greece*. Ziti Publications, Thessaloniki. pp. 356.

Papazachos, B. C., Karakaisis, G. F., Papazachos, C. B., and Scordilis, E. M. (2000). Earthquake triggering in the North and East Aegean plate boundaries due to the Anatolia westward motion. *Geophys. Res. Lett.*, 27(23):3957–3960.

Papazachos, B. C., Papaioannou, C. A., Papazachos, C. B., and Savvaidis, A. S. (1999). Rupture zones in the Aegean region. *Tectonophysics*, 308:205–221.

Papazachos, C. B. (1999). Seismological and GPS evidence for the aegean - anatolia interaction. *Geophys. Res. Lett.*, 26(17):2653–2656.

Papazachos, C. B. and Kiratzi, A. A. (1996). A detailed study of the active crustal deformation in the Aegean and surrounding area. *Tectonophysics*, 253:129–153.

PCGIAP Working Group 1 (1998). *Proceedings of the Workshop on Regional Geodetic Network, Canberra, Australia*. Australian Surveying and Land Information Group, Belconnen, ACT, Australia.

Peltzer, G. and Saucier, F. (1996). Present-day kinematics of Asia derived from geologic fault rates. *J. Geophys. Res.*, 101(12):27,943–27,956.

Peltzer, G. and Tapponnier, P. (1988). Formation and evolution of strike-slip faults, rifts, and basins during the India-Asia collision: an experimental approach. *J. Geophys. Res.*, 93(12):15,085–15,117.

Pham, V. N., Bernard, P., Boyer, D., Chouliaras, G., Mouël, J. L. L., and Stavrakakis, G. N. (2000). Electrical conductivity and crustal structure beneath the central Hellenides around the Gulf of Corinth (Greece) and their relationship with the seismotectonics. *Geophys. J. Int.*, 142(3):948–969.

Pollitz, F. F., Peltzer, G., and Bürgmann, R. (2000). Mobility of continental mantle: Evidence from postseismic geodetic observations following the 1992 Landers earthquake. *J. Geophys. Res.*, 105(4):8035–8054.

Prawirodirdjo, L., Bock, Y., Genrich, J., Puntodewo, S. S. O., Rais, J., Subarya, C., and Sutisna, S. (2000). One century of tectonic deformation along the Sumatran fault from triangulation and Global Positioning System surveys. *J. Geophys. Res.*, 105(12):28,343–28,362.

Prawirodirdjo, L., Bock, Y., McCaffrey, R., Genrich, J., Calais, E., Stevens, C., Puntodewo, S. S. O., Subarya, C., Rais, J., Zwick, P., and Fauzi (1996). Geodetic observations of interseismic strain segmentation at the Sumatra subduction zone. *Geophys. Res. Lett.*, 24(21):2601–2604.

Press, W. H., Flannery, B. P., Teukolsky, S. A., and Vetterling, W. T. (1992). *Numerical Recipes, the art of Scientific computing (Fortran Version)*. Cambridge University Press, New York.

Puntodewo, S. S. O., McCaffrey, R., Calais, E., Bock, Y., Rais, J., Subarya, C., Poewariardi, R., Stevens, C., Genrich, J., Fauzi, Zwick, P., and Wdowinski, S. (1994). GPS measurements of crustal deformation within the Pacific-Australia plate boundary zone in Irian Jaya, Indonesia. *Tectonophysics*, 237:141–153.

Quebral, R. D., Pubellier, M., and Rangin, C. (1996). The onset of movement on the Philippine Fault in eastern Mindanao: A transition from collision to a strike-slip environment. *Tectonics*, 15(4):713–726.

Rangin, C. (1989). The Sulu sea: a backarc basin setting within a Neogene collision zone. *Tectonophysics*, 161:119–141.

Rangin, C., Pichon, X. L., Mazzotti, S., Pubellier, M., Chamot-Rooke, N., Aurelio, M., Walpersdorf, A., and Quebral, R. (1999). Plate convergence measured by GPS across the Sundaland/Philippine Sea Plate deformed boundary: the Philippines and eastern Indonesia. *Geophys. J. Int.*, 139(2):296–316.

Ranken, B., Cardwell, R. K., and Karig, D. E. (1984). Kinematics of the philippine sea plate. *Tectonics*, 3:555–575.

Reilinger, R., McClusky, S., Oral, M., King, R., Toksoz, M., Barka, A., Kinik, I., Lenk, O., and Sanli, I. (1997). Global Positioning System measurements of present-day crustal movements in the Arabia-Africa-Eurasia plate collision zone. *J. Geophys. Res.*, 102(5):9983–9999.

Rietbrock, A., Tiberi, C., Scherbaum, F., and Lyon-Caen, H. (1996). Seismic slip on a low angle normal fault in the Gulf of Corinth: evidence from high resolution cluster analysis of microearthquakes. *Geophys. Res. Lett.*, 14:1817–1820.

Rigo, A., Lyon-Caen, H., Armijo, R., Descamps, A., Hatzfeld, D., Makropoulos, K., Papadimitriou, P., and Kassaras, I. (1996). A microseismic study in the western part of the Gulf of Corinth (Greece): implications for large-scale normal faulting mechanisms. *Geophys. J. Int.*, 126:663–688.

Rothacher, M. and Mervart, L. (1996). Bernese GPS software version 4.0. Technical report, Astronomical Institute, University of Berne.

Ruppert, J. (1985). A Delaunay refinement algorithm for quality two-dimensional mesh generation. *Journal of algorithms*, 18(3):548–585.

Samuel, M. A. and Harbury, N. A. (1996). The Mentawai fault zone and deformation of the Sumatran Forearc in the Nias area. In Hall and Blundell [1996], pages 337–351.

Saucier, F. and Humphreys, E. (1993). Horizontal crustal deformation in southern California from joint models of geology and very long baseline interferometry measurements. In Smith and Turcotte [1993], pages 139–176.

Savage, J. C. (1990). Equivalent strike-slip earthquake cycles in half-space and lithosphere-astenosphere earth models. *J. Geophys. Res.*, 95(4):4873–4879.

Savage, J. C. and Burford, R. O. (1973). Geodetic determination of relative plate motion in central California. *J. Geophys. Res.*, 78:832–845.

Savage, J. C., Prescott, W. H., Lisowski, M., and King, N. E. (1979). Geodolite measurements of deformation near hollister, california. *J. Geophys. Res.*, 84:7599–7615.

Scales, J. A., Docherty, P., and Gerztenkorn, A. (1990). Regularisation of nonlinear inverse problems: imaging the near-surface weathering layer. *Inverse Problems*, 6:115–131.

Scholz, C. H. and Cowie, P. A. (1990). Determination of total strain from faulting using slip measurements. *Nature*, 346:837–839.

Seno, T., Stein, S., and Gripp, A. E. (1993). A model for the motion of the Philippine Sea plate consistent with NUVEL-1 and geological data. *J. Geophys. Res.*, 98(10):17,941–17,948.

Shewchuk, J. R. (1996). Triangle: Engineering a 2D quality mesh generator and Delaunay triangulator. First workshop on applied computational geometry, Philadelphia, Pennsylvania.

Sieh, K. and Natawidjaja, D. (2000). Neotectonics of the Sumatran faulr, Indonesia. *J. Geophys. Res.*, 105(12):28,295–28,326.

Sieh, K., Rais, J., and Bock, Y. (1991). Neotectonic and paleoseismic studies in West and North Sumatra (abstract). *Eos Trans. AGU*, 72.

Sieh, K., Zachariasen, J., Edwards, L., Taylor, F., and Gans, P. (1994). Active tectonics of Sumatra. *Geol. Soc. Am., Abstracts with programs*, 26(7).

Sillard, P., Altamimi, Z., and Boucher, C. (1998). The ITRF96 realization and its associated velocity field. *Geophys. Res. Lett.*, 25(17):3223–3226.

Silver, E. A., Breen, N. A., Prasetyo, H., and Hussong, D. M. (1986). Multibeam study of the Flores backarc thrust belt, Indonesia. *J. Geophys. Res.*, 91(3):3489–3500.

Silver, E. A., McCaffrey, R., and Smith, R. B. (1983a). Collision, rotation, and the initiation of subduction in the evolution of Sulawesi, Indonesia. *J. Geophys. Res.*, 88(11):9407–9418.

Silver, E. A., Reed, D., McCaffrey, R., and Joyodiwiryo, Y. (1983b). Back arc thrusting in the eastern Sunda arc, Indonesia: A consequence of arc-continent collision. *J. Geophys. Res.*, 88(9):7429–7448.

Simons, W. J. F., Ambrosius, B. A. C., Noomen, R., Angermann, D., Wilson, P., Becker, M., Reinhart, E., Walpersdorf, A., and Vigny, C. (1999). Observing plate motion in SE Asia: Geodetic results of the GEODYSSEA project. *Geophys. Res. Lett.*, 26:2081–2084.

Smith, D. E., Kolenkiewicz, R., Dunn, P. J., Robbins, J. W., Torrence, M. H., Klosko, S. M., Williamson, R. G., Pavlis, E. C., Douglas, N. B., and Fricke, S. K. (1990). Tectonic motion and deformation from satellite laser ranging to LAGEOS. *J. Geophys. Res.*, 95:22013–22041.

Smith, D. E., Kolenkiewicz, R., Robbins, J. W., Dunn, P. J., and Torrence, M. H. (1994). Horizontal crustal motion in the central and eastern Mediterranean inferred from satellite laser ranging measurements. *Geophys. Res. Lett.*, 21:1979–1982.

Smith, D. E. and Turcotte, D. L., editors (1993). *Contributions of Space Geodesy to Geodynamics: Crustal Dynamics*. Number 23 in Geodyn. Ser. AGU, Washington D.C.

Snyder, D. B., Prasetyo, H., Blundell, D. J., Pigram, C. J., Barber, A. J., Richardson, A., and Tjokosapoetro, S. (1996). A dual doubly vergent orogen in the Banda Arc content-arc collision zone as observed on deep seismic reflection profiles. *Tectonics*, 15:34–53.

Stevens, C., McCaffrey, R., Bock, Y., Genrich, J., Endang, Subarya, C., Puntodewo, S. S. O., Fauzi, and Vigny, C. (1999). Rapid rotations about a vertical axis in a collisional setting revealed by the Palu fault, Sulawesi, Indonesia. *Geophys. Res. Lett.*, 26:2677–2680.

Stiros, S. C. (1998). Historical seismicity, paleoseismicity and seismic risk in western Macedonia, northern Greece. *J. Geodynamics*, 26:271–287.

Straub, C. (1996). *Recent Crustal Strain Accumulation in the Marmara Sea Region, NW Anatolia, inferred from GPS Measurements*. PhD dissertation, Eidgenössischen Technischen Hochschule, Zürich, Institut für Geodäsie und Photogrammetrie.

Straub, C., Kahle, H.-G., and Schindler, C. (1997). GPS and geologic estimates of the tectonic activity in the Marmara Sea region, NW Anatolia. *J. Geophys. Res.*, 102:27,587–27,601.

Suppe, J. (1981). Mechanics of mountain building and metamorphism in Taiwan. *Geol. Soc. China Mem.*, 4:67–89.

Surmont, J., Laj, C., Kissel, C., Rangin, C., Bellon, H., and Priadi, B. (1994). New paleomagnetic constraints on the Cenozoic tectonic evolution of the North Arm of Sulawesi, Indonesia. *Earth planet. Sci. Lett.*, 121:629–638.

Tapponnier, P. and Molnar, P. (1976). Slip-line field theory and large scale continental tectonics. *Nature*, 264:319–324.

Tapponnier, P., Peltzer, G., and Armijo, R. (1986). On the mechanics of the collision between India and Asia. In Coward and Ries [1986], pages 115–157.

Taymaz, T., Jackson, J., and McKenzie, D. (1991). Active tectonics of the north and central Aegean Sea. *Geophys. J. Int.*, 106:433–490.

Thatcher, W. (1995). Microplates versus continuum descriptions of active tectonic deformation. *J. Geophys. Res.*, 100(3):3885–3895.

Tiberi, C., Lyon-Caen, H., Hatzfeld, D., Achauer, U., Karagianni, E., Kiratzi, A., Louvari, E., Panagiotopoulos, D., Kassaras, I., Kaviris, G., Makropoulos, K., and Papadimitriou, P. (2000). Crustal and upper mantle structure beneath the Corinth rift (Greece) from a teleseismic tomography study. *J. Geophys. Res.*, 105:28,159–28,171.

Tikoff, B. and Theyssier, C. (1994). Strain modeling of displacement-field partitioning in transpressional orogens. *J. Struct. Geol.*, 16(11):1575–1588.

Tregoning, P., Brunner, F. K., Bock, Y., Puntodewo, S. S. O., McCaffrey, R., Genrich, J. F., Calais, E., Rais, J., and Subarya, C. (1994). First geodetic measurements of convergence across the Java Trench. *Geophys. Res. Lett.*, 21:2135–2138.

Tregoning, P., Lambeck, K., Stolz, A., Morgan, P., McClusky, S. C., van der Beek, P., McQueen, H., Jackson, R. J., Little, R. P., Laing, A., and Murphy, B. (1998). Estimation of current plate motions in Papua New Guinea from Global Positioning System observations. *J. Geophys. Res.*, 6:12,181–12,203.

Veis, G., Billiris, H., Nakos, B., and Paradissis, D. (1992). Tectonic strain in Greece form geodetic measurements. *C. R. Acad. Sci. Athens*, 67:129–166.

Walcott, C. R. and White, S. H. (1998). Constraints on the kinematics of post-orogenic extension imposed by stretching lineations in the aegean region. *Tectonophysics*, 298:155–175.

Walpersdorf, A., Vigny, C., Subarya, C., and Manurung, P. (1998). Monitoring of the Palu-Koro Fault (Sulawesi) by GPS. *Geophys. Res. Lett.*, 25(13):2313–2316.

Walsh, J., Watterson, J., and Yielding, G. (1991). The importance of small-scale faulting in regional extension. *Nature*, 351:391–393.

Ward, S. N. (1998a). On the consistency of earthquake moment rates, geological fault data, and space geodetic strain: the United States. *Geophys. J. Int.*, 134:172–186.

Ward, S. N. (1998b). On the consistency of earthquake moment release and space-geodetic strain rate: Europe. *Geophys. J. Int.*, 135:1011–1018.

Webb, F. H. and Zumberge, J. F. (1997). An introduction to GIPSY-OASIS II. Jet propulsion laboratory document jpl d-11088, California Institute of Technology, USA.

Wessel, P. and Smith, W. H. F. (1995). New version of the generic mapping tools released. *Eos, Trans. AGU*, 76.

Wilson, P., Rais, J., Reigber, C., Seeger, H., Ambrosius, B. A. C., Pichon, X. L., Kasser, M., Suharto, P., Majid, D., Yaakub, D. A. H. O. B. H., and Almeda, R. (1998). Study provides data on active plate tectonics in Southeast Asian region. *Eos, Trans. AGU*, 79:545–549.

Yu, S.-B., Jackson, D. D., Yu, G.-K., and Liu, C.-C. (1990). Dislocation model for crustal deformation in the Longitudinal Valley Area, eastern Taiwan. *Tectonophysics*, 183:97–109.

Yu, S.-B., Kuo, L.-C., Punongbayan, R., and Ramos, E. G. (1999). GPS observation of crustal deformation in the Taiwan-Luzon region. *Geophys. Res. Lett.*, 26(7):923–926.

Zerbini, S., Bastos, L., and an B. Richter, H.-P. P., editors (1998). *WEGENER: An interdisciplinary contribution to unraveling the geodynamics of the European and Mediterranean area*, volume 294 of *Tectonophysics*. Elsevier Science B.V., The Netherlands.

Zhang, J., Johnson, Y. B. H., Fang, P., Williams, S., Genrich, J., Wdowinski, S., and Behr, J. (1997). Southern California permanent GPS geodetic array: Error analysis of daily position estimates and site velocities. *J. Geophys. Res.*, 102:18035–18055.